



**DEVELOPMENT OF METHODOLOGY AND NOVEL
COMPOSITE ELECTRODES FOR THE SELECTIVE
ELECTROCHEMICAL FLUORINATION OF ORGANIC
COMPOUNDS FOR USE IN POSITRON EMISSION
TOMOGRAPHY**

Thesis submitted by:

DAVID MOLYNEUX

For the degree of Doctor of Philosophy

Newcastle University

School of Chemical Engineering and Advanced Materials

September 2013

Declaration

The work carried out contributing to this thesis was conducted between September 2009 and September 2012 within the research laboratories of Prof. Paul Christensen and Dr Michael Carroll located in the Bedson Building, Newcastle University, Newcastle-upon-Tyne, NE1 7RU. This work was conducted in collaboration with the laboratories of: Prof. David Wood located within the School of Engineering and Computer Sciences, South Road, Durham University, DH1 3LE, Prof. David Collison located within the School of Chemistry, The University of Manchester, Oxford Road, Manchester, M13 9PL and Prof. Lothar Dunsch located within the Leibniz Institute for Solid State and Materials Research, Helmholtzstraße 20, Dresden, Germany.

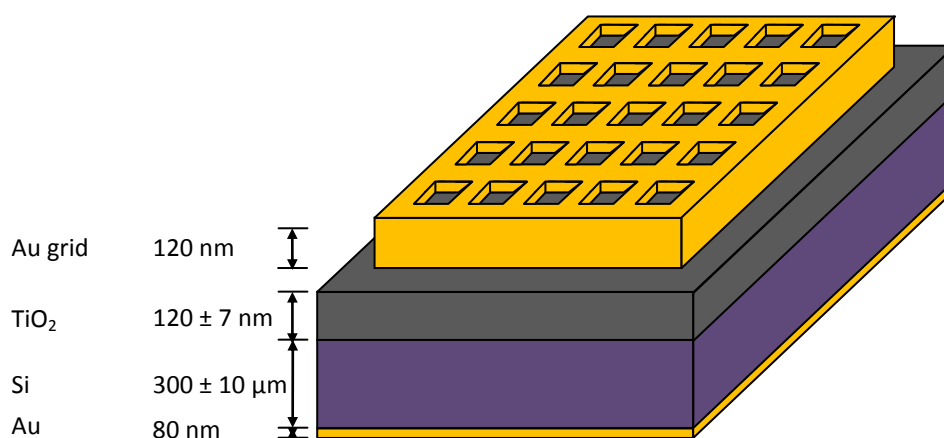
All of the work presented in this thesis is original in context and does not include any material or ideas published or presented by others authors except where due reference is given in the text.

No part of this thesis has previously been submitted for a degree, diploma or any other qualification at any other university.

products of each reaction were characterised fully by NMR for the first time, highlighting the interesting AA'XX' spin system displayed by the di-fluorinated compounds (3) and (4). *In-situ* electrochemical electron pair resonance (EPR) spectroscopy was performed in an attempt to elucidate the mechanism by which ECF occurs. The results of these studies were inconclusive; however, a radical-cation mechanism is postulated, based on a combination of molecular modelling calculations and literature.

The second section is concerned with the development of a completely new type of composite electrode which could potentially allow greater control of regioselectivity in ECF reactions as well as expanding the number of substrates to which the technique can be applied.

The composite anodes are comprised of a TiO₂ doped Si substrate upon which is deposited a metal grid. A battery connected between the metal grid and the back of the Si wafer allow a flow of electrons through the device (providing the bias circuit) in addition to the standard electrochemical circuit. The application of bias potential allows increased currents at lower electrochemical potentials.



Fundamental investigation into the electrochemical behaviour of the anodes resulted in the postulation of a theoretical model detailing the mechanism by which the anodes work. The model is based on the theory of hole generation and transport through the device by means of Anderson localisation and Miller-Abrahams hopping. It was found that irradiation of the anode surface further increased bias current, hence affording greater control by presenting a three-dimensional surface on which to operate, as opposed to a one-dimensional axis, as is the case with conventional electrodes.

Dedication

I would like to dedicate this thesis to my parents, Julie and Ian, my grandparents Alec, Florrie, Austin and Jean and my beautiful wife Lauren for all of their continued love and support over the years, without which I wouldn't be where I am today.

Acknowledgments

First and foremost I would like to thank my supervisors Prof. Paul Christensen and Dr Mike Carroll, without whom, this work would not have been possible. I would like to thank them for their patience, their knowledge and their kindness in all aspects of my training. I would also like to thank all the members of the PAC and MAC groups, both past and present: Dr Douglas Linares-Moya, Dr Ajchara Imkum, Dr Panos Moussas, Danny Lawrence, Steve Jones, Khalid Zakaria, Abdullah Al-Abduly, Pon Chiarasumran, Dr Pierrot Attidekou, Christopher Reed, Dr Stephen Hobson, Dr Guillaume Launay, Dr Luke Dixon, Michael Charlton, Sam Bhatt and Caroline McCardle for their friendship and support. I would also like to thank my mother-in-law, Dorothy Barrett and my father-in-law Kevin Barrett for their extensive support throughout my studies.

I would like to thank Prof. William McFarlane and Dr Corinne Wills for their expertise and continued support in NMR.

I would also like to thank Prof. David Wood and Dr Mark Rosamund from the School of Engineering and Computing Sciences at Durham University for their collaboration on the development of the composite anodes.

I would like to thank Prof. David Collison and Dr Jonathan Hawkett at the EPSRC national EPR service at the University of Manchester, and Prof. Lothar Dunsch and his group at the Leibniz Institute for Solid State and Materials research in Dresden for their collaboration with the EPR spectroscopy.

Finally, I would like to thank the EPSRC for providing the funding for this project and Newcastle University, particularly the schools of CEAM and Chemistry for providing me with the facilities and the opportunity to undertake this research.

Table of Contents

Declaration	1
Abstract	2
Dedication	4
Acknowledgments	5
Table of Contents	6
List of Figures, Schemes & Tables	10
Abbreviations	21
1. Introduction	25
1.1. General principles of organofluorine chemistry	25
1.1.1. <i>Examples and uses of fluorinated organic systems in industry</i>	25
1.1.2. <i>Fluorine in medicinal chemistry</i>	26
1.1.3. <i>Fluorine in Positron Emission Tomography (PET)</i>	29
1.1.3.1. Background to the use of PET in medicine.....	29
1.1.3.2. Isotope production.....	29
1.1.3.3. [¹⁸ F]Fluorination of target molecules.....	31
1.1.3.4. Electrochemical radiofluorination.....	32
1.1.3.5. Mechanism of detection.....	33
1.1.4. <i>Traditional methods of fluorination</i>	35
1.1.5. <i>Limitations of current synthetic routes</i>	36
1.2. Electrochemical fluorination	36
1.2.1. <i>Historical survey of selective electrochemical fluorination</i>	36
1.2.2. <i>The Simons process</i>	38
1.2.3. <i>The general electrochemical procedure</i>	40
1.2.4. <i>Electrochemical cell design</i>	41
1.2.5. <i>Electrodes</i>	42
1.2.6. <i>Experimental conditions</i>	43
1.2.7. <i>Substrates</i>	44
1.2.7.1. Aromatic substrates.....	44
1.2.7.2. Functionalised/heterocyclic substrates.....	45
1.2.8. <i>Molten salt electrolytes</i>	46
1.2.9. <i>Mechanisms of electrochemical fluorination</i>	49

1.3.	Project aims.....	50
2.	Experimental.....	51
2.1.	General information.....	51
2.2.	General procedure for the conventional ECF of ethylene carbonate.....	52
2.2.1.	<i>1,3-Dioxolan-2-one (1).....</i>	54
2.2.2.	<i>(±)-4-Fluoro-1,3-dioxolan-2-one (2).....</i>	54
2.2.3.	<i>Syn-(±)-4,5-difluoro-1,3-dioxolan-2-one (3).....</i>	54
2.2.4.	<i>Anti-(±)-4,5-difluoro-1,3-dioxolan-2-one (4).....</i>	55
2.3.	General procedure for the conventional ECF of propylene carbonate.....	55
2.3.1.	<i>(±)-4-Methyl-1,3-dioxolan-2-one (5).....</i>	56
2.3.2.	<i>(±)-4-Fluoro-4-methyl-1,3-dioxolan-2-one (6).....</i>	56
2.3.3.	<i>Syn-(±)-4-fluoro-5-methyl-1,3-dioxolan-2-one (7).....</i>	56
2.3.4.	<i>Anti-(±)-4-fluoro-5-methyl-1,3-dioxolan-2-one (8).....</i>	57
2.4.	Fitted electrode construction.....	57
2.5.	General procedure for the fabrication of the composite anodes.....	57
2.6.	General procedure for the preparation of Pt/Ti mesh electrodes.....	59
2.6.1.	<i>Preparation of the platinising solution.....</i>	59
2.6.2.	<i>Preparation of Ti meshes.....</i>	60
2.6.3.	<i>Platinum electrodeposition procedure.....</i>	60
2.7.	General procedure for the characterisation of the composite anodes.....	62
2.7.1.	<i>General procedure for obtaining the device characteristic curve.....</i>	62
2.7.2.	<i>General procedure for performing cyclic voltammetry with the composite anodes.....</i>	62
2.7.3.	<i>The electrochemical and bias circuits.....</i>	64
2.8.	Composite anodes for anhydrous ECF.....	65
2.8.1.	<i>Platinisation of composite anodes.....</i>	65
2.8.2.	<i>Determination of Pt quasi RE limits.....</i>	66
2.8.3.	<i>Anhydrous characterisation of composite anodes.....</i>	67

2.9.	Effects of varying H₂SO₄/HClO₄/NaOH concentration.....	67
2.10.	The composite electrolysis of KF.....	67
2.11.	General procedure for the conventional ECF of benzotrifluoride.....	68
2.11.1.	2,5 – Difluorobenzotrifluoride (9).....	69
2.11.2.	3,4 – Difluorobenzotrifluoride (10).....	70
2.11.3.	Benzotrifluoride standard (11).....	70
2.11.4.	2-Fluorobenzotrifluoride standard (12).....	71
2.11.5.	3-Fluorobenzotrifluoride standard (13).....	71
2.11.6.	4-Fluorobenzotrifluoride standard (14).....	71
2.11.7.	2,5-Difluorobenzotrifluoride standard (15).....	72
2.11.8.	2,6-Difluorobenzotrifluoride standard (16).....	72
2.11.9.	3,4-Difluorobenzotrifluoride standard (17).....	73
2.11.10.	3,5-Difluorobenzotrifluoride standard (18).....	73
2.12.	Composite electrolyses.....	73
2.12.1.	<i>The composite electrolysis of benzotrifluoride on the anode surface.....</i>	73
2.12.2.	<i>The composite electrolysis of anisole on the anode surface.....</i>	74
2.12.3.	<i>The composite electrolysis of anisole in solution.....</i>	75
2.12.4.	<i>The composite electrolysis of anisole in solution (with bias).....</i>	76
2.13.	Electrochemical fluoride capture.....	76
3.	ECF of Cyclic Carbonates.....	78
3.1.	Cyclic carbonates background.....	78
3.2.	Electrolysis of cyclic carbonates.....	79
3.3.	¹⁹F NMR of cyclic carbonates.....	83
3.3.1.	<i>Fluorinated ethylene carbonate.....</i>	83
3.3.2.	<i>Fluorinated propylene carbonate.....</i>	86
3.4.	Mechanistic studies.....	91
3.4.1.	<i>In-situ electrochemical EPR spectroscopy.....</i>	91
3.4.2.	<i>Proposed ECF mechanism.....</i>	108
4.	Composite Anodes.....	110
4.1.	Introduction.....	110
4.2.	Background and previous work.....	110
4.3.	The model.....	112

4.3.1.	<i>Electron transport through the composite anode</i>	112
4.3.2.	<i>Electrochemical circuit</i>	116
4.4.	Results and discussion	118
4.4.1.	<i>The current/voltage characteristic of the Si/TiO₂/Au composite electrode in air</i>	118
4.4.2.	<i>The electrochemical behaviour of the composite electrode at low bias voltages</i>	120
4.4.3.	<i>The oxidation of I₃⁻</i>	133
4.4.4.	<i>The electrochemical behaviour of the composite electrode at higher bias voltages</i>	137
4.4.5.	<i>Electrodeposition and characterisation of Pt composite anode.</i>	139
4.4.6.	<i>Effect of concentration and electrolyte</i>	147
4.4.7.	<i>Irreversibility study</i>	153
4.4.8.	<i>Anhydrous characterisation of composite anodes</i>	156
4.4.9.	<i>Initial studies on the oxidation of fluoride</i>	162
5.	Composite ECF of Aromatics	170
5.1.	Benzotrifluoride	170
5.1.1.	<i>Conventional electrolysis of benzotrifluoride</i>	170
5.1.2.	<i>Composite electrolysis of benzotrifluoride on anode surface</i>	172
5.2.	Anisole	175
5.2.1.	<i>Composite electrolysis of anisole on anode surface</i>	175
5.2.2.	<i>Composite electrolysis of anisole in solution (no bias)</i>	177
5.2.3.	<i>Biased composite electrolysis of anisole</i>	180
6.	Electrochemical Fluoride Capture	182
7.	Conclusions	185
8.	Future Work	187
	References	189

List of Figures, Schemes & Tables

Figure 1.1.	The chemical structure of (i) polymer unit of PTFE; (ii) Desflurane®;(iii) 5-fluorouracil; (iv) [¹⁸ F]FDOPA.....	26
Figure 1.2.	Fluorine containing drugs launched, worldwide, between 1957-2006, excluding biologics, inorganics, reformulations and agricultural agents.....	27
Figure 1.3.	The chemical structure of (i) Prozac®; (ii) Faslodex®; (iii) Fluorithromycin; (iv) Efavirenz.....	27
Figure 1.4.	Synthesis of simple [¹⁸ F]fluoroaromatic precursors by direct nucleophilic substitution with [¹⁸ F]fluoride. EWG = electron withdrawing group (NO ₂ , CN, carbonyl); LG = leaving group (NO ₂ , halide, OTf, OMs, trialkylammonium halide); X = I or Br...	31
Figure 1.5.	General structure of phenylalanine derivatives labelled by Rieschl et al. X = acetyl, trifluoroacetyl, butoxycarbonyl, 2,4-dinitrophenyl; Y = ethyl, methyl; R = H, t-Bu.....	33
Figure 1.6.	Chemical structure of [¹⁸ F]FDG.....	33
Figure 1.7.	Schematic representation of positron annihilation and detection.....	34
Figure 1.8.	An example of PET imaging of mGluR5 receptors in human brain with [¹⁸ F]SP203.....	34
Figure 1.9.	Schematic representation of the solvent/acid mediated electrophilic fluorination of a nucleophile using F ₂	35
Figure 1.10.	The first example of anodic partial fluorination.....	37
Figure 1.11.	The ECF of naphthalene using HF derived ammonium salts.....	38
Figure 1.12.	Selective ECF α-to an electron withdrawing group.....	38
Figure 1.13.	A schematic representation of the Phillips petroleum cell for electrochemical fluorination.....	41
Figure 1.14.	The ECF of benzotrifluoride.....	44
Figure 1.15.	The selective ECF of 2-indanone.....	45
Figure 2.1.	Diagram of the 20 cm ³ , five-necked, Schlenk compatible electrochemical cell shown from (a) side-view and (b) aerial view.....	53

Figure 2.2.	Schematic representation of fitted electrodes, designed to fit the cell shown in fig. 2.1.....	53
Figure 2.3.	Diagrammatical representation of (a) an Au/Si/TiO ₂ /Au composite wafer and (b) a quarter segment of an Au/Si/TiO ₂ /Au composite wafer to be fabricated into a composite anode.....	58
Figure 2.4.	(a) Aerial photograph of a fabricated composite anode showing the 2 connections to the Au grid covered with araldite rapid and the single connection to the back of the wafer and (b) side-view, close-up of both the Au and Si connections.....	59
Figure 2.5.	(a) EDX analysis of platinised Ti mesh and SEM images of platinised Ti mesh surface at magnification (b) x 1500 and (c) x 5000.....	61
Figure 2.6.	(a) Diagram of 20 cm ³ electrochemical cell used for composite electrolysis and (b) photograph of the same glass electrochemical cell configured for cyclic voltammetry.....	63
Figure 2.7.	The composite anode and electrochemical cell. (1) Battery, (2) Au Ohmic contact on the silicon wafer (3), (4) the TiO ₂ layer, (5) the gold grid, (6) the Pt/Ti mesh counter electrode and (7) the reference electrode and (8) the electrolyte.....	64
Figure 2.8.	The circuit employed to maintain constant voltages across the composite anode when using a battery: (i) 1 kΩ potentiometer, (ii) CA3140 op-amp, (iii) 470 Ω resistor and (iv) BD139 NPN transistor.....	65
Figure 2.9.	Coulometry of Au/Si/TiO ₂ /Au anode in 0.01 M chloroplatinic Acid/0.01 M H ₂ SO ₄ . Cell voltage = -1 V, t = 3600 s, Charge = -1 C, data points recorded every 0.5 s.....	66
Figure 2.10.	Diagram showing irradiation of composite anode thorough a 5 cm water filter.....	74
Figure 2.11.	Schematic representation of the remote-controlled ModularLab flow system.....	77
Figure 3.1.	Cyclic voltammogram of the 1.0 cm × 0.5 cm Pt mesh working electrode immersed in Et ₄ NF ₄ HF in the (i) absence and (ii) presence of 18.2 mmol PC at a scan rate of 100 mV s ⁻¹	80

Figure 3.2.	Schematic representation of an AA'XX' system, indicating the plane of symmetry which relates the two halves.....	84
Figure 3.3.	(a) ¹⁹ F NMR spectrum of <i>syn</i> -(±)-4,5-difluoro-1,3-dioxolan-2-one (3) showing the pattern typical of AA'XX' spin systems with the separations equal to: i) K ii) N iii) M iv) 2R; (b) simulated ¹⁹ F NMR spectrum constructed from coupling constants calculated from the actual spectrum.....	85
Figure 3.4.	Arrangement and assignation of atoms in <i>syn</i> -(±)-4,5-difluoro-1,3-dioxolan-2-one (3).....	86
Figure 3.5.	(a) ¹⁹ F NMR spectrum of (±)-4-fluoro-4-methyl-1,3-dioxolan-2-one (6) showing the unusual splitting pattern; (b) simulated ¹⁹ F NMR spectrum constructed from coupling constants calculated from the actual spectrum.....	87
Figure 3.6.	Stacked ¹ H NMR spectra showing selective homonuclear spin decoupling of the double doublet at δ/ppm 4.33.....	89
Figure 3.7.	Difference NOE Spectra of the propylene carbonate product mixture, showing through-space interactions between protons in: 5-fluoro-5-methyl-1,3-dioxolan-2-one (6), <i>syn</i> -(±)-4-fluoro-5-methyl-1,3-dioxolan-2-one (7) and <i>anti</i> -(±)-4-fluoro-5-methyl-1,3-dioxolan-2-one (8).....	90
Figure 3.8.	Structures of <i>syn</i> - and <i>anti</i> -(±)-4-fluoro-5-methyl-1,3-dioxolan-2-one (7 & 8).....	91
Figure 3.9.	Relative energies of electron spins in the absence of a magnetic field.....	92
Figure 3.10.	A schematic representation of the effect of a magnetic field of strength B ₀ on the energies of electrons where S = ½.....	93
Figure 3.11.	Diagram showing the modulation of a magnetic field by means of localised electrical fields generated by coils in the walls of the cavity.....	93
Figure 3.12.	Schematic representation of the <i>in-situ</i> electrochemical EPR cell used at the EPSRC national EPR service in Manchester.....	95
Figure 3.13.	<i>In-situ</i> electrochemical EPR spectrum of ethylene carbonate in 0.15 M Bu ₄ BF ₄ in MeCN after 5 scans.....	96

Figure 3.14.	<i>In-situ</i> electrochemical EPR spectrum of ethylene carbonate in 0.15 M Bu ₄ BF ₄ in MeCN after 13 scans.....	97
Figure 3.15	Schematic representation of <i>in-situ</i> electrochemical EPR/ UV-vis-NIR set-up.....	98
Figure 3.16.	Photograph showing <i>in-situ</i> EPR/UV-vis-NIR equipment.....	98
Figure 3.17.	Diagram of the <i>in-situ</i> electrochemical EPR cell from (a) the front and (b) the side.....	100
Figure 3.18.	(a) CV and (b) Current trace CV of PC in Et ₄ NF ₄ HF between 0.0 V and 2.0 V vs. CE obtained in conjunction with pulse EPR.....	101
Figure 3.19.	(a) CV and (b) Current trace CV of PC in Et ₄ NF ₄ HF between 0.0 V and 1.19 V vs. CE obtained in conjunction with pulse EPR.....	102
Figure 3.20.	Typical EPR spectrum obtained during CV of 1.82 mmol PC in 4.36 mmol Et ₄ NF ₄ HF.....	103
Figure 3.21.	EPR signal from the electrolysis of propylene carbonate at 5 V constant potential in 0.3 M Bu ₄ NBF ₄ /MeCN (1.0:2.4) obtained at the anode.....	104
Figure 3.22.	EPR signal from the electrolysis of propylene carbonate at 5 V constant potential in 0.3 M Bu ₄ NBF ₄ /MeCN (1.0:2.4) obtained at the cathode.....	105
Figure 3.23.	EPR signal from the electrolysis of propylene carbonate at 5 V constant potential in 0.3 M Bu ₄ NBF ₄ /MeCN (1.0:2.4) – cathode...	106
Figure 3.24.	Resonance stabilisation of an acetonitrile radical.....	107
Figure 3.25.	Schematic representation of the change in energy of the SOMO upon stabilisation by the electron-withdrawing nitrile group.....	108
Figure 3.26.	Proposed mechanism for the electrochemical fluorination of cyclic carbonates.....	109
Figure 3.27.	Proposed mechanism of the deprotonation step.....	109
Figure 4.1.	Schematic representation of a cross-section of a gold composite anode.....	110
Figure 4.2.	The proposed band structure of the Si/TiO ₂ /Au composite anode: (a) at zero bias and (b) high positive bias on the Si with respect to the Au. The Fermi levels (E _F) of the Si and TiO ₂ are shown in grey.....	113

Figure 4.3.	Transmission Electron Micrograph (TEM) of TiO ₂ layer of a composite anode.....	114
Figure 4.4.	Schematic representation of bias circuit (red) and electrochemical circuit (blue).....	116
Figure 4.5.	Graphical representation of hole-facilitated hydroxide oxidation by the transport of holes to the TiO ₂ surface.....	117
Figure 4.6.	(a) Typical bias current vs. bias voltage plot for a Si/TiO ₂ /Au composite anode. (b) Bias current vs. voltage plots for a Si/TiO ₂ /Au composite anode (i) in the dark, (ii) irradiated by a 635 nm, 4.0 mW LED and (iii) irradiated by a 1550 nm, 2.0 mW LED. The LED's were positioned 1 mm from the TiO ₂ /Au face of the anode.....	119
Figure 4.7.	Cyclic voltammograms of the Si/TiO ₂ /Au composite anode immersed in 0.5 M H ₂ SO ₄ as a function of bias voltage in the dark between V _b = 0 (i) and 0.8 V (ix) in 0.1 V steps. (a) full potential range, (b) the voltammograms in (a) showing just the potential range -0.2 V to 0.8 V vs. SCE.....	121
Figure 4.8.	(a) Schematic representation of the blank experiment set-up; (b) I/V plot generated during the blank experiment.....	123
Figure 4.9.	Plot of the peak potential of the small cathodic peak in fig. 4.7 vs. bias voltage.....	124
Figure 4.10.	(a) Cyclic voltammograms of the (Au)/Si/TiO ₂ /Au composite anode as a function of bias voltage, V _b from (i) no bias to (x) V _b = 0.9 V in 100 mV steps and (b) Selected voltammograms from fig. 4.10(a) for V _b = 0 (i), 0.9 V (ii) and 0.5 V (iii)	125
Figure 4.11.	Plots of the peak potentials of (i) peak (II) and (ii) peak (III) in fig. 4.10(a) as a function of V _b	127
Figure 4.12.	Cyclic voltammograms of a 0.2 mm diameter, 16 cm long Au wire immersed in 0.5 M H ₂ SO ₄ at a scan rate of 100 mV s ⁻¹ . Anodic limit: (i) – (vi) 0.7 V to 1.2 V in 0.1 V steps; (vii) – (xiii) 1.3 V to 1.65 V in 0.05 V steps.....	128
Figure 4.13.	Plot of the peak potential of the cathodic stripping feature in fig. 4.12 as a function of anodic limit.....	129

- Figure 4.14.** Cyclic voltammograms of (Au)/Si/TiO₂/Au electrode at **(a)** 0.3 V bias and **(b)** 0.5 V bias as function of scan rate: (i) 10, (ii) 50, (iii) 100, (iv) 250 and (v) 500 mV s⁻¹; **(c)** A comparison of the CV's in (a) at (i) 500 mVs⁻¹ and (ii) 10 mVs⁻¹, the latter voltammogram is increased by a factor of 10 for clarity; **(d)** A comparison of the CV's in (b) at (i) 500 mVs⁻¹ and (ii) 10 mVs⁻¹, the latter voltammogram is increased by a factor of 14 for clarity..... 130
- Figure 4.15.** Plots of peak current vs. $\sqrt{\text{Scan rate}}$ for the cathodic peaks in figs. 4.14(a) & (b). (i) Peak II $V_b = 0.3$ V, (ii) peak III $V_b = 0.3$ V, (iii) peak II $V_b = 0.5$ V and (iv) peak III $V_b = 0.5$ V..... 133
- Figure 4.16.** **(a)** Cyclic voltammograms of the (Au)Si/TiO₂/Au electrode in 0.5 M H₂SO₄ at $V_b =$ (i) 0 and (ii) 0.2 V to (v) 0.5 V vs. SCE in fig. 4.10(a); **(b)** CV's collected at $V_b =$ (i) 0 and (ii) 0.2 V to (v) 0.5 V vs. SCE in 0.5 M H₂SO₄ + 0.05 mM KI; **(c)** the cyclic voltammograms collected at zero bias in (a) & (b) in (i) the presence and (ii) absence of 0.05 mM KI; cyclic voltammograms of a Au wire coiled to expose 2 cm² to the electrolyte in the (iii) absence and (iv) presence of 0.05 mM KI; **(d)** direct comparison of the CV's collected at $V_b = 0.4$ V in figs. 4.16(a) and (b)..... 134
- Figure 4.17.** Cyclic voltammograms of the (Au)Si/TiO₂/Au composite anode immersed in 0.5 M H₂SO₄ as a function of bias voltage at $V_b = 0.9$ V (red), 1.0 V (black), 1.5 V (blue) and 2.0 V (green)..... 138
- Figure 4.18.** Plots of bias current vs. bias voltage collected during experiments where the potential of the (Au)Si/TiO₂/Au composite anode was held at (\blacktriangle) -0.1 V and (\blacksquare) +1.65 V vs. SCE in 0.5 M H₂SO₄..... 139
- Figure 4.19.** Comparison of DCCs of gold composite anode in air and in 0.5 M H₂SO₄ between -0.1 V and 3 V (pre bias)..... 140
- Figure 4.20.** Comparison of CVs of gold composite anode in 0.5 M H₂SO₄ between -0.25 V and 1.65 V vs. SCE, scan rate = 100 mV s⁻¹, $V_b =$ 0.0 V, 0.2 V, 0.5 V and 1.0 V..... 141
- Figure 4.21.** Comparison of CVs of a gold composite anode in 0.5 M H₂SO₄ between -0.25 V and 1.65 V vs. SCE, scan rate = 100 mV s⁻¹, $V_b =$ 0.0 V, pre and post the experiment shown in fig. 4.20..... 141

Figure 4.22.	Comparison of DCCs of a gold composite anode in 0.5 M H ₂ SO ₄ between -0.1 V and 3.0 V, pre and post bias.....	142
Figure 4.23.	Comparison of DCCs of Pt coated gold composite anode in air and in 0.5 M H ₂ SO ₄ between -0.1 V and 3 V (pre bias).....	143
Figure 4.24.	Comparison of CVs of a Pt coated gold composite anode in 0.5 M H ₂ SO ₄ between -0.25 V and 0.85 V vs. SCE, scan rate = 100 mV s ⁻¹ , V _b = 0.0 V, 0.2 V, 0.5 V and 1.0 V.....	144
Figure 4.25.	Comparison of CVs of a Pt coated gold composite anode in 0.5 M H ₂ SO ₄ between -0.25 V and 0.85 V vs. SCE, scan rate = 100 mV s ⁻¹ , V _b = 0.0 V, pre and post bias.....	144
Figure 4.26.	Comparison of DCCs of a Pt coated gold composite anode in 0.5 M H ₂ SO ₄ between -0.1 V and 3 V, pre and post bias.....	145
Figure 4.27.	CV of Pt wire in 0.5 M H ₂ SO ₄ between -0.80 V and 0.40 V vs. Pt (quasi reference electrode), scan rate = 100 mV s ⁻¹	146
Figure 4.28.	Comparison of CVs of a Pt coated gold composite anode in 0.5 M H ₂ SO ₄ between -0.8 V and 0.4 V vs. Pt (quasi), scan rate = 100 mV s ⁻¹ , V _b = 0.0 V, 0.2 V, 0.5 V and 1.0 V.....	146
Figure 4.29.	Comparison of CVs of a Pt coated gold composite anode in 0.5 M H ₂ SO ₄ between -0.8 V and 0.4 V vs. Pt (quasi), scan rate = 100 mV s ⁻¹ , V _b = 0.0 V, pre and post bias.....	147
Figure 4.30.	Comparison of DCCs of a Pt coated gold composite anode in air, pre and post H ₂ SO ₄ , between -0.1 V and 3 V, scan rate = 100 mV s ⁻¹	148
Figure 4.31.	Comparison of DCCs of a Pt coated gold composite anode in: H ₂ O, 0.001 M H ₂ SO ₄ , 0.01 M H ₂ SO ₄ , 0.1 M H ₂ SO ₄ , 0.5 M H ₂ SO ₄ and 1.0 M H ₂ SO ₄ between -0.1 V and 3 V, scan rate = 100 mV s ⁻¹ ..	149
Figure 4.32.	Comparison of DCCs of a Pt coated gold composite anode in air, pre and post HClO ₄ , between -0.1 V and 3 V, scan rate = 100 mV s ⁻¹	150
Figure 4.33.	Comparison of DCCs of a Pt coated gold composite anode in: H ₂ O, 0.001 M HClO ₄ , 0.01 M HClO ₄ , 0.1 M HClO ₄ , 0.5 M HClO ₄ and 1.0 M HClO ₄ between -0.1 V and 3 V, scan rate = 100 mV s ⁻¹ .	150

Figure 4.34.	Comparison of DCCs of a Pt coated gold composite anode in air (pre H ₂ SO ₄ and HClO ₄), between -0.1 V and 3 V, scan rate = 100 mV s ⁻¹	151
Figure 4.35.	Comparison of DCCs of a Pt coated gold composite anode in air, pre and post NaOH, between -0.1 V and 3 V, scan rate = 100 mV s ⁻¹	152
Figure 4.36.	Comparison of DCCs of a Pt coated gold composite anode in: H ₂ O, 0.001 M NaOH, 0.01 M NaOH, 0.1 M NaOH, 0.5 M NaOH and 1.0 M NaOH between -0.1 V and 3 V, scan rate = 100 mV s ⁻¹ ..	152
Figure 4.37.	Comparison of DCCs of a Pt coated gold composite anode in air, pre and post solutions, between -0.1 V and 3 V, scan rate = 100 mV s ⁻¹	154
Figure 4.38.	Comparison of DCCs of a Pt coated gold composite anode in H ₂ O, before and after each solution, between -0.1 V and 3 V, scan rate = 100 mV s ⁻¹ in run order (i, ii and iii).....	155
Figure 4.39.	Comparison of DCCs of a Pt coated gold composite anode in: H ₂ O, 1.0 M H ₂ SO ₄ , 1.0 M HClO ₄ and 1.0 M NaOH, between -0.1 V and 3 V, scan rate = 100 mV s ⁻¹ in run order (i, ii and iii).....	156
Figure 4.40.	Comparison of DCCs of a Pt coated gold composite anode in air, outside and inside the glove box, between -0.1 V and 3 V, scan rate = 100 mV s ⁻¹	157
Figure 4.41.	Comparison of DCCs of a Pt coated gold composite anode in air (inside glove box) and Et ₄ NF ₄ HF, between -0.1 V and 3 V, scan rate = 100 mV s ⁻¹	158
Figure 4.42.	Comparison of CVs of a Pt coated gold composite anode in Et ₄ NF ₄ HF, between -0.2 V and 1.2 V, scans 2 and 3, scan rate = 100 mV s ⁻¹	159
Figure 4.43.	Comparison of CVs of a Pt coated gold composite anode in Et ₄ NF ₄ HF, between -0.2 V and 1.4 V, scans 1, 2 and 3, scan rate = 100 mV s ⁻¹	160
Figure 4.44.	Comparison of CVs of a Pt coated gold composite anode in Et ₄ NF ₄ HF, between -0.2 V and 1.2 V vs. Pt (after 1.4 V vs. Pt), scans 1, 2 and 3, scan rate = 100 mV s ⁻¹	161
Figure 4.45.	SEM showing imperfections at the edges of the Pt grid.....	161

Figure 4.46.	Cyclic voltammograms of the (Au)Si/TiO ₂ /Pt composite anode (Pt grid area <i>ca.</i> 2 cm ²) immersed in pH 9.7 NaOH/0.1 M Na ₂ SO ₄ in the (i) absence and (ii) presence of 0.1 M KF at, (a) V _b = 0 V and (b) V _b =1.0 V. scan rate 100 mVs ⁻¹	162
Figure 4.47.	Cyclic voltammograms of the (Au)Si/TiO ₂ /Pt electrode in figs. 4.19(a) & (b) in the (i) absence and (ii) presence of 0.1 M KF at, (a) V _b = 2 V and (b) V _b = 3 V. scan rate 100mVs ⁻¹	164
Figure 4.48.	SEM image of the damaged composite anode taken at a resolution x 50 using electron back scattering under low vacuum.....	167
Figure 4.49.	EDX spectrum of an (a) undamaged and (b) damaged section of the destroyed composite anode. (c) An overlay of figs 4(a) and (b) for direct comparison.....	168
Figure 5.1.	Chronoamperomogram showing electrolysis of benzotrifluoride in 1.0 M TBAF/MeCN at 3.2 V vs Pt quasi reference electrode for 23324 s, recording data points every 28 s.....	171
Figure 5.2.	Structures of the main products observed from the ECF of benzotrifluoride: 2,5-difluorobenzotrifluoride (9) and 3,4-difluorobenzotrifluoride (10).....	172
Figure 5.3.	Comparison of DCCs of a gold composite anode, with and without benzotrifluoride/TBAF, in air between -0.1 V and 3.0 V, scan rate = 100 mV s ⁻¹ , hv = 250 lux (ambient light) and max. lux.....	173
Figure 5.4.	Chronoamperomogram of a gold composite anode with TFT/TBAF at potential of 3 V, hv = max. lux, t = 7200 s.....	174
Figure 5.5.	Comparison of DCCs of a gold composite anode doped with an anisole/TBAF/EtOAC substrate with and without irradiation, between -0.1 V and 3.0 V at a scan rate of 100 mV s ⁻¹	176
Figure 5.6.	Chronoamperomogram of a gold composite anode in anisole/TBAF/EtOAC, at an EC potential of 3.0 V and at maximum light intensity for 24 hours, recording a data point every 9 s.....	177
Figure 5.7.	Comparison of DCCs of a gold composite anode in 0.25 M TBAF/MeCN between -0.1 V and 3 V, hv = 250 lux and max lux..	178

Figure 5.8.	Comparison of DCCs of a gold composite anode in: air, 0.25 M TBAF/MeCN and 0.25 M TBAF/MeCN + 0.25 M Anisole, between -0.1 V and 3 V at (a) 250 lux and (b) max lux.....	179
Figure 5.9.	Comparison CVs of a gold composite anode in 0.5 M TBAF/MeCN with and without 0.25 M Anisole between 0 V and 3 V vs. SCE, scan rate = 100 mV s ⁻¹	180
Figure 5.10.	Comparison CVs of a gold composite anode in 0.5 M TBAF/MeCN + 0.25 M Anisole, between 0 V and 3 V vs. SCE, scan rate = 100 mV s ⁻¹ , V _b = 3 V at minimum and maximum light intensity.....	181
Figure 5.11.	Photograph of the gold composite anode after DCCs and CVs with applied bias potential.....	181
Figure 6.1.	Schematic representation of the electrochemical fluoride capture flow cell.....	183
Figure 6.2.	Schematic representation of the remote-controlled ModularLab flow system.....	184
Figure 8.1.	Suggested cyclic carbonates for further ECF.....	187
Figure 8.2.	(i) Schematic showing current situation of gold grid with respect to TiO ₂ on the composite anodes; (ii) schematic depicting suggested recession of gold grid into TiO ₂	187
Scheme 1.1.	A mechanism depicting the ECF of thiazolidinones.....	46
Scheme 1.2.	Rozhkov's proposed radical-anion mechanism of ECF.....	50
Scheme 3.1	Major products obtained from the electrolysis of ethylene carbonate (1) and propylene carbonate (5) . x = 3, 4; Y = 50, 100, 200.....	82
Scheme 3.2.	The proposed mechanism of the electrochemical Thorpe reaction.....	107
Scheme 5.1.	Schematic representation of the conventional ECF of benzotrifluoride.....	170
Scheme 5.2.	Proposed route of electrochemical oxidation by generation of hypofluorous acid intermediate.....	175
Scheme 5.3.	Proposed mechanism of electrophilic oxidation of anisole by hypofluorous acid.....	175

Table 1.1.	A selection of substrates and products of selective ECF reported by Fuchigami et al.....	47
Table 3.1.	Summary of product yields and distribution from the ECF of ethylene carbonate (1) and propylene carbonate (5).....	81
Table 4.1.	Characteristics of the voltammograms in fig. 4.10(b).....	127
Table 4.2.	The slopes of the plots in fig. 4.15 in $10^{-4}AV^{-0.5}s^{-0.5}$	133
Table 4.3.	Comparison of effect of concentration on DCCs in acidic and basic media.....	153

Abbreviations

Å	-	Angstroms
A	-	Amperes
AcOH	-	Acetic Acid
¹³ C NMR	-	Carbon 13 NMR
CA	-	Chronoamperomogram
<i>ca.</i>	-	<i>circa</i> (around/approximately)
cat.	-	Catalytic
CE	-	Counter Electrode
cm	-	Centimetre(s)
CV	-	Cyclic Voltammety/Voltammogram
°C	-	Degrees Celsius
d	-	Doublet
DCC	-	Device Characteristic Curve
DCM	-	Dichloromethane
dd	-	Double doublet
DMSO	-	Dimethyl Sulfoxide
e ⁻	-	Electron(s)
EC	-	Electrochemical
ECF	-	Electrochemical Fluorination
EDX	-	Energy Dispersion X-ray Spectroscopy
<i>e.g.</i>	-	<i>Exempli gratia</i> (For example)
EI-MS	-	Electron Ionisation Mass Spectrometry
EPR	-	Electron Pair Resonance Spectroscopy
Eq.	-	Equivalents
Et	-	Ethyl
<i>et al.</i>	-	<i>Et alia</i> (and others)
Fig.	-	Figure
FT-IR	-	Fourier Transform Infra Red

g	-	Grams
GC-MS	-	Gas Chromatography Mass Spectrometry
^1H NMR	-	Proton NMR
h	-	Hour
H	-	Hydrogen
Hz	-	Hertz
<i>i.e.</i>	-	<i>id est</i> (that is)
IR	-	Infrared
<i>J</i>	-	Coupling constant
kcal	-	kilocalories
M	-	Molar
M^+	-	Molecular ion peak
$[\text{M}+\text{H}]^+$	-	Mass of molecular ion plus the mass of proton
$[\text{M}+\text{Na}]^+$	-	Mass of molecular ion plus the mass of a sodium ion
m (NMR)	-	Multiplet
mA	-	Milliamps
Me	-	Methyl
MeCN	-	Acetonitrile
MeOH	-	Methanol
mg	-	Milligrams
MHz	-	Megahertz
min	-	Minutes
ml	-	Millilitre
mm	-	Millimetre
mm/Hg	-	Millimetres of mercury
MMO	-	Mercury/Mercury Oxide [reference electrode]
mmol	-	Millimoles
mol	-	Moles

m.pt.	-	Melting point
mV	-	Millivolts
m/z	-	Mass to charge ratio
NHE	-	Normal Hydrogen Electrode
NMR	-	Nuclear Magnetic Resonance
p	-	Pentet
Petrol	-	Petroleum ether 40-60
Ph	-	Phenyl
ppm	-	Parts per million
q	-	Quartet
RE	-	Reference Electrode
Rf	-	Retention factor
RT	-	Room Temperature
s (NMR)	-	Singlet
s	-	Seconds
SCE	-	Standard Calomel Electrode
SEM	-	Scanning Electron Microscopy
S _N 2	-	Bimolecular Nucleophilic Substitution
S _N Ar	-	Nucleophilic Aromatic Substitution
SSCE	-	Silver/Silver Chloride Electrode
t	-	Triplet
<i>t</i> -BuOH	-	Tertiary butanol
TBAF	-	Tetrabutylammonium Fluoride
TBAHS	-	Tetrabutylammonium Hydrogen Sulfate
td	-	Triple Doublet
TEMPO	-	2,2,6,6-Tetramethylpiperidine-1-oxyl
THF	-	Tetrahydrofuran
TLC	-	Thin Layer Chromatography

tt	-	Triple triplet
$\nu_{\max}/\text{cm}^{-1}$	-	Maximum vibrational frequency in cm^{-1}
V	-	Volts
V_b	-	Bias Voltage
vs.	-	<i>Versus</i> (against)
WE	-	Working Electrode
XRD	-	X-ray Diffraction

1. Introduction

1.1. General principles of organofluorine chemistry

From as early as 1530 *A.D.*, fluorine (from the Latin: *fluere*, meaning “to flow”) was used, in the form of the mineral fluorspar (or fluorite as it is sometimes known), as a flux in the mining industry, as described by the German physician Georg Bauer in his “*De re Metallica*”.¹ In spite of its frequent use as a flux and, from 1670, a glass etching agent in the form of hydrofluoric acid (HF), it was not until 1886 that the French chemist, Henri Moissan, isolated elemental fluorine, by electrolysis of potassium fluoride (KF) in hydrofluoric acid (HF_(aq.)) at a platinum anode (eq. (1.1) & (1.2)),² for which he was awarded the Nobel Prize in Chemistry in 1906.³



On the Pauling scale, fluorine is the most electronegative of all the elements known ($\chi = 4$).⁴ This value was calculated using equation (1.3), where the energies required to dissociate two non-polar, covalent bonds A-A and B-B are E_{AA} and E_{BB} , and Δ is the difference in electronegativity between A and B.

$$E_{AB} = \frac{1}{2} E_{AA} + \frac{1}{2} E_{BB} + \Delta^2 \quad (1.3)$$

It is the electronegativity of fluorine that makes its chemistry unique. The high electronegativity means that fluorine forms highly polarised bonds with carbon, the character of which is often considered to be more ionic than covalent.⁵ As a consequence of this large dipole, the C-F bond is the strongest bond in organic chemistry (441 kJ mol⁻¹ or 105.4 kcal mol⁻¹),⁵ making the inclusion of fluorine into a molecule extremely attractive for a variety of applications.

1.1.1. Examples and uses of fluorinated organic systems in industry

Throughout the last century, fluorinated organics have proved to have widespread application throughout the chemical industry: from refrigerants (hydrofluorocarbons), fire extinguishers (bromofluorocarbons), lubricants (perfluoropolyethers) and materials (polytetrafluoroethene (PTFE), fig. 1.1(i)) to anaesthetics (Desflurane®, fig. 1.1(ii)),

pharmaceuticals (5-fluorouracil, fig. 1.1(iii)) and positron emission tomography (PET) imaging agents ($[^{18}\text{F}]\text{FDOPA}$, fig. 1.1(iv)).⁶ One area, in particular, in which fluorine compounds feature prominently, is in the design of drug molecules, largely owing to the increased hydrophilicity/bioavailability and metabolic stability, and hence potency often observed upon inclusion of fluorine into such molecules.⁷ The many important applications coupled with the fact that very few naturally occurring compounds contain fluorine (only about 13 naturally occurring metabolites are known),⁸ means that the synthesis of fluorinated compounds has been the focus of much research in previous years.

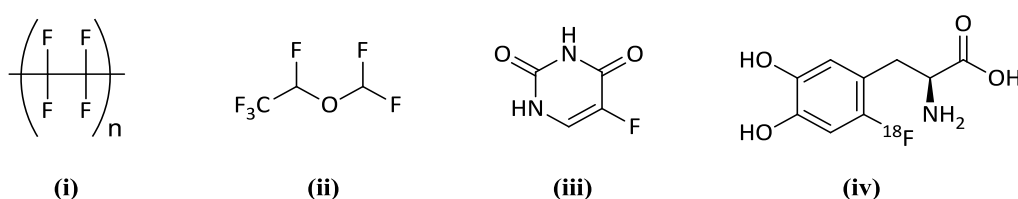


Figure 1.1. The chemical structure of (i) polymer unit of PTFE; (ii) Desflurane®; (iii) 5-fluorouracil; (iv) $[^{18}\text{F}]\text{FDOPA}$.

1.1.2. Fluorine in medicinal chemistry

As mentioned above, one area in which fluorinated organics have found widespread application is in the design of small molecule active pharmaceutical ingredients (APIs). Today, more than 150 drugs, including many of the most potent drugs in the world used for the treatment of a variety of different diseases, contain one or more fluorine atoms (fig. 1.2).⁹ These include: antidepressants such as Eli Lilly's Prozac® (fluoxetine, fig. 1.3(i)), anti-tumour agents such as AstraZeneca's Faslodex® (fig. 1.3(ii)), antibiotics such as Pharmacia's Flurithromycin (fig. 1.3(iii)) and anti-virals such as Bristol-Myers Squibb's Efavirenz (fig. 1.3(iv)).¹⁰

The pharmacokinetics (PK) (e.g. absorption, distribution, metabolism, excretion and toxicity (ADMET)) and pharmacodynamics (e.g. receptor binding ability) of a molecule *in vivo* determine the effectiveness of a compound as a drug.¹¹

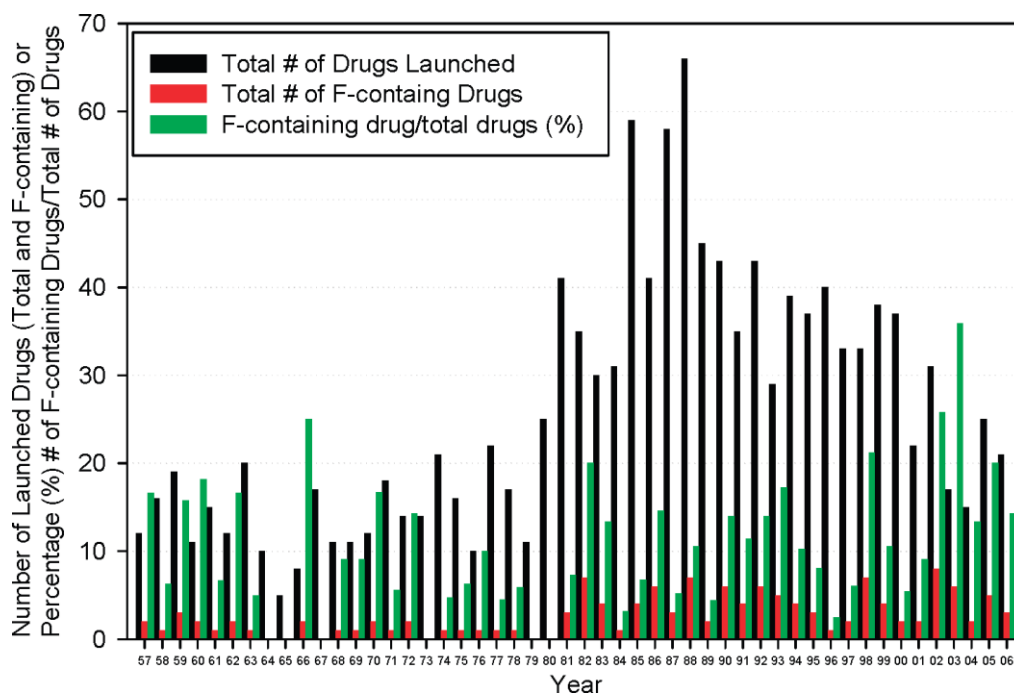


Figure 1.2. Fluorine containing drugs launched, worldwide, between 1957-2006, excluding biologics, inorganics, reformulations and agricultural agents.¹²

The PK properties are often controlled by the steric and electronic nature of the functional groups surrounding the pharmacophore (i.e. the core structure responsible for biological activity).

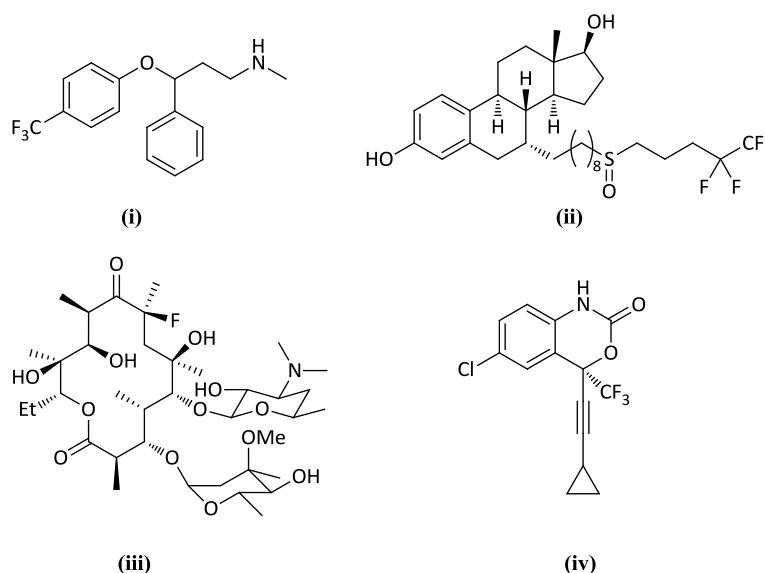


Figure 1.3. The chemical structure of (i) Prozac®; (ii) Faslodex®; (iii) Fluorithromycin; (iv) Efavirenz.

There are a number of methods used to improve these properties (a process known as “lead modification”) and, hence, the potency of lead compounds, including: homologation (screening a series of compounds that differ by a constant unit e.g. a CH₂ group, in order to determine the optimum chain length for desired pharmacokinetics/pharmacodynamics), chain branching (to decrease lipophilicity of a compound), ring change transformations (the transformation of alkyl substituents into cyclic analogues to increase lipophilicity, decrease metabolism or hold the molecule in a certain conformation) and bioisosterism (the substitution of one or more functional groups for others with similar physical/chemical properties to change the pharmacokinetic/pharmacodynamic properties of a compound).¹¹ The Hammett equation (eq. (1.4) & (1.5)) is usually employed to determine the correct electronic properties (both inductive and resonant) of benzene-derived substituents.¹¹ This equation relates, linearly, reactions rates (k) and equilibrium constants (K) for *meta*- and *para*- substituted benzoic acids relative to a constant (k₀/K₀) as determined when the substituent is hydrogen. The substituent constant (σ) depends only on the specific substituent (R), and the reaction constant (ρ) depends solely on the type of reaction, independent of the substituent. This equation is based on the assumption that when changing only the substituent, the free energy of activation is proportional to the change in Gibbs free energy.

$$\text{Log } K/K_0 = \sigma\rho \quad (1.4)$$

$$\text{Log } k/k_0 = \sigma\rho \quad (1.5)$$

Many different atoms and functional groups are used in combination to ensure that all of the desirable properties of a lead compound are included. However, of all the possible atoms and groups, fluorine is unique in that it is able to elicit a number of different effects at any one time. Fluorine is a classical isostere which can be used to replace a number of different groups including methyl groups (CH₃), amines (NH₂) and, most commonly, hydroxyl groups (OH).¹¹ The latter is due to the fact that fluorine exhibits a van der Waals radius (1.47 Å) between oxygen (1.52 Å) and hydrogen (1.20 Å).¹² It is also for this reason that F atoms are able to participate in hydrogen bonding, as evidenced by their role in the binding of type 2 statins (e.g. fluvastatin) to the Arg⁵⁹⁰ residue of the catalytic domain of the 3-hydroxy-3-methylglutaryl-coenzyme A reductase (HMGR) protein.¹² In terms of sterics, however, fluorine is usually a good

isosteric replacement for a hydrogen atom, maintaining the spatial structure of the molecule whilst influencing, significantly, the electronic properties.¹¹⁻¹² Aside from its isosteric properties, the large electronegativity of fluorine means that inclusion of a fluorine atom increases the acidity of neighbouring functional groups by withdrawal of electron density, thus lowering the pKa of the groups adjacent to the fluorine and hence influencing the physicochemical properties of the molecule such as solubility (log *D*), pharmacodynamics (binding affinity) and pharmacokinetics (ADMET).¹² This effect is also known to be cumulative, as the inclusion of subsequent fluorine atoms further withdraw electron density by the same degree as the first.

1.1.3. Fluorine in Positron Emission Tomography (PET)

1.1.3.1. Background to the use of PET in medicine

Further to the list of unique properties described above, fluorine is also often used for radiolabelling molecules for PET imaging in the form of the radioactive isotope fluorine-18.¹² This is the most widely used isotope in positron emission tomography, mainly due to the relatively short half-life of the isotope (110 min).¹³ This is beneficial as it means that the patient will be exposed to the radiation for a relatively short period of time, minimising damaging side effects to both them and others.¹⁴ As well as the favourable half-life, the use of fluorine-18 means that the radio-tracers/ligands benefit from the additional properties of the fluorine atom as discussed above.

Positron Emission Tomography (PET) is a non-invasive medical imaging technique which is used widely to visualize human physiology. The main advantage of PET over other medical imaging techniques such as MRI is that PET provides metabolic as well as anatomical information.¹³ The technique is used in the diagnosis of a number of prevalent diseases including cancer, Parkinson's disease, Alzheimer's disease, attention deficit hyperactivity disorder (ADHD), atherosclerosis, schizophrenia and many others. As well as this specific use, PET imaging is also used widely in drug discovery and medical research to image metabolic processes.^{13, 15}

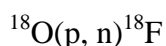
1.1.3.2. Isotope production

There are 2 types of fluorine-18 radionuclide that can be generated,¹⁶ known as:

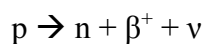
- 1) No Carrier Added (NCA), e.g. [¹⁸F]fluoride ([¹⁸F]F⁻)
- 2) Carrier Added (CA), e.g. [¹⁸F]fluorine ([¹⁸F]F₂)

The most desirable form of fluorine-18 is the No Carrier Added (NCA) [¹⁸F]fluoride, as this is comprised solely of fluorine-18.¹⁵ This means that [¹⁸F]F⁻ has a much higher specific activity (SA), which is defined as the amount of radioactivity per unit mass of the radionuclide, compared with carrier added (CA) radionuclides such as [¹⁸F]F₂.¹⁷ The CA nuclide has a lower specific activity as it comprises one atom of fluorine-18 and one atom of fluorine-19; the latter lowers the overall radioactivity per unit mass of the molecule.

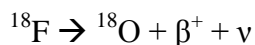
The most common production method for [¹⁸F]F⁻ involves proton irradiation of ¹⁸O enriched water in a metal (typically silver) target.¹⁶ The protons (p) can have energy of anywhere between 4 MeV and 14 MeV which is sufficient for a proton to displace a neutron (n) from the nucleus of an ¹⁸O atom.¹⁶ This process can be described by the nuclear reaction detailed below:



Once generated, the fluorine-18 atom begins to decay, predominantly by positron (or beta positive, β⁺) emission (*ca.* 97%), but also, to a lesser extent, by electron capture (*ca.* 3%).¹⁶ By emitting a positron, the additional proton in the nucleus of the fluorine-18 atom becomes a neutron and a neutrino particle (ν), returning the nucleus to the stable ¹⁸O state.¹⁶ This can be expressed as:



which equates to:



A positron is the antimatter equivalent of an electron, having an identical mass, rest energy and charge magnitude, but with the opposite sign. It is this characteristic that is exploited for imaging.

1.1.3.3. [^{18}F]Fluorination of target molecules

Once generated, the [^{18}F]fluoride must be separated from the ^{18}O enriched water, and subsequently reacted with a substrate to become chemically inserted into a target molecule. This is typically done by trapping the [^{18}F]F $^-$ from the target on an ion-exchange column and subsequently eluting the [^{18}F]fluoride using potassium carbonate.¹³ The relatively poor nucleophilicity of the fluoride is increased by chelation of the potassium using a phase-transfer agent such as kryptofix-222 (K₂₂₂), resulting in the production of “naked” [^{18}F]fluoride, which can then undergo the same nucleophilic reactions as its ^{19}F analogue.^{13, 18}

Direct nucleophilic substitution can be an extremely effective method to incorporate [^{18}F]F $^-$, particularly for electron-poor, aromatic compounds that are activated for nucleophilic attack by an electron-withdrawing group in the *ortho* and/or *para* positions to act as an effective leaving group (fig. 1.4).¹³ However, the harsh conditions required for these reactions (i.e. high reaction temperatures and polar organic solvents) limit the number of substrates for which this is applicable, necessitating the time-costly use of precursors or prosthetic groups.¹³ This method is also not suitable for labelling electron rich, aliphatic molecules, further limiting substrate applicability.

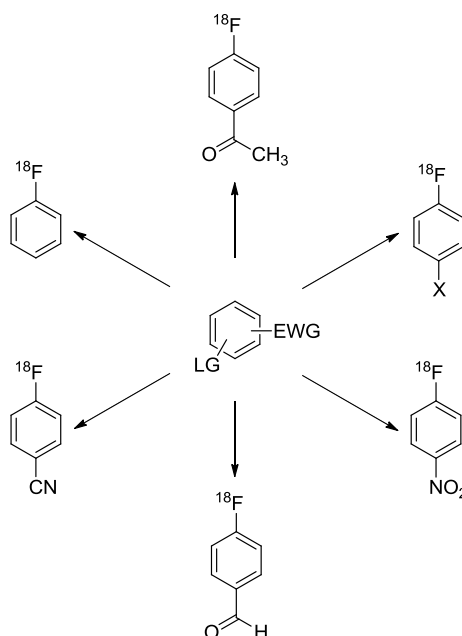


Figure 1.4. Synthesis of simple [^{18}F]fluoroaromatic precursors by direct nucleophilic substitution with [^{18}F]fluoride. EWG = electron withdrawing group (NO_2 , CN, carbonyl); LG = leaving group (NO_2 , halide, OTf, OMs, trialkylammonium halide); X = I or Br.

1.1.3.4. Electrochemical radiofluorination

The literature relating to electrochemical radiofluorination is extremely limited with only three papers dedicated to the topic. The seminal paper published by Reischl et al.¹⁹ in 2002 details a pilot study whereby benzene was successfully radiolabelled using [¹⁸F]fluoride in triethylammonium trihydrofluoride, and a mixture of the former with triethylammonium trihydrochloride. Electrolysis was performed using Pt working and counter electrodes and a Ag/AgNO₃ reference electrode separated from the electrolyte *via* a tetrabutylammonium perchlorate/MeCN salt bridge in an undivided electrochemical cell. The maximum radiochemical yields of 7 – 25% were obtained using a 1 M benzene solution, and the maximum specific activity of 27 GBq/mmol was achieved after passing 50 C of charge through a 0.03 M solution of benzene. The low specific activity is perhaps intuitive owing to the fact that the electrolyte contains 3 fluorine-19 atoms per mole.

In a follow-up paper from the same group in 2003,²⁰ the authors report the effects of electron donating (*t*-Bu) and electron withdrawing (Cl, Br, C(O)Me) substituents on the electrochemical radiofluorination of mono-substituted benzenes. They found that in each case, the dominant process was nucleophilic addition rather than substitution, but they neglect to comment on the regiochemistry of the additions. For both processes, a general trend was observed indicating a decrease in radiochemical yield as the positive inductive effect of the substituent decreased. The decrease in radiochemical yield was also correlated with increasing oxidation potential of the substrate.

The final paper on the subject came from the same authors in 2005,²¹ and focused on the direct labelling of phenylalanine derivatives with the general structure shown in fig. 1.5 using [¹⁸F]fluoride. A series of protected phenylalanines (amine protecting groups = acetyl, trifluoroacetyl, butoxycarbonyl and 2,4-dinitrophenyl; carboxylic protecting groups = methyl and ethyl) were labelled using a variety of different electrolyte media. Contrary to their previous findings, it was reported that the compound with the highest oxidation potential (2.15 V vs. Ag/Ag⁺, R = H, X = trifluoroacetyl, Y = Me) gave the best radiochemical yield (10.5% ± 2.5%), perhaps due to the instability of the other compounds to the reaction conditions. The product distribution showed a bias towards the *ortho/para* isomers, indicating the formation of a phenylic carbenium ion

intermediate. The optimum conditions for maximum radiochemical yield were found to be at temperatures between $-10\text{ }^{\circ}\text{C}$ and $0\text{ }^{\circ}\text{C}$ using the supporting electrolyte $\text{Et}_3\text{N}\cdot 3\text{HF}$ at a potential of 2.0 V vs. Ag/Ag^+ , giving a specific activity of $1.2\text{ GBq}/\text{mmol}$.

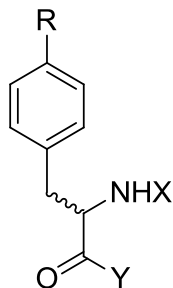


Figure 1.5. General structure of phenylalanine derivatives labelled by Rieschl *et al.* $X = \text{acetyl, trifluoroacetyl, butoxycarbonyl, 2,4-dinitrophenyl}$; $Y = \text{ethyl, methyl}$; $R = \text{H, t-Bu}$.

1.1.3.5. Mechanism of detection

The target molecule to be labelled is chosen to be taken specifically to the site of interest *in vivo*. For example, $[\text{}^{18}\text{F}]$ fluorodeoxyglucose (FDG) (fig. 1.6) is a glucose analogue used typically to indicate tissue metabolic activity due to the regional uptake of glucose.¹⁴ The increased metabolic activity, characteristic of cancerous cells, makes this a powerful tool to explore the possibility of metastasis in cancer patients. Once the radiotracer has been formed, it is administered to the patient and allowed time to concentrate at the site of interest.

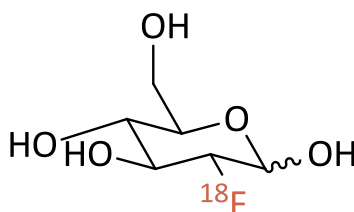


Figure 1.6. Chemical structure of $[\text{}^{18}\text{F}]$ FDG.

The patient is placed into a scanner comprising of a ring of photon detectors made of scintillator crystals and photomultiplier tubes. Positrons emitted by decay of the radionuclide combine with nearby electrons in the body, resulting in an annihilation event from which two equal and opposite gamma rays are emitted with an energy of 511

keV.¹³ These gamma photons are detected by the photon detectors and the source localised along a line of coincidence (fig. 1.7).²²

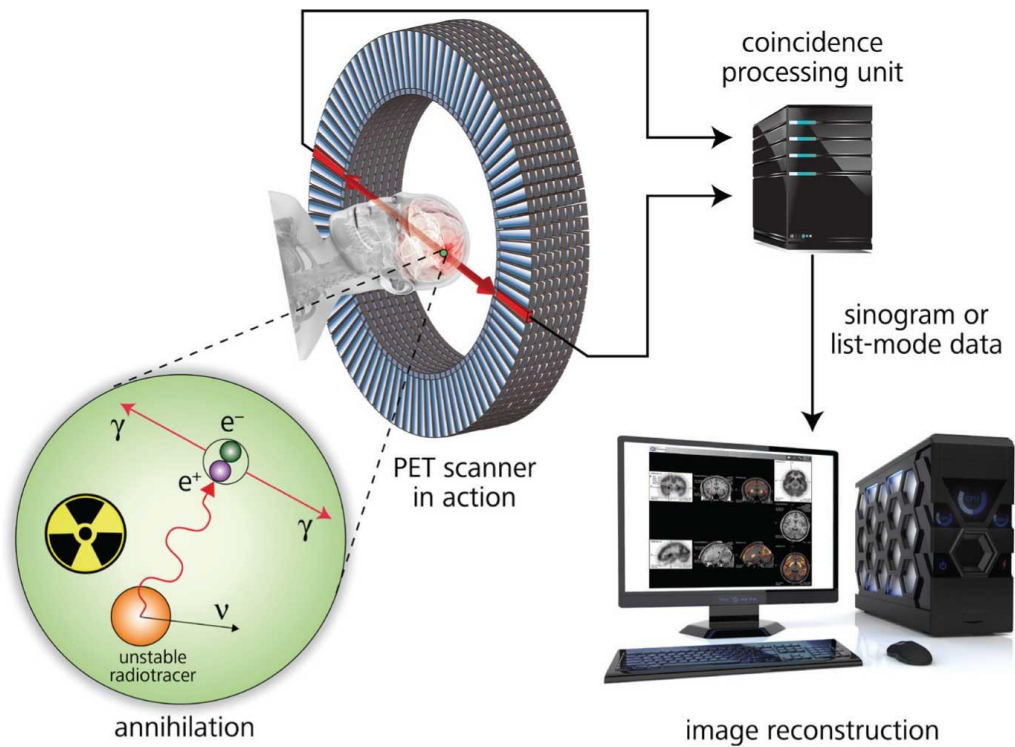


Figure 1.7. Schematic representation of positron annihilation and detection.

The data collected regarding the localization of each annihilation event allows the mathematical reconstruction of the image, creating a map highlighting the tissues in which the radiotracer has become concentrated (fig. 1.8).

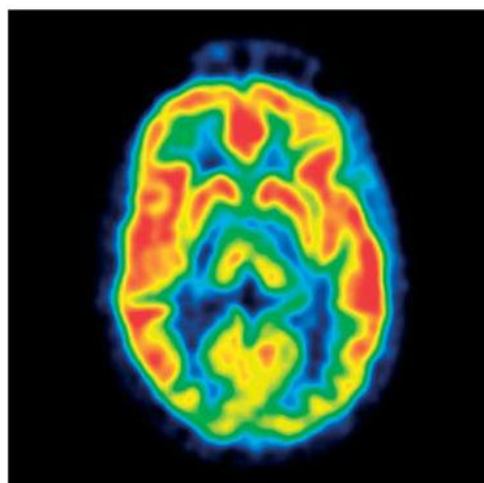


Figure 1.8. An example of PET imaging of mGluR5 receptors in human brain with [^{18}F]SP203.¹⁵

1.1.4. Traditional methods of fluorination

With so many useful applications, the synthesis of fluorinated organics has become the focus of much research. The main methods of fluorination used in organic chemistry can be divided into two categories: electrophilic fluorination and nucleophilic fluorination. The method of fluorination chosen is usually dependent upon the nature of the substrate. Electrophilic fluorination involves the attack of electrophilic fluorine (hypothetically “F⁺”) by a nucleophilic centre on the substrate (e.g. unsaturated hydrocarbons, aromatics etc.). Another common fluorinating agent utilised for electrophilic fluorination is elemental fluorine (F₂). As a result of the relative weakness of the F-F bond (36.6 kcal mol⁻¹) observed as a result of the strong lone pair repulsion,⁸ elemental fluorine is one of the most chemically reactive substances known. High dielectric, aprotic solvents or protonic acids are generally used to solvate these reactions, as the nucleophilic substrate attacks one of the F atoms in the molecule, breaking the F-F bond and generating a fluoride ion (F⁻), which can subsequently react with a proton to generate HF gas (fig. 1.9).²³

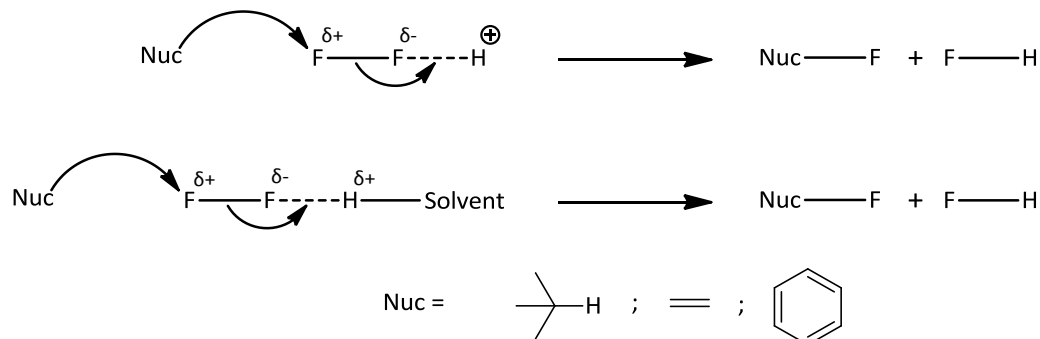


Figure 1.9. Schematic representation of the solvent/acid mediated electrophilic fluorination of a nucleophile using F₂.

Due to the high reactivity of elemental fluorine and the hazards associated with its handling, a number of milder, less reactive electrophilic fluorinating agents are commonly used. These include, N-fluorinated amines (e.g. 1-Chloromethyl-4-fluoro-1,4-diazoniabicyclo [2.2.2]octanebis(tetrafluoroborate)), quaternary salts, amides and sulfonamides.²⁴ There are also a number of inorganic, electrophilic fluorinating agents available, including xenon fluoride (XeF₂), cobalt(II)fluoride (CoF₂), silver(I)fluoride (AgF). Finally, the last group of common electrophilic fluorinating agents is the hypofluorites (i.e. trifluoromethyl hypofluorite and acetyl hypofluorite).²⁵

In spite of the relatively poor nucleophilicity of fluoride compared with the other halides, nucleophilic substitution of chloride, bromide or iodide by fluoride can be effected due to the high stability of alkyl fluorides as well as the poor leaving group ability of F⁻.²⁶ Inorganic fluorides (e.g. KF) are a good source of F⁻, however, their poor solubility in organic solvents can be problematic. The addition of a crown ether (such as 18-crown-6 in the case of KF) or kryptofix (such as 4,7,13,16,21,24-Hexaoxa-1,10 diazabicyclo[8.8.8]hexacosane (K-222)) can often stabilise the solution by chelation of the metal atom.²⁵ The much more soluble tetralkylammonium fluoride salts (e.g. tetrabutylammonium fluoride (TBAF)) can also be employed, although, these are often now used for the selective cleavage of silyl protecting groups. In aromatic systems, fluorination occurs by nucleophilic aromatic substitution (S_NAr), whereas alkyl substrates are usually fluorinated by S_N2 reactions.²⁶

A number of other fluorinating agents such as sulfur tetrafluoride, antimony pentafluoride and HF derivatives (e.g. Pyridine-HF) have been employed for a number of specific transformations, however, these are not widely applicable.²⁵ Other common methods of fluorination include the formation of diazonium salt intermediates followed by subsequent nucleophilic attack of fluoride (e.g. the Balz-Schiemann reaction).²⁷

1.1.5. Limitations of current synthetic routes

In spite of the variety of different fluorinating agents available, there are limitations. In each case, the reagents tend to be extremely toxic, damaging to the environment and often difficult to handle (e.g. F₂ gas, HF gas etc.)²⁸. The inorganic reagents tend to utilise toxic metals, which are not only hazardous to handle, but also, from a practical standpoint, very difficult to extract after the synthesis. Also, the diazonium salt intermediates and hypofluorites can be highly explosive and shock sensitive,²⁵ presenting yet more hazards. Further to this, fluorination by any of these methods often requires a number of synthetic steps, causing a steady decline in the overall yield of the product.

1.2. Electrochemical fluorination

1.2.1. Historical survey of selective electrochemical fluorination

In principle, electrochemical methods of synthesis offer several advantages over conventional synthetic approaches e.g. precise control through the current and/or

electrode potential, and no need for toxic, expensive, environmentally damaging redox reagents (an electrode is an extremely clean sink for, or source of, electrons).

Since its discovery in the 1950s, research into selective electrochemical fluorination (ECF) focussed largely on the oxidative addition of fluorine to alkenes.²⁹ The first known example of selective ECF was reported by Schmidt and Schmidt in 1953.²⁹ This involved the anodic, partial fluorination of diphenylethylene in KHF_2/AcOH (fig. 1.10). Fluorination of diphenylethylene was also attempted using other common fluoride sources such as AgF and HF in a variety of aprotic solvents. These conditions were found to be relevant only to this reaction; therefore, researchers began to concentrate on the identification of a more generally-applicable ECF system.

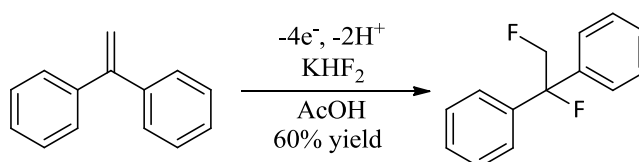


Figure 1.10. The first example of anodic partial fluorination

The most effective conditions for ECF, that are still employed to date, were discovered in 1970, when Knunyants et al. performed their selective ECF of naphthalene (fig. 1.11) using tetraethylammonium fluoride trihydrofluoride in acetonitrile at 1.8 V vs. the Standard Calomel Electrode (SCE).³⁰ These salts (of the general structure $\text{R}_n\text{N}(\text{F})_m\text{HF}$ where R = alkyl, $n = 3,4$ and $m = 3-5$) proved to be applicable to a variety of different substrates as evidenced by the fact that the conditions are still utilised today. This work marked the beginning of a transition from olefins to aromatic and heterocyclic substrates, representing a major breakthrough for ECF, as so many fluorinated aromatic and heterocyclic compounds are used in the synthesis of a vast array of products; most notably, pharmaceuticals.³¹ However, one problem often encountered with these substrates was passivation of the electrodes i.e. the formation of an insulating or fouling film on the surface of the electrode rendering it inactive.²⁹⁻³⁰ In spite of this, research into the anodic fluorination of aromatic, heteroaromatic and heterocyclic compounds is still a matter of significant interest today, providing further evidence of the usefulness of fluorinated analogues of these substrates.³²⁻³³

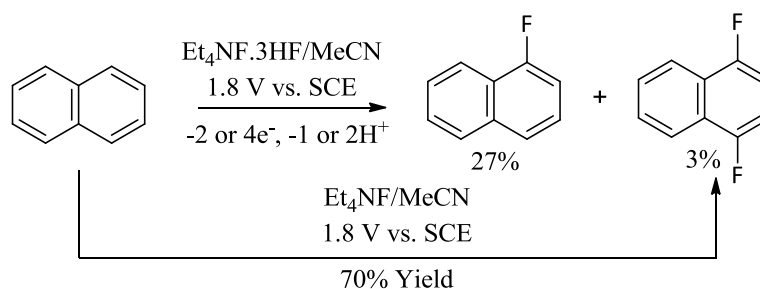


Figure 1.11. The ECF of naphthalene using HF derived ammonium salts

In the late 1980s, it was shown that side chain methylene groups (particularly with sulfide linkages) undergo efficient fluorination, without passivation of the electrodes.³⁰ Fuchigami and co-workers found that regioselective monofluorination of aryl 2,2,2-trifluoroethylsulfides in acetonitrile gave, exclusively, aryl 1,2,2,2-tetrafluoroethyl sulfides in up to 65% yield when passing a charge of 7.2 F mol⁻¹ at a constant anodic potential of 2.0 V vs. the silver-silver chloride electrode (SSCE) (fig. 1.12).³⁴ This work represents another landmark in the history of ECF, demonstrating the efficacy of the technique as a method of facilitating nucleophilic substitution α to electron-withdrawing group i.e. trifluoromethyl. Such transformations are rarely achieved by conventional synthetic methods; hence, the current renaissance in ECF.

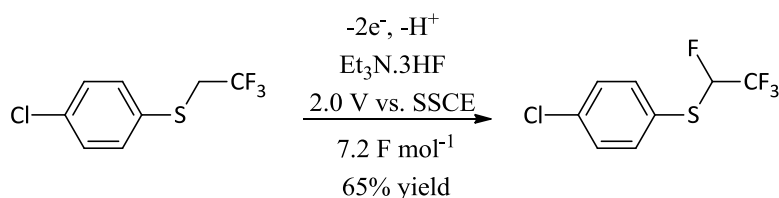
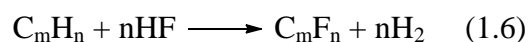


Figure 1.12. Selective ECF α -to an electron withdrawing group

1.2.2. The Simons process

For the most part, research into ECF has been concerned with the production of perfluorinated products, i.e. the substitution of every C-H bond in a compound for a C-F bond, such as in the industrial Simons process.³⁵ The Simons process was developed in the 1930s at Pennsylvania State College in the U.S.A, by Joseph H. Simons and co-workers. However, the research was not published until 1949 due to the application of the work in the production of uranium hexafluoride, a precursor in the manufacture of explosives for nuclear weapons.

The Simons process is rare in that, not only are all the saturated C-H bonds converted to C-F bonds, but any unsaturated C=C bonds are converted to saturated C-F bonds (see eq. (1.6)).³⁵ The process utilises a nickel anode with anhydrous HF at very high potentials, typically between 4.5-7 V vs. the Normal Hydrogen Electrode (NHE).³⁶ Because of the consumption of fluoride at the anode, an accumulation of protons can cause a local increase in acidity, often resulting in acid catalysed degradation of sensitive functionalities such as alcohols and olefins;³⁰ however, retention of more robust functional groups e.g. esters is usually observed. Also, as the relative energy of the C-F bond (*ca.* 105.4 kcal mol⁻¹) is much greater than that of a typical saturated C-C bond (*ca.* 83.1 kcal mol⁻¹),⁵ destruction of the carbon skeleton can also take place. Fluorination has been postulated to occur as a result of the formation of an anodic film comprising a conductive passivating layer of metal fluorides beneath a thicker layer of the polymerised substrate.³⁰ This film, which is largely insoluble in the HF electrolyte, is believed to be crucial to the process as it serves as the solvent medium for the fluorination.



Despite the long history of ECF represented by the Simons process, relatively little research has been conducted in the area of *selective* ECF, i.e. monofluorination. The main factors that have mitigated against the inclusion of ECF as a routine synthetic approach are:

- At the high potentials required for ECF, competitive polymerisation of the solvents and/or substrates can occur, leading to low product yields and poor current efficiencies.²⁹
- Due to the nature of the highly reactive fluorine species generated at these potentials, electrode and cell materials were highly susceptible to chemical attack.³⁷
- Both fluorine and its derivatives are extremely toxic and harmful, thus deterring potential researchers on the grounds of safety.³⁷

With increasing research into the area, these factors are becoming less of an issue, and the usefulness of ECF as a synthetic technique is becoming ever more apparent.

1.2.3. *The general electrochemical procedure*

Electrolysis is generally carried out in an electrochemical cell containing the substrate dissolved in a solvent and conducting salt (together termed the electrolyte); for ECF, the salt usually contains fluoride (F^-), as with the molten salts $R_nN(F).mHF$ ($R = \text{alkyl}$, $n = 3, 4$ and $m = 3-5$), and either two or three electrodes. Small scale, investigative electrolysis, e.g. employing electrodes $\leq 1 \text{ cm}^2$, generally use three electrodes: the working, counter and reference electrodes. The potential of the working electrode (WE) is monitored and maintained using a potentiostat with respect to the reference electrode (RE). The potential of the WE is usually chosen to be sufficiently positive (anodic) or negative (cathodic) to effect chemical oxidation or reduction, respectively. The potential of the counter electrode (CE) then moves until a redox couple is encountered such that an equal and opposite current to that passing across the WE/electrolyte interface can be sustained. Thus, for example, in aqueous solution, if the WE is effecting an oxidative transformation, the CE will typically be reducing the solvent, water, to hydrogen gas.

Potentials are typically quoted vs. the Normal Hydrogen Electrode (NHE) which is defined as having a Standard Reduction Potential of 0.³⁸ The NHE consists of a high surface area Pt black electrode immersed in 1.0 M H_2SO_4 and in contact with H_2 gas at 1 atm pressure.³⁸ Reference electrodes are chosen according to the electrolyte employed. Thus, in aqueous solution, the mercury/mercury sulfate ($Hg|Hg_2SO_4$) electrode (MME) is employed for low pH, saturated calomel ($Hg|Hg_2Cl_2$) electrode (SCE) or silver/silver chloride ($Ag|AgCl$) electrode (SSCE) for neutral pH and mercury/mercury oxide ($Hg|Hg_2O$) electrode (MMO) for high pH.³⁸ All of the reference electrodes employed in aqueous solution have standard reduction potentials defined vs. NHE. No current is allowed to flow through a RE; it simply provides a reference potential against which the potential of the WE is measured and controlled, by the potentiostat.

There is no point in employing a RE with electrodes $> 1 \text{ cm}^2$ as the luggin capillary of the RE will sense only local potentials of larger electrodes. Hence, preparative electrolysis is usually carried out in 2-electrode cells, where a cell voltage (potential difference) is applied across the 2 electrodes. Thus, for example, in an oxidative transformation, the WE is made sufficiently positive of the CE for the required net current to flow.

1.2.4. Electrochemical cell design

The main difficulties associated with ECF are related to the conditions necessary for fluorination to take place. Whilst milder than most traditional synthetic fluorination procedures (i.e. F_2 gas) the high potentials required for the oxidation of fluoride as well as the corrosive nature of the reagents can be problematic. As the majority of processes use HF, or a derivative thereof in which HF is formed *in-situ*, electrochemical cells employed in ECF tend to be made of steel, e.g. the Simons process.³⁵ A glass cell would be attacked by the HF generated during the reaction which would cause etching to occur;³⁷ for this reason, glass cells only tend to be used if the actual concentration of HF is suitably low (typically between 0.1 M and 1.0 M).³⁹

Childs et al. designed and patented a novel electrochemical cell made of carbon and steel for the industrial use of the Phillips petroleum process (fig. 1.13).³⁹

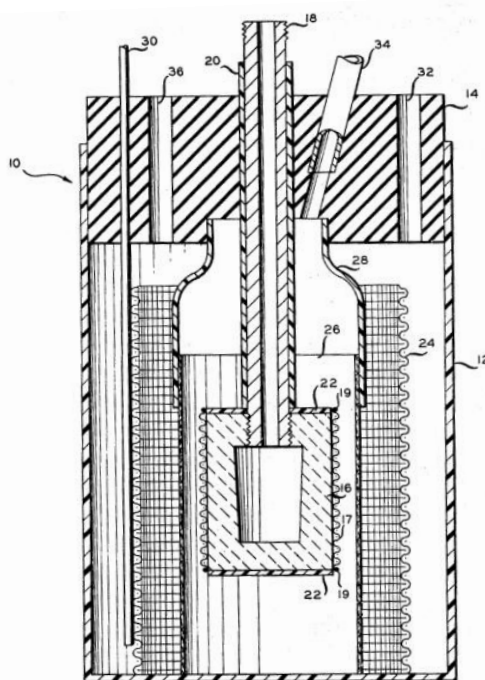


Figure 1.13. A schematic representation of the Phillips petroleum cell for electrochemical fluorination.³⁹

This process is similar to the Simons process, with the adoption of a porous, graphite anode in molten KHF_2 . Fluorination was thought to occur in the porous cavities of the anode when the substrate was in the “vapour phase”; therefore the process is most

suited to fluorination of volatile substrates such as hydrocarbons and chlorohydrocarbons.⁴⁰

1.2.5. Electrodes

Standard calomel electrodes (SCE), also known as mercury-mercury chloride (Hg_2Cl_2), are a popular choice for reference electrodes in ECF. However, since the conditions required for ECF are largely anhydrous, it is often easier and more appropriate to use quasi-reference electrodes, such as platinum or palladium wire, which are usually calibrated using a reference compound such as ferrocene ($\text{Fc}/\text{Fc}^+ = 0.64 \text{ V vs. NHE}$). Quasi-reference electrodes have an additional advantage in ECF, as acetonitrile, which is commonly used as a solvent for ECF, can cause Hg_2Cl_2 to disproportionate.³⁸ For this same reason, two electrode systems are also employed.

The counter electrodes generally employed tend to be platinum (e.g. Pt mesh). No doubt, this is because of the noble nature of the metal, rendering it resistant to chemical attack from the highly reactive species generated *in-situ*, as well as its general electrocatalytic activity.

Initially, it was thought that only nickel anodes were able to facilitate ECF (as in the Simons Process). Further to this, it was believed that factors such as the manufacturer of the nickel and its crystalline structure influenced, directly, the yields of fluorinated products obtained.³⁰ This assumption was based on the theory that electrochemical fluorination was facilitated by the formation of known fluorinating agents such as NiF_2 and NiF_3 at the surface of the anode. It was not until 1970 when Knunyants and co-workers³⁰ discovered that carbon-fluorine bonds could be formed by the anodic oxidation of organic substrates at platinum, followed by subsequent addition of fluoride, that materials other than nickel were considered for the working electrode.

Platinum became, and remains to this day, the anode material of choice for ECF as a number of different organic substrates were found to be oxidised on Pt, paving the way for further research into the mechanisms of ECF.

1.2.6. *Experimental conditions*

Historically, the electrolyte system used for selective ECF is HF or a HF containing salt in a suitably stable solvent, typically acetonitrile or chloroform.²⁹ The electrolytic salts most commonly used are triethylamine-nHF or tetraethylammonium fluoride-nHF (n = 3-5). These salts have the advantage that HF is formed *in-situ*, making them relatively easy to handle compared with HF gas.²⁹

As mentioned above, due to high anodic potentials used in ECF, the systems must be non-aqueous; otherwise, the electrolysis of water to O₂ and H₂, which occur at relatively low potentials (solvent window = 1.23 V)⁴¹ can interfere with the desired reaction as well as lowering current efficiency.

As a result of the anhydrous nature of the fluorinations, aprotic solvents must be used. The most common solvent is acetonitrile, probably due to its relative electrochemical stability with a solvent window of 2.7 V.⁴¹ However, there are a number of disadvantages of using solvents for ECF given the high potentials required. At higher potentials, solvents can undergo anodic oxidation, the products of which may compete/interfere with the fluorination procedure, either by reaction directly with the substrate forming undesirable by-products, or by reaction with the fluoride source, hence limiting the amount of fluoride available for reaction.²⁹ Also, solvents can form passivating films at the anode, increasing the resistance of the electrode and hence limiting ECF at a given potential.⁴¹ Finally, it can be difficult to find a suitable solvent to solvate fully all of the reactants, for example, if the fluoride source is an ionic salt and the substrate organic. This combination of factors can reduce the reaction yield and current efficiency significantly; hence, it would be desirable to develop solvent-free systems in order to eliminate these effects.

Fuchigami et al. reported that the addition of dimethoxyethane (DME) to acetonitrile improved, significantly, the observed yields and efficiencies by causing a reduction in anode passivation. The authors postulate that DME solvates the cations of the fluoride salts more effectively, increasing the nucleophilicity, and hence reactivity, of the fluoride anions. They also found that DME was oxidised during electrolysis, preventing over-oxidation of the substrates and/or products.⁴²

1.2.7. Substrates

1.2.7.1. Aromatic substrates

In 1971, Knunyants et al. published their selective electrochemical oxidation of benzotrifluoride to 3-fluorobenzotrifluoride using the HF salt tetraethyl ammonium fluoride trihydrofluoride ($\text{Et}_4\text{NF}\cdot 3\text{HF}$) in acetonitrile.⁴³ Assuming a 2 electron process, they electrolysed for just over 5 hours, passing 80% of the theoretical amount of charge, at a platinum anode with a potential of 3.2 V vs. SCE, giving a 60% yield of 3-fluorobenzotrifluoride (fig. 1.14).

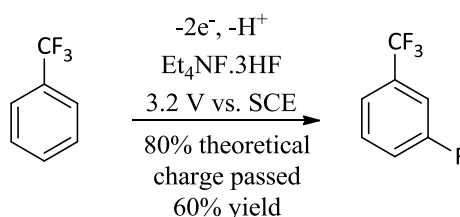


Figure 1.14. The ECF of benzotrifluoride.

Momota et al. performed ECF of benzotrifluoride under different conditions.^{32, 44} They obtained a mixture of fluorinated products, and the maximum yield of 3-fluorobenzotrifluoride obtained was only 2.1% using $\text{Et}_4\text{NF}\cdot 4\text{HF}$ at an applied anodic potential of 2.7 V vs. Ag/AgClO_4 for 430 min. The primary product (with a yield of only 14.5%) was 2,5-difluorobenzotrifluoride. Although the selectivity observed was not as good as that obtained by Knunyants et al., the authors did isolate and identify, all the products obtained from the reaction, postulating a possible mechanism for the formation of each.

Using standard organic chemistry to perform the equivalent transformation, i.e. the synthesis of 3-fluorobenzotrifluoride from benzotrifluoride, would require the use of extremely hazardous materials such as fluorine gas or diazonium salts. Beyond that, a number of synthetic steps would be required, lowering the overall yield and efficiency of the process as well as introducing more room for experimental error.

Recently, Noel et al. demonstrated the selective electrochemical fluorination of 1-indanone, 2-indanone and 1,3-indandione at both glassy carbon and platinum anodes in $\text{Et}_3\text{N}\cdot 4\text{HF}$, an ionic liquid, with constant potentials ranging from 2.15 V – 2.40 V vs. SCE and, separately, at constant cell voltages ranging from 2.84 V – 3.05 V.³² In each

case, the desired monofluorinated product was obtained in good yield (up to 72%) under both galvanostatic and potentiostatic control (fig. 1.15). Improved selectivity was observed under potentiostatic control at Pt anodes. This was postulated by the authors to be due to the preferable oxidation of free base from the electrolyte (triethylamine in this case), upon reduction in substrate concentration, preventing over-oxidation of the monofluorinated product.

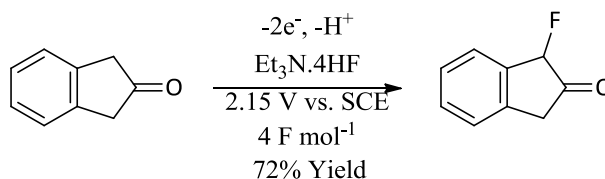


Figure 1.15. The selective ECF of 2-indanone.

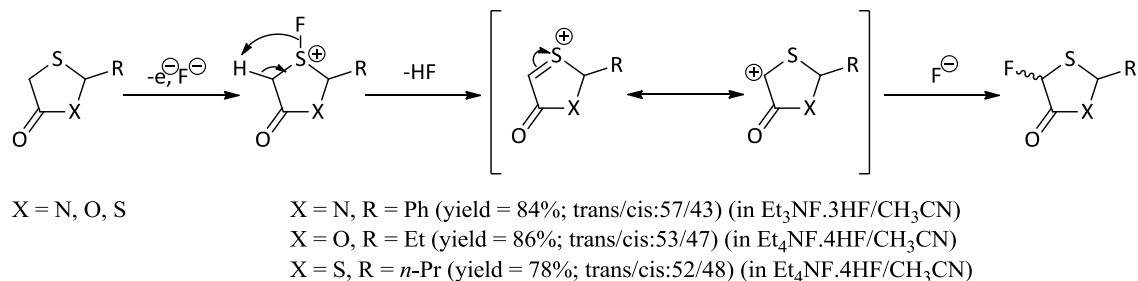
1.2.7.2. Functionalised/heterocyclic substrates

Shainyan et al. demonstrated the selective electrochemical aromatic fluorination of a number of substrates including methyl phenyl sulfone,⁴⁵ acetophenone,⁴⁶ benzophenone,⁴⁶ anisole, phenylacetonitrile, bromobenzamide and *p*-bromonitrobenzene.⁴⁷ These transformations were performed, typically, using anhydrous HF and nickel anodes at extremely high cell voltages, ranging from 5.8 V to 7.4 V. These results are significant as they demonstrate the stability of the specified functionalities, i.e. sulfones, ketones etc. to the high electrochemical potentials used, showing the viability of ECF for use on a variety of functionalised aromatics.

Fuchigami et al. have performed the selective ECF of a wide variety of substrates in a series of papers entitled, “Electrolytic Partial Fluorination of Organic Compounds”. A selection of these substrates are summarised in Table 1.1 below.

The selective ECF of heterocyclic substrates has received much attention in more recent literature.⁴⁸ Highly stereo/regio-selective mono-fluorinated products have been obtained for a number of heterocycles, including thiazolidinones, flavones, quinolinyl/pyrimidyl sulfides, thiazoles, pyrroles, and oxazolidines, all of which are synthetically useful.⁴⁸ These transformations were performed, typically, in alkylammonium fluoride salts compounded with HF in acetonitrile. For example, scheme 1.1 shows the mechanism by which the thiazolidinone is fluorinated. This mechanism explains the high regioselectivity observed, as the electron withdrawing effects of the carbonyl group

increases the acidity of the proton α -to the fluorosulfonium ion, hence facilitating deprotonation and elimination of HF, generating the unstable sulfonium/carbocation intermediate which subsequently undergoes nucleophilic attack from fluoride.

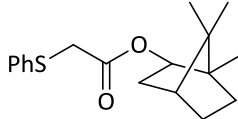
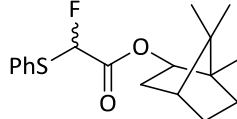
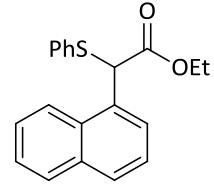
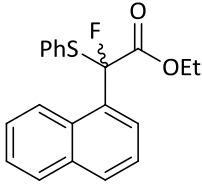
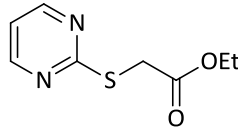
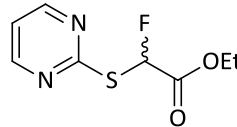
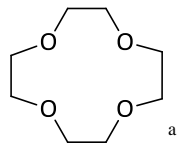
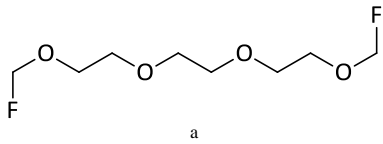
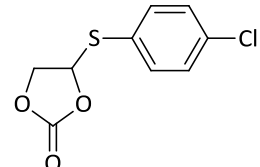
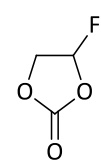


Scheme 1.1. A mechanism depicting the ECF of thiazolidinones.

1.2.8. Molten salt electrolytes

Most current research focuses on solvent free systems, whereby the electrolytic salt is used to solvate and facilitate the reaction. This has proven to increase both yield and current efficiency, probably due to the reduction of competitive polymerisation reactions such as the Kolbe reaction, a decarboxylative dimerisation which occurs as a direct result of the oxidation of free acetate, often at high anodic potentials.⁴⁹

In spite of the relative novelty of solventless ECF, the area has developed very quickly over the last 3 to 5 years. There have been a number of successful solvent-free ECFs of organics such as arenes, furans, phenathrolines, aldehydes, cyclic ketones, cyclic unsaturated esters, and phenols using Et_nN(F)_mHF (n = 3, 4; m = 3-5) reported in the literature.^{44, 49-52} These salts are thought to destabilise radical-cation intermediates, which are thought to be integral in the formation of products by the mechanism postulated by Rozhkov et al. (scheme 1.2), in much the same way as solvents such as dichloromethane (DCM).

Year	Substrate	Substrate Conc./mmol	Temperature /°C	Supporting Electrolyte/solvent	Anodic Potential/Material	Product	Yield /%	Ref.
1995		1.5	Ambient	0.37 M Et ₃ N.3HF/MeCN	1.6 V vs. SSCE/Pt		69	53
1998		1.5	Ambient	1.0 M Et ₃ N.3HF/MeCN	1.49 V vs. Ag Ag ⁺ /Pt		99	54
1999		1.0	20	10 equiv. Et ₄ NF.4HF/DME	5 mA cm ⁻² constant current/Pt		98	55
2000		1.0	20	0.4 M Et ₃ N.5HF/MeCN ^a	10 mA cm ⁻² constant current/Pt		94 ^a	56
2001		1.0	RT	1.0 M Et ₃ N.5HF/DCM	5 mA cm ⁻² constant current/Pt		96	57

Year	Substrate	Substrate Conc./mmol	Temperature /°C	Supporting Electrolyte/solvent	Anodic Potential/Material	Product	Yield /%	Ref.
2004		1.0	20	40 equiv. Et ₃ N.3HF/(PC/MeCN) (1:1)	10 mA cm ⁻² constant current/Pt		99	58
2006		1.0	Not stated	1.0 M Et ₄ NF.5HF/MeCN	5 mA cm ⁻² constant current/Pt		90	59
2007		0.5	RT	1.0 M Et ₄ NF.4HF/MeCN	10 mA cm ⁻² constant current/Pt		62	60
2009		1.0	20	40 equiv. Et ₃ N.3HF/DME	1.45 V vs. SCE/Pt		69	61

Table 1.1. A selection of substrates and products of selective ECF reported by Fuchigami et al.

^a The paper from which this substrate was taken shows some discrepancy in the numbering of the compounds, therefore it is not clear if 94% yield was achieved for the fluorination of 12-crown-4 or 18-crown-6.

Systems containing a mixture of molten salts have proved to be highly effective in the fluorination of barely oxidisable substrates such as phthalide. The high oxidation potential of phthalide (2.81 V vs. SCE) means that solvents such as DME are oxidised preferentially using conventional ECF. However, Fuchigami et al. showed that by using a combination of the ionic liquid [EMIMF][OTf] and Et₃N.5HF, 3-fluoro phthalide was successfully obtained in 90% yield.⁵²

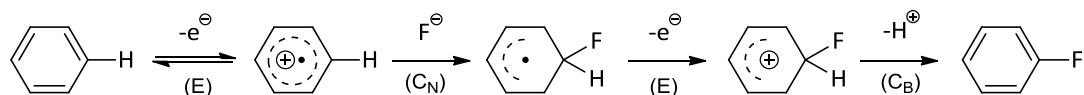
There appear to be many advantages to the use of molten salts in place of solvents, namely: recyclability, low flammability, low volatility, thermal/electrochemical stability, good conductivity, and of course, the improved yields and current efficiencies observed. However, these advantages are only realised for a limited number of substrates as the high viscosity of the salts often results in extremely slow mass transport, leading to limited success across a variety of different reactants.⁴⁹

Most recently, Fuchigami et al. have shown that ultrasonication of the reaction mixture in solvent-free systems further increases yield, selectivity and current efficiency. These observations are thought to be facilitated by non-inertial cavitation collapse, hence promoting mass transport of the substrate to the anode surface. This was shown by the ECF of ethyl α -(phenylthio)acetate, the monofluorinated product of which was obtained in 90% yield with 100% selectivity upon ultrasonication compared with 79% yield and 91% selectivity without sonication.⁴⁹

1.2.9. Mechanisms of electrochemical fluorination (ECF)

The exact mechanisms of ECF are not fully understood, prompting much debate in the area. For example, as stated above, it was suggested that in the Simons process the observed transformations occur as a result of the formation of inorganic fluorinating agents such as NiF₂ and NiF₃ at the anode surface.³⁰ Until recently, this suggestion was not supported by experimental data and an alternative mechanism, proposed by I. N. Rozhkov on the basis of the hypothesis stated by Burdon et al., was generally accepted.³⁰ Rozhkov proposed an EC_NEC_B mechanism based on experimental results obtained using aprotic solvents and platinum anodes. This was suggested to work by anodic oxidation of the adsorbed substrate (E) forming a radical-cation, which subsequently undergoes nucleophilic attack by a fluoride ion (C_N), forming a radical.

The radical is then thought to be further electrochemically oxidised (E) to the resultant carbocation which is subsequently deprotonated (C_B) to form the resultant aryl fluoride.³⁰



Scheme 1.2. Rozhkov's proposed radical-anion mechanism of ECF.

However, whilst Rozhkov's radical-cation postulate is still applied to explain the ECF of many organic substrates, it is now known that the Simons process does indeed occur *via* the formation of high valence nickel fluorides at the anode surface as shown by Sartori et al.⁶²

1.3. Project aims

The overall aim of the project was twofold:

- 1) To investigate the regio- and stereo-selectivity observed in the ECF of electron-rich aliphatic model compounds in order to gain a better mechanistic understanding of the process.
- 2) To develop new composite electrodes for increased control and selectivity of ECF reactions.

2. Experimental

2.1. General information

All commercial solvents and reagents were purchased from Sigma-Aldrich, Apollo Scientific, Fluorochem, TCI, Fisher Scientific or Alfa Aesar and used without further purification unless otherwise specified.

All ^1H , ^{13}C and ^{19}F NMR spectra were recorded on a Jeol Eclipse 500 NMR spectrometer. ^1H and ^{13}C chemical shifts were reported in ppm relative to residual protic solvent as an internal reference, using CDCl_3 as the solvent. ^{19}F NMR chemical shifts were reported in ppm relative to the external CFCl_3 standard, using CDCl_3 as the solvent. NMR simulations were performed using gNMR software version 5.0.6.0, written by P. H. M. Budzelaar.¹

FT-IR spectra were obtained using a Scimitar Series Varian 800 FT-IR spectrometer. EI-MS data were obtained using a Varian CP-3800 Gas Chromatograph and Varian Saturn 2200 GC/MS. Using a Varian Factor 4 BF5MS column, an EI split method was used with a split ratio of 20:1 on a sample volume of 1 μL ; detection range = 40 – 650 m/z and oven temperature = 60 – 270 $^\circ\text{C}$ at a rate of 15 $^\circ\text{C}/\text{min}$ for a total of 22 min.

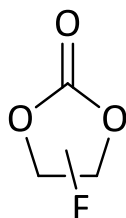
Potentiostatic/galvanostatic measurements were performed using either a Windsor Scientific AutoLab PGSTAT12 and AutoLab GPES version 4.9.007 software or a Radiometer Analytical VoltaLab PGZ301 as specified. Composite anode resistance measurements were performed using a TTI 1604 40,000 count digital multimeter and the light source used to illuminate the composite anodes was a Cole Parmer 9741-52 Low-noise Fibre Optic Illuminator.

Column chromatography was performed using a Varian 971-FP Discovery Scale Flash Purification System, Model AX1600-1, on 40 μm normal phase silica unless otherwise specified.

¹ Software obtained from Budzelaar, P. H. M.,
<http://home.cc.umanitoba.ca/~budzelaa/gNMR/gNMR.html> - 11 July 2011

All SEM/EDX data was obtained by Mrs Pauline Carrick from the ACMA service at Newcastle University using a Jeol JSM 5300-LV microscope and Rontec EDX at 25 kV. All XRD data was obtained by Miss Maggie White from the materials analysis group in the school of CEAM at Newcastle Univeristy, using a PANalytical X'Pert Pro Multipurpose Diffractometer, fitted with an X'Celerator and a secondary monochromator. A Cu anode was supplied with 40 kV and a current of 40 mA to generate Cu K-alpha radiation ($\lambda = 1.54180 \text{ \AA}$) or Cu K-alpha1 ($\lambda = 1.54060 \text{ \AA}$). Data were acquired over a range of $20\text{-}100^\circ 2\theta$ with a nominal step size of $0.0167^\circ 2\theta$ and time per step of 150 s. To avoid seeing reflections from the Si(100) substrate a series of scans were run using an offset scan axis (a $2\theta\Omega$ scan, where $\Omega = 2^\circ$). All scans were carried out in "continuous" mode using the X'Celerator RTMS detector. Where relevant, phase identification was carried out by means of the X'Pert accompanying software program High Score Plus and the ICDD Powder Diffraction File 2 database (1999).

2.2. General procedure for the conventional ECF of ethylene carbonate



In order to ensure that the reaction was kept as dry as possible, the experiment was carried out in a glove box.

Tetraethylammonium fluoride tri/tetrahydrofluoride ($\text{Et}_4\text{NF}\cdot 3/4\text{HF}$, 2.4 equivalents, i.e. for $\text{Et}_4\text{NF}\cdot 4\text{HF}$, 43.6 mmol, 10.00 g) was weighed into a 20 mL, tapered, glass electrochemical cell (fig. 2.1) with fitted electrodes (fig. 2.2), before ethylene carbonate (1 equivalent, i.e. for $\text{Et}_4\text{NF}\cdot 4\text{HF}$, 18.2 mmol, 1.60 g) was added and the mixture stirred for 1 min to melt the reagents. A platinum mesh electrode ($0.5 \text{ cm} \times 1.0 \text{ cm}$) was placed into the cell so that the mesh was submerged as far as possible in the solution, *ca.* 5 mm away from a platinum counter/reference electrode ($1.0 \text{ cm} \times 2.0 \text{ cm}$). The stirrer was stopped and a CV recorded between 0 V and 3 V vs. CE. The solution was stirred

during the electrolyses under galvanostatic control at 50, 100 and 200 mA cm⁻², passing 100% of the theoretical amount of charge. The resultant dark brown liquid was extracted in DCM (3 × 15 mL) and washed with ice water (3 × 15 mL). The organic fractions were combined and dried (MgSO₄) before the organic product was filtered and the solvents removed *in vacuo*. The products were analysed by ¹H and ¹⁹F NMR as well as by EI-MS.

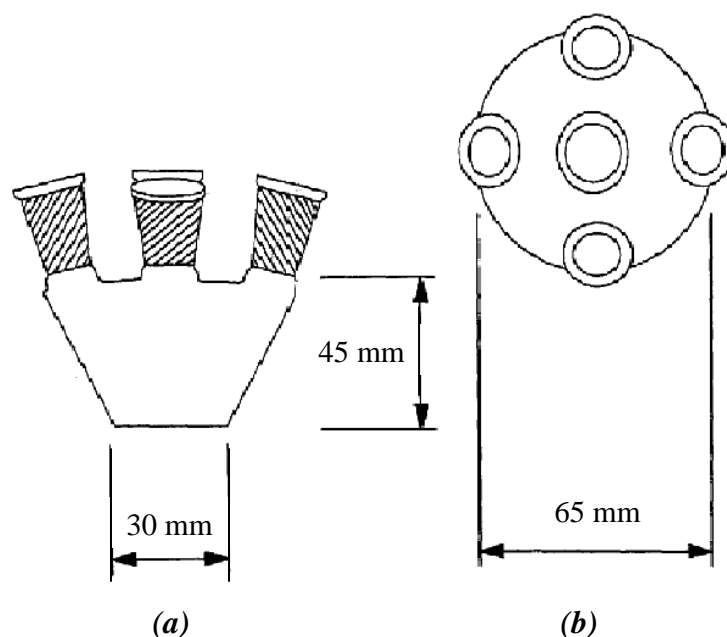


Figure 2.1. Diagram of the 20 cm³, five-necked, Schlenk compatible electrochemical cell shown from (a) side-view and (b) aerial view.

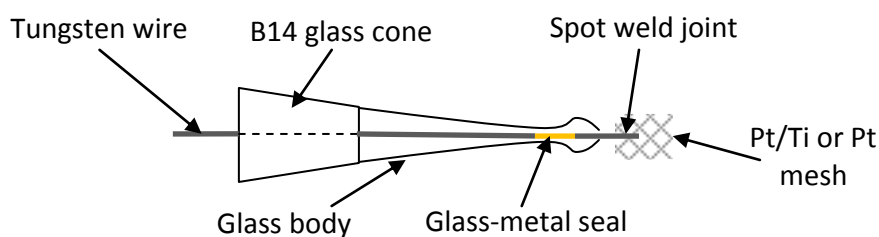
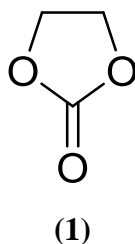
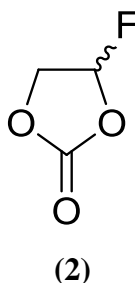


Figure 2.2. Schematic representation of fitted electrodes, designed to fit the cell shown in fig. 2.1.

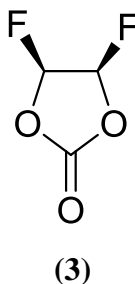
2.2.1. 1,3-Dioxolan-2-one (1)



Determined as a component in the reaction mixture, yellow oil (71%). ^1H NMR (500 MHz, CDCl_3) δ /ppm 4.51 (s, 4H); EIMS (probe) 70 eV, m/z (% rel. int.) $[\text{M} + \text{H}]^+$ 89 (100), 44 (20), 43 (47).

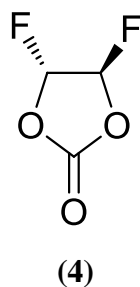
2.2.2. (\pm)-4-Fluoro-1,3-dioxolan-2-one (2)

Determined as a component in the reaction mixture, yellow oil (17%). ^{19}F NMR (500 MHz, CDCl_3) δ /ppm -120.9 (ddd, $J = 21.5$ Hz, 32.8 Hz, 63.9 Hz, 1F); EIMS (probe) 70 eV, m/z (% rel. int.) $[\text{M} + \text{H}]^+$ 107 (92), 62 (100), 46 (28), 43 (54), 42 (37).

2.2.3. *Syn*-(\pm)-4,5-difluoro-1,3-dioxolan-2-one (3)

Determined as a component in the reaction mixture, yellow oil (trace). ^{19}F NMR (500 MHz, CDCl_3) δ /ppm -148.35 (AA'XX', $J = 3.1$ Hz, 6.0 Hz, 12.6 Hz, 61.0 Hz, 2F, see fig. 2); EIMS (probe) 70 eV, m/z (% rel. int.) $[\text{M} + \text{Na}]^+$ 147 (100), 133 (68), 89 (40).

2.2.4. Anti-(±)-4,5-difluoro-1,3-dioxolan-2-one (4)

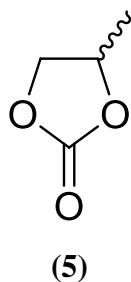


Determined as a component in the reaction mixture, yellow oil (trace). ^{19}F NMR (500 MHz, CFCl_3) δ /ppm -135.08 (unresolved AA'XX' system, 2F); EIMS (probe) 70 eV, m/z (% rel. int.) $[\text{M} + \text{Na}]^+$ 147 (100), 133 (68), 89 (40).

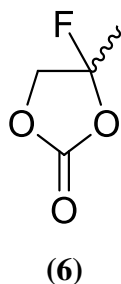
2.3. General procedure for the conventional ECF of propylene carbonate

In order to ensure that the reaction was kept as dry as possible, the experiment was carried out in a glove box.

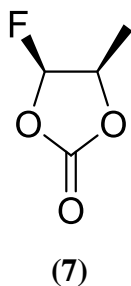
Tetraethylammonium fluoride tetrahydrofluoride ($\text{Et}_4\text{NF}\cdot 4\text{HF}$, 43.6 mmol, 10.00 g) was weighed into a 20 mL, tapered, glass electrochemical cell (fig. 2.1) with fitted electrodes (fig. 2.2), before a platinum mesh electrode (0.5 cm \times 1.0 cm) was placed into the cell so that the mesh was submerged as far as possible in the solution, *ca.* 5 mm away from a platinum counter/reference electrode (1.0 cm \times 2.0 cm) and a CV was recorded between 0 V and 3 V vs. CE. Propylene carbonate (18.2 mmol, 1.86 g) was added and the mixture was stirred for *ca.* 1 min. The stirrer was stopped and another CV was obtained. The solution was stirred during electrolysis under galvanostatic control at 100 mA cm^{-2} for 70,237 s, collecting data points every 7.1 s. The resultant brown liquid was extracted in DCM (3 \times 15 mL) and washed with ice water (3 \times 15 mL). The organic fractions were combined and dried (MgSO_4) before the organic product was filtered and the solvents removed *in vacuo*. The resultant yellow oil (1.35 g) was analysed by ^1H and ^{19}F NMR as well as by EI-MS.

2.3.1. (\pm)-4-Methyl-1,3-dioxolan-2-one (5)

Determined as a component in the reaction mixture, yellow oil (55%). ^1H NMR (500 MHz, CDCl_3) δ /ppm 4.51 (s, 4H); ^{13}C NMR (125 MHz, CDCl_3) δ /ppm 64.77 (s), 152.65 (s); FT-IR (cm^{-1}); EIMS (probe) 70 eV, m/z (% rel. int.) $[\text{M} + \text{H}]^+$ 89 (100), 44 (20), 43 (47).

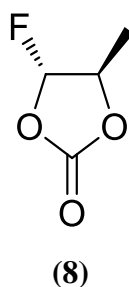
2.3.2. (\pm)-4-Fluoro-4-methyl-1,3-dioxolan-2-one (6)

Determined as a component in the reaction mixture, yellow oil (25%). ^1H NMR (500 MHz, CDCl_3) δ /ppm 4.55 (dd, $^3J_{\text{H-F}} = 17.4$ Hz, $^2J_{\text{H-H}} = 10.3$ Hz, 1H), 4.33 (dd, $^3J_{\text{H-F}} = 30.6$ Hz, $^2J_{\text{H-H}} = 10.3$ Hz, 1H), 1.82 (d, $^3J_{\text{H-F}} = 17.4$ Hz, 3H); ^{19}F NMR (470 MHz, CDCl_3) δ /ppm -92.23 (m, $^3J_{\text{H-F (anti)}} = 30.6$ Hz, $^3J_{\text{H-F (syn)}} = 17.4$ Hz, $^3J_{\text{Me-F}} = 17.4$ Hz, 1F, see. fig. 3); EIMS (probe) 70 eV, m/z (rel. int.) $[\text{M}]^+$ 103 (100), 57 (93).

2.3.3. Syn-(\pm)-4-fluoro-5-methyl-1,3-dioxolan-2-one (7)

Determined as a component in the reaction mixture, yellow oil (7%). ^1H NMR (500 MHz, CDCl_3) δ /ppm 6.10 (dd, $^2J_{\text{H-F}} = 63.6$ Hz, $^3J_{\text{H-H}} = 4.1$ Hz, 1H), 4.82 (ddq, $^3J_{\text{H-F}} = 24.8$ Hz, $^3J_{\text{Me-H}} = 6.5$ Hz, $^3J_{\text{H-H}} = 4.1$ Hz 1H), 1.52 (dd, $^3J_{\text{Me-H}} = 6.5$ Hz, $^4J_{\text{Me-F}} = 2.0$ Hz, 3H); ^{19}F NMR (500 MHz, CDCl_3) δ /ppm -138.99 (ddq, $^2J_{\text{H-F}} = 63.6$ Hz, $^3J_{\text{H-F}} = 24.8$ Hz, $^4J_{\text{H-F}} = 2.0$ Hz, 1F); EIMS (probe) 70 eV, m/z (rel. int.) $[M + H]^+$ 121 (100), 59 (77), 57 (31), 43 (99).

2.3.4. *Anti-(±)-4-fluoro-5-methyl-1,3-dioxolan-2-one* (8)



Determined as a component in the reaction mixture, yellow oil (5%). ^1H NMR (500 MHz, CDCl_3) δ /ppm 5.86 (dd, $^2J_{\text{H-F}} = 63.5$ Hz, $^3J_{\text{H-H}} = 0.9$ Hz, 1H), 4.78 (ddq, $^3J_{\text{H-F}} = 19.1$ Hz, $^3J_{\text{Me-H}} = 6.5$ Hz, $^3J_{\text{H-H}} = 0.9$ Hz 1H), 1.47 (d, $^3J_{\text{Me-H}} = 6.5$ Hz, 3H); ^{19}F NMR (500 MHz, CDCl_3) δ /ppm -120.02 (ddd, $^2J_{\text{H-F}} = 63.5$ Hz, $^3J_{\text{H-F}} = 19.1$ Hz, $^3J_{\text{H-H}} = 0.9$ Hz, 1F); EIMS (probe) 70 eV, m/z (rel. int.) $[M + H]^+$ 121 (70), 59 (52), 57 (29), 43 (100).

2.4. Fitted electrode construction

In order to ensure a vacuum tight seal, fitted electrodes were constructed (fig. 2.2), by welding tungsten wire into a B14 glass cone. Tungsten was chosen as it is known to achieve the best metal-glass seal. However, tungsten is extremely difficult to spot weld; therefore, the exposed end of the tungsten wire nearest the glass-metal seal was electrodeposited with Pt, in order to achieve a more secure spot weld to the Pt or the Pt/Ti mesh.

2.5. General procedure for the fabrication of the composite anodes

The fabrication of the Au/Si/TiO₂/Au composite electrodes employed in this work has been reported previously⁶³ and utilised a TiO₂ layer deposited *via* magnetron sputtering of a compound target in argon, as opposed to reactive sputtering which would involve a Ti target in Ar O₂.

Silicon wafers (n-type phosphorus doped, $10 - 30 \Omega \text{ cm}$, (100) orientation, $300 \pm 10 \mu\text{m}$ thickness) of 50.8 mm diameter were used as substrates. An Ohmic contact to the back of the wafer was formed *via* an electron beam evaporated 100 nm 99% Au:1% Sb layer, annealed at $400 \text{ }^\circ\text{C}$ under nitrogen for 15 minutes, followed by a 80 nm Au layer. The wafer was then cleaned in dilute hydrofluoric acid before a $120 \pm 7 \text{ nm TiO}_2$ layer was sputtered on the front. The Ti target employed (Kurt J. Lesker Co. Ltd) was 99.9% TiO_2 with As (0.001 wt.%), Fe (0.002 wt.%) and Zn (0.001 wt.%) as the main impurities. The TiO_2 layer so formed may be considered to be a disordered dielectric. Finally, a square metal (Au or Pt) grid was patterned on top of the TiO_2 layer by *lift-off*. The metal was 120 nm thick and the grid was $375 \mu\text{m}$ wide with 1 mm^2 open area. A 10 nm Ti layer of the same dimensions as the grid was used to ensure strong adhesion of the Au to the TiO_2 . Once deposition was complete, the substrates were divided into four segments (see. fig. 2.3(a)).

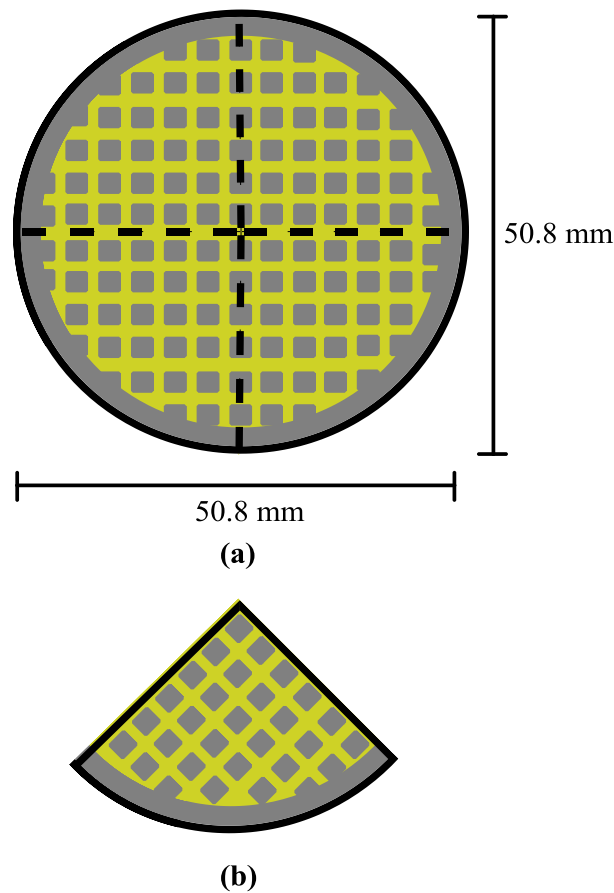


Figure 2.3. Diagrammatical representation of (a) an Au/Si/TiO₂/Au composite wafer and (b) a quarter segment of an Au/Si/TiO₂/Au composite wafer to be fabricated into a composite anode.

One quarter of a substrate (fig. 2.3(b)) was fabricated into a single anode by making two contacts to the Au grid, and one to the centre of the Si, using silver araldite (RS silver loaded epoxy adhesive/hardener system) covered with Araldite Rapid resin to provide support for the contacts and protect them from electrolyte (see fig. 2.4). The wires were then encased within a plastic tube and affixed using Araldite Rapid resin. The geometric area of the Au grid was 2.1 cm^2 .

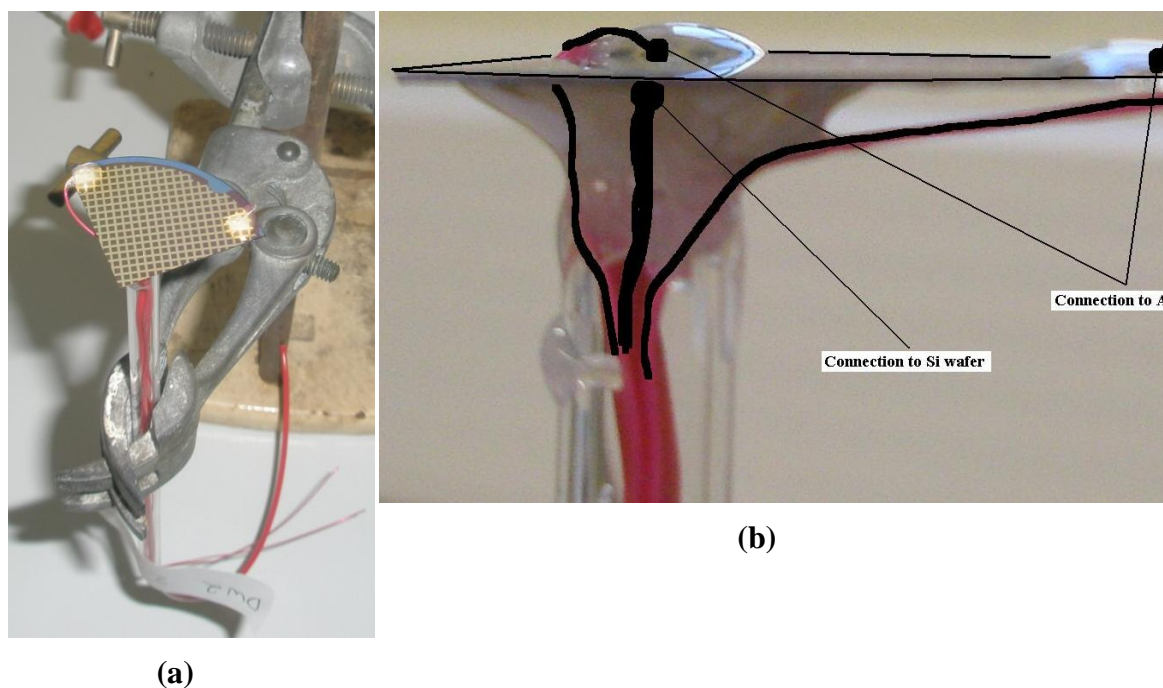


Figure 2.4(a) Aerial photograph of a fabricated composite anode showing the 2 connections to the Au grid covered with araldite rapid and the single connection to the back of the wafer and **(b)** side-view, close-up of both the Au and Si connections.

2.6. General procedure for the preparation of Pt/Ti mesh electrodes

2.6.1. Preparation of the platinising solution

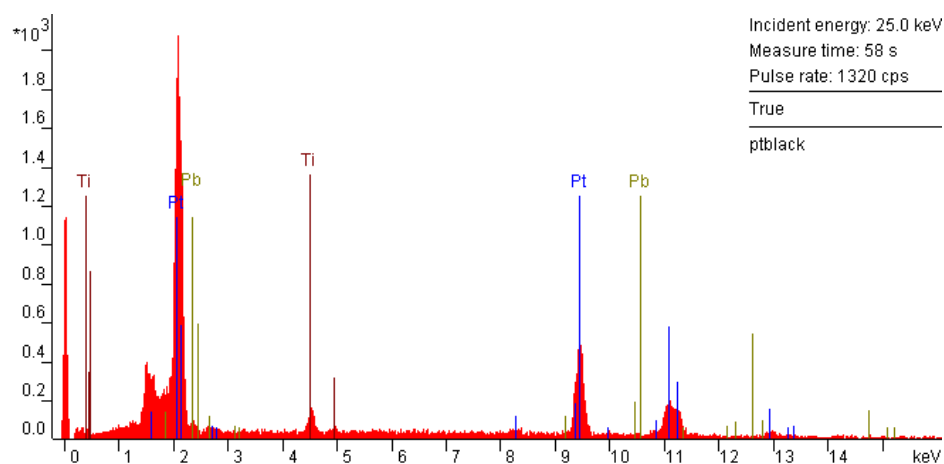
Chloroplatinic acid (1.00 g) and lead tetraacetate (0.012 g) were accurately weighed into a 100 cm^3 volumetric flask. The flask was filled to *ca.* 2 cm below the 100 cm^3 mark. Using a Pasteur pipette, the conc. perchloric acid (0.10 g) was accurately weighed into a sample vial. Finally, the conc. perchloric acid was pipetted into the volumetric flask and the flask was filled to the 100 cm^3 mark using a pipette. The resultant yellow solution was well shaken, to ensure a homogenous mix before the flask was covered with aluminium foil, to avoid photo-degradation of the solution.

2.6.2. Preparation of Ti meshes

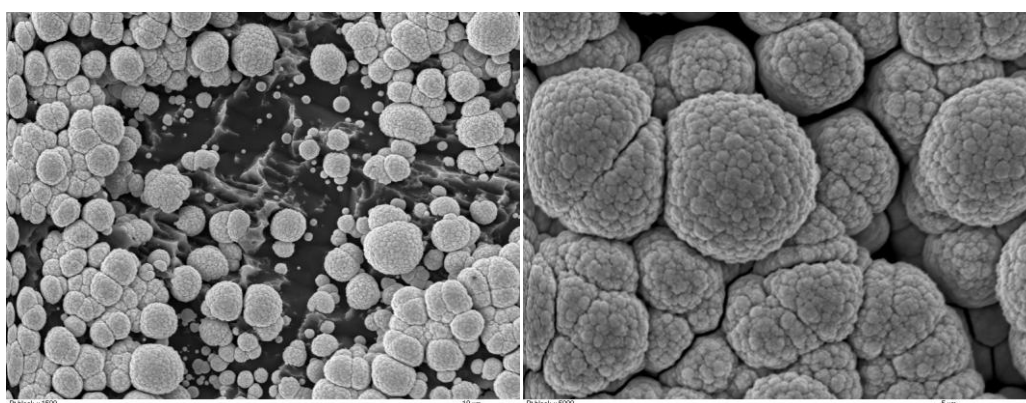
The Ti meshes and the Ti wire were both cut to the required size. The burrs of the meshes were flattened by placing each mesh between two metal plates in the hot press at *ca.* 1000 N for 5 min (no heat applied). The meshes were spot welded to Ti wire (0.5 mm diameter) before being degreased by washing thoroughly with acetone (20 cm³), followed by DI water (20 cm³). A 10% oxalic acid solution was prepared in DI water (20 g oxalic acid in 200 cm³ DI water) and the meshes were immersed in the solution and boiled for 30 min after which time the solution turned brown in colour. The solution was allowed to cool to room temperature and was decanted before the meshes were washed thoroughly with DI water (20 cm³). The meshes were immersed in a beaker containing 150 cm³ DI water and sonicated for 10 min, before the DI water was changed and the sonication process repeated. This occurred 3 times or until no more oil/grease was visible on the surface of the water. Finally, the meshes were washed a final time with DI water (20 cm³) and placed in the oven at 60 °C for at least 30 min to dry.

2.6.3. Platinum electrodeposition procedure

The Ti mesh/wire to be platinised was weighed and the mass recorded. The platinising solution (50 cm³, made as per section 2.6.1) was decanted into a 50 cm³ beaker and the cleaned meshes/wires were immersed into the solution and clamped co-facial to and *ca.* 5 mm away from a Pt mesh counter electrode (2.25 cm²). The positive wire was connected to the counter electrode and the negative wire to the mesh/wire to be platinised. Using a DC power supply at a voltage of 1.5 V, the solution was electrolysed for 7 h. The mesh/wire was then rinsed with DI water (10 cm³) and placed in the oven at 60 °C for at least 30 min to dry. Once dry, the mesh was allowed to cool to room temperature and weighed to determine the mass of Pt deposited. To ascertain whether or not there were any Pb impurities present in the Pt layer, scanning electron microscopy (SEM) and energy dispersive X-ray (EDX) analysis was performed as shown in fig. 2.5.



(a)



(b)

(c)

Figure 2.5(a) EDX analysis of platinised Ti mesh and SEM images of platinised Ti mesh surface at magnification (b) $\times 1500$ and (c) $\times 5000$.

It is clear from figs. 2.5(b) and (c) that the surface of the mesh contains imperfections; however, the Pt has been deposited as individual clusters creating the sponge like effect. These clusters are most probably formed by Pt particles surrounding a particle of Pb in a similar way to the formation of a micelle, with the hydrophobic tails facing inwards and the hydrophobic heads forming a protective outer barrier. The clusters are then being individually deposited onto the surface of the Ti mesh. This would provide no problems in terms of the electrochemistry as there are no Pb surfaces exposed as evidenced by the EDX (fig. 2.5(a)).

2.7. General procedure for the characterisation of the composite anodes

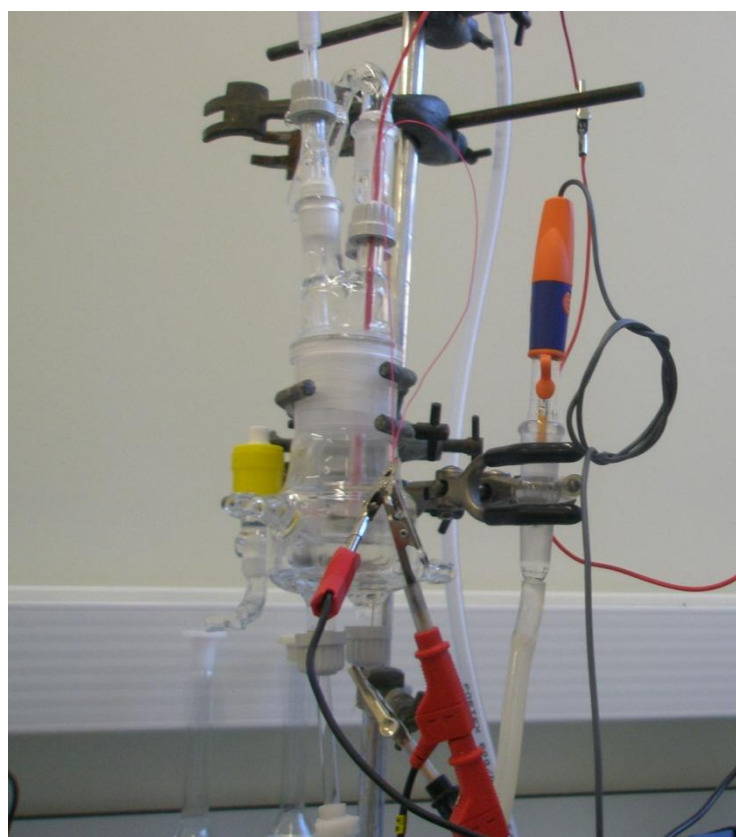
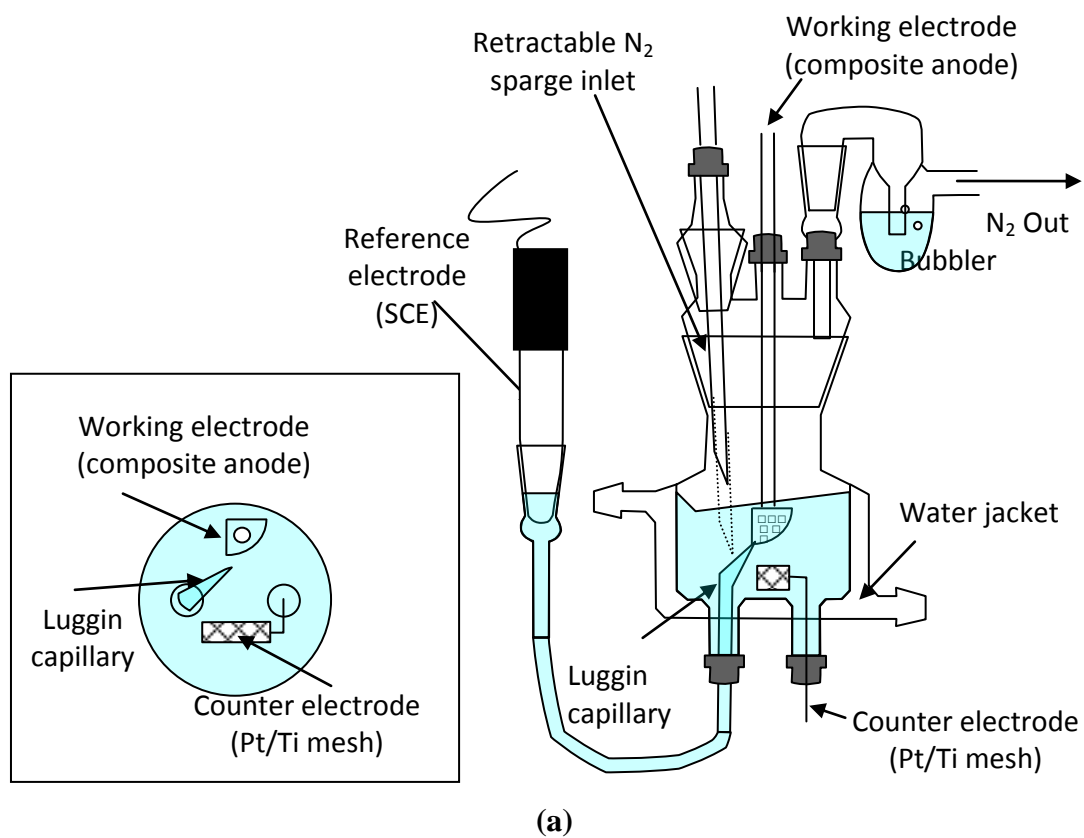
2.7.1. General procedure for obtaining the device characteristic curve

The device characteristic curve (DCC) of each composite anode was obtained in both air and 0.5 M H₂SO₄ in order to determine the currents flowing through the device. This was done by connecting the anode to the potentiostat, with the Si acting as the WE and the metal grid acting as the CE/RE. A CV was run between -0.1 V and 3 V at a scan rate of 100 mV s⁻¹, producing an I/V plot. A typical example of a DCC in air and H₂SO₄ is shown in fig. 4.6(a). Information regarding the resistance (R) of the anode could be obtained using Ohm's law (2.1).

$$V = IR \quad (2.1)$$

2.7.2. General procedure for performing cyclic voltammetry with the composite anodes

The Au grid of the composite electrode was held *ca.* 1 cm from, and cofacial with, a 4 cm² Pt or Pt/Ti mesh counter electrode in the electrochemical cell (fig. 2.6). The Au Ohmic layer on the Si was protected by a layer of Araldite rapid and hence not immersed in the 0.5 M H₂SO₄ electrolyte in the cell. A Saturated Calomel (SCE, Sentek) reference electrode was in ionic contact with the cell electrolyte *via* a Luggin capillary. The potential of the Au grid was controlled with respect to the reference electrode using an Autolab PGStat 12 potentiostat. The 'bias voltage' V_b between Au grid and Si (grid negative with respect to Si) results in a bias current I_b. These parameters distinguish the current through, and voltage across, the composite anode from the electrochemical potential on the Au grid and electrochemical current between the grid and counter electrode.



(b)

Figure 2.6(a) Diagram of 20 cm³ electrochemical cell used for composite electrolysis and **(b)** photograph of the same glass electrochemical cell configured for cyclic voltammetry.

2.7.3. The electrochemical and bias circuits

The application of bias voltage during electrolysis results in the establishment of 2 separate circuits as shown in fig. 2.7. The standard electrochemical circuit remains between the metal grid of the composite anode (WE) and the Pt/Ti mesh counter electrode, and the bias circuit exists through the composite anode *via* the battery.

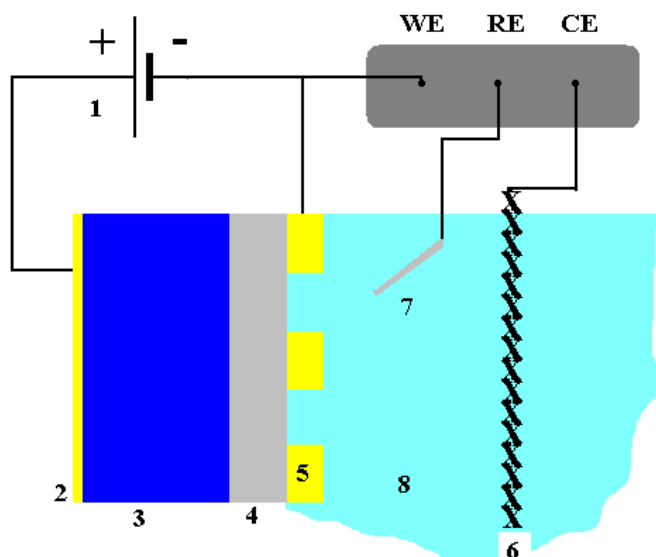


Figure 2.7. The composite anode and electrochemical cell. (1) Battery, (2) Au Ohmic contact on the silicon wafer (3), (4) the TiO₂ layer, (5) the gold grid, (6) the Pt/Ti mesh counter electrode and (7) the reference electrode and (8) the electrolyte.

The Au grid was biased relative to the Au Ohmic contact on the reverse of the Si wafer *via* a AM 6 – 12 (Maplin) 6 V – 12 Ah SLA (sealed lead acid) battery using the circuit shown in fig. 2.8.

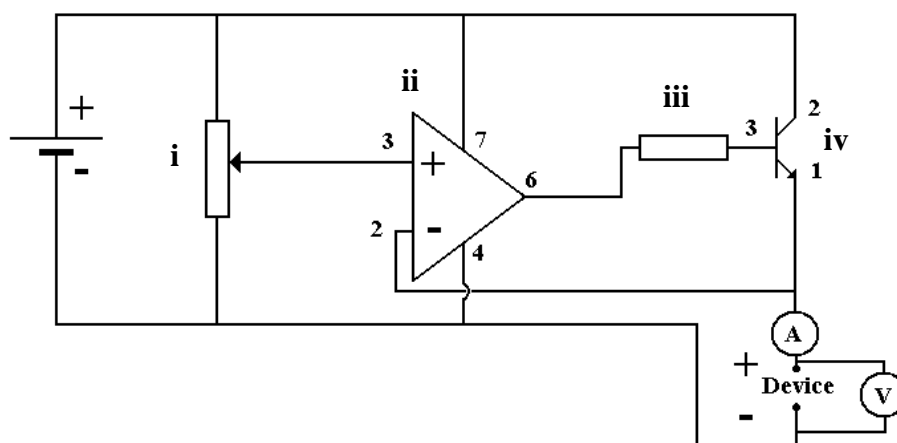


Figure 2.8. The circuit employed to maintain constant voltages across the composite anode when using a battery: (i) 1 k Ω potentiometer, (ii) CA3140 op-amp, (iii) 470 Ω resistor and (iv) BD139 NPN transistor.

A battery was chosen as a DC power supply to avoid complications due to earth loops. The grid was also employed as the working electrode in a standard, 3-electrode cell (fig. 2.6).

2.8. Composite anodes for anhydrous ECF

2.8.1. Platinisation of composite anodes

An Au/Si/TiO₂/Au composite anode (2.1 cm²) was clamped *via* its connecting wire vertically down in a solution of 0.01 M chloroplatinic acid in 0.01 M H₂SO₄ (20 cm³), co-facial to, and roughly 0.5 cm away from, a 2.4 cm² platinum mesh. The CE and RE were connected together and the cell was connected to the potentiostat before -1 C of charge was passed at -1 V for 1 hour as shown in fig. 2.9. The new Au/Si/TiO₂/Au/Pt anode was removed from the cell and washed with DI water before being allowed to dry in air.

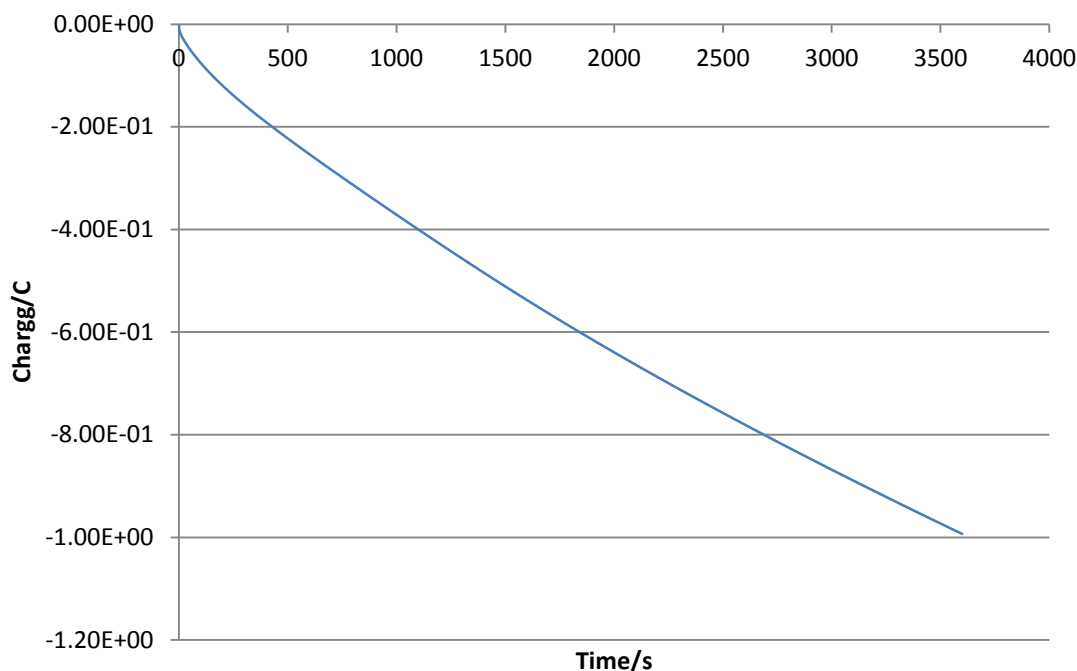


Figure 2.9. Coulometry of Au/Si/TiO₂/Au anode in 0.01 M chloroplatinic Acid/0.01 M H₂SO₄. Cell voltage = -1 V, $t = 3600$ s, Charge = -1 C, data points recorded every 0.5 s

2.8.2. Determination of Pt quasi RE limits

A Pt wire (surface area = 1.51 cm²) was clamped vertically down in an N₂ sparged, 0.5 M solution of H₂SO₄ (20 cm³), co-facial to, and roughly 0.5 cm away from, a 2.4 cm² platinum mesh. The Pt quasi reference electrode was connected to the cell, close to the WE, before the cell was connected to the potentiostat and a CV obtained between -0.80 V and 0.40 V vs. Pt.

Once the anodic and cathodic potential limits were established, the Au/Si/TiO₂/Au/Pt electrode (active area = 2.1 cm²) was reinstated in place of the Pt wire (*i.e.* it was clamped *via* its connecting wire vertically down in an N₂ sparged, 0.5 M solution of H₂SO₄ (20 cm³), co-facial to, and roughly 0.5 cm away from, a 2.4 cm² platinum mesh). The Pt quasi reference electrode was connected to the cell, close to the WE, before the cell was connected to the potentiostat and CVs were obtained between -0.80 V and 0.40 V vs. Pt at bias potentials of 0 V, 0.2 V, 0.5 V and 1.0 V. A second CV was obtained at $V_b = 0$ V after the application of bias potential in order to ensure reversibility of the system.

2.8.3. Anhydrous characterisation of composite anodes

DCCs of the Si/TiO₂/Au/Pt electrode were obtained in air outside and inside the glove box between -0.1 and 3 V, at a scan rate of 100 mV s⁻¹ as well as in Et₄NF₄HF between -0.2 V and 1.2 to 1.4 V, at a scan rate of 100 mV s⁻¹.

An Au/Si/TiO₂/Au/Pt electrode (2.1 cm²) was clamped *via* its connecting wire vertically down in air, before the device was connected to the potentiostat (with the Si acting as the working electrode and the gold grid as the counter/reference electrode) and a DCC was obtained between -0.1 V and 3 V. The electrode and cell were then placed into a glove box under N₂, and another DCC obtained in the N₂ atmosphere. The anode was submerged subsequently in Et₄NF₄HF between -0.2 and 1.2 to 1.4 V.

2.9. Effects of varying H₂SO₄/HClO₄/NaOH concentration

DCCs of the composite anode were obtained in air and H₂O as well as 0.001 M, 0.01 M, 0.1 M, 0.5 M and 1.0 M solution between -0.1 and 3 V, at a scan rate of 100 mV s⁻¹.

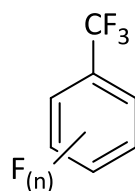
An Au/Si/TiO₂/Au/Pt electrode (2.1 cm²) was clamped *via* its connecting wire vertically down in air, before the device was connected to the potentiostat (with the Si acting as the working electrode and the gold grid as the counter/reference electrode) and a DCC was obtained between -0.1 V and 3 V. The electrode was submerged subsequently in H₂O and the solutions in turn (in order of increasing concentration) and again DCCs were obtained between -0.1 V and 3 V. Between each run, the cell was emptied and both the cell and the anode were washed thoroughly with DI water. After the final solution run, the anode was washed with DI water and a final DCC was obtained in air. The data were plotted and combined for comparison.

2.10. The composite electrolysis of KF

An Au/Si/TiO₂/Pt composite electrode (2.1 cm²) was clamped *via* its connecting wire vertically down in an N₂ sparged, 0.1 M solution of Na₂SO₄/NaOH (pH 9.7) (20 cm³), co-facial to, and roughly 0.5 cm away from, a 2.4 cm² platinised titanium mesh in a 20 cm³ glass electrochemical cell (fig. 2.6). The calomel reference electrode was connected to the cell so that it was in ionic contact with the WE *via* a luggin capillary, before the cell was connected to the potentiostat and the CV was run, at different bias potentials, registering current vs. potential. The experiment was performed using potential limits of

-0.75 V and 1.00 V vs. SCE, at a scan rate of 100 mV s⁻¹. Bias potentials from 0 V – 3 V were applied. 0.1 M KF (1 cm³ of 2.0 M KF in 20 cm³ of 0.1 M Na₂SO₄/NaOH) was added and the CVs obtained again, using the same bias potentials as in the previous experiment. The reference electrode used was Hg|Hg₂Cl₂ in sat. KCl, and the experiment was performed at room temperature (20 °C – 25 °C). The buffered Na₂SO₄ solution was sparged of O₂ prior to the experiment by bubbling N₂ gas through the solution for 15 min. The N₂ bubbler was raised prior to running the experiment in order to keep the solution under an N₂ atmosphere, whilst refraining from agitating the solution during the scan. The system was electrolysed using chronoamperometry at 1 V, with a 3 V applied bias potential for 10 minutes. After this time, anisole (1 cm³) was added, with vigorous shaking, in an attempt to trap any “F⁺” species generated. The anisole was extracted from the mixture using diethyl ether (20 cm³) and dried by the addition of MgSO₄ before being filtered under vacuum, and the solvent removed under reduced pressure. The resultant pale yellow oil was analysed by ¹H and ¹⁹F NMR.

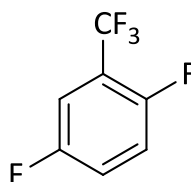
2.11. General procedure for the conventional ECF of benzotrifluoride



The electrolysis of benzotrifluoride was performed using a procedure adapted from Knunyants et al.⁴³ with a 20 cm³ un-divided, tapered, glass cell on top of which was five, B14 ground glass sockets for the insertion of fitted electrodes and connection to a Schlenk line (fig. 2.1.). Fitted electrodes (fig. 2.2) were made as per the details above (section 2.4) and used in conjunction with the cell to ensure a vacuum tight seal. The cell was attached to a Schlenk line and dried under vacuum before being filled with N₂ to ensure that the reaction was kept completely anhydrous throughout. Anhydrous acetonitrile (20 cm³) was transferred to a dried, N₂ saturated, Schlenk compatible EC cell (into which a Pt/Ti mesh (1 cm x 0.5 cm) (WE) was fixed, co-facial to and roughly 0.5 cm away from another Pt/Ti mesh (2 cm x 1 cm)(CE)), by canula filtration (to remove any dust particles present as a result of the decomposition of the 4Å molecular sieves over which the acetonitrile was stored). Tetrabutylammonium fluoride (20.0 mmol) was added, by syringe, and the resultant colourless mixture was stirred using a magnetic stirrer bar to ensure a homogeneous state. The electrodes were connected to

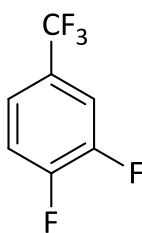
the potentiostat, the stirrer stopped, and a cyclic voltammograms (CV) run between 0 V and 3.2 V vs. Pt at a scan rate of 100 mV s⁻¹. Benzotrifluoride (1.00 g, 6.8 mmol) was added by syringe, under N₂ and the colourless mixture was stirred while the voltage was cycled under potentiostatic control at 3.2 V vs. Pt for 23324 s (passing 80% of the theoretical amount of electricity). The product was extracted from the reaction mixture with diethyl ether (3 x 15 cm³) and washed with DI water (3 x 15 cm³), before being dried over MgSO₄ and the solvents removed *in vacuo*, leaving the crude product (0.38 g, 31%) in the form of an orange/brown oily solid. ¹⁹F NMR showed that a mixture of fluorinated products had been obtained, therefore, the crude product was purified by column chromatography. This was done by dry loading the compound onto silica (5.59 g) by rotary evaporation with ethyl acetate. Once loaded, the silica was packed into a DASi[®] column for automatic injection, and the crude product was columned using an 8 g normal phase cartridge (SF10-8g). The solvents used were petroleum ether (40-60) (solvent A) and ethyl acetate (solvent B), over a period of 40 min. The pure products, 2,5-difluorobenzotrifluoride (**1**) (0.066 g, 5%) and 3,4-difluorobenzotrifluoride (**2**) (0.021 g, 2%) were obtained both in the form of a yellow oil.

2.11.1. 2,5 – Difluorobenzotrifluoride (**9**)



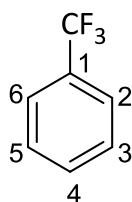
(**9**)

Yellow oil (0.066 g, 5%); IR (KBr) 3281, 3056, 1670, 1504 cm⁻¹; ¹⁹F NMR (376 MHz, CDCl₃) δ/ppm -61.15 (3F, s, CF₃), -115.03 (1F, s, F-2), -119.58 (1F, s, F-5)

2.11.2. 3,4 – Difluorobenzotrifluoride (**10**)**(10)**

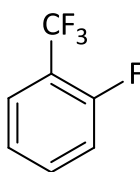
Yellow oil (0.021 g, 2%); IR (KBr) 3260, 3056, 1689, 1534 cm^{-1} ; ^{19}F NMR (376 MHz, CDCl_3) δ /ppm -61.16 (3F, s, CF_3), -129.81 (1F, s, F-4), -133.57 (1F, s, F-3).

Analytical data of the authentic samples of benzotrifluoride and all expected mono and di-fluorinated products of the benzotrifluoride electrolysis (except for the 2,3 and 2,4 isomers which were, unfortunately, unobtainable before the submission of this manuscript) were purchased from Apollo Scientific. All subsequent benzotrifluoride derivatives are numbered as per the benzotrifluoride standard (**11**).

2.11.3. Benzotrifluoride standard (**11**)**(11)**

Colourless oil: ^{19}F NMR (376 MHz, CDCl_3) δ -62.69 (3F, s, CF_3); ^1H NMR (400 MHz, CDCl_3) δ /ppm 7.64 (2H, d, H-2/H-6, $J = 7.8$ Hz), 7.55 (2H, t, H-3/H-5, $J = 7.8$ Hz), 7.48 (1H, t, H-4, $J = 7.3$ Hz).

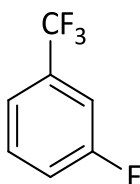
2.11.4. 2-Fluorobenzotrifluoride standard (12)



(12)

Colourless oil: ^{19}F NMR (376 MHz, CDCl_3) δ/ppm -61.36 (3F, s, CF_3), -114.38 (1F, s, ArF); ^1H NMR (400 MHz, CDCl_3) δ/ppm 7.61 (1H, td, H-4, $J = 7.8$ Hz), 7.54 (1H, m, H-3), 7.26 – 7.17 (2H, m, H-5/H-6)

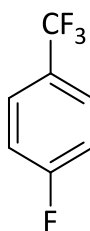
2.11.5. 3-Fluorobenzotrifluoride standard (13)



(13)

Colourless oil: ^{19}F NMR (376 MHz, CDCl_3) δ/ppm -62.74 (3F, s, CF_3), -110.75 (1F, s, ArF); ^1H NMR (400 MHz, CDCl_3) δ/ppm 7.46 (1H, dd, H-6, $J = 8.2$ Hz), 7.42 (1H, t, H-5, $J = 7.8$ Hz), 7.31 (1H, d, H-4, $J = 8.7$ Hz), 7.24 (1H, t, H-2, $J = 8.7$ Hz)

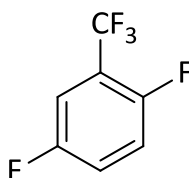
2.11.6. 4-Fluorobenzotrifluoride standard (14)



(14)

Colourless oil: ^{19}F NMR (376 MHz, CDCl_3) δ/ppm -61.88 (3F, s, CF_3), -107.50 (1F, s, ArF); ^1H NMR (400 MHz, CDCl_3) δ/ppm 7.61 (2H, dd, H-2/H-6, $J = 5.1$ Hz, 8.72), 7.15 (2H, t, H-3/H-5, $J = 8.72$ Hz).

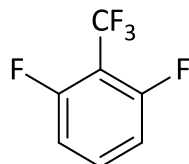
2.11.7. 2,5-Difluorobenzotrifluoride standard (15)



(15)

Colourless oil: ^{19}F NMR (376 MHz, CDCl_3) δ/ppm -61.84 (3F, s, CF_3), -116.77 (1F, s, F-2), -120.15 (1F, s, F-5); ^1H NMR (400 MHz, CDCl_3) δ/ppm 7.32 – 7.28 (1H, m, H-6), 7.26 – 7.14 (2H, m, H-3/H-4)

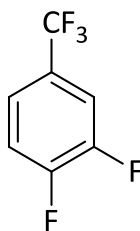
2.11.8. 2,6-Difluorobenzotrifluoride standard (16)



(16)

Pink oil: ^{19}F NMR (376 MHz, CDCl_3) δ/ppm -56.32 (3F, t, CF_3), -110.80 (2F, s, F-2/F-6); ^1H NMR (400 MHz, CDCl_3) δ/ppm 7.53 – 7.46 (1H, m, H-4), 6.99 (2H, t, H-3/H-5, $J = 8.7$ Hz)

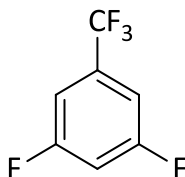
2.11.9. 3,4-Difluorobenzotrifluoride standard (17)



(17)

Colourless oil: ^{19}F NMR (376 MHz, CDCl_3) δ/ppm -62.17 (3F, s, CF_3), -131.62 (1F, s, F-4), -134.80 (1F, s, F-3); ^1H NMR (400 MHz, CDCl_3) δ/ppm 7.47 – 7.38 (2H, m, H-5/H-6), 7.28 (1H, m, H-2)

2.11.10. 3,5-Difluorobenzotrifluoride standard (18)



(18)

Colourless oil: ^{19}F NMR (376 MHz, CDCl_3) δ/ppm -63.07 (3F, s, CF_3), -106.49 (2F, s, F-3/F-5); ^1H NMR (400 MHz, CDCl_3) δ/ppm 7.15 (2H, d, H-2/H-6, $J = 5.5$ Hz), 7.00 (1H, tt, H-4, $J = 8.7$ Hz)

2.12. Composite electrolyses

2.12.1. The composite electrolysis of benzotrifluoride on the anode surface

An Au/Si/TiO₂/Au composite anode was clamped facing upwards. In order to disperse any heat generated by the light source, a water filter comprising a beaker filled with a 5 cm depth of deionised water was placed on a tripod 1 cm above the surface of the anode. Placed 1 mm above the surface of the water, the light source was pointing directly through the water to the face of the anode, meaning that the overall distance from the light source to the surface of the anode was *ca.* 6.1 cm (see fig. 2.10). The anode was then connected to the potentiostat with the silicon acting as the working

electrode and the gold grid as the counter/reference electrode. A DCC was run between -0.1 V and 3.0 V in air at a scan rate of 100 mV s^{-1} before the surface of the anode was irradiated at max. lux, and the DCC run again as before. Next, the light source was turned off and roughly 6 drops of sat. TBAF in TFT were added to the surface of the anode using a Pasteur pipette and the DCC was again run as previously. Finally, the anode was irradiated again at $h\nu = \text{max. lux}$ and a final DCC was run before the mixture on the anode was electrolysed for 2 h at $E = 3.0$ V and $h\nu = \text{max. lux}$. This procedure was then repeated a further two times.

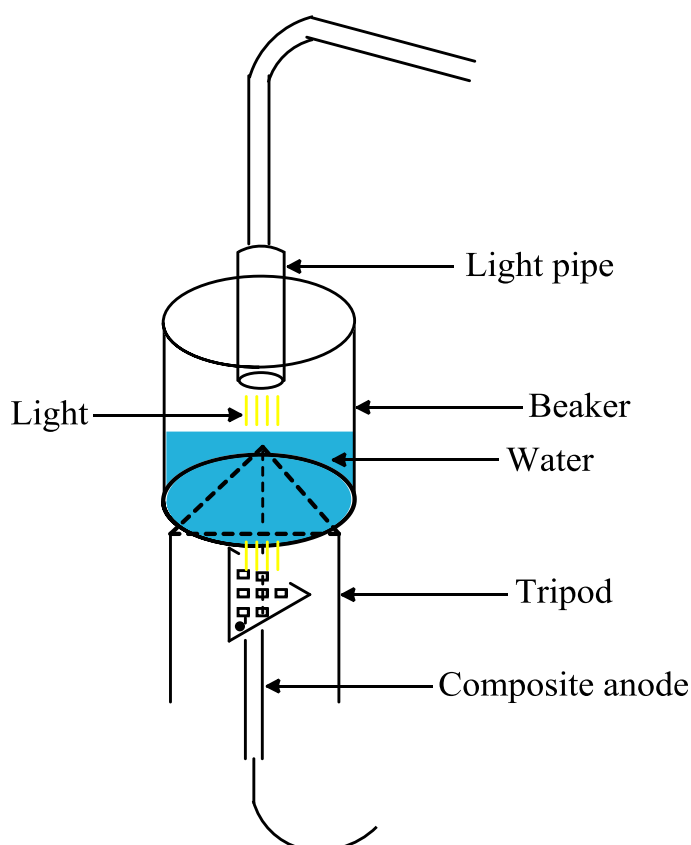


Figure 2.10. Diagram showing irradiation of composite anode through a 5 cm water filter.

2.12.2. The composite electrolysis of anisole on the anode surface

An Au/Si/TiO₂/Au composite anode was clamped facing upwards in a glass EC cell. A solution (20 drops = *ca.* 0.5 cm^3) containing 1 equivalent of anisole (0.5 g) and 2 equivalents of TBAF (2.42 g) in ethyl acetate (*ca.* 10 cm^3) was dropped onto the surface of the anode using a Pasteur pipette, before a greased, fitted blank stopper was fitted to close the cell. In order to disperse any heat generated by the light source, a water filter comprising a beaker filled with a 5 cm depth of deionised water was clamped roughly 1 cm above the surface of the anode (this distance includes the distance from anode

surface to the blank stopper). Roughly 1 mm above the surface of the water was the light source pointing directly through the water and the blank to the face of the anode, meaning that the overall distance from the light source to the surface of the anode was roughly equal to 6.1 cm. The anode was then connected to the potentiostat with the silicon acting as the working electrode and the gold grid as the counter/reference electrode. A DCC was run between -0.1 V and 3.0 V in air at a scan rate of 100 mV s^{-1} before the anode was irradiated at $h\nu = \text{max. lux}$ and a final DCC run as before. The mixture on the anode was then electrolysed for 24 h at $E = 3.0 \text{ V}$ and $h\nu = \text{max. lux}$. After electrolysis, the anode was rinsed with methanol (1 cm^3) and the resultant solution was analysed by ^{19}F NMR.

2.12.3. The composite electrolysis of anisole in solution

An Au/Si/TiO₂/Au composite anode was clamped facing downwards in air and the device characteristic curve (DCC), also called an I/V plot, was obtained by running a CV between -0.1 V and 3 V at a scan rate of 100 mV s^{-1} with the Si acting as the working electrode and the gold grid acting as the reference and counter electrodes. The surface of the electrode was then illuminated to max lux and another DCC run as before. The glass EC cell (fig. 2.6) was filled with the TBAF/MeCN solution (25 cm^3) and the anode was clamped downwards so that the anode surface rested on the surface of the solution. The solution was sparged with N₂ for 10 min before the bubbler was lifted out of solution, maintaining an inert atmosphere, whilst not disturbing the surface of the solution. Again DCCs were obtained at 250 lux (ambient light) and max lux, irradiating at an angle of 45° through the walls of the cell. The light source was *ca.* 2 cm away from the anode surface. Anisole (0.68 cm^3) was then added to the electrolyte/solvent mixture using a Gilson pipette, making a 0.25 M solution of anisole in 0.25 M TBAF/MeCN. The solution was stirred for 10 min using a magnetic stirrer bar, before stirring was stopped and the DCCs obtained, again at 250 lux and max lux. Finally, the stirrer was started again and the solution was electrolysed using chronoamperometry at a constant potential of 3 V, with maximum irradiation for 18,000 s (5 h). Data points were recorded every 1.8 s. After the electrolysis, 0.6 cm^3 of the resultant solution was removed and analysed by ^{19}F NMR.

2.12.4. The composite electrolysis of anisole in solution (with bias)

An Au/Si/TiO₂/Au composite anode was clamped facing downwards in air and the device characteristic curve (DCC) was obtained by running a CV between -0.1 V vs. SCE and 3 V vs. SCE at a scan rate of 100 mV s⁻¹ with the Si acting as the working electrode and the gold grid acting as the reference and counter electrodes. The surface of the electrode was then illuminated to max lux and another DCC run as before. The glass EC cell was filled with the TBAF/MeCN solution (25 cm³) and the anode was clamped downwards so that the anode surface rested on the surface of the solution, *ca.* 0.5 cm away from a 2 cm² Pt/Ti mesh counter electrode. A calomel (Hg/Hg₂Cl₂) reference electrode was placed in ionic contact with the anode *via* a luggin capillary and the solution was sparged with N₂ for 10 min before the bubbler was lifted out of solution, maintaining an inert atmosphere, whilst not disturbing the surface of the solution. Again DCCs were obtained at 250 lux (ambient light) and max lux, irradiating at an angle of 45 ° through the walls of the cell. The light source was approximately 2 cm away from the anode surface. Next, CVs of the electrolyte/solvent mixture were obtained, between 0 V vs. SCE and 3 V vs. SCE, at both V_b = 0 V and 3 V. For each bias potential, CVs were recorded at both hν = 250 lux (ambient light) and hν = max lux.

Anisole (0.68 cm³) was then added to the electrolyte/solvent mixture using a Gilson pipette, making a 0.25 M solution of anisole in 0.5 M TBAF/MeCN. The solution was stirred for 10 min using a magnetic stirrer bar, before stirring was stopped and the DCCs obtained, again at 250 lux and max lux. Again, CVs were recorded at V_b = 0 V and 3 V and hν = 250 lux and max lux.

2.13. Electrochemical fluoride capture

The reagents were set-up as shown in fig. 2.11, using 0.001 M aqueous KF in place of ¹⁸F in the first instance. A potential of 10 V was set across the electrodes, with the GC electrode set positive with respect to the Pt before 0.001 M KF (3 ml) was withdrawn through the cell to the syringe pump at a flow rate of 0.7 ml min⁻¹. Valve number 3 was set to the 2/3 position and the water mixture was infused into a collection vial. The collection vial was removed and replaced before valves 2 and 3 were set to the 1/3 position and valve 1 was set to the 2/3 position. Acetonitrile (3 ml) was withdrawn into

the syringe pump, through the cell at a flow rate of 1 ml min^{-1} and, again, valve 3 was set to the 2/3 position before the mixture was infused into the new collection vial. The collection vial was removed and replaced before all values were set to the 1/3 position. The voltage was reversed and the cell heated to $200 \text{ }^\circ\text{C}$ over a period of 2 minutes (making the temperature in the chamber of the cell equal to $80 \text{ }^\circ\text{C}$). The phase transfer agent (PTA, 3 ml) consisting of potassium kryptofix (75 mg), potassium carbonate (12.5 mg) ($[\text{K}/\text{K}.222]\text{HCO}_3$), acetonitrile (4.75 ml) and water (0.25 ml) was withdrawn through the cell and into the syringe at a flow rate of 0.2 ml min^{-1} . Valve 3 was set to the 2/3 position and the mixture was infused into the collection vial at a flow rate of 1.0 ml min^{-1} .

The fluoride and water content of each of the mixtures collected in the collection vials were analysed using a selective fluoride ion probe and Karl-Fisher Titration respectively.

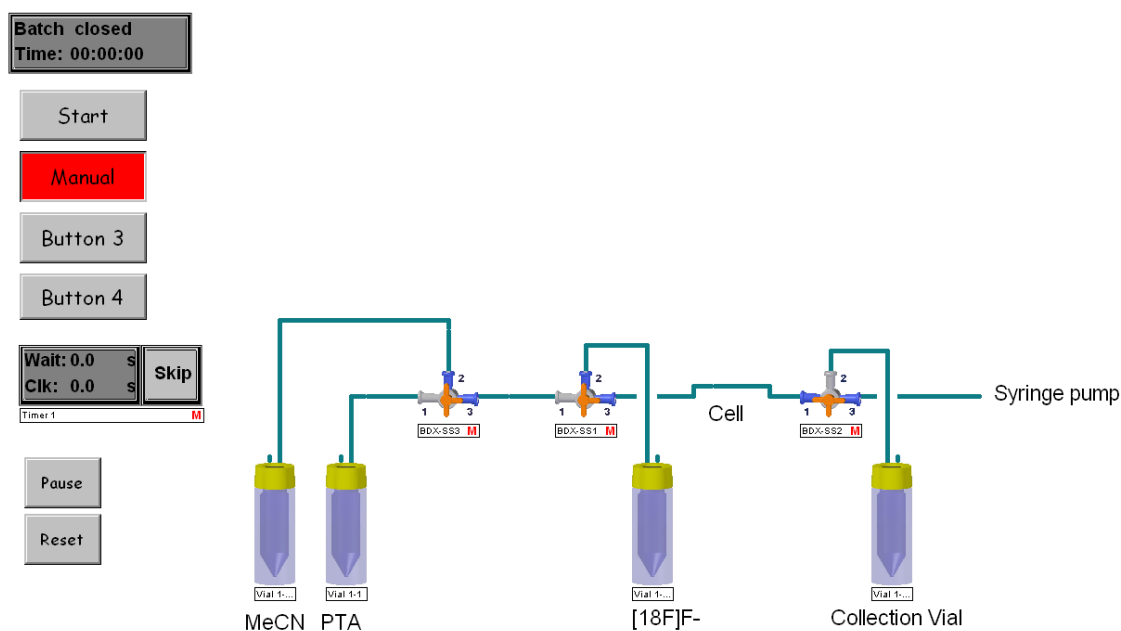


Figure 2.11. Schematic representation of the remote-controlled ModularLab flow system.

3. ECF of Cyclic Carbonates

3.1. Cyclic carbonates background

The ever-increasing use of fluorinated organic compounds in a variety of industries across the chemical sector renders the search for novel, efficient and environmentally friendly fluorination methods more important than ever.^{8, 64-66} Many direct fluorination methods are limited by the necessary use of extremely hazardous reagents (e.g. F₂ gas and liquid HF), which inevitably requires highly specialized equipment and training⁶⁶ and due to the highly reactive nature of these materials, also restricts the range of compatible substrates.^{23, 67} Selective electrochemical fluorination (ECF) has the potential to dramatically expand the substrate scope with the added benefit of using less-hazardous reagents²⁸ which is why interest in the area of ECF continues today;⁶⁸ in spite of this, relatively little is still known about the scope of the process and the mechanisms by which ECF occurs with different substrates.⁶⁹

In order to study the scope of selective ECF, cyclic carbonates were selected as the initial class of materials to be examined as their fluorinated derivatives such as (±)-4-fluoro-1,3-dioxolan-2-one (**2**) are known to increase the cell efficiency of lithium ion batteries by the reduction of electrolyte decomposition⁷⁰⁻⁷³ and that their production — from waste CO₂ and the relevant epoxide — has been demonstrated many times in the recent literature.⁷⁴⁻⁷⁵ The latter provides an efficient and environmentally friendly route to these precursors, thereby dramatically increasing the availability of these compounds as environmentally acceptable solvents.⁷⁶ For these reasons, research into the formation of fluorinated cyclic carbonates has been ongoing throughout the last decade, resulting in the development of both chemical and electrochemical routes to the products.^{56, 77}

Fluorination of ethylene carbonate (EC) (**1**) has been performed using elemental fluorine under a nitrogen atmosphere at 50 °C giving the desired product (±)-4-fluoro-1,3-dioxolan-2-one (**2**) in good yield (70%).⁷⁷ Similarly, Fuchigami et al. showed that the same fluorinated product (**2**) can be synthesized successfully from ethylene carbonate by ECF using the tetraalkylammonium salt, tetraethylammonium fluoride pentahydrofluoride (Et₄NF·5HF) as the fluoride source, providing a less hazardous and more efficient/environmentally friendly⁷⁸ route to the desired fluorinated carbonate (**2**) than that employing elemental fluorine and with an isolated yield of 76%.⁷⁹

Surprisingly, the focus of research in this area has been mainly on the fluorination of ethylene carbonate (EC)(**1**) with no procedure reported for the fluorination of analogous substrates such as propylene carbonate (PC)(**5**), which may also possess desirable solvent properties for Li-ion batteries.

In this chapter, data is reported on the yield and distribution of fluorinated products from the ECF of ethylene carbonate as a function of electrolyte and current density. As the molten salt used by Fuchigami et al.⁷⁹ ($\text{Et}_4\text{NF}\cdot 5\text{HF}$) is no longer commercially available, the electrolyses were repeated using the analogous salts $\text{Et}_4\text{NF}\cdot 3\text{HF}$ and $\text{Et}_4\text{NF}\cdot 4\text{HF}$. The optimum conditions were then applied to the ECF of propylene carbonate, a reaction that has not been reported previously, in an attempt to control the distribution of fluorinated products obtained by differentiating between the two saturated carbon atoms in the 1,3-dioxolan-2-one ring system.

3.2. Electrolysis of cyclic carbonates

Cyclic voltammograms were collected prior to the electrolyses using Pt mesh working and counter electrodes immersed in $\text{Et}_4\text{NF}\cdot x\text{HF}$ ($x = 3, 4$) in the absence and presence of 18.2 mmol ethylene/propylene carbonate, and a representative voltammogram is shown in fig. 3.1. In each case, a clear oxidation peak was visible at 1.1 V vs. counter electrode (CE) in the presence of the substrate. Selective ECF of EC (**1**) was performed at current densities of 50, 100 and 200 mA cm^{-2} using the molten salt electrolyte $\text{Et}_4\text{NF}\cdot x\text{HF}$ ($x = 3, 4$). The overall yield and distribution of products (Scheme 3.1) were found to vary with electrolyte and current density as summarized in Table 3.1.

The optimum yield (17.2%) was obtained using the electrolyte $\text{Et}_4\text{NF}\cdot 4\text{HF}$ at a current density of 100 mA cm^{-2} ; ECF is thought to proceed *via* a radical/cation intermediate,⁸⁰ therefore propylene carbonate (**5**) was subjected to the same conditions, the extra methyl substituent providing a tertiary centre which may afford stabilization of any intermediates leading to an improvement in the yield and/or selectivity of the process,

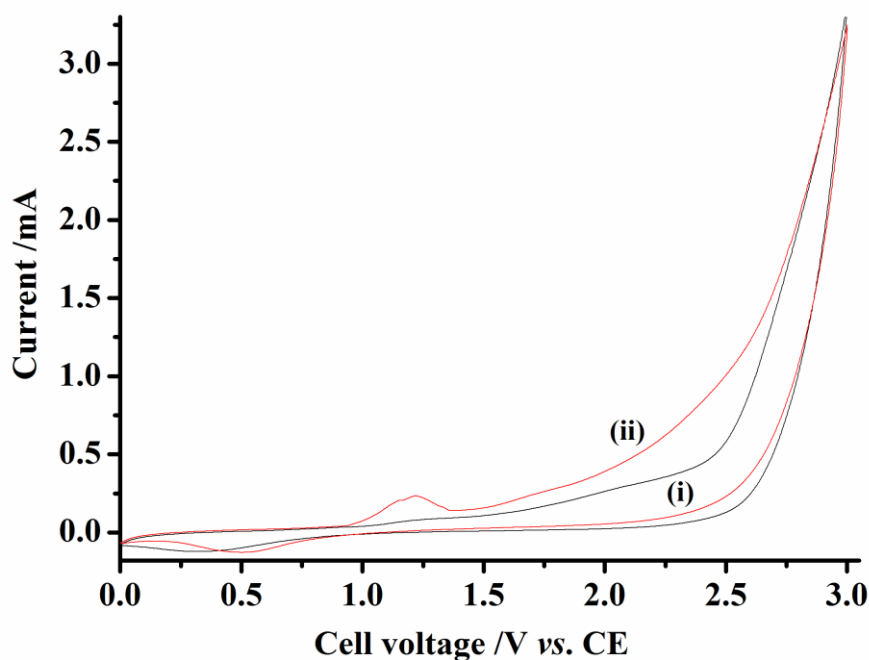
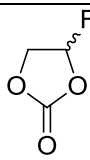
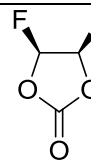
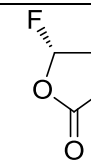
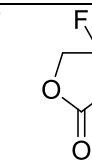
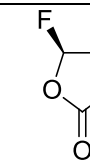
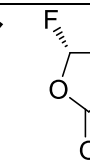


Figure 3.1. Cyclic voltammogram of the 1.0 cm × 0.5 cm Pt mesh working electrode immersed in $\text{Et}_4\text{NF} \cdot 4\text{HF}$ in the (i) absence and (ii) presence of 18.2 mmol PC at a scan rate of 100 mV s^{-1}

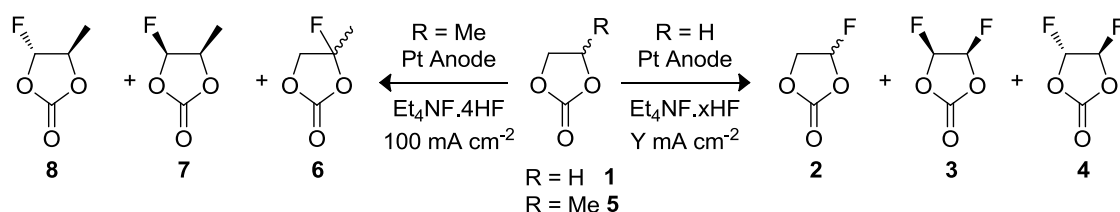
From Table 3.1 it is clear that, in each case, the major product observed from the ECF of EC (**1**) was the mono-fluorinated compound, (\pm)-4-fluoro-1,3-dioxolan-2-one (**2**). It does not seem unreasonable to postulate that the addition of the first fluorine has an inductive effect, there by deactivating the substrate towards further oxidation by withdrawing electron density from the adjacent carbon atom.^{5, 81}

Table 3.1. Summary of product yields and distribution from the ECF of ethylene carbonate (**1**) and propylene carbonate (**5**)

Experiment	Substrate	Electrolyte	I/mA cm ⁻²	Electrolysis time/h ^[a]	Yield/% ^[b]					
										
1	EC	Et ₄ NF.3HF	200	4.88	2.0	<0.1	-	-	-	-
2	EC	Et ₄ NF.3HF	100	9.76	16.4	0.4	0.3	-	-	-
3	EC	Et ₄ NF.3HF	50	19.51	15.8	0.2	<0.1	-	-	-
4	EC	Et ₄ NF.4HF	200	4.88	11.4	0.1	-	-	-	-
5	EC	Et ₄ NF.4HF	100	9.76	17.2	0.6	<0.1	-	-	-
6	EC	Et ₄ NF.4HF	50	19.51	17.0	0.2	0.1	-	-	-
7	PC	Et ₄ NF.4HF	100	9.76	-	-	-	25.7	7.1	4.7

[a] Electrolysis times based on 2 e⁻ process passing 100% theoretical amount of charge (substrate = 18.2 mmol) [b] Yields calculated by ¹⁹F NMR (reference = 0.05 M PhF)

In addition, as the electrolysis is a diffusion-controlled process, the product distribution relies largely on the concentration of the species present in solution.⁸² As there is a greater amount of starting material than mono-fluorinated product present in the reaction mixture, the probability of EC (**1**) being at the anode at any one time is greater than that of the mono-fluorinated product (**2**), thereby decreasing the probability of formation of the difluorinated products (**2** & **3**) until sufficient mono-fluorinated product is generated.



Scheme 3.1. Major products obtained from the electrolysis of ethylene carbonate (**1**) and propylene carbonate (**5**). $x = 3, 4$; $Y = 50, 100, 200$.

The product with the second highest yield upon ECF of EC (**1**), was *syn*-(±)-4,5-difluoro-1,3-dioxolan-2-one (**3**). The preferential formation of the *syn*-isomer (**3**) over the *anti*-isomer (**4**) in each case, suggests that the product distribution may be influenced by the fluorination mechanism which is currently being investigated using spectroelectrochemical techniques. The trend observed for the formation of *syn*-(±)-4,5-difluoro-1,3-dioxolan-2-one (**3**) follows that observed for the formation of (±)-4-fluoro-1,3-dioxolan-2-one (**2**), i.e. the highest yield was observed using the electrolyte $\text{Et}_4\text{NF}\cdot 4\text{HF}$ at a current density of 100 mA cm^{-2} . Under all the conditions applied to the ECF of EC, only small amounts of *anti*-(±)-4,5-difluoro-1,3-dioxolan-2-one (**4**) were obtained, along with trace amounts of eight other undetermined fluorinated products. The main component of the mixture in each case was starting material, as evidenced by ^1H NMR and electron ionization mass spectrometry (EI-MS).

The electrolyses performed at a current density of 200 mA cm^{-2} yielded the lowest amount of product overall, irrespective of the electrolyte used; however, a *ca.* six fold increase in the yield of mono-fluorinated product obtained was observed when the HF content of the electrolyte was increased from 3HF to 4HF, highlighting the importance of the HF content on the overall yield of the product. The decrease in yield observed at

200 mA cm⁻² is thought to be due to the increased presence of competing reactions at higher potentials caused by further oxidation of species in solution.

Conversely, the decrease in yield observed at current densities of 50 mA cm⁻² is believed to be due to the fact that the potential achieved is not sufficient to initiate reaction. Hence, a current density of 100 mA cm⁻² was found to be the optimum in both electrolytes.

The major product obtained from the ECF of PC was (±)-4-fluoro-4-methyl-1,3-dioxolan-2-one (**6**), *via* the insertion of a single fluorine atom geminal to the methyl group. This product was obtained in a moderate yield of 26%, which is *ca.* 50% greater than the equivalent product from the ECF of EC (**2**). The two minor products were identified as *syn*-/*anti*-(±)-4-fluoro-5-methyl-1,3-dioxolan-2-one (**7** & **8**) (*syn* and *anti* described with respect to the methyl group). Again, the distribution of *syn* to *anti* is biased somewhat in favor of the *syn* product (**7**). Interestingly, no di-fluorination was observed when PC (**5**) was used as the substrate, and no other minor products were evident in the ¹⁹F NMR spectrum, in contrast to the electrolysis of EC, suggesting that the fluorination of propylene carbonate is significantly more selective than that of ethylene carbonate.

3.3. ¹⁹F NMR of cyclic carbonates

3.3.1. Fluorinated ethylene carbonate

Literature data for the products arising from the ethylene carbonate electrolyses have been reported by Kobayashi et al.⁷⁷ The ¹⁹F NMR data quoted for *syn* and *anti*-(±)-4,5-difluoro-1,3-dioxolan-2-one (**3** & **4**) were simply reported to be two multiplets at chemical shifts of δ/ppm (CDCl₃; ex. ref. CFC₃) -148.1 and -134.8 respectively. Our data suggest that the peaks at these shifts display the distinctive splitting pattern of an AA'XX' spin system⁸³ and thus provide detailed information to confirm the structural assignments of the products. AA'XX' systems occur when two sets of adjacent, spin-active nuclei are related through a plane of symmetry, with no axis of symmetry (fig. 3.2) such that they are chemically equivalent but magnetically inequivalent as a result of the coupling relationships between each nucleus, e.g. A is ²J with respect to X, but ³J with respect to X', thus rendering X and X' magnetically inequivalent with respect to A.

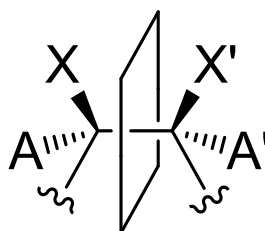


Figure 3.2. Schematic representation of an $AA'XX'$ system, indicating the plane of symmetry which relates the two halves.

The system results in two identical half spectra each of which consists of a maximum of 10 lines and is symmetrical about its midpoint. Each half spectrum consists of a 1:1 doublet, the intensity of which accounts for 50% of the overall intensity of the half spectrum, with a separation of N , and two “AB quartets”, each with normal intensity ratios and a separation of L (fig. 3.3(a), L calculated from $2R$ using eq. 3.1).

In terms of analysis of $AA'XX'$ systems, the coupling constants between each of the atoms are related according to the following terms:⁸³

$$K = J_{AA'} + J_{XX'}$$

$$L = J_{AX} - J_{AX'}$$

$$M = J_{AA'} - J_{XX'}$$

$$N = J_{AX} + J_{AX'}$$

Using the separations highlighted in fig. 3.2, it is possible to measure the values corresponding to the terms K , N , M and $2R$ and hence deduce, using eq. 3.1, the values corresponding to the remaining term, L :

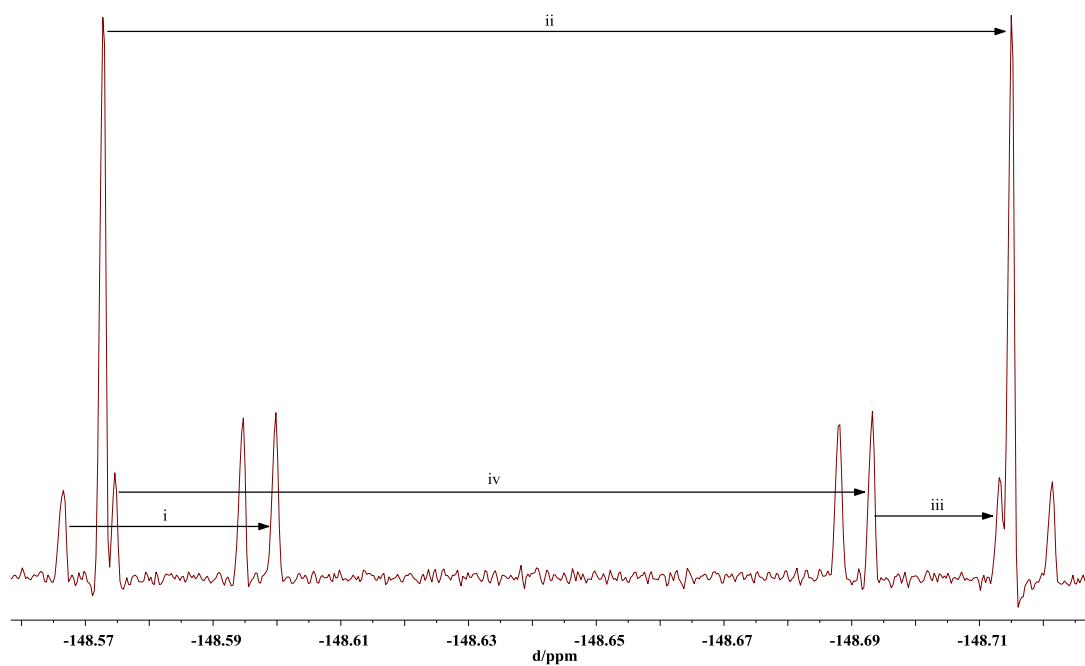
$$L = \sqrt{((2R)^2 - M^2)} \quad (3.1)$$

$$K = 15.7 \text{ Hz}$$

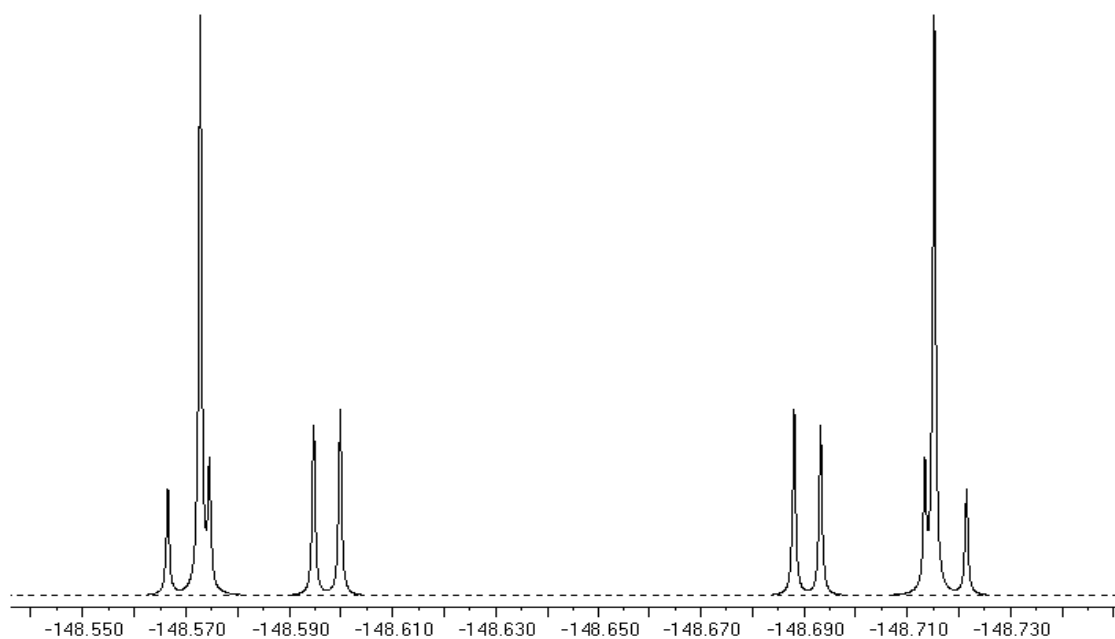
$$L = 55.0 \text{ Hz}$$

$$M = 9.5 \text{ Hz}$$

$$N = 67.0 \text{ Hz}$$



(a)



(b)

Figure 3.3. (a) ^{19}F NMR spectrum of *syn*-(\pm)-4,5-difluoro-1,3-dioxolan-2-one (**3**) showing the pattern typical of $AA'XX'$ spin systems with the separations equal to: i) K ii) N iii) M iv) $2R$; (b) simulated ^{19}F NMR spectrum constructed from coupling constants calculated from the actual spectrum.

From these values, the coupling constants relating to each of the spin active atoms in the system were calculated⁸³ as:

$${}^3J_{AA'} = ((K + M) / 2) = 12.6 \text{ Hz}$$

$${}^3J_{XX'} = ((K - M) / 2) = 3.1 \text{ Hz}$$

$${}^2J_{AX} = ((N + L) / 2) = 61.0 \text{ Hz}$$

$${}^3J_{AX'} = ((N - L) / 2) = 6.0 \text{ Hz}$$

The coupling constants calculated above correspond to the atoms labelled in fig. 3.4.

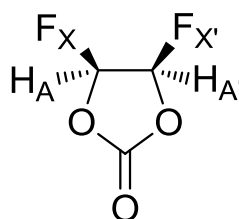


Figure 3.4. Arrangement and assignment of atoms in *syn*-(±)-4,5-difluoro-1,3-dioxolan-2-one (**3**).

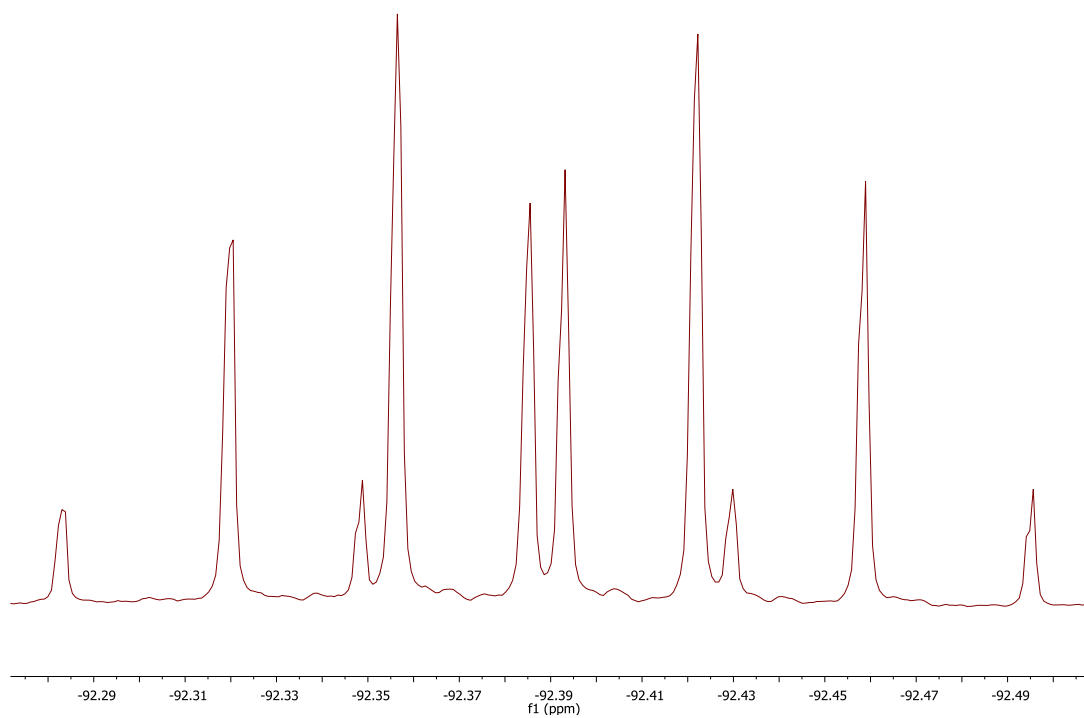
It is important to note that the ${}^{19}\text{F}$ NMR spectrum expected from the coupling constants calculated is identical to that obtained, as shown by comparison of the actual spectrum shown in fig. 3.3(a), with the computer simulation (fig. 3.3(b)).

In the case of the *anti*-difluorinated isomer, *anti*-(±)-4,5-difluoro-1,3-dioxolan-2-one (**4**), this spectrum should also show the characteristics of an AA'XX' spin system; however, as the product was only obtained in trace amounts, the peaks were poorly resolved resulting in considerable overlap. This made it impossible to establish the exact coupling constants.

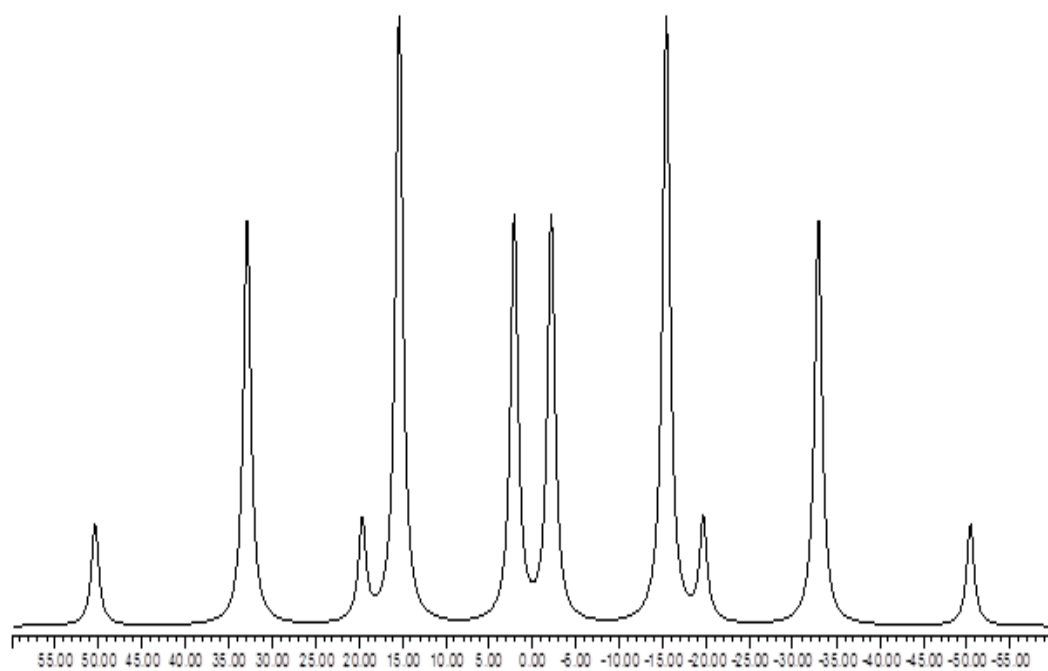
3.3.2. Fluorinated propylene carbonate

No literature NMR data could be found for the fluorinated propylene carbonate products obtained; therefore a full NMR analysis was conducted as part of this study.

In the ${}^{19}\text{F}$ NMR spectrum, the major signal at δ/ppm -92.4 was found to have the splitting pattern shown in fig. 3.5(a). This resonance has been assigned to the geminal fluorinated product (±)-4-fluoro-4-methyl-1,3-dioxolan-2-one (**6**).



(a)



(b)

Figure 3.5. (a) ^{19}F NMR spectrum of (\pm)-4-fluoro-4-methyl-1,3-dioxolan-2-one (**6**) showing the unusual splitting pattern; (b) simulated ^{19}F NMR spectrum constructed from coupling constants calculated from the actual spectrum.

The splitting pattern for this compound would usually be expected to show a doublet of doublets of quartets as a result of coupling to the two inequivalent, single protons and the three equivalent protons of the methyl group surrounding the fluorine atom. However, it appears that the unusual pattern observed results from the overlapping of peaks arising from the fact that the value of the $^3J_{\text{HF}}$ (*anti*) coupling is 17.4 Hz, and the value of the $^3J_{\text{HF}}$ (*gem.*) coupling is also 17.4 Hz. These two coupling constants are independent but because their values are identical, two of the expected doublets overlap producing the pattern shown in fig. 3.5(a).

In principle, this could be confirmed from the ^1H NMR spectrum, but unfortunately all of the lines of the double doublet from the proton *anti* to the methyl group (δ/ppm 4.55) are hidden by signals from the unreacted starting material also present in the mixture. This was therefore verified by selective decoupling experiments whereby the sample was simultaneously irradiated at the frequency of one or the other of the two-proton-split doublets at δ/ppm 4.53 and 4.57 (i.e. separated by $^3J_{\text{HF}}$ (*anti*)). This resulted in the selective homonuclear spin decoupling, and hence simplification, of the double doublet at δ/ppm 4.33 (fig. 3.6).

It was necessary to perform two separate experiments as the large coupling constant produced by the influence of the fluorine made it impossible to irradiate the entire peak at δ/ppm 4.55 corresponding to the proton.

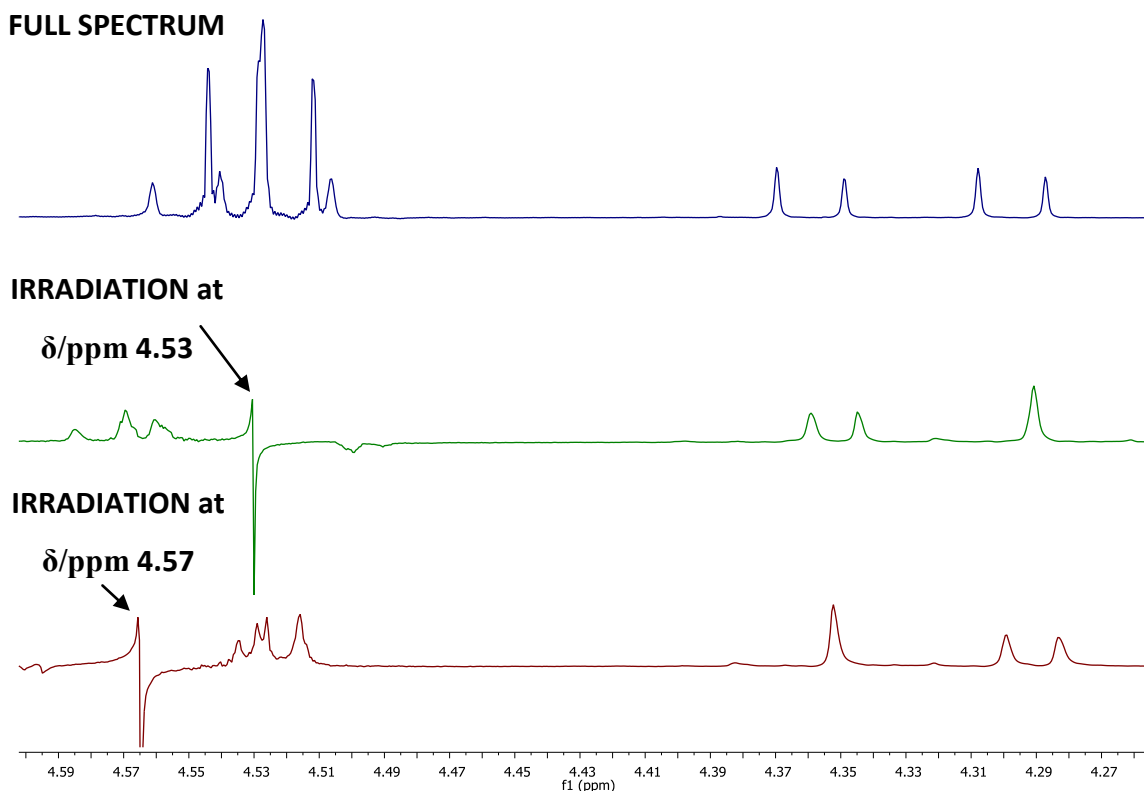


Figure 3.6. Stacked ^1H NMR spectra showing selective homonuclear spin decoupling of the double doublet at δ/ppm 4.33.

In separate experiments, the entire signal at δ/ppm 4.55 was revealed by gradient enhanced nuclear Overhauser effect (NOE) difference spectroscopy. A weak 180° irradiating pulse was used to selectively invert the methyl proton resonance at δ/ppm 1.82 before the normal spectrum was subtracted from the irradiated spectrum, leaving only the signals affected by through-space interaction with the proton to which the irradiation frequency corresponds (i.e. the methyl protons), along with an intense (negative) signal at the irradiating frequency (fig. 3.7). This allowed the coupling constants for the previously hidden peaks to be measured accurately. Further to this, the observed splitting pattern has been proven by simulation of the spectrum using the coupling constants calculated (see fig. 3.5(b)).

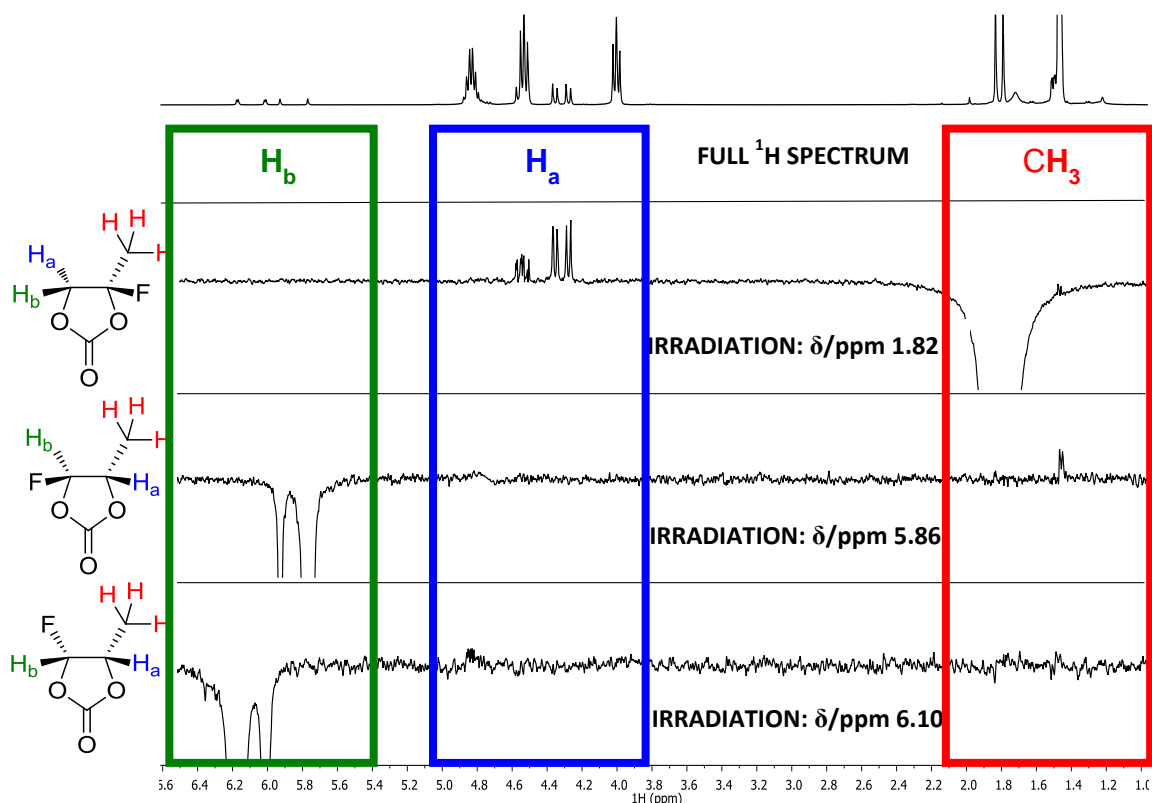


Figure 3.7. Difference NOE Spectra of the propylene carbonate product mixture, showing through-space interactions between protons in: 5-fluoro-5-methyl-1,3-dioxolan-2-one (**6**), *syn*-(\pm)-4-fluoro-5-methyl-1,3-dioxolan-2-one (**7**) and *anti*-(\pm)-4-fluoro-5-methyl-1,3-dioxolan-2-one (**8**).

The mono-fluorinated products (**7** & **8**) in fig. 3.8 have been assigned as *syn* and *anti* respectively (with respect to the vicinal methyl group) using a combination of 2-D hetero- and homo-nuclear spectroscopy (i.e. Nuclear Overhauser Effect (NOE) and proton-proton correlation (COSY) respectively) as well as selective proton decoupling. It was not possible to assign the stereochemistry of the products based on coupling constants alone as the non-planar geometry of the system meant that the proton-proton couplings did not necessarily follow the normal Karplus relationship.⁸⁴

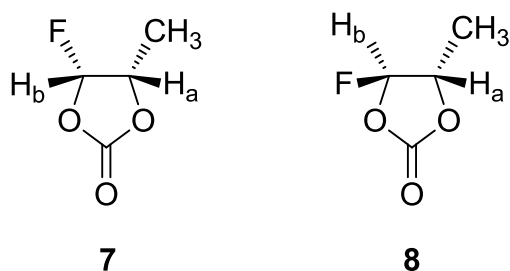


Figure 3.8. Structures of *syn*- and *anti*-(±)-4-fluoro-5-methyl-1,3-dioxolan-2-one (**7** & **8**).

The structure of the *syn* mono-fluorinated product (**7**) is such that the proton vicinal to the methyl group (H_b) is *anti* with respect to the methyl group (fig. 3.8). Therefore, when this proton is irradiated (δ /ppm 6.10) using difference NOE, no signal is observed for the methyl protons (at δ /ppm 1.52), and a weak signal is visible at δ /ppm 4.82 (corresponding to H_a , fig. 3.7). This suggests that H_a and H_b are coupled through space, and must therefore be *syn* with respect to each other. Conversely, the structure of the *anti* mono-fluorinated product (**8**) is such that H_b is *syn* with respect to the methyl group. As expected, when H_b is irradiated (at δ /ppm 5.86), a clear signal is observed at δ /ppm 1.47, corresponding to the methyl protons, and no signal is observed at δ /ppm 4.78 (the frequency at which H_a would be visible, fig. 3.7). This, therefore, confirms that product (**8**) is indeed the *anti* mono-fluorinated isomer. These assignments were further confirmed by selective decoupling of H_a . In each case, the peaks corresponding to H_b were simplified as expected. As before, in each case, once the coupling constants were measured, the spectra were verified by simulation.

3.4. Mechanistic studies

3.4.1. *In-situ* electrochemical EPR spectroscopy

As mentioned earlier, the introduction of a tertiary centre (i.e. propylene carbonate in place of ethylene carbonate) changed both the yield and selectivity of the process when ECF was performed under the same conditions. This may suggest that a radical-cation intermediate (which could be stabilised further by a tertiary centre than a secondary) is formed during electrolysis. In order to investigate this hypothesis and gain an insight into the mechanism of the ECF of cyclic carbonates, a technique known as *in-situ*, electrochemical Electron Paramagnetic Resonance (EPR) spectroscopy was employed.

EPR, also referred to as Electron Spin Resonance (ESR), spectroscopy can be used to identify a singly unpaired electron (i.e. a radical), as well as the environment in which the unpaired electron resides. It works on the principle that each electron has a spin, which can be understood as an angular momentum leading to an intrinsic magnetic moment as described by eq. 3.2:⁸⁵

$$\mu_s = g \cdot \mu_B \cdot S \quad (3.2)$$

where S is the spin, g is the g -factor Lande (2.0023 for a free electron) and μ_B is the Bohr magneton.

In the absence of a magnetic field this is unimportant as there is no difference in energy between the “spin-up” and “spin-down” conformations (fig. 3.9).⁸⁵

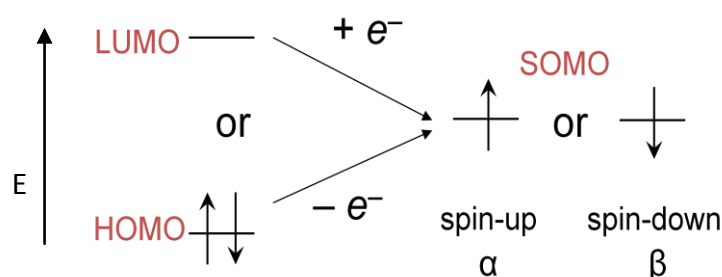


Figure 3.9. Relative energies of electron spins in the absence of a magnetic field

When the spin equals a half ($S = 1/2$), the electron spin state is 2-fold degenerate and characterised by the quantum number $m_s = \pm 1/2$; therefore, when a magnetic field (H_0) is applied, degeneracy is lifted such that:

$$E_{\pm} = \pm 1/2 g \cdot \mu_B \cdot B_0 \quad (3.3)$$

where B_0 is the strength of the applied magnetic field; this is known as Zeeman splitting or the “Zeeman effect” (fig. 3.10).⁸⁵

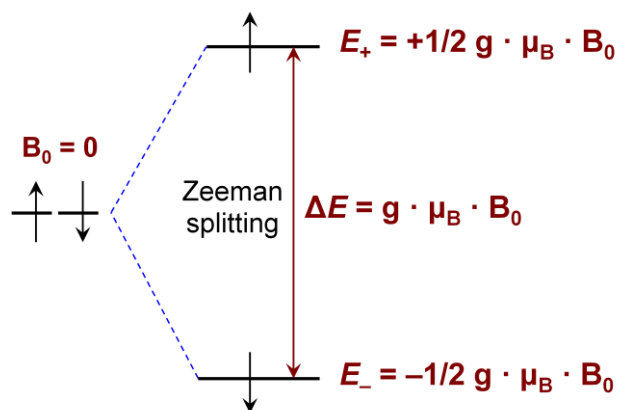


Figure 3.10. A schematic representation of the effect of a magnetic field of strength B_0 on the energies of electrons where $S = 1/2$.

As equation 3.3 suggests, the greater the strength of the magnetic field applied, the greater the difference in energy observed between the spin pairs.

Since it is much more efficient to detect an AC signal in the presence of a large DC background, the magnetic field is modulated (typically at 100 KHz) by means of coils embedded in the walls of the cavity (fig. 3.11).⁸⁵

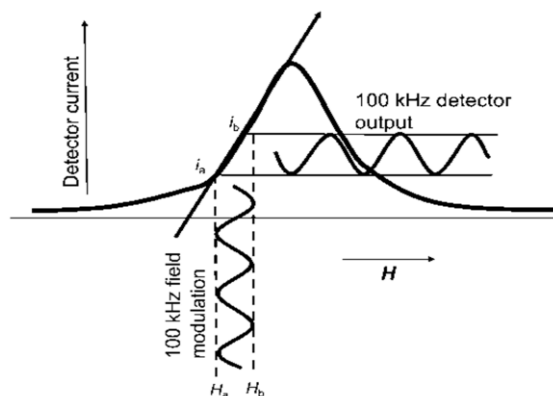


Figure 3.11. Diagram showing the modulation of a magnetic field by means of localised electrical fields generated by coils in the walls of the cavity.

The number of spins in each energy level can be measured for a given sample since *absorption* of electromagnetic radiation (typically microwaves) is proportional to the number of spins in the lower level, whereas *emission* of radiation is proportional to the

number of spins in the upper level. In practice, the frequency of the microwave irradiation is usually held at a constant value whilst the external magnetic field is increased until the energy of the applied field matches the energy of the microwaves, widening the gap between the 2 energy states. At this point, the unpaired electrons are able to move between their 2 spin states.

Since there are typically more electrons in the lower state at equilibrium (as given by the Boltzmann distribution (see eq. 3.4), there is a net absorption of energy (e.g. at 298 K, X-band microwave frequencies ($\nu \approx 9.75$ GHz) give $n_{\text{upper}} / n_{\text{lower}} \approx 0.998$, meaning the lower level has a higher population of spins than the upper state, making transitions from the lower energy level to the higher more probable than the reverse).⁸⁵ It is this energy absorption which is detected and converted to the observed EPR spectrum.

$$n_{\text{upper}} / n_{\text{lower}} = \exp(-(E_{\text{upper}} - E_{\text{lower}})/kT) = \exp(-(\Delta E)/kT) = \exp(-(\epsilon)/kT) = \exp(-(h\nu)/kT) \quad (3.4)$$

Initial measurements were performed at the EPSRC national EPR service at the University of Manchester in conjunction with Dr Jonathan Hawkett and Prof. David Collison. The cell used to perform the measurements is shown in fig. 3.12. This cell comprised: an X-band, quartz glass tube ($d = 5$ mm), Pt wire working and counter electrodes ($d = 0.1$ mm) and Ag wire reference electrode ($d = 0.1$ mm). The wire electrodes were coated in teflon, with *ca.* 10 mm of the wire exposed; further to this, the wires differed in length as shown in fig. 3.12. These measures were taken to ensure that the wires could not come into physical contact with each other within the cell, whilst ensuring that ionic contact was maintained when the electrodes were submerged in a conducting solution.

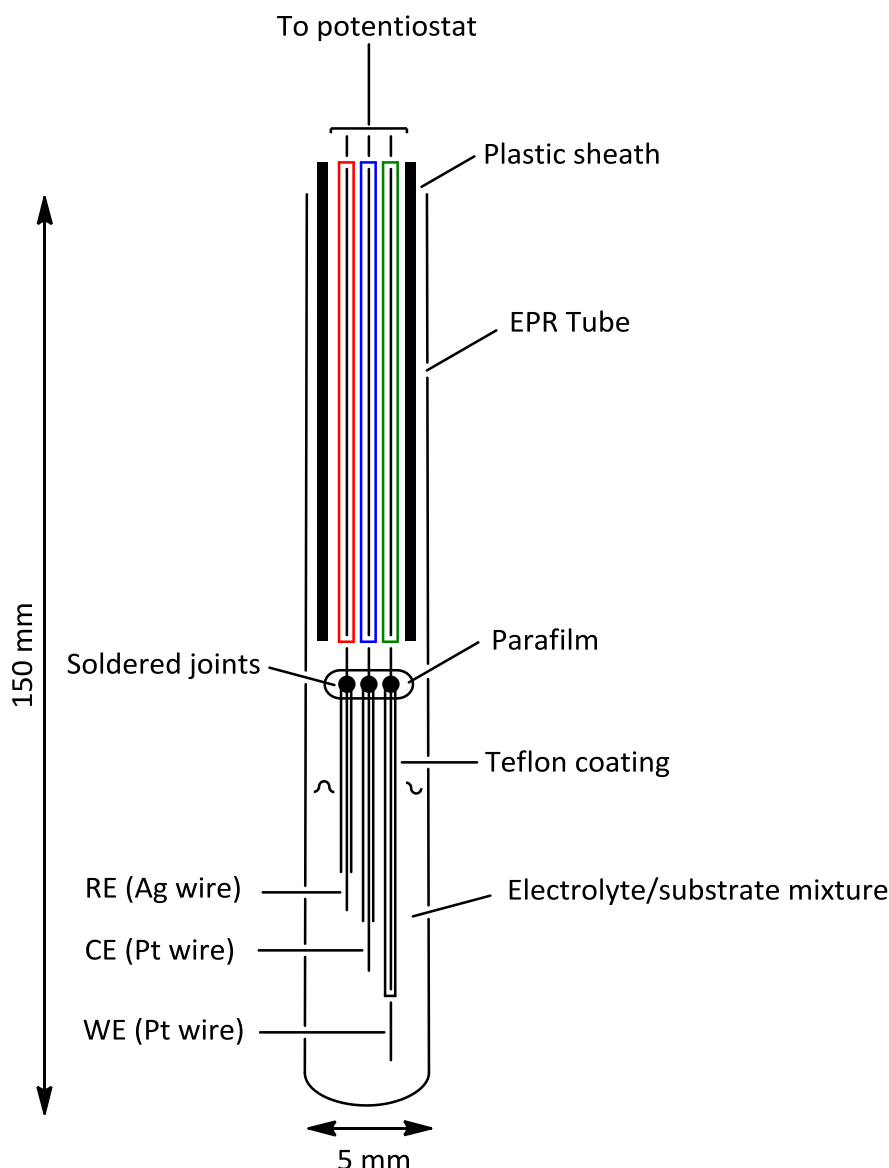


Figure 3.12. Schematic representation of the *in-situ* electrochemical EPR cell used at the EPSRC national EPR service in Manchester.

In-situ electrochemical EPR spectroscopy was performed using a mixture comprising 1 equivalent of ethylene carbonate and 2.4 equivalents of the molten salt electrolyte $\text{Et}_4\text{NF} \cdot 4\text{HF}$. Based on the chronopotentiograms obtained during electrolysis at 100 mA cm^{-2} , a potential of 5 V was chosen and the mixture was electrolysed *in-situ* for 10,000 s. A steady current of *ca.* 10 mA was achieved and the solution turned dark brown in colour, which is consistent with what is observed during the *ex-situ* electrolyses; however, no EPR signal was obtained. It was postulated that this was a result of the fluorinated electrolyte reacting quickly with the substrate; hence the radical could not be generated in sufficient concentration for detection. In order to test this hypothesis, the reactive electrolyte $\text{Et}_4\text{NF} \cdot 4\text{HF}$ was replaced with a relatively “inert” electrolyte,

tetrabutylammonium tetrafluoroborate (Bu_4NBF_4) (0.15 M in MeCN). Again, a ratio of 1 equivalent of ethylene carbonate to 2.4 equivalents of 0.15 M Bu_4NBF_4 in MeCN was used and all electrolysis conditions were the same as previously.

The signal shown in fig. 3.13 was obtained within a matter of seconds and the solution turned dark brown in colour as expected. The observed signal was extremely short-lived and the hyperfine structure was lost with each subsequent scan (fig. 3.14).

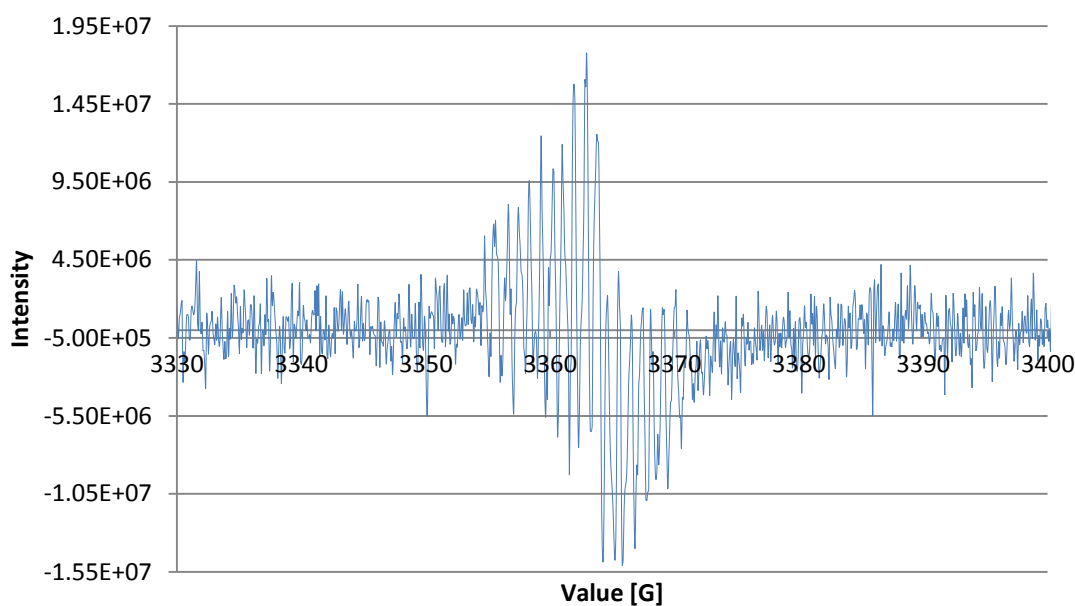


Figure 3.13. *In-situ electrochemical EPR spectrum of ethylene carbonate in 0.15 M Bu_4BF_4 in MeCN after 5 scans.*

A blank experiment was performed (i.e. no ethylene carbonate) to ensure that the signal was caused by the formation of substrate radicals and not disproportionation of the electrolyte, and no EPR signal was observed.

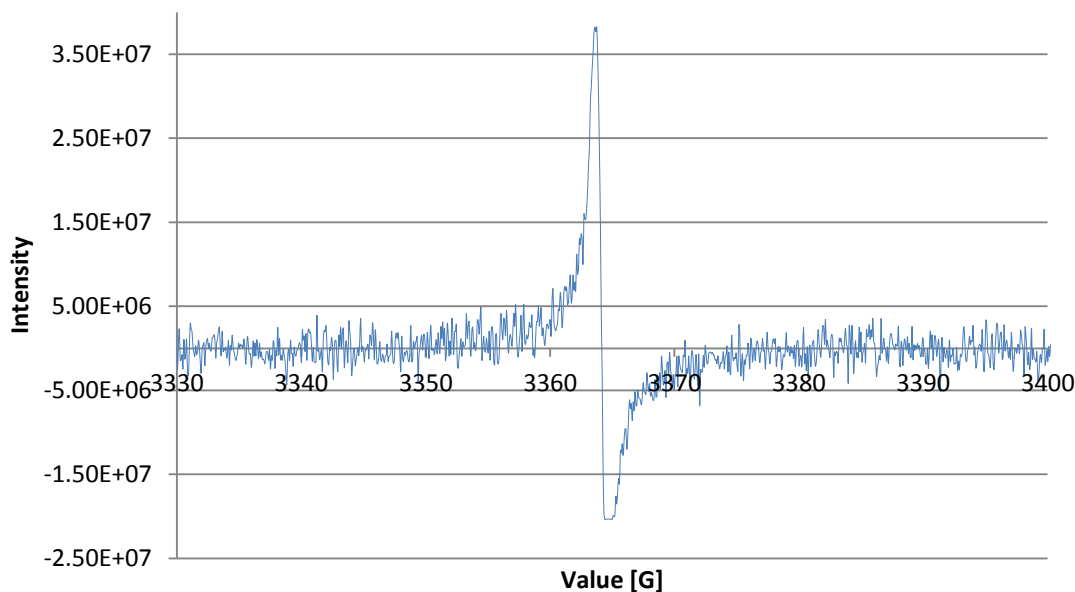


Figure 3.14. *In-situ electrochemical EPR spectrum of ethylene carbonate in 0.15 M Bu_4BF_4 in MeCN after 13 scans.*

The preliminary data suggested the presence of substrate radicals; however, the signal was extremely short lived. Therefore, in order to study the process more closely, the work was repeated using the facilities at the Leibniz-Institut für Festkörper- und Werkstofforschung (IFW), which translates as the Leibniz Institute for Solid State and Materials Research in Dresden, Germany. These facilities are amongst the best in the world for performing *in-situ* electrochemical EPR measurements. In addition, the facilities also possess the capability to perform UV-vis and near infrared (NIR) measurements in parallel with the *in-situ* EPR spectroscopy.

Three separate computers were required to control the potentiostat, the UV-vis/NIR spectrometer and the EPR spectrometer (figs 3.15 & 3.16). However, using a Heka potentiostat, the three systems could be linked and, although separate computers were required to obtain the data, each scan obtained by the individual spectrometers could be set to run according to an external potentiostatic trigger. This meant that although the scans ran on different time scales, they could be set to coincide and so provided a measurement at the same point.

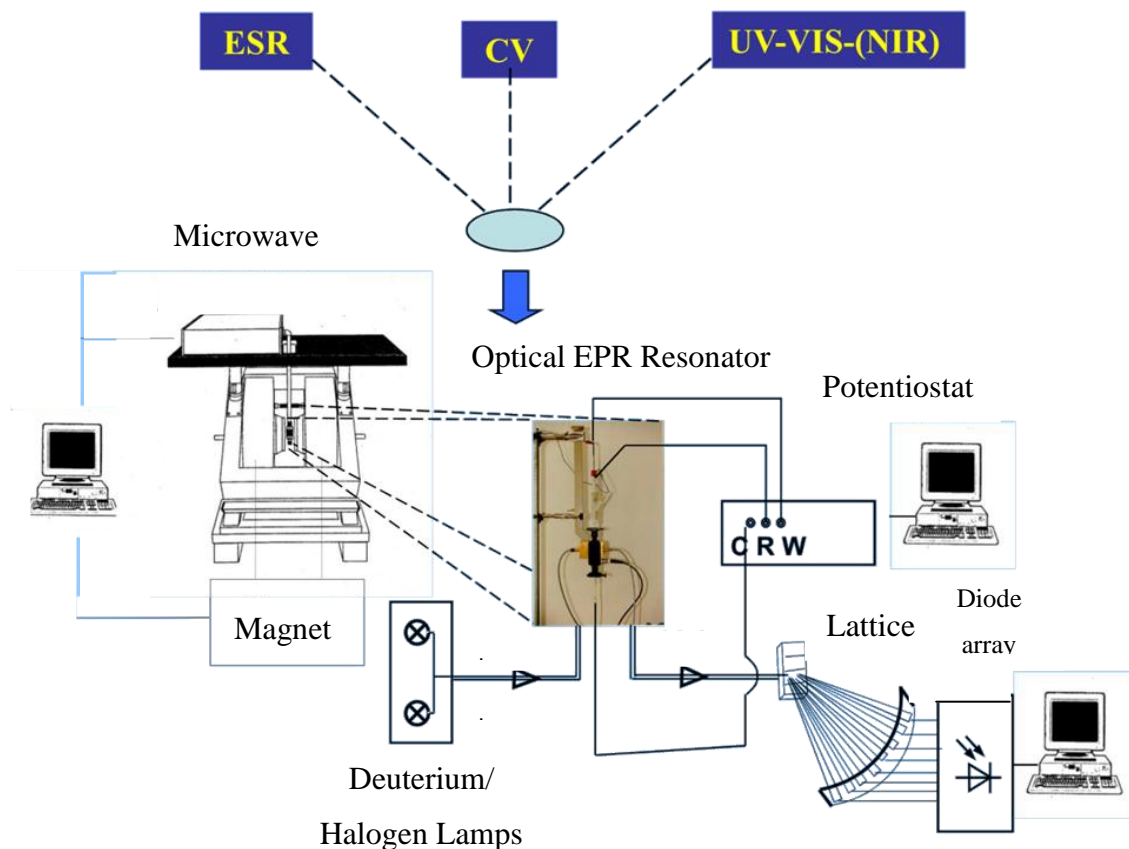


Figure 3.15. Schematic representation of in-situ electrochemical EPR/UV-vis-NIR set-up.

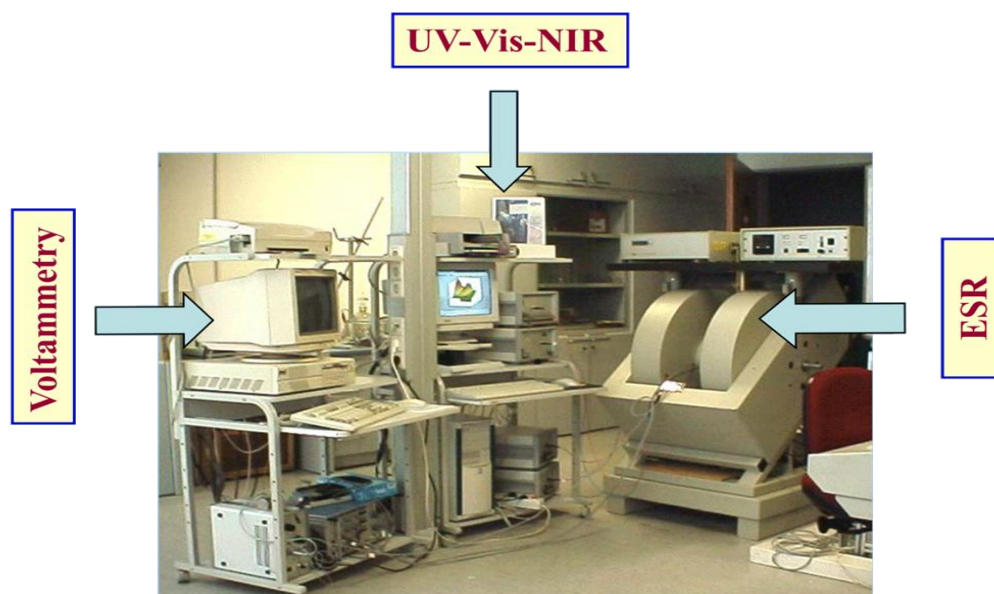


Figure 3.16. Photograph showing in-situ EPR/UV-vis-NIR equipment.

The ability to obtain both UV-vis-NIR and EPR data simultaneously was made possible by the use of fibre optic leads, and a unique cell design, consisting of a mesh working

electrode (to allow the light to pass through). Figure 3.17 shows a diagram of the *in-situ* electrochemical cell from: (a) the front and (b) the side.

The anode consisted of a Pt mesh (4 x 7 mm) attached to gold foil (40 x 60 x 0.1 mm), which in turn was connected to Cu wire (diameter = 0.3 mm). Each connection was maintained by the laminated sheet, the second function of which was to prevent the electrolyte from coming into contact with any material other than the Pt mesh. The Pt mesh maintained contact with the electrolyte *via* the small hole in the laminate. Within the EPR spectrometer, this hole was also aligned such that the light from the halogen and deuterium lamps could pass through the solution, and Pt mesh, to the detector in order to measure the UV-vis-NIR absorptions. The Ag wire reference electrode (diameter = 0.1 mm) was placed in the cell alongside the WE, where ionic contact between the electrodes could be maintained, without any risk of physical contact which would cause the system to short circuit. The counter electrode consisted of a Pt wire (diameter = 0.3 mm), which was positioned relatively far away from the WE (*ca.* 2 cm). Whilst this increased the resistance of the system, it was necessary to prevent the detection of products formed at the CE. The final important feature of the cell was the relative flatness of the part of the cell which sat in the cavity of the spectrometer. Again this increased the resistance, but was necessary to ensure effective tuning of the EPR spectrometer. The relatively thin width of this part of the cell improved the tuning of the spectrometer as samples/solvents with high dielectric constants absorb microwave energy (which is used to balance the applied magnetic field) in a non-resonance way. This effect becomes more pronounced with increasing sample diameter because of the penetration in the electric component of the microwave field.

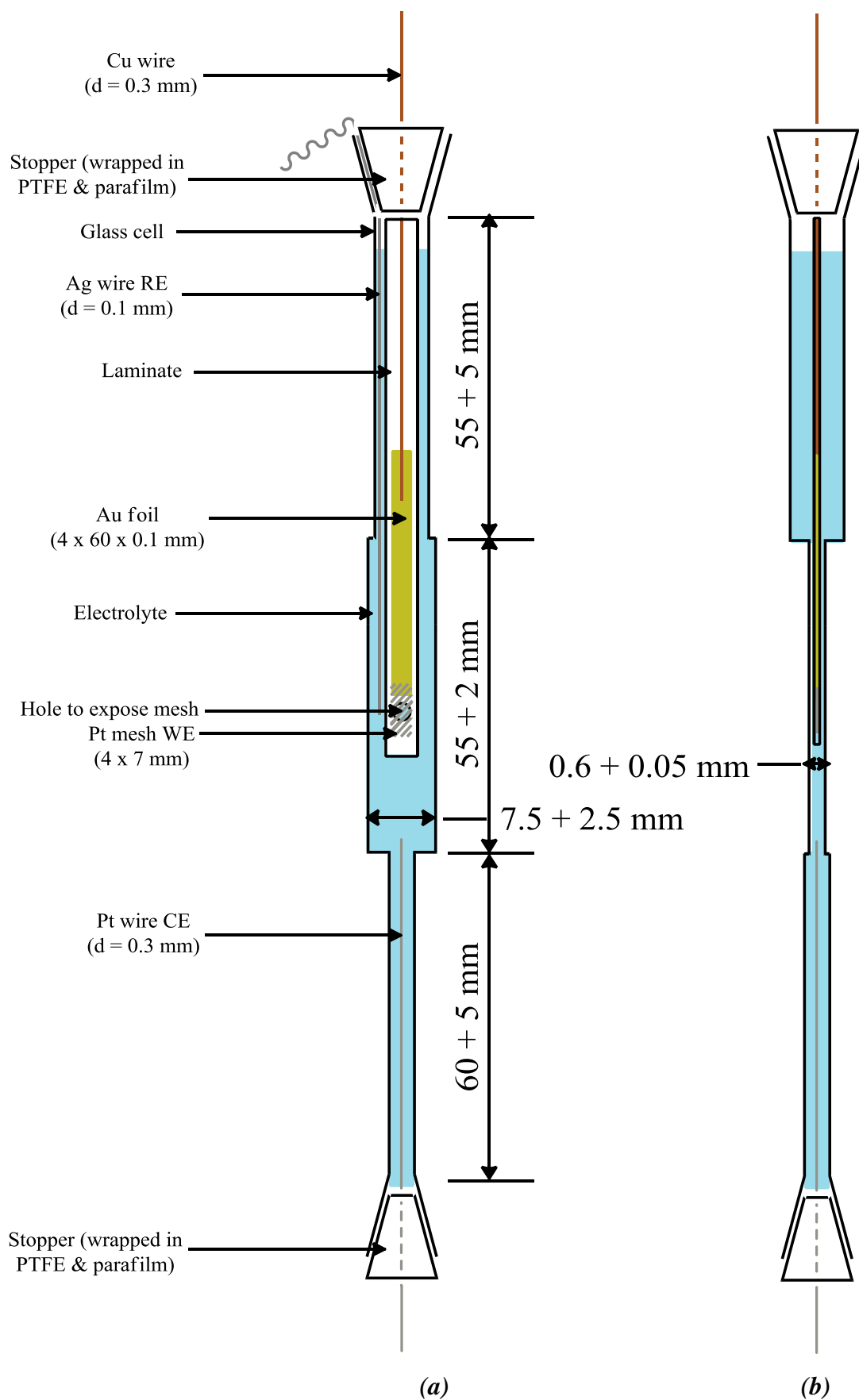
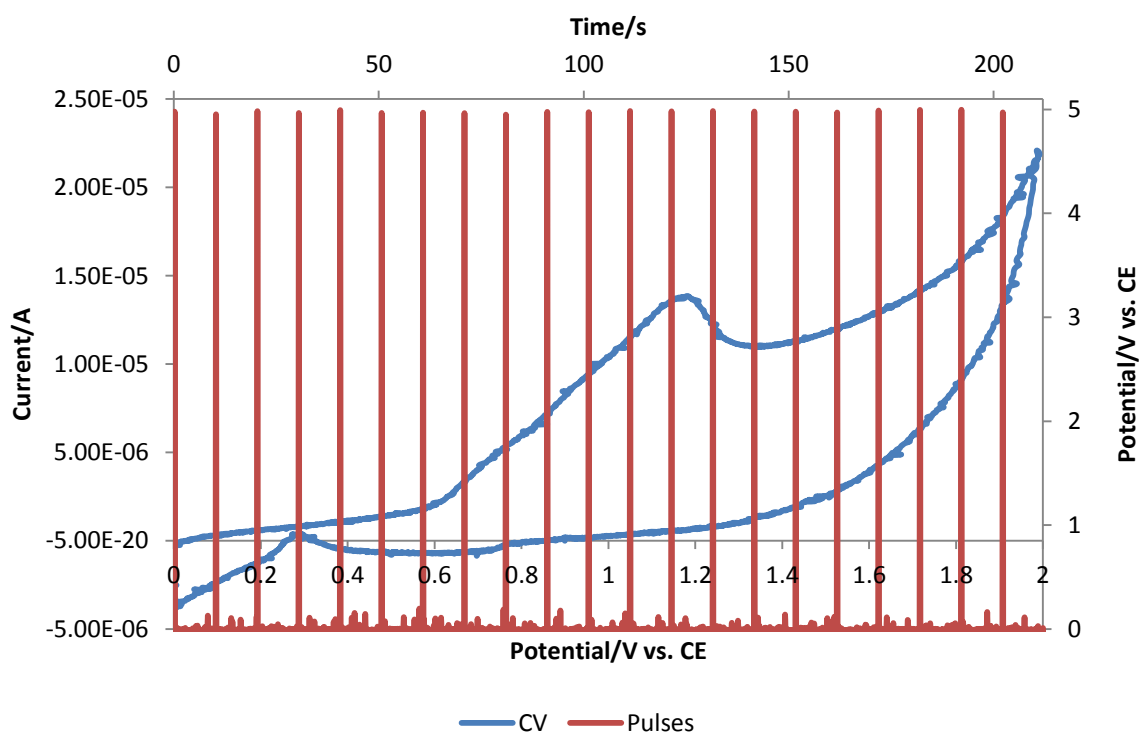
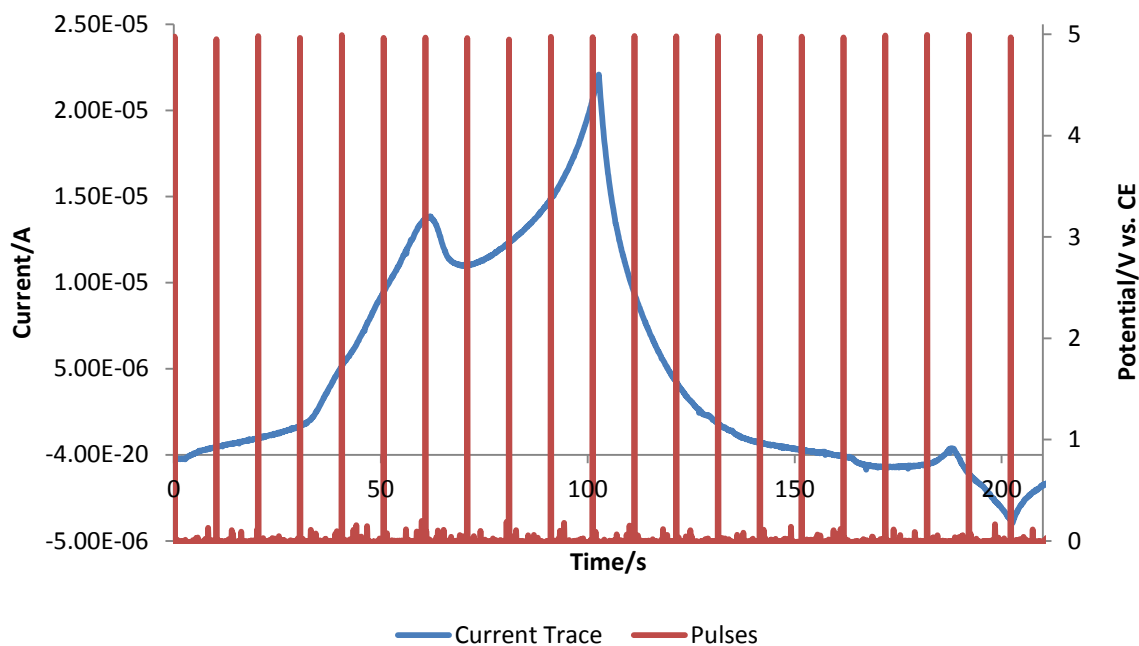


Figure 3.17. Diagram of the in-situ electrochemical EPR cell from (a) the front and (b) the side.

The first experiment performed at the IFW was a CV of the substrate/electrolyte mixture in the EPR cell ($E = 0.0 \text{ V} - 2.0 \text{ V}$ vs. CE) recording EPR spectra at various intervals, to see if a signal could be obtained at lower potentials. Using the Heka potentiostat, it was possible to trigger the EPR spectrometer to record a spectrum at regular intervals based on pulses which occurred at predetermined potentials as shown by the red trace in fig. 3.18(a). The CV shown in the blue trace of fig. 3.18(a) displays the small oxidation peak at *ca.* 1.17 V as expected when the substrate is present; however, unfortunately, no EPR signal was observed during the CV. This may be because the concentration of any radical formed during the CV would be very small, and therefore potentially undetectable by EPR. Consequently, constant electrolysis would have to be performed to generate a radical of sufficient concentration for detection. The trace in fig. 3.18(b) shows the change in current as a function of time during the CV.



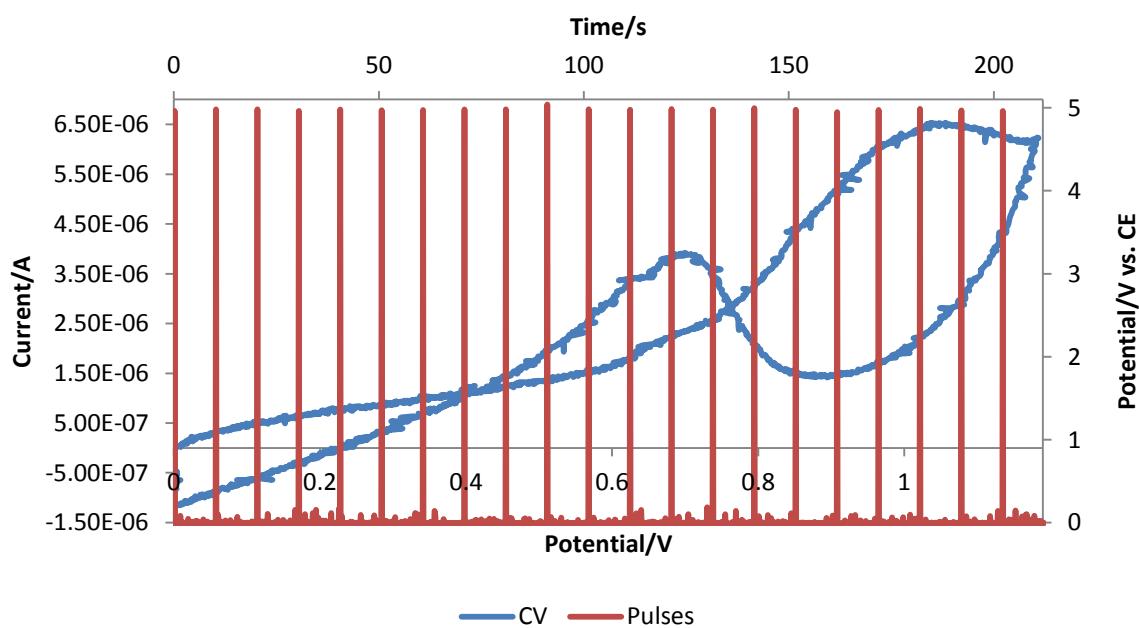
(a)



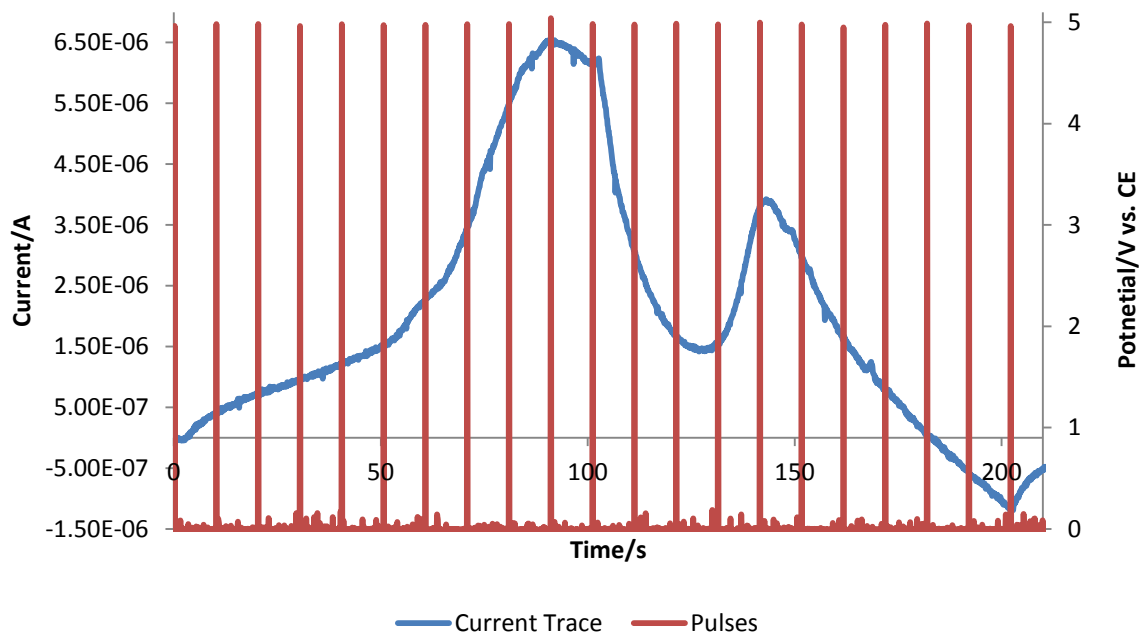
(b)

Figure 3.18. (a) CV and (b) Current trace CV of PC in Et₄NF₄HF between 0.0 V and 2.0 V vs. CE obtained in conjunction with pulse EPR.

The potential limit was lowered to 1.19 V to observe the behaviour of the oxidation peak at 1.17 V, and the CV was repeated, again recording EPR spectra at defined intervals (figs. 3.19(a) and 3.19(b)). This time, a second oxidation peak was observed during the cathodic sweep, causing a hysteresis in the voltammogram.



(a)



(b)

Figure 3.19. (a) CV and (b) Current trace CV of PC in $\text{Et}_4\text{NF} \cdot 4\text{HF}$ between 0.0 V and 1.19 V vs. CE obtained in conjunction with pulse EPR.

Unfortunately, again, no EPR signal could be obtained as shown by the representative spectrum in fig. 3.20.

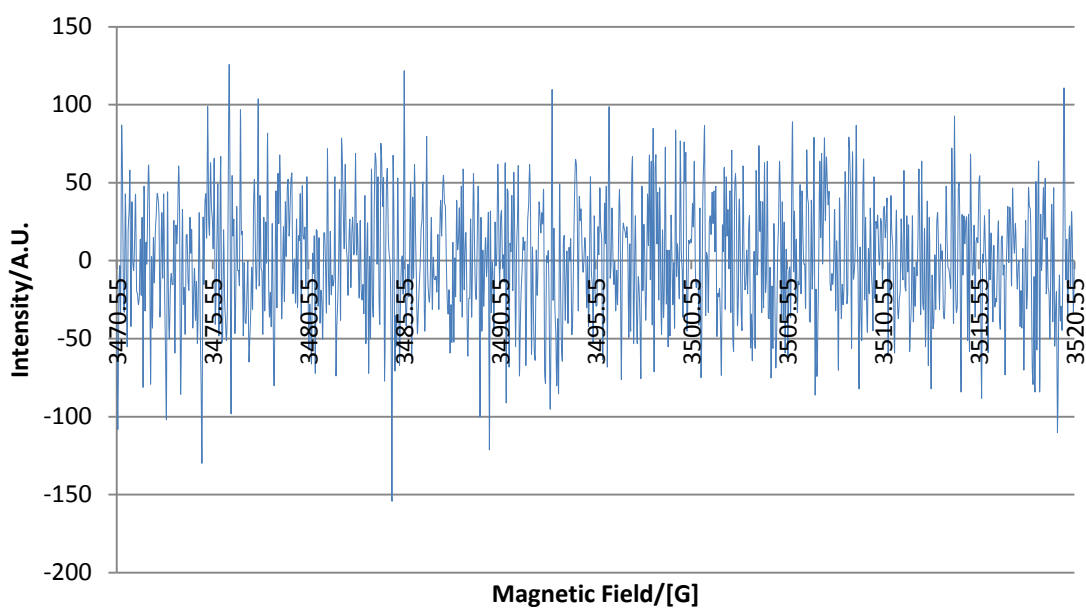


Figure 3.20. Typical EPR spectrum obtained during CV of 1.82 mmol PC in 4.36 mmol $\text{Et}_4\text{NF} \cdot 4\text{HF}$.

Since no signals were observed during the cyclic voltammetry experiments, it was decided that electrolysis at a constant potential would have to be performed in order to generate a higher concentration of radical species; therefore, a repeat of the Manchester work was performed, involving electrolysis of the substrate in an inert electrolyte using the new cell as described in fig. 3.17. In the time between the experiments being completed in Manchester and begun in Germany, it was found that the ECF of propylene carbonate gives a 50% greater yield of fluorinated product than the ECF of ethylene carbonate, suggesting that a higher concentration of the intermediate is formed; therefore the studies in Dresden were performed using propylene carbonate in the first instance, as a higher concentration of intermediate means a higher probability of observing a signal.

The *in-situ* electrochemical EPR/UV-vis-NIR of propylene carbonate in 0.3 M $\text{Bu}_4\text{NBF}_4/\text{MeCN}$ (1.0:2.4) was performed. A constant potential of 5 V was applied and after *ca.* 30 scans, a weak signal was observed (fig. 3.21); however, no hyperfine structure was visible. The application of the potential was ceased and further scans obtained, showing that the signal was persistent. The undefined nature of the signal combined with the persistence would suggest that the signal was due to the formation of a polymer.⁸⁶ The previously colourless solution turned dark brown in colour which was consistent with the observations from the Manchester experiments.

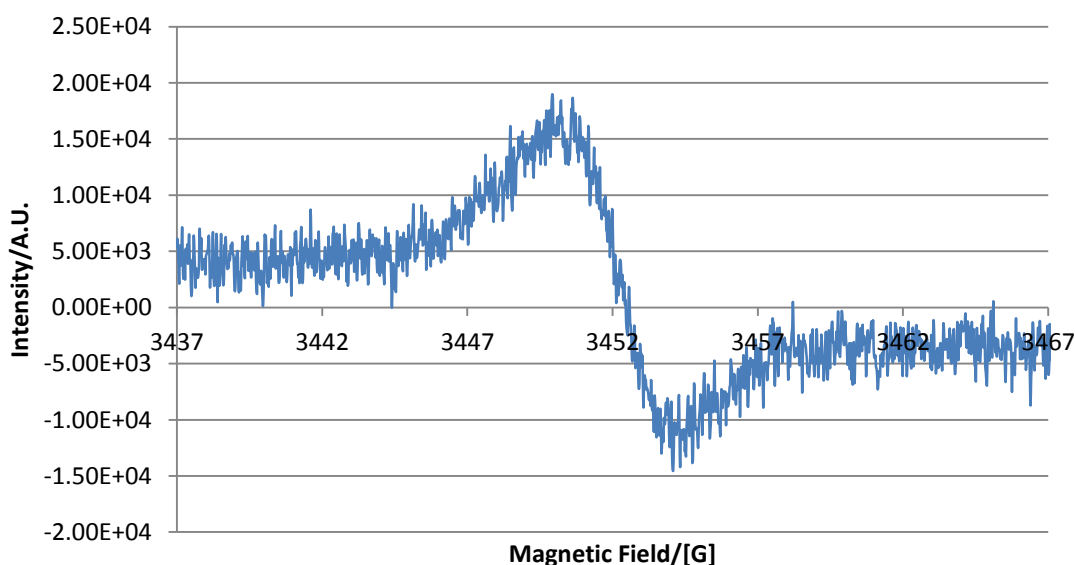


Figure 3.21. EPR signal from the electrolysis of propylene carbonate at 5 V constant potential in 0.3 M $\text{Bu}_4\text{NBF}_4/\text{MeCN}$ (1.0:2.4) obtained at the anode.

It was then considered that, as a result of the design of the cell utilised in Manchester (fig. 3.12), it was possible that the signal observed there (fig. 3.13) was due to a reaction at the counter electrode, not the working electrode. In order to test this hypothesis, the CE and WE in the IFW cell (fig. 3.17) were reversed (i.e. Pt mesh = CE, Pt wire = WE) such that the CE was in the cavity of the EPR spectrometer.

The conditions employed were identical to those above and this time, a signal was observed instantly with excellent signal-noise ratio and hyperfine splitting (fig. 3.22). The electrolysis was allowed to run for *ca.* 1 hour and the signal remained unchanged. Upon cessation of the current, the signal began to lose resolution/intensity and eventually ceased after *ca.* 5 min. This was probably due to either termination of the radical or diffusion from the cavity of the spectrometer. The hyperfine splitting observed was different to that observed in the Manchester experiments, but the broad, asymmetric nature of the signal would suggest that there are two overlapping resonances; a sharp signal with hyperfine splitting, most probably caused by an organic radical, and a broad singlet which can be indicative of polymer formation on the surface of the electrode.⁸⁶

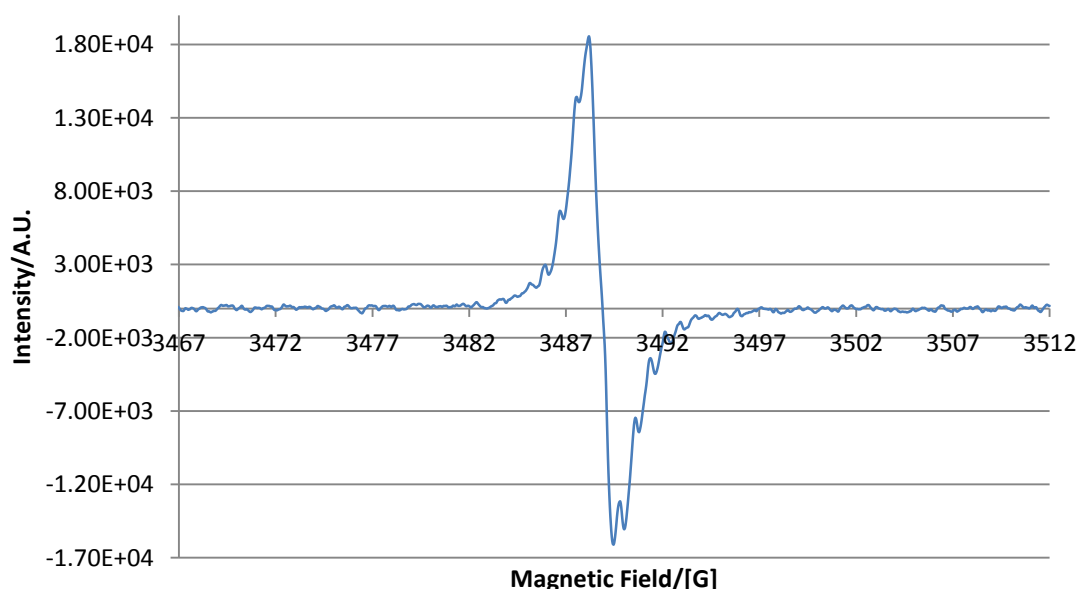


Figure 3.22. EPR signal from the electrolysis of propylene carbonate at 5 V constant potential in 0.3 M $Bu_4NBF_4/MeCN$ (1.0:2.4) obtained at the cathode.

It is thought that the defined signal observed during the cathodic reaction at the IFW is caused by the same radical that was observed in the Manchester experiment. It was considered that the reason why a number of scans were required to observe a signal during the Manchester experiments was to allow time for the radical to diffuse from the CE into the cavity of the spectrometer. In order to determine whether the cathodic signal was due to the reduction of the substrate or the electrolyte, the experiment was repeated under exactly the same conditions, omitting the substrate. Unfortunately, an identical signal was observed during this blank experiment (fig. 3.23).

Since the signal appears to be caused by the electrolyte mixture and occurs at the cathode, it seems reasonable to postulate that the radical formed is an intermediate in the reduction of acetonitrile. Since electrochemical deprotonation, involving single electron reduction at the cathode, is not uncommon, it is possible that the acetonitrile undergoes a radical version of the Thorpe reaction⁸⁷, as detailed in scheme 3.2.

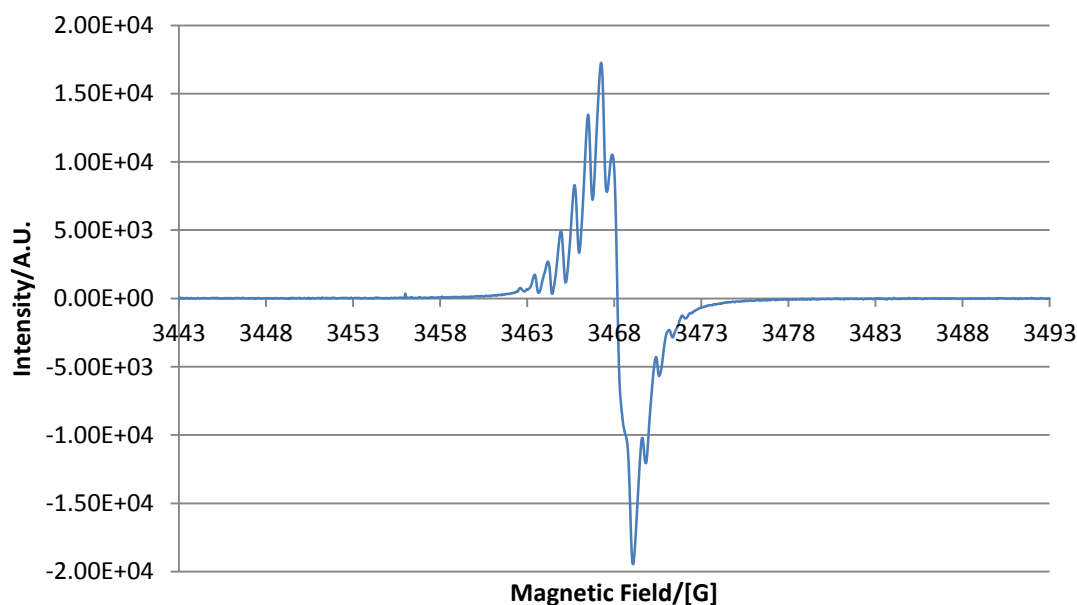
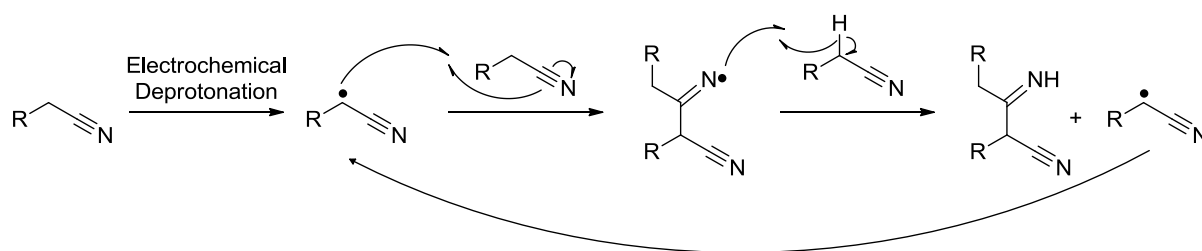


Figure 3.23. EPR signal from the electrolysis of propylene carbonate at 5 V constant potential in 0.3 M $Bu_4NBF_4/MeCN$ (1.0:2.4) – cathode.

The first step is electrochemical deprotonation of the acetonitrile forming a capto-dative stabilised, secondary, carbon-centred radical. This radical could then attack the electrophilic nitrile carbon of a second acetonitrile molecule, forming a relatively unstable N-centred radical. This unstable radical could terminate by abstracting a proton

from a third MeCN molecule, propagating the reaction by reforming the MeCN radical as shown in scheme 3.2.



R = H for MeCN

Scheme 3.2. The proposed mechanism of the electrochemical Thorpe reaction.

The acetonitrile radical would be quite easily formed as the $\text{CNCH}_2\text{-H}$ bond has a relatively low dissociation energy of 360 kJ mol^{-1} .⁸⁸ These radicals should also be long lived as they are stabilised both by resonance (fig. 3.24) and by the electron-withdrawing effects of the nitrile functional group (fig. 3.25).⁸⁸ Groups like CN are electron-withdrawing as they possess a low-lying, empty π^* -orbital, which, when overlapped with the SOMO p-orbital of the radical, forms 2 new molecular orbitals. The electron from the SOMO can occupy the new lower energy orbital, causing stabilisation of the system.⁸⁸

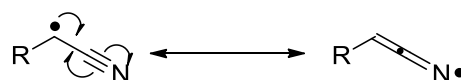


Figure 3.24. Resonance stabilisation of an acetonitrile radical.

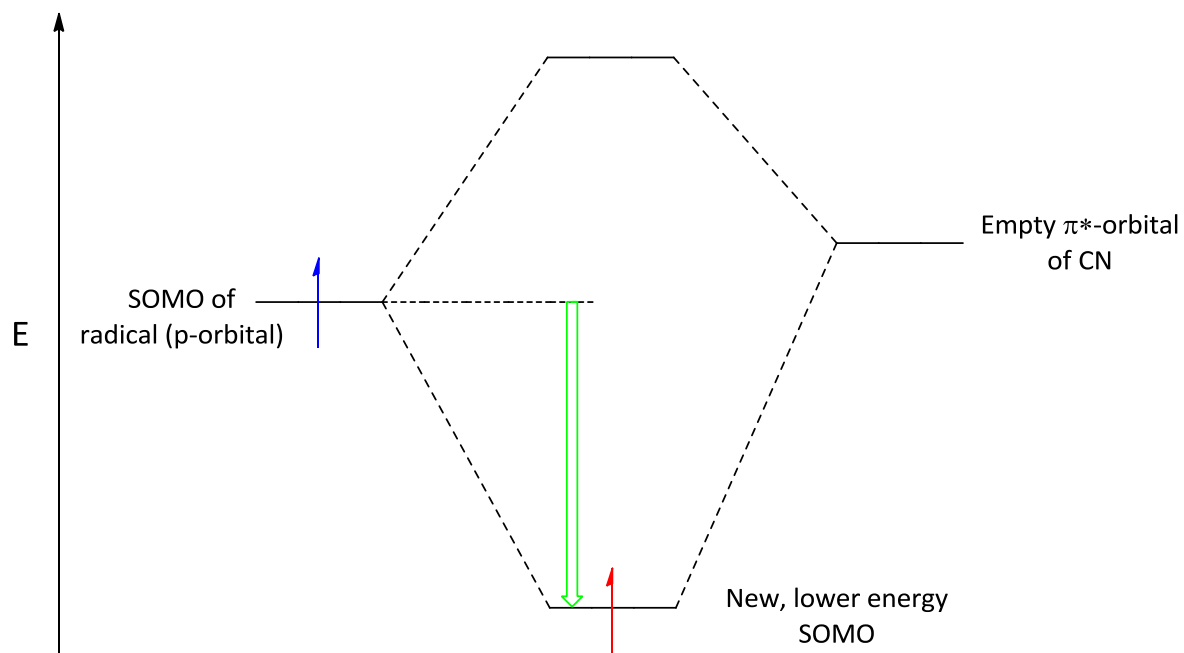


Figure 3.25. Schematic representation of the change in energy of the SOMO upon stabilisation by the electron-withdrawing nitrile group.

3.4.2. Proposed ECF mechanism

In spite of the inconclusive EPR studies, it still seems highly likely that the electrochemical fluorination of cyclic carbonates proceeds *via* a radical-cation intermediate. The mechanism postulated (fig. 3.26) is in accordance with the mechanism of ECF proposed by Rozhkov et al.³⁰ in the 1970s, and seems perfectly reasonable in terms of the chemistry of each transformation. This would be known as an EC_BEC_N mechanism; the first step involves the anodic oxidation of the cyclic carbonate. The most electron rich position in the molecule is the carbonate moiety, so it is expected that the electrons would be removed from this part of the molecule upon oxidation allowing the charge to be delocalised.

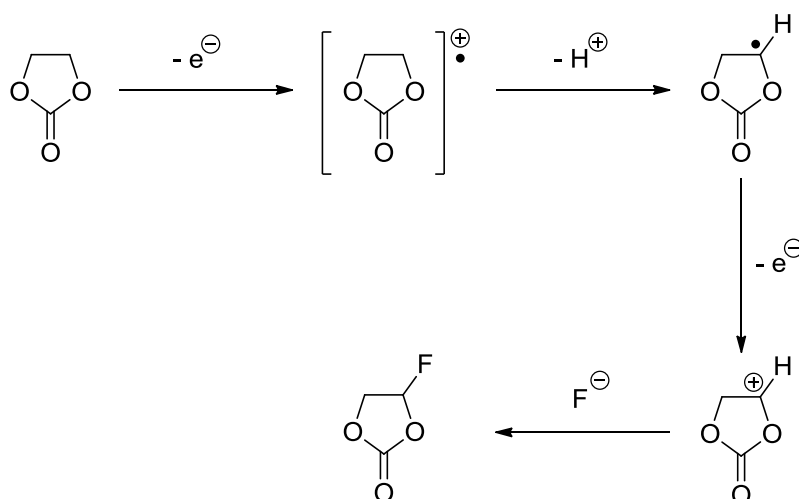


Figure 3.26. Proposed mechanism for the electrochemical fluorination of cyclic carbonates.

The second step involves chemical deprotonation adjacent to oxygen as depicted in fig. 3.27 (the base in this case would most likely be fluoride). For simplicity, the radical-cation has been localised onto the oxygen adjacent to the deprotonation, to show how the charges can cancel to give the carbon centred radical intermediate.

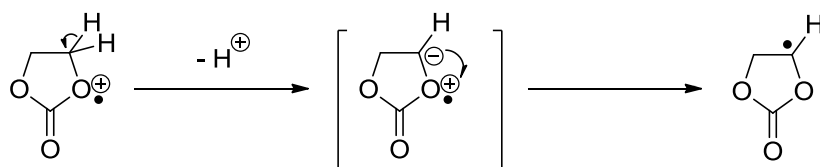


Figure 3.27. Proposed mechanism of the deprotonation step.

The third step would be a second anodic oxidation, making the radical a full cation, and finally nucleophilic attack of the fluoride to quench the cation and hence furnish the neutral, fluorinated product. When propylene carbonate is used as the substrate, the major product is the geminal mono-fluorinated product 4-fluoro-4-methyl-1,3-dioxolan-2-one (**6**), in a yield which is *ca.* 50% greater than the equivalent transformation using ethylene carbonate; these findings support our proposed mechanism, as the tertiary centre introduced by the methyl group would further stabilise both the radical, and cation intermediates, making the geminal position the most likely site of fluorination, and increasing the yield when a tertiary centre was introduced.

4. Composite Anodes

4.1. Introduction

This chapter concerns studies of a novel composite anode consisting of a thin TiO₂ layer sandwiched between silicon and a metal grid (Pt or Au) as shown in fig. 4.1. It was discovered that, in principle, this type of anode had the potential to oxidise solution species such as hydroxide, to generate powerful oxidants at low electrochemical potentials; it was therefore reasoned that this may be utilised for the electro-oxidation of fluoride, and hence the selective electro-fluorination of organic compounds.

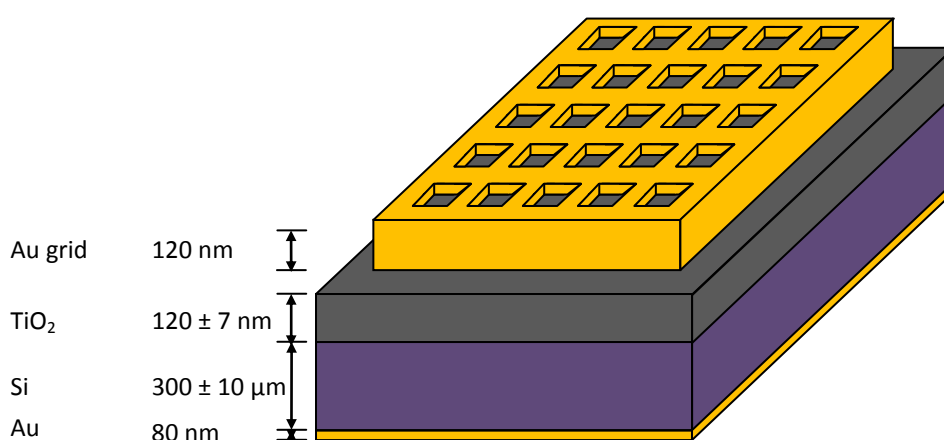


Figure 4.1. Schematic representation of a cross-section of a gold composite anode

4.2. Background and Previous Work

The interest in the combination of materials detailed above (i.e. Si, TiO₂ and Au/Pt) arose out of a search for more active TiO₂ photoanodes for the detoxification and disinfection of water⁸⁹ by the investigation of new synthetic approaches. The surface of TiO₂ is known to convert holes, usually generated photochemically in the TiO₂ via UV irradiation, into hydroxyl radicals.⁹⁰ It was postulated⁶³ that holes thermally generated in the Si layer of a Si/TiO₂/Au composite anode (in the dark) could be accelerated to the surface of the TiO₂ by the application of a bias voltage, V_b , between the positively charged Si and the negatively charged gold grid; at the surface they would be converted into OH radicals which could potentially oxidise solution species in contact with the anode surface. The postulate was supported by data showing the bias voltage-dependent disinfection of water inoculated with 10^7 cfu cm⁻³ *E. Coli* in the dark.⁶³ It was then reasoned that, OH radicals being a form of ‘active oxygen’, the electro-oxidation of small organic molecules could be enhanced at the Pt grid of a Si/TiO₂/Pt composite

anode through the application of a bias voltage, and this was also observed.⁹¹ It was also found that the onset potential for methanol oxidation at the composite anode decreased as V_b increased, further supporting the theory. In addition, in the absence of a bias voltage, both the onset potential for methanol oxidation and the peak current increased as the perimeter between the Pt and TiO_2 increased.

From the previous work summarized above, it appeared that the application of a bias potential between the metal grid and Si of the composite anodes: (1) facilitates the transport of holes thermally generated in the Si to the TiO_2 surface; (2) results in the generation of active species at the TiO_2 surface, and that (3) these active species can spillover from the TiO_2 to the metal grid; (4) the rate of spillover can be controlled *via* the bias voltage. Thus, the composite electrodes offer independent control of spillover at the metal/ TiO_2 /electrolyte interface, an effect hitherto not available and offering a wholly novel electrocatalytic effect with potential applications in e.g.: electro-organic synthesis, water & air detoxification (including *via* the visible light irradiation of our composite anodes) and fuel cell technology. This led to the formulation of the model detailed in below in order to better understand the electrochemistry of these novel electrodes.

The previous work also suggested that it may be possible to ‘tune’ the electrochemical characteristics of the TiO_2 /gold grid (*via* the holes arriving at the TiO_2 surface) on the composite anode by selecting a position on the surface created by bias voltage, visible light intensity and the electrochemical potential, rather than (as with conventional electrodes) just potential. Thus, the final aim of this work was to investigate if, and to what extent, charge transfer could take place between the holes arriving at the TiO_2 surface and redox-active species in solution. In particular, it was decided to carry out preliminary experiments exploring the possible application of the composite anodes in electrofluorination.

4.3. The model

The model described below is separated into 2 sections detailing: (1) the postulated theory of electron transport through the device; (2) the effect of bias potential on the electrochemical behaviour of the anode.

4.3.1. Electron transport through the composite anode

The complex structure of the composite anodes makes it difficult to predict the detailed potential distribution within the electrode with any degree of certainty. For the isolated components, *n*-Si and *n*-TiO₂, the flat-band potentials are both close to 0.1 V⁹²⁻⁹³ and the work-function of gold is *ca.* 0.6 V (taking the potential of the SHE as 4.44 eV vs. vacuum).⁹⁴ Placing the three components in contact and arranging zero bias between gold and silicon will lead to the situation shown schematically in fig. 4.2(a) where a small internal potential develops at the TiO₂/Au interface owing to the transfer of some electrons from the TiO₂ to the gold. In addition, as can be seen from fig. 4.2(b), the valence and conduction band edges near the TiO₂/grid interface bend, hence equilibrating the Fermi levels. The region over which this occurs is termed the depletion layer.⁹⁵ Electrons and holes generated in this region will separate, enhancing charge separation with holes migrating to more positive potentials, and electrons to more negative potentials..

At the Si/TiO₂ interface, there is probably little charge since the flat-band potentials are similar for these two materials. If the silicon is now biased negative with respect to the gold (corresponding to ‘forward bias’) electrons will flow from the *n*-Si through the Si/TiO₂ interface into the conduction band of the TiO₂ and thence to the gold. The rise in electron flow with increased negative V_b will be very pronounced, since electrons have a high mobility in the conduction band of the TiO₂ and at more negative potentials the depletion layer will be neutralised completely; the electron flow will be determined in effect by the build-up of electron density at the Si/TiO₂ interface and by the kinetics of electron flow from the gold either back to the silicon or, in the complete electrode, the flow of electrons into the solution. The high carrier mobility of electrons in the TiO₂ conduction band will mean that there is little potential drop within the TiO₂ itself, and the increasing potential change within the electrode will be accommodated at the Si/TiO₂ interface and the TiO₂/Au interface.

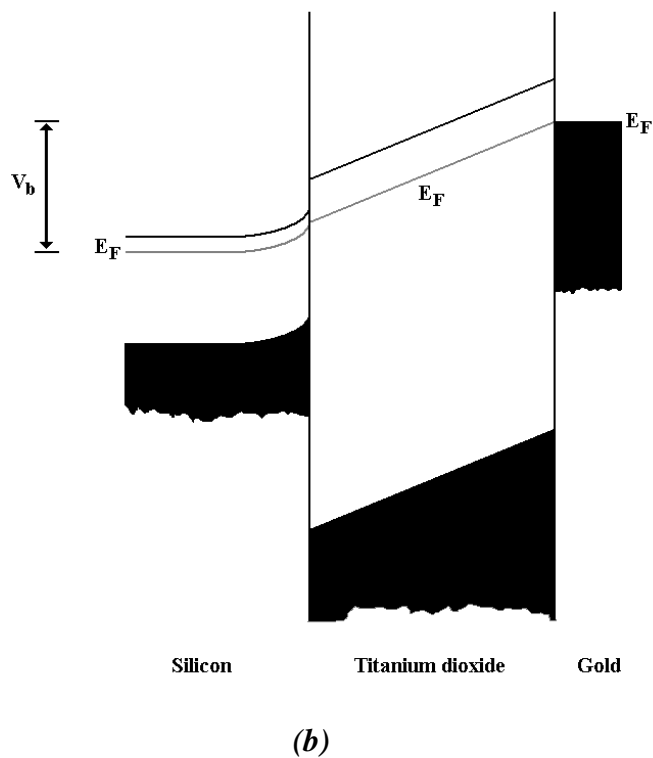
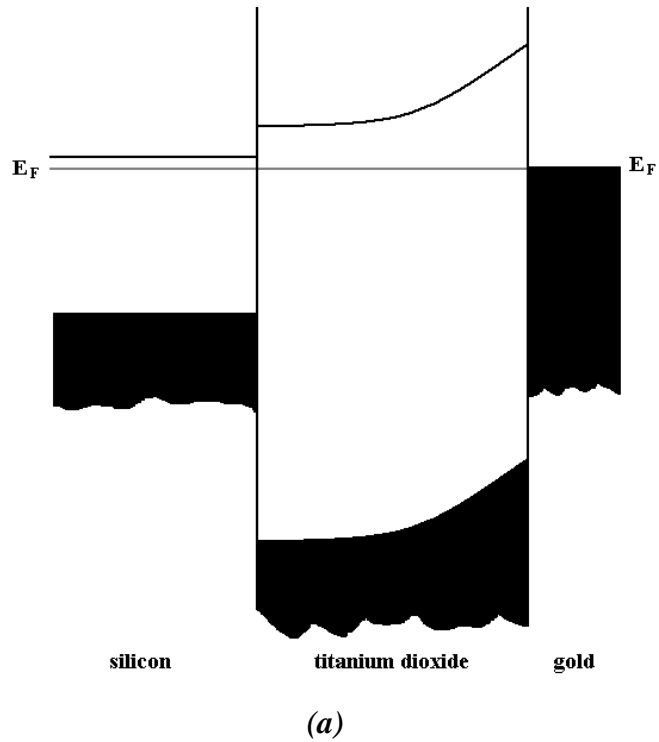


Figure 4.2. The proposed band structure of the Si/TiO₂/Au composite anode: (a) at zero bias and (b) high positive bias on the Si with respect to the Au. The Fermi levels (E_F) of the Si and TiO₂ are shown in grey.

If the polarity of the potential is reversed, so that the n -Si is made more positive than the gold, then a more complex situation develops. The situation shown in fig. 4.2(a) no longer holds; now, V_b will be accommodated both at the Si/TiO₂ interface and within the TiO₂ itself. The fact that at least some of the bias potential is dropped within the Si is clearly demonstrated by the fact that, on illumination with visible light of energy above the band gap of silicon (1.17 eV) but below that of TiO₂ (3.2 eV), a substantial photocurrent flows (see fig. 4.6(b) and discussion below), and this photocurrent can only be generated by absorption of light in a depletion region formed within the Si at the Si/TiO₂ interface. Some of the potential must also be accommodated within the TiO₂; this is clear because there is no doubt that holes are migrating through the TiO₂, and this must be by some form of field-assisted hopping. It is necessary also to recognise that the TiO₂ is likely to be amorphous, as evidenced by the absence of diffraction points in the Transmission Electron Micrograph (TEM) shown in fig. 4.3 (the weak dots visible on the image arise from interactions with the Si substrate). The amorphous nature of the TiO₂ means that the edges of the conduction band and valence band will be much less well defined.⁹⁶

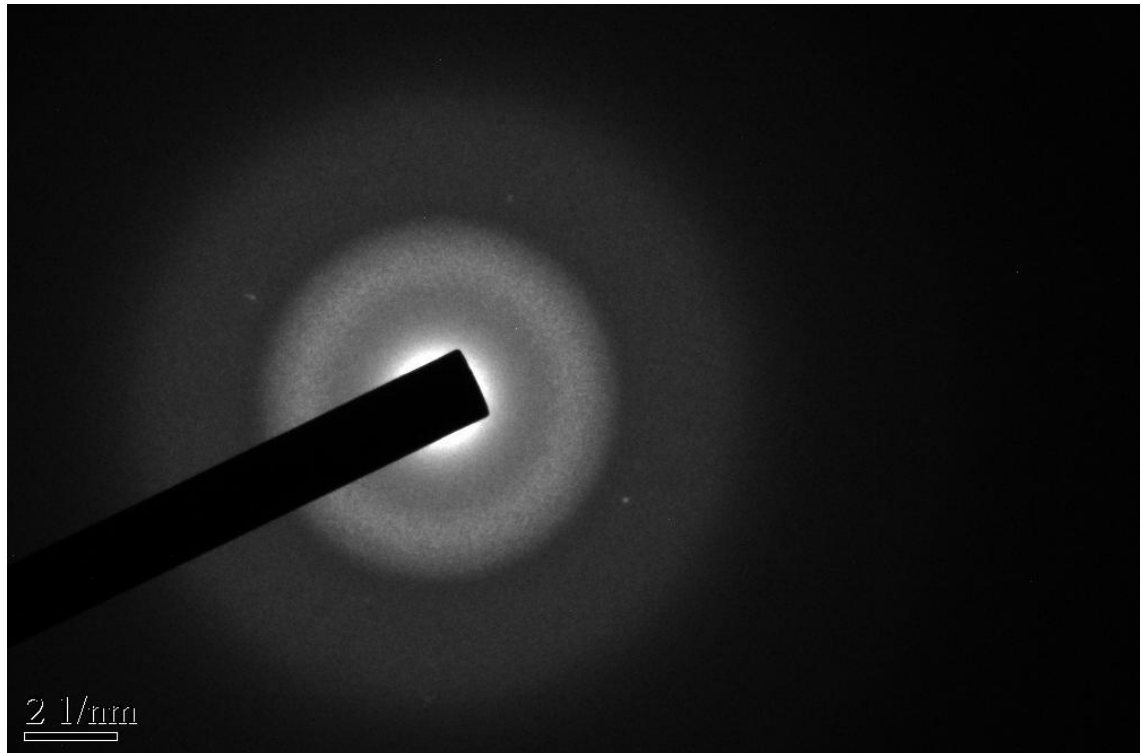


Figure 4.3. Transmission Electron Micrograph (TEM) of TiO₂ layer of a composite anode.

The direction of conventional current flow is now from Si to Au, presenting two possibilities: electrons pass from the gold to the TiO₂ conduction band, either by tunnelling or thermal excitation, and thence to the conduction band of the silicon; or holes form at the Si/TiO₂ interface and pass through the TiO₂ to the gold. The former process is almost certainly the dominant one at low positive bias ($V_b > 0$) and in this case, as V_b increases, the potential change will be accommodated primarily at the Si/TiO₂ interface. As V_b increases, however, (see fig. 4.2(b)) a second possible channel opens in which holes generated at the Si/TiO₂ interface at high positive bias pass through the TiO₂ layer *via* an inversion layer formed near to the valence band edge within the silicon.

At first sight, the postulate of a significant contribution to conduction in TiO₂ from hole hopping would appear very counter-intuitive. It would be expected that conduction is dominated by electron flow, particularly as it has been reported that the deposition of metals onto TiO₂ results in the creation of surface states *ca.* 1 eV below the conduction band edge which would facilitate electron transfer into the conduction band.⁹⁷⁻⁹⁸ However, direct observation of hole transport across high dielectric constant materials such as HfO₂ and TiO₂ has been reported by Mizubayashi and co-workers,⁹⁹ and Deskins and Dupuis¹⁰⁰ have modelled electron and hole transport in TiO₂ and compared their data to experimental results. In addition, the disinfection studies summarised above^{63, 101} support the production of OH radicals at the surface of the TiO₂ and it is not unreasonable to postulate that this process takes place *via* hole transport. Given the relatively large thickness of the TiO₂ layer, direct elastic tunnelling of holes or electrons through the TiO₂ is highly unlikely, whilst the amorphous nature of the TiO₂ would suggest Anderson localisation¹⁰² within the semiconductor, with conduction *via* Miller-Abrahams hopping.^{96, 103} This process will be substantially facilitated by the presence of any potential field that may build up in the TiO₂ itself. Unlike the situation with regard to carriers in the conduction band, the holes will probably be transported through the TiO₂, at an energy close to the valence band edge of Si (*ca.* +3 eV), by some form of field-assisted hopping; accommodation of potential change within the TiO₂ will substantially assist this process, and will also facilitate electron tunnelling into the conduction band from the gold.

4.3.2. Electrochemical circuit

This model does rationalise much of the behaviour of the composite electrode as an isolated artefact, and we now need to consider the effects associated with the immersion of the composite in an electrolyte with a counter electrode connected effectively through the potentiostat back to the gold. We now have two circuits as shown in fig. 4.4: the bias circuit (silicon-TiO₂-Au-silicon) and the electrochemical circuit (TiO₂-gold-electrolyte-[counter-electrode]-TiO₂-gold); the common elements being the TiO₂ surface and the gold grid.

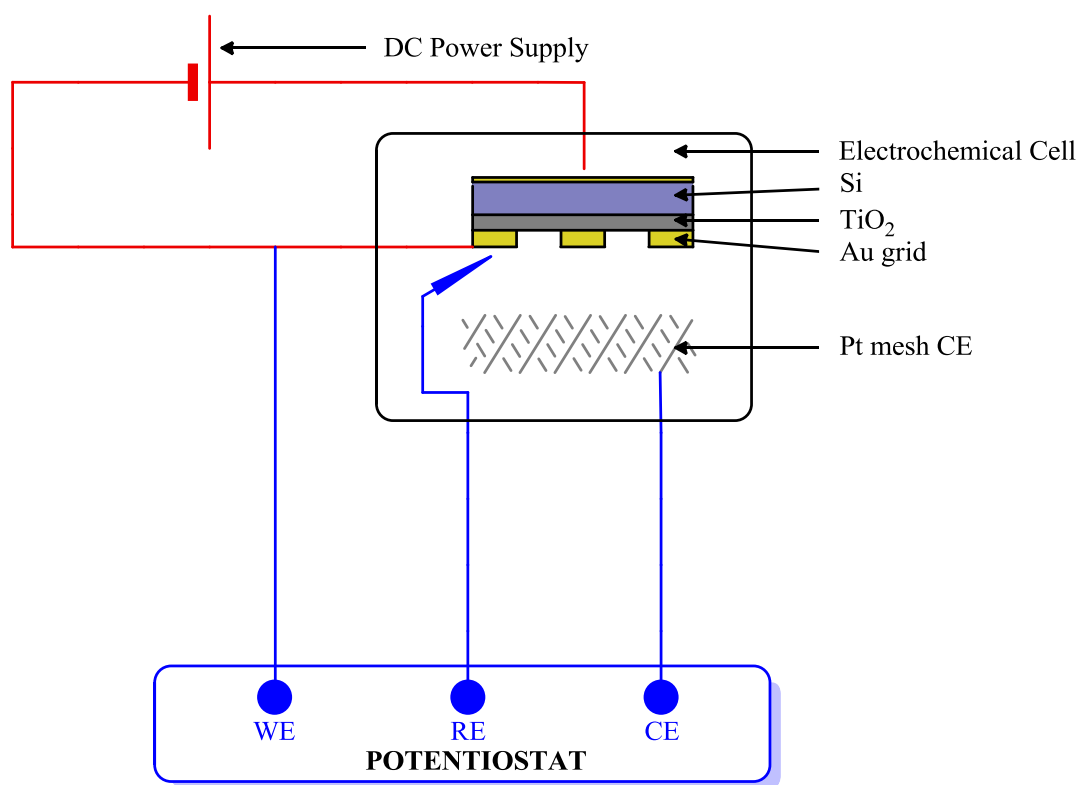
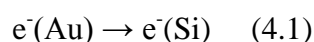


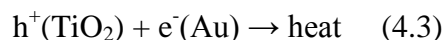
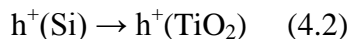
Figure 4.4. Schematic representation of bias circuit (red) and electrochemical circuit (blue).

For $V_b > 0$, positive charges forming at the surface either by electron-transfer to the interior of the TiO₂ (equation (4.1)):



or by holes arriving at the TiO₂/Au interface, may then be transferred back to the silicon or may react with oxidisable species present in the electrolyte itself. If we concentrate for a moment on conduction by holes, then once such holes have reached the TiO₂

surface, see equation (4.2) below, several different reactions may take place. Holes arriving beneath the Au grid will be effectively annihilated, equation (4.3), generating heat and contributing to the bias current, I_b , passing through the device:



Holes arriving at the TiO_2 surface physically close to the gold gridlines can hop to the gold where they can be captured and annihilated, at the metal surface, contributing both to the electrochemical response of the grid (i.e. electrons crossing the grid/electrolyte interface) and I_b . If the holes are not captured by the gold grid, then they may react with water or OH^- ions¹⁰⁴ generating OH^\cdot radicals at the TiO_2 surface (equation (4.4), see fig. 4.5); for convenience we may take OH^\cdot radicals as the hole carriers at the surface, as typical diffusion lengths (20 to 75 μm) are known for these species.¹⁰⁵⁻¹⁰⁷ There are several fates for the OH^\cdot radicals generated at the TiO_2 surface: they may be captured by the gold surface, generating initially AuOH (equations (4.5) and (4.6)), they may re-inject a hole into a suitable surface state of the TiO_2 (see below), they may react with other radical species to generate peroxy compounds, or they may react with adventitious oxidisable impurities.

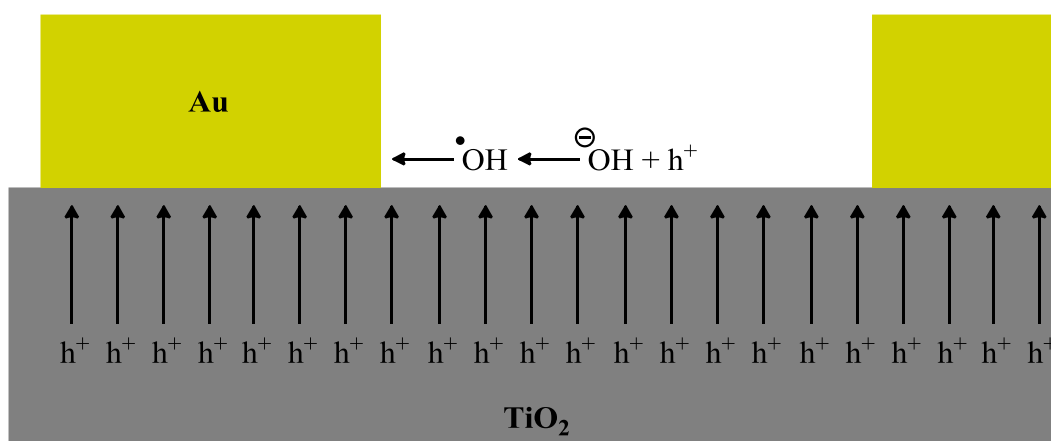
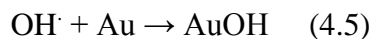
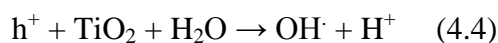


Figure 4.5. Graphical representation of hole-facilitated hydroxide oxidation by the transport of holes to the TiO_2 surface.

When a grid separation of 1000 μm and a grid width of 375 μm is used, between 4 and 17% of the bias current goes on to produce OH^\cdot radicals in a region where subsequent capture by the gold surface is possible. Once the gold is covered with AuOH species,

then further interaction with $\text{OH}\cdot$ radicals may generate oxygen, especially at higher values of V_b :



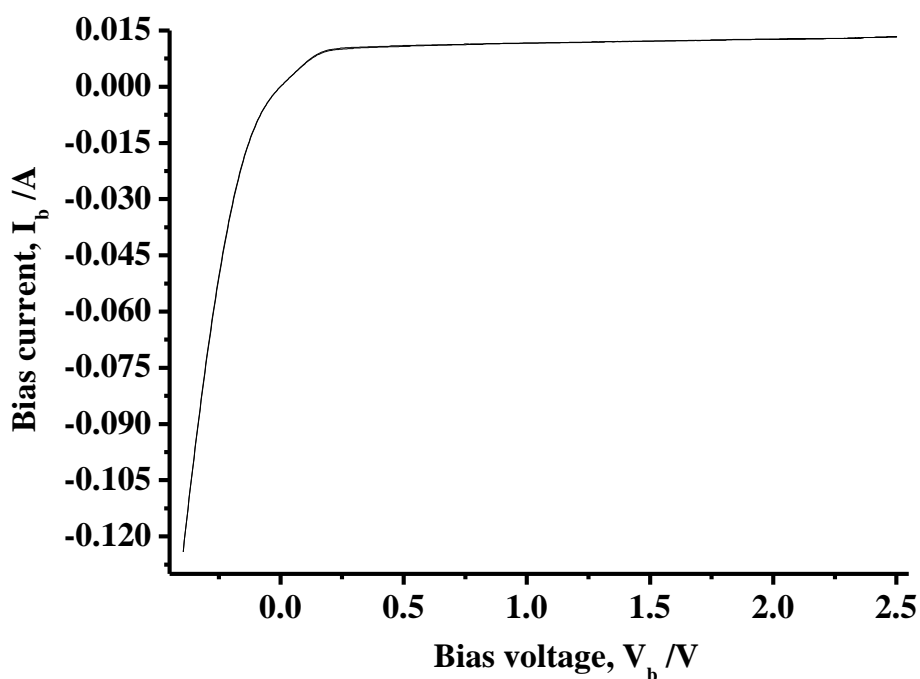
At sufficiently high V_b there is the possibility of still more interesting electrochemistry, as surface states have been postulated at energies that span almost the entire band-gap of TiO_2 : these include states at 1 eV below the conduction band edge,¹⁰⁸⁻¹⁰⁹ 0.5 eV above the valence band edge,¹¹⁰ 1.8 eV above valence band edge,¹¹¹ and 1.3 – 3.2 eV below the conduction band edge.¹¹² Such surface states could provide acceptor sites at the surface for highly energetic holes. These surface states may then drive quite new electrochemical reactions.

Finally, at sufficiently positive V_b , holes may be sufficiently energetic to be captured by the valence band at the TiO_2 surface, effectively opening up new channels for holes at the surface of the TiO_2 . It is clear, then, that the model predicts the possibility of some highly novel chemistry being generated by this composite system, the novelty arising from the presence of highly oxidising species arriving at the surface from the interior of the electrode. In some respects, this is similar to the photoelectrochemical phenomena observed on TiO_2 , but the use of an auxiliary gold electrode permits us to tune the surface in a way that is not really possible with simple photoelectrochemical devices.

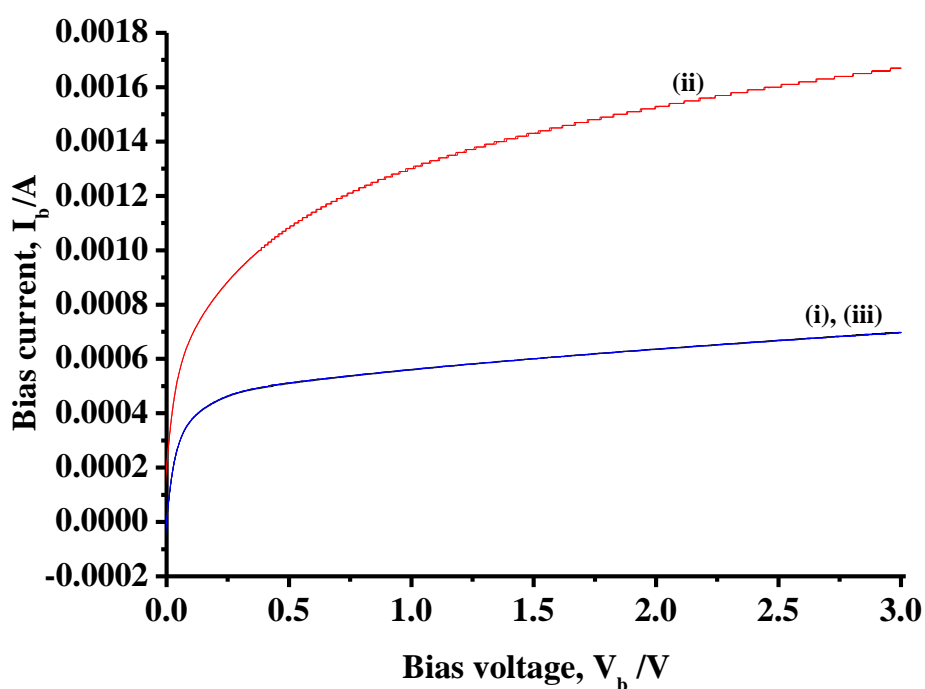
4.4. Results and discussion

4.4.1. The current/voltage characteristic of the Si/ TiO_2 /Au composite electrode in air

Figure 4.6(a) shows a typical I_b (bias current)/ V_b plot for a Si/ TiO_2 /Au composite anode in air; as may be seen from the plot, at $V_b < 0$ (“forward bias”), the negative current increases steadily with increasing, negative bias voltage. I_b is zero at $V_b = 0$, after which it increases as V_b increases to more positive values until, at $V_b \approx 0.25$ V; at this potential there appears to be a significant change in behaviour, as the bias current shows very little dependence upon the electric field across the electrode.



(a)



(b)

Figure 4.6(a) Typical bias current vs. bias voltage plot for a Si/TiO₂/Au composite anode. **(b)** Bias current vs. voltage plots for a Si/TiO₂/Au composite anode (i) in the dark, (ii) irradiated by a 635 nm, 4.0 mW LED and (iii) irradiated by a 1550 nm, 2.0 mW LED. The LED's were positioned 1 mm from the TiO₂/Au face of the anode.

Figure 4.6(a) is in accord with the model detailed above, of electron transport from Si to Au grid at $V_b < 0$ being replaced by hole transport from Si to TiO_2 at $V_b > 0$. However, the almost field-independent region at $V_b > 0.25$ V provides an insight into the distribution of V_b between Si and TiO_2 as it strongly suggests that: (1) the potential dropped between the gold grid and the gold Ohmic contact on the Si (i.e. the bias voltage, V_b) is divided between the Si and the TiO_2 , and that (2) the thermal generation of holes in the Si is rate limiting at $V_b > 0$. Further evidence that the photocurrent arises from charge carrier generation in the Si rather than the TiO_2 is provided by the data in fig. 4.6(b), which shows plots of bias current vs. bias voltage obtained during the irradiation of a Si/Au/ TiO_2 anode by a (ii) 635 nm and (iii) 1550 nm LED, compared to the response obtained in the dark (i). The intensities of these two sources were chosen to be comparable in terms of photon flux; i.e. 1.28×10^{16} photons s^{-1} and 1.56×10^{16} photons s^{-1} for the 635 nm and 1550 nm LED's, respectively. The wavelength of the latter was chosen deliberately, as the photon energy would be incapable of excitation of either Si or TiO_2 ; as such, this represents a control experiment. As may be seen from the figure, whilst the visible LED is incapable of exciting electrons in the TiO_2 , it gives a clear photocurrent through excitation of the Si. In contrast, the near-IR is incapable of exciting electrons in either material.

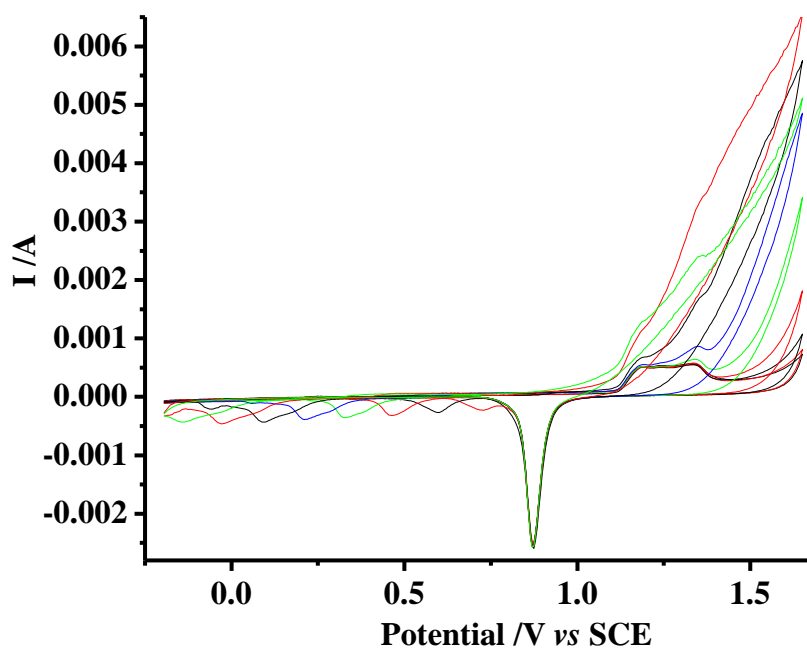
4.4.2. The electrochemical behaviour of the composite electrode at low bias voltages

Figures 4.7(a) and (b) show cyclic voltammograms of the composite anode in 0.5 M H_2SO_4 as a function of V_b collected in the dark. A potential range that encompassed Au oxide formation and stripping (-0.25 to 1.65 V vs SCE) was chosen initially to determine the effects of V_b on the redox behaviour of the device. With the battery disconnected ($V_b = 0$), the cyclic voltammograms so obtained were very similar to those reported using deposited polycrystalline Au electrodes under similar experimental conditions by other workers.¹¹³⁻¹¹⁴ Using $390 \mu\text{C cm}^{-2}$ for the charge under the oxide stripping peak¹¹⁵ near 0.87 V gives an area of 4.4 cm^2 , suggesting a roughness factor of *ca.* 2 as calculated below:

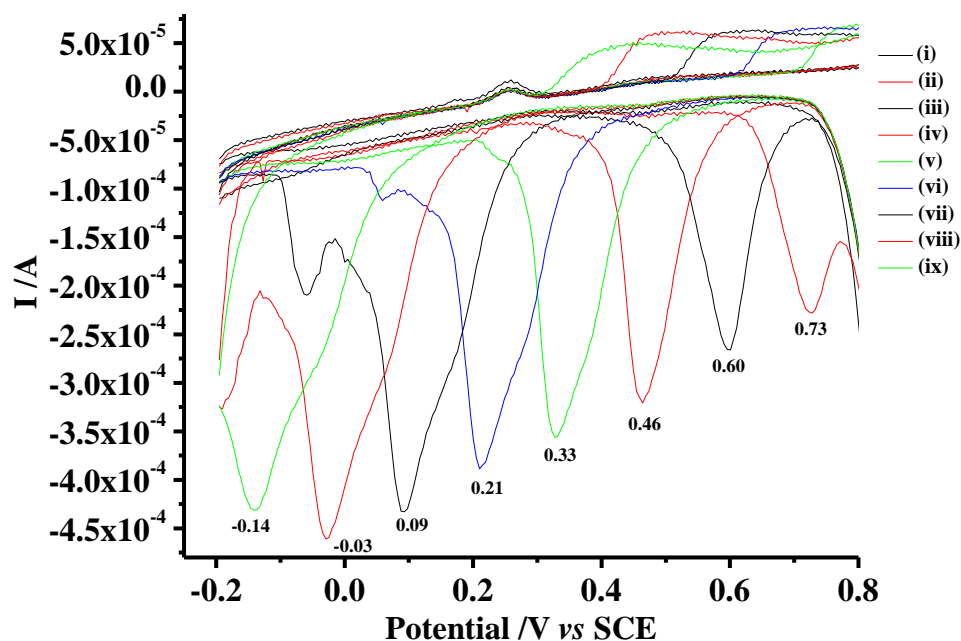
$$x \mu\text{C} / 390 \mu\text{C cm}^{-2} = 4.4 \text{ cm}^2, \text{ geometric area} = 2 \text{ cm}^2, \text{ therefore roughness} = 2$$

The application of a bias voltage across the composite anode clearly has a major effect upon the electrochemical behaviour of the Au grid. At $V_b = 0.1$ V, a small anodic current appears to underlie the anodic sweep of the Au voltammogram at potentials > 1.5 V. With increasing V_b , the magnitude of this underlying anodic (and irreversible) current increases, and the onset moves towards more cathodic potentials. The oxide stripping peak near 0.87 V on the cathodic sweep appears to be unaffected by V_b , neither do the oxide formation peaks in the anodic sweep; the latter just appear to be superimposed upon the exponentially rising, underlying current.

No deterioration of the Au grid electrode was observed in terms of its physical appearance. Similarly, there was no variation in the oxide formation and stripping peaks with $V_b = 0$ over a number of experiments.



(a)



(b)

Figure 4.7. Cyclic voltammograms of the Si/TiO₂/Au composite anode immersed in 0.5 M H₂SO₄ as a function of bias voltage in the dark between $V_b = 0$ (i) and 0.8 V (ix) in 0.1 V steps. (a) full potential range, (b) the voltammograms in (a) showing just the potential range -0.2 V to 0.8 V vs. SCE.

At this point, it is important to note the results from a blank experiment in which one terminal of a 1 k Ω resistor was connected to the counter and reference electrode outputs of the potentiostat. The other terminal of the resistor was connected to one contact of the Au grid and the other contact on the grid connected to the working electrode output of the potentiostat (see fig. 4.8(a)). The Au grid was connected to the Au Ohmic contact on the Si *via* the battery as described in section 2. The potential of the Au grid with respect to the counter and reference electrodes was cycled between -1.0 and +1.0 V at 100 mV s⁻¹ as a function of V_b between 0 and 3 V. The expected Ohmic response of the resistor was unaffected by V_b (see fig. 4.8(b)); hence, in the absence of oxidisable species or “receptors” (e.g. H₂O), see equation (4.4), holes do not initiate their journey across the TiO₂.¹¹⁶

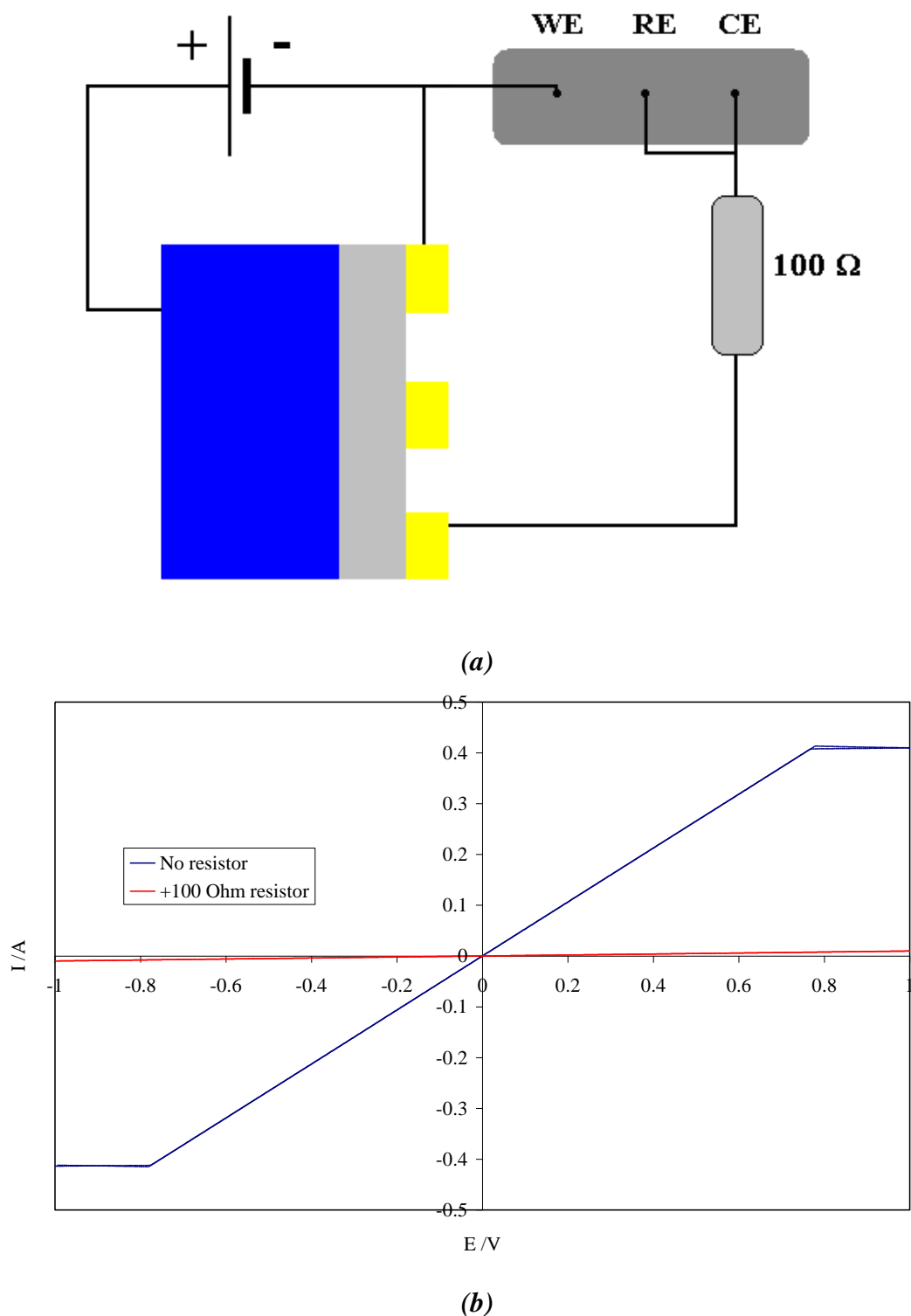


Figure 4.8(a) Schematic representation of the blank experiment set-up; **(b)** I/V plot generated during the blank experiment.

Given the relatively simple composition of the electrolyte in the experiment in figs. 4.7(a) and (b), and the absence of any evidence for the dissolution of the Au grid, the only likely process to account for the V_b -dependent anodic currents observed in the

figure is the oxidation of water, and hence the data in the figure are entirely in accord with the postulated model, equations (4.4) – (4.6).

In contrast to the increasing anodic current observed at high potentials as V_b is increased, there is little change in the cathodic sweep of the voltammograms in figs. 4.7(a) and (b) apart from the appearance of a small cathodic peak at $V_b = 0.1$ V which moves to more negative potentials as V_b is increased. The plot of the small peak potential vs. V_b is a straight line with a slope of -1.2 ± 0.01 (see fig. 4.9). The intercept at $V_b = 0$ is 0.84 ± 0.01 V, under the oxide stripping wave, but not at the same potential as the peak current (0.87 ± 0.01 V). Again, given the simplicity of the chemical composition of the system under investigation, the small cathodic peak is probably due to the re-reduction of small regions of the Au grid, most likely the perimeter with the TiO_2 , oxidised during the anodic sweep. The area under the small cathodic peak observed at $V_b = 0.2$ V is *ca.* 12% of that calculated from the charge under the stripping peak near 0.87 V, equivalent to a surface area of 0.5 cm^2 .

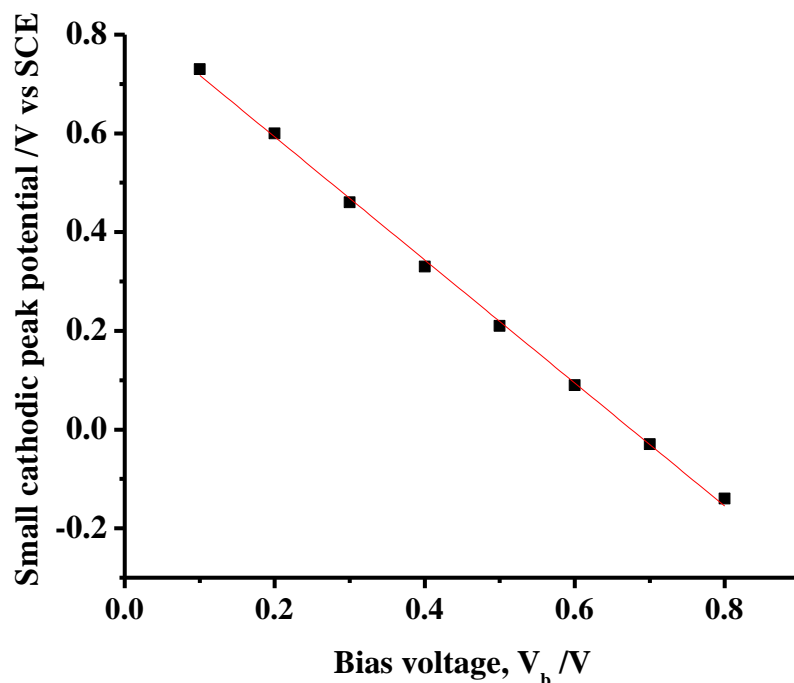
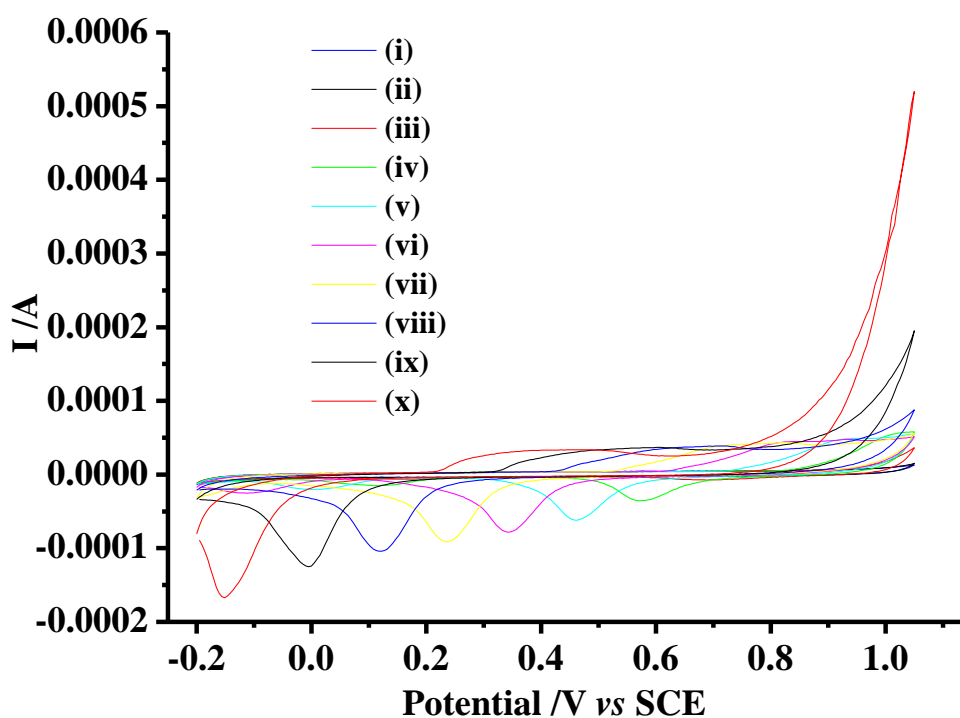


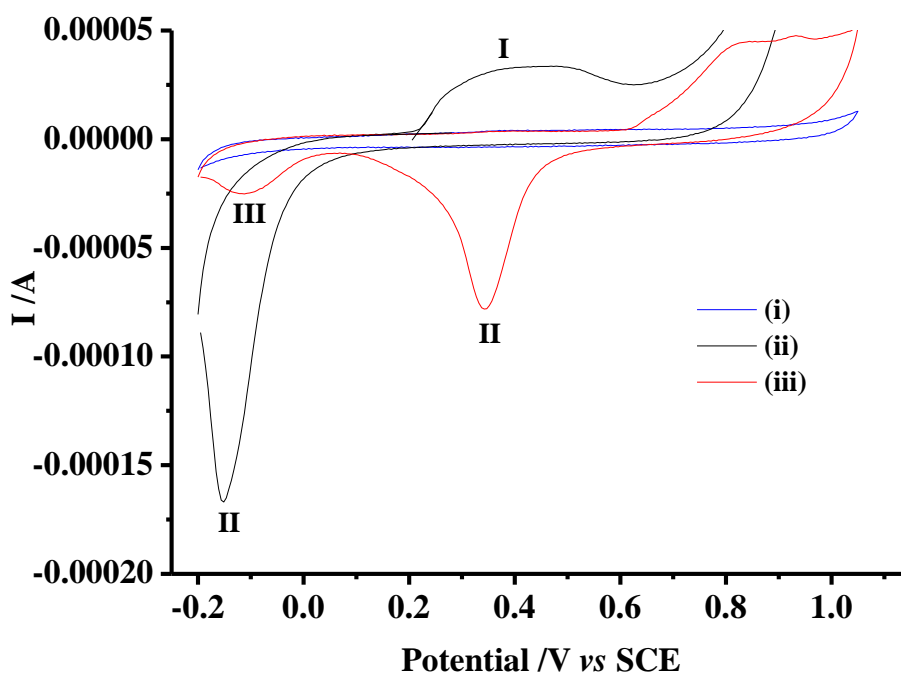
Figure 4.9. Plot of the peak potential of the small cathodic peak in fig. 4.7 vs. bias voltage.

In order to further understand the effects of V_b on the underlying anodic current displayed in fig. 4.7(b), it was decided to investigate the voltammetric response over a potential range from -0.2 V to an anodic limit of 1.05 V (i.e. just below the onset of oxide formation).

Figure 4.10(a) shows cyclic voltammograms obtained using a (Au)/Si/TiO₂/Au anode immersed in 0.5 M H₂SO₄ between -0.2 V and 1.05 V vs. SCE collected as a function of bias voltage. Figure 4.10(b) shows the CV's in fig. 4.10(a) collected at " $V_b = 0$ " (i.e. battery disconnected), 0.5 V & 0.9 V. As expected, the CV recorded without an applied bias voltage is featureless; however, at $V_b \geq 0.2$ V an anodic wave (I) and two cathodic waves (II & III) appear, see fig. 4.10(b).



(a)



(b)

Figure 4.10(a) Cyclic voltammograms of the (Au)/Si/TiO₂/Au composite anode as a function of bias voltage, V_b from (i) no bias to (x) $V_b = 0.9$ V in 100 mV steps and (b) Selected voltammograms from fig. 4.10(a) for $V_b = 0$ (i), 0.9 V (ii) and 0.5 V (iii).

Peaks I and II are similar to those associated with Au oxide formation and stripping; the onset potential of I and the peak potentials of II & III move cathodic as V_b is increased, and the charges under all three features increase. Table 1 shows various characteristics of the voltammograms in fig. 4.10(b); specifically the onset potentials of peak I and O₂ evolution (assuming the irreversible exponential increase in current observed at high anodic potentials in figs. 4.10(a) & (b) is O₂ evolution; a not unreasonable assumption given the simple composition of the electrolyte) and the peak potential of peak II. The shift in the peak potential of II in fig. 4.10(a) vs. V_b is presented in fig. 4.11(i); the plot has a slope of -1.2 which is the same as the slope of the analogous plot shown in fig. 4.9.

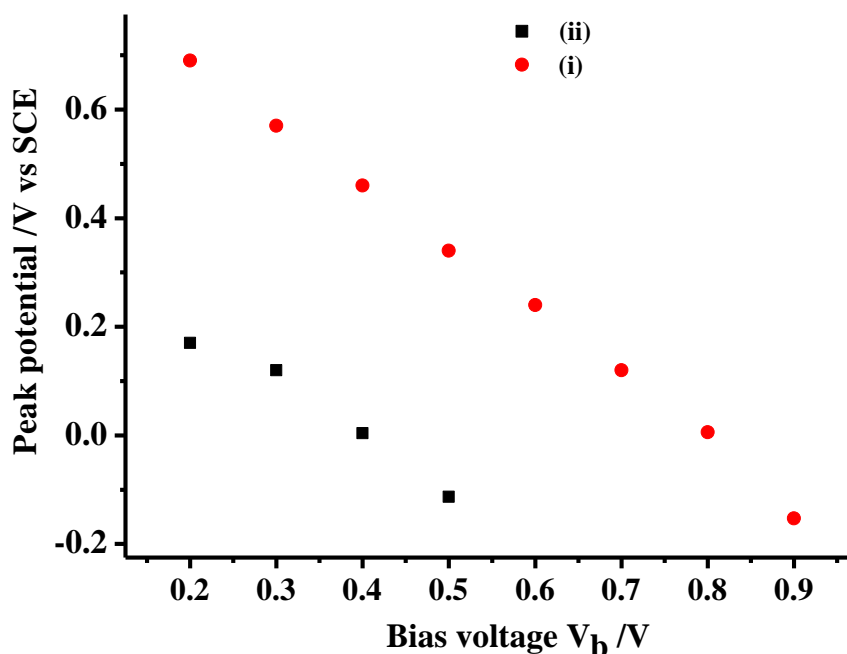


Figure 4.11. Plots of the peak potentials of (i) peak (II) and (ii) peak (III) in fig. 4.10(a) as a function of V_b .

V_b /V	Peak (I) onset potential /V vs. SCE	Peak potential peak (II) /V vs. SCE	Onset of O ₂ evolution /V vs. SCE
No bias	-	-	-
0.5	0.62	0.34	1.01
0.9	0.18	-0.15	0.64

Table 4.1. Characteristics of the voltammograms in fig. 4.10(b).

The shift of the peak potential of (I) in fig. 4.10(b) resembles the behaviour of the oxide stripping peaks on gold electrodes when the anodic potential limits increases.¹¹⁷ Thus fig. 4.12 shows cyclic voltammograms of a 16 cm long, 0.2 mm diameter Au wire (Goodfellow, 99.99%) coiled to expose 1cm² to the 0.5 M H₂SO₄ electrolyte as a function of the anodic limit of the CV. As may be seen from the figure, the oxide stripping peak increases in charge and moves steadily more cathodic as the anodic potential limit is increased.

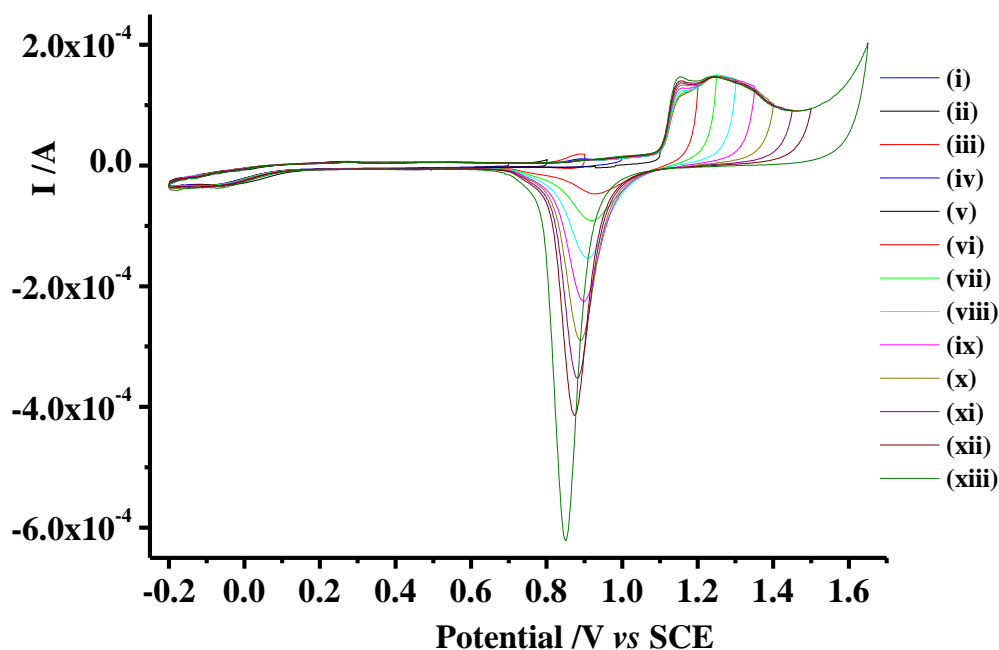


Figure 4.12. Cyclic voltammograms of a 0.2 mm diameter, 16 cm long Au wire immersed in 0.5 M H_2SO_4 at a scan rate of 100 mV s^{-1} . Anodic limit: (i) – (vi) 0.7 V to 1.2 V in 0.1 V steps; (vii) – (xiii) 1.3 V to 1.65 V in 0.05 V steps.

Thus, a first approximation to the data in fig. 4.10(a) is that the ‘actual’ anodic limit ($E_{a,act}$) experienced by the gold grid of the composite anode in the CV’s in fig. 4.10(a) and (b) may be written simply as:

$$E_{a,act} = E_{a,pot} + V_b \quad (4.7)$$

where $E_{a,pot}$ is the anodic limit imposed by the potentiostat. This postulate is supported further by the data in fig. 4.13 which shows a plot of the peak potential of the oxide stripping peak in fig. 4.12 vs. the anodic limit, which is also linear. However, the slope of the plot in fig. 4.13 is *ca.* -0.2, suggesting a significantly weaker dependence of the gold wire oxide stripping peak position on the anodic limit compared to the dependence of peak II on V_b (see fig. 4.11(i)). It is also clear from fig. 4.10(b) that increasing the bias voltage not only decreases the peak potentials of I and II, but also causes marked changes in the shapes of the features: compare the width and peak current of peak (II) at $V_b = 0.5 \text{ V}$ and 0.9 V . This argues against the simple ‘additive’ relationship represented by equation (4.7); furthermore, peak III behaves in concert with peak II, moving more

cathodic as V_b increased and showing a linear dependence of peak potential with V_b , see fig. 4.11(ii), having a slope of *ca.* -0.97. The peak potential of III moves < -0.2 V vs. SCE (i.e. into the hydrogen evolution region) when $V_b > 0.5$ V.

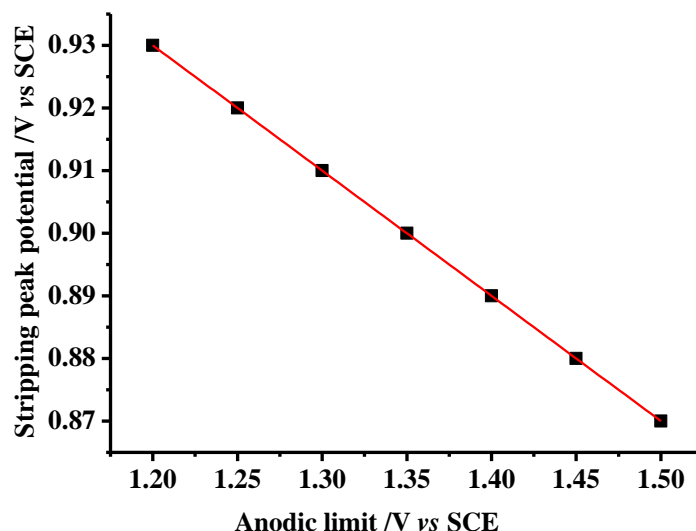


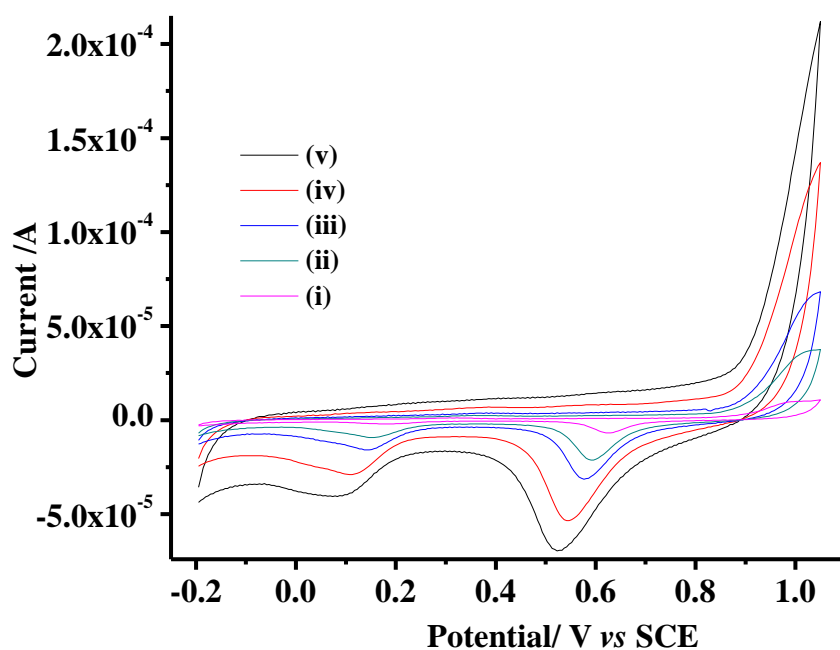
Figure 4.13. Plot of the peak potential of the cathodic stripping feature in fig. 4.12 as a function of anodic limit.

The charge under peak I in the anodic sweep of the CV collected at the $V_b = 0.5$ V in fig. 4.10(b) was *ca.* 1.6×10^{-4} C; this is identical (within experimental error) to the sum of the cathodic charges under peaks II and III, suggesting that the oxidised gold formed over the potential range of peak (I) in the anodic sweep is reduced in two processes during the cathodic sweep, represented by peaks (II) and (III).

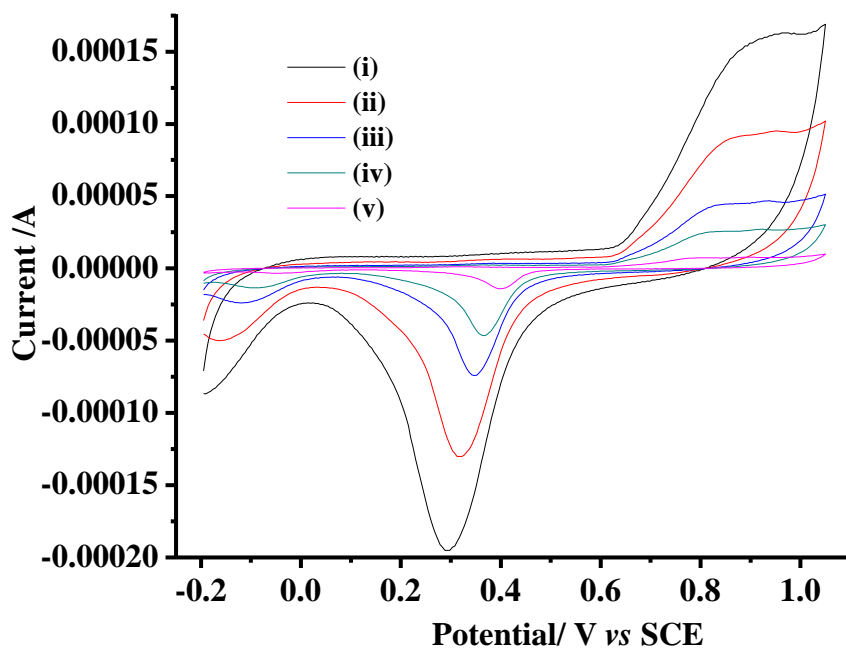
From the discussion above it would appear that applying a bias voltage between the Si and the Au grid of the composite anodes increases the electrochemical potential experienced by the latter, but not in a straightforward manner, in that the electrochemistry observed is not the same as when the electrochemical potential does not have a component supplied by V_b .

In order to investigate the possible origin of the various features in fig. 4.10(a), scan rate dependence experiments were carried out.

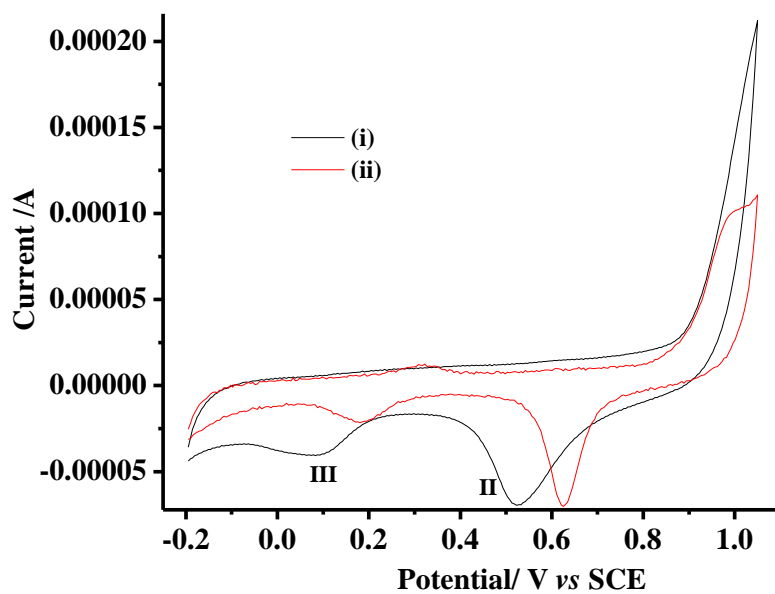
Figures 4.14(a) & (b) show voltammograms collected as a function of scan rate at two bias voltages, 0.3 V and 0.5 V, and figs. 4.14(c) & (d) show the voltammograms in figs. 4.14(a) & (b) collected at 500 mVs^{-1} and 10 mVs^{-1} . As may be seen from the figures, increasing the scan rate increases the peak currents of all three features: I, II and III (see fig. 4.14(c)) whilst peaks II and III are broadened and shift to more cathodic potentials. The effect of increasing the bias potential is to move the small cathodic peaks II and III to lower potentials.



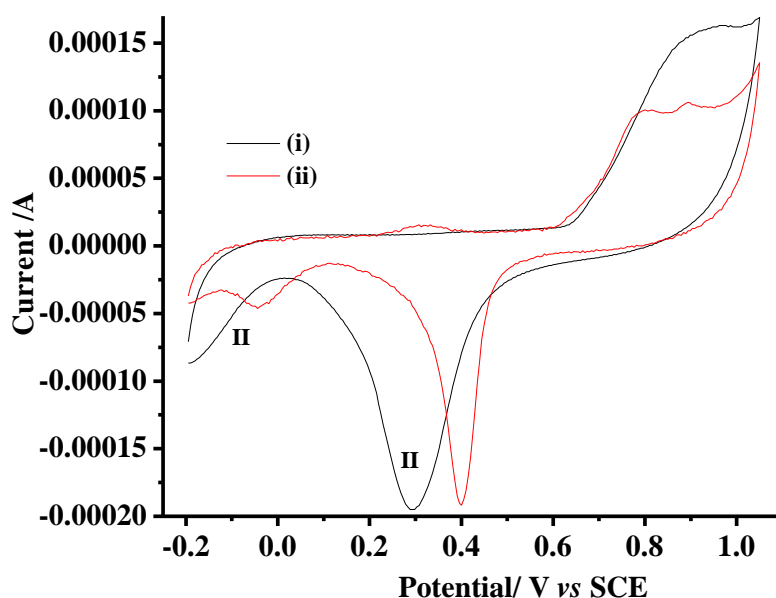
(a)



(b)



(c)



(d)

Figure 4.14. Cyclic voltammograms of (Au)/Si/TiO₂/Au electrode at (a) 0.3 V bias and (b) 0.5 V bias as function of scan rate: (i) 10, (ii) 50, (iii) 100, (iv) 250 and (v) 500 mV s⁻¹; (c) A comparison of the CV's in (a) at (i) 500 mVs⁻¹ and (ii) 10 mVs⁻¹, the latter voltammogram is increased by a factor of 10 for clarity; (d) A comparison of the CV's in (b) at (i) 500 mVs⁻¹ and (ii) 10 mVs⁻¹, the latter voltammogram is increased by a factor of 14 for clarity.

Figure 4.15 shows plots of peak current vs. the square root of scan rate for peaks II and III in figs. 4.14(a) and (b); all are linear with non-zero intercepts. Table 2 summarises the slopes of the plots in fig. 4.15. Despite peaks II and III being attributed to the reduction of gold oxide, a surface process, it is clear that both peaks vary with $\sqrt{(\text{scan rate})}$, as well as showing different slopes to each other and variation with V_b .

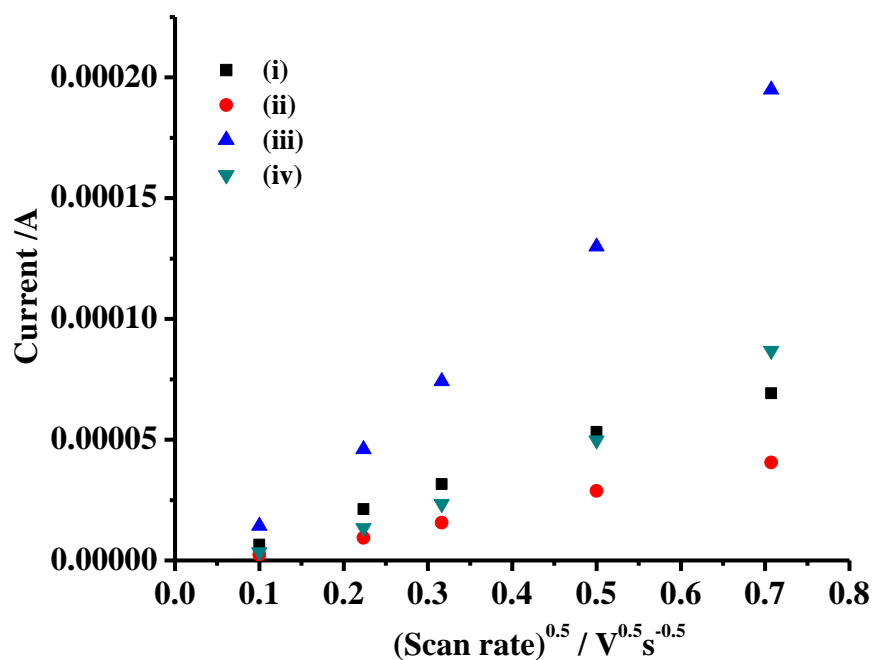


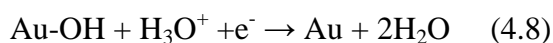
Figure 4.15. Plots of peak current vs. $\sqrt{\text{Scan rate}}$ for the cathodic peaks in figs. 4.14(a) & (b). (i) Peak II $V_b = 0.3$ V, (ii) peak III $V_b = 0.3$ V, (iii) peak II $V_b = 0.5$ V and (iv) peak III $V_b = 0.5$ V.

Peak	$V_b = 0.3\text{V}$	$V_b = 0.5\text{V}$
II	1.0	3.0
III	0.6	1.4

Table 4.2. The slopes of the plots in fig. 4.15 in $10^{-4} \text{AV}^{-0.5} \text{s}^{-0.5}$.

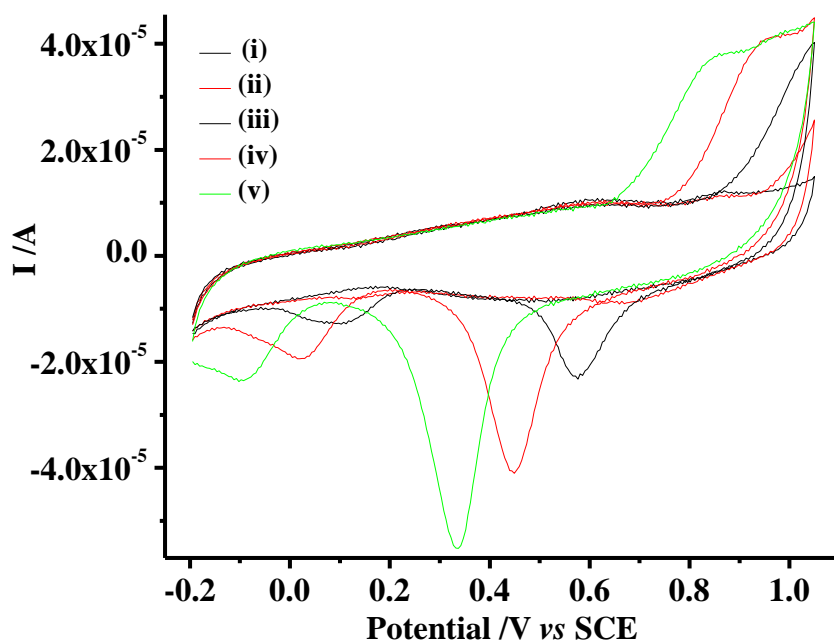
4.4.3. The oxidation of I_3^-

A dependence on the square root of scan rate is usually taken as being indicative of electron transfer to/from a solution specie;⁴¹ but this will inevitably involve solution species:

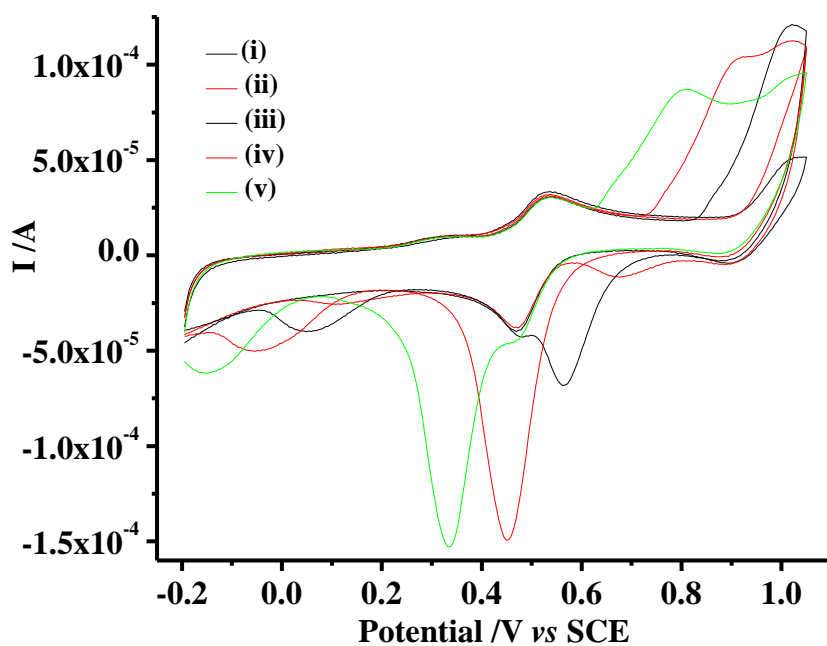


It was decided to see if electrons could be exchanged between the Au-OH species responsible for peaks II and/or III and a solution redox couple. To this end the I_2/I^- couple was chosen, as its E^0 lies in the region of peak II.¹¹⁸

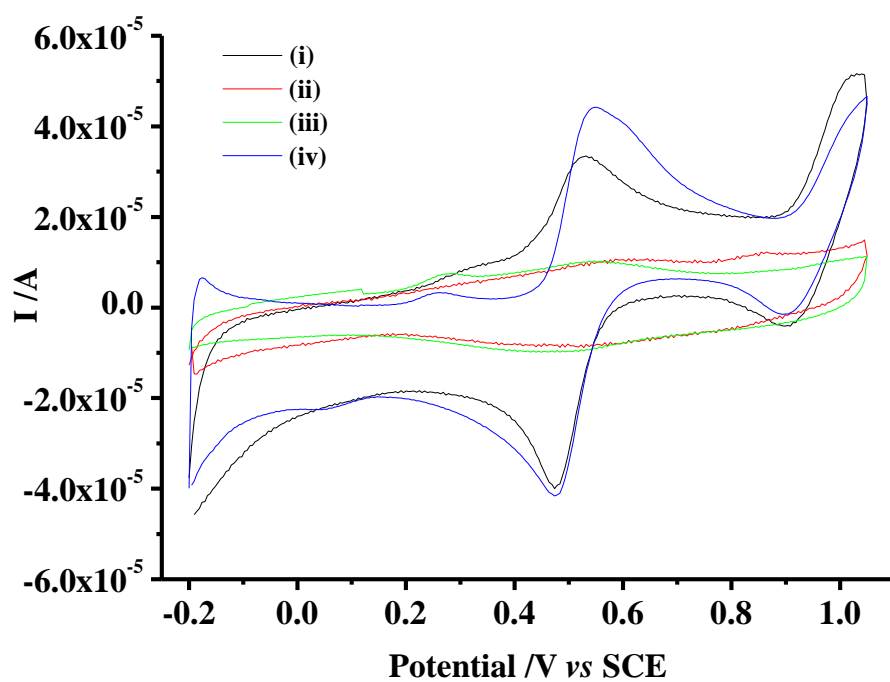
Figure 4.16(a) shows the CV's collected at $V_b = 0.2$ V to 0.5 V in fig. 4.10(a) in the absence of KI (i.e. essentially duplicating the experiment in fig. 4.10(a)) the latter being the V_b range relevant to the potential of the I_2/I^- couple. Figure 4.16(b) shows the corresponding data in the presence of 50 μ M KI. For comparison, fig. 4.16(c) shows the CV's in figs. 4.16(a) and (b) collected at zero bias and CV's taken using a Au wire (0.2 mm dia., 32 cm long, Goodfellow, 99.99%) coiled to expose *ca.* 2 cm² to the electrolyte in the absence and presence of 50 μ M KI. The CV's in the absence of KI in fig. 4.16(c) suggest that the gold grid and gold wire were of approximately the same area.



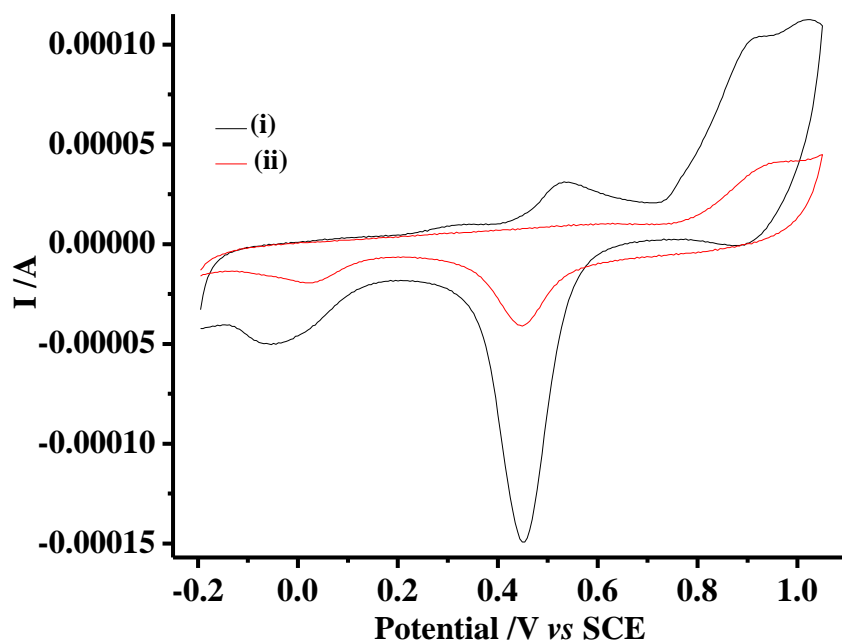
(a)



(b)



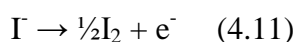
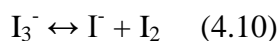
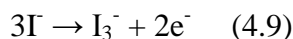
(c)



(d)

Figure 4.16(a) Cyclic voltammograms of the (Au)Si/TiO₂/Au electrode in 0.5 M H₂SO₄ at $V_b =$ (i) 0 and (ii) 0.2 V to (v) 0.5 V vs. SCE in fig. 4.10(a); **(b)** CV's collected at $V_b =$ (i) 0 and (ii) 0.2 V to (v) 0.5 V vs. SCE in 0.5 M H₂SO₄ + 0.05 mM KI; **(c)** the cyclic voltammograms collected at zero bias in (a) & (b) in (i) the presence and (ii) absence of 0.05 mM KI; cyclic voltammograms of a Au wire coiled to expose 2 cm² to the electrolyte in the (iii) absence and (iv) presence of 0.05 mM KI; **(d)** direct comparison of the CV's collected at $V_b = 0.4$ V in figs. 4.16(a) and (b).

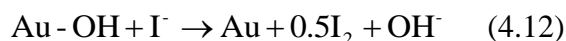
The redox waves centred near 0.55 V vs. SCE and 1.0 V vs. SCE may be attributed to the following processes:¹¹⁹



The presence of KI has a significant effect upon the voltammetric response, even in the absence of a bias voltage, see fig. 4.16(b) cff. fig. 4.16(a). At $V_b > 0$, all three peaks I, II and III are enhanced in terms of their peak currents, see fig. 4.16(d) for example which shows the CV's collected at $V_b = 0.4$ V in figs. 4.16(a) and (b). In addition,

whilst peak II increases with V_b monotonically in fig. 4.16(a), it increases from $V_b = 0$ up to $V_b = 0.4$ V in fig. 4.16(b) but the peak current is then unchanged at $V_b = 0.5$ V; the change in peak current from 0.3 V to 0.4 V is disproportionately high compared to that in fig. 4.16(a) and suggests that the reduction of I_2 to I^- is contributing to the enhancement of peak II.

As detailed above, the small cathodic peaks (II and III) are due to the reduction of Au-OH at the perimeter line between Au and TiO_2 . At $V_b = 0$ V, peak II lies under the bulk Au oxide stripping peak. The peak areas are very small, hence the total areas under peaks II and III are much smaller than the area under the bulk stripping peak. As V_b increases, the energy of holes increases, which means that they can penetrate through deeper barriers i.e. more of the Au is oxidised near to TiO_2 ; thus the potential required to reduce Au-OH moves negative (higher overpotential), hence the 1:1.0-1.2 relationship between the peak potentials of II and III and V_b . The KI data suggests that the Au-OH at the perimeter is catalytic for the oxidation of I^- :



The work thus far detailed within this chapter has focussed upon the development of our understanding of the composite anodes at low bias potentials; however, in order to generate currents sufficient to oxidise fluoride, higher bias voltages must be employed. Therefore, it was decided to investigate the behaviour of the composite anodes at higher V_b , using the same systems as those utilised to characterise the behaviour at lower bias potentials for direct comparison.

4.4.4. The electrochemical behaviour of the composite electrode at higher bias voltages

Figure 4.17 shows cyclic voltammograms collected using the electrode in figs. 4.7(a) and (b) at $V_b = 0.9, 1.0, 1.5$ and 2.0 V.

It is clear from the figure that there is a major transition in behaviour at $V_b > 1.0$ V, as predicted by the model, with the onset of O_2 evolution shifts markedly towards negative potentials with increasing bias voltage at $V_b > 1.0$ V. The onset for O_2 evolution at $V_b = 2.0$ V is 0.0 V vs. SCE, well below the potential expected from electrochemical

considerations alone. Again, the oxide formation and stripping processes on the bulk of the Au grid seem essentially unaffected as V_b increases, apart from a peak near 1.35 V which appears to become more prominent. This peak may be due to the formation of Au(111) facets on the Au grid.¹¹⁴

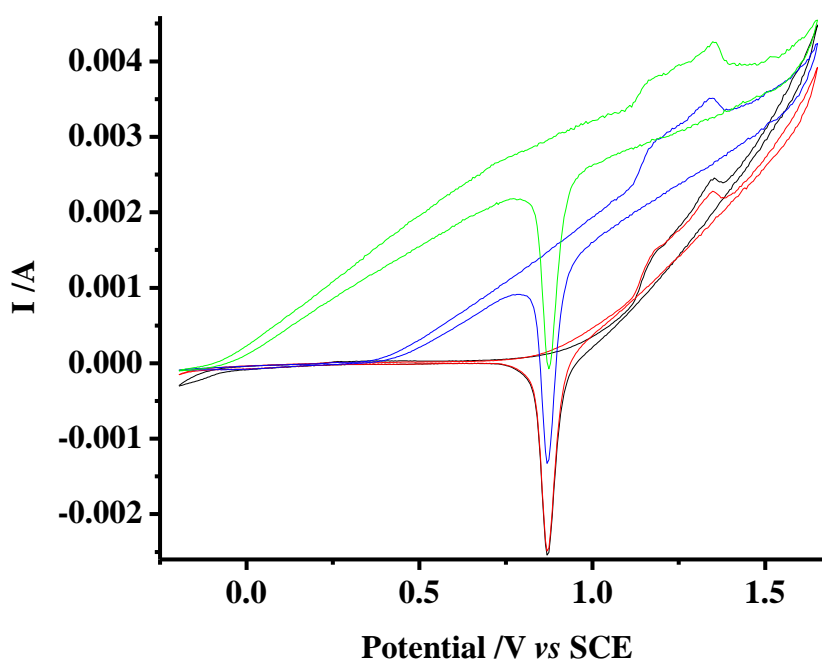


Figure 4.17. Cyclic voltammograms of the (Au)Si/TiO₂/Au composite anode immersed in 0.5 M H₂SO₄ as a function of bias voltage at $V_b = 0.9$ V (red), 1.0 V (black), 1.5 V (blue) and 2.0 V (green).

Figure 4.18 shows the bias current, I_b , through the composite anode as a function of V_b at the electrochemical potential of the anodic limit of the CV's in figs. 4.7 & 4.17, 1.65 V, and at -0.1 V. Figs. 4.7 & 4.17 show that V_b influences the electrochemistry taking place at the Au grid/electrolyte interface; fig. 4.18 shows that the electrochemistry at the Au grid has a direct influence on the bias current, I_b , flowing through the composite anode. Again, data entirely in accord with the postulated model: when the TiO₂ face of the anode is exposed to electrolyte, additional acceptors are, in principle, available compared to the situation in air, enhancing I_b , hence giving rise to Faradaic current over and above that expected from the electrochemistry at the gold/electrolyte interface.

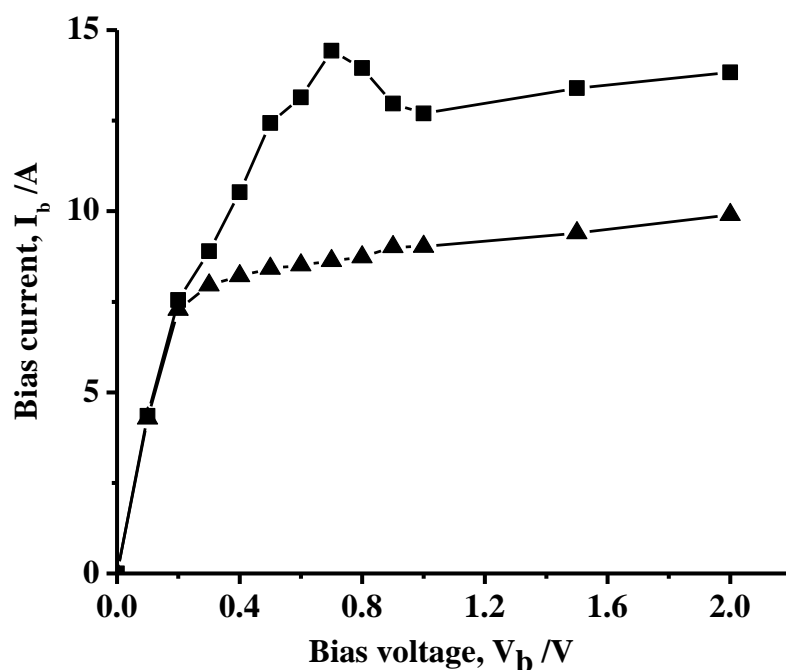


Figure 4.18. Plots of bias current vs. bias voltage collected during experiments where the potential of the (Au)Si/TiO₂/Au composite anode was held at (▲) -0.1 V and (■) +1.65 V vs. SCE in 0.5 M H₂SO₄.

4.4.5. Electrodeposition and characterisation of Pt composite anode

Much of the work described on the behaviour of the composite anodes was performed using a Si/TiO₂/Au electrode; however, as discussed in chapter 1, the most common anode material used for ECF is Pt, due largely to the resistance of the metal to chemical attack by fluoride. Therefore, in order to develop an anode suitable for ECF, a Si/TiO₂/Pt electrode was fabricated.

Initial studies into the characterisation of the Pt composite anode showed much lower currents could be achieved compared with the gold anodes. This observation was attributed to the high resistivity of Pt ($1.922 \times 10^{-8} \Omega\text{m}$)¹²⁰ compared with gold ($0.481 \times 10^{-8} \Omega\text{m}$).¹²⁰

It was therefore considered that it may be possible to exploit the electrochemistry of Pt whilst improving the resistivity of the anode by electrodepositing Pt onto a Si/TiO₂/Au anode.

The gold composite electrode was characterised prior to electrodeposition by the acquisition of DCCs in both air and a 0.5 M aqueous solution of H_2SO_4 (fig. 4.19) and the acquisition of CVs in 0.5 M H_2SO_4 between -0.25 V and 1.65 V vs. SCE at bias potentials of 0 V, 0.2 V, 0.5 V and 1.0 V (fig. 4.20). A second CV was obtained at $V_b = 0$ V after the application of bias potential in order to ensure reversibility of the system, before a final DCC was obtained in solution as before.

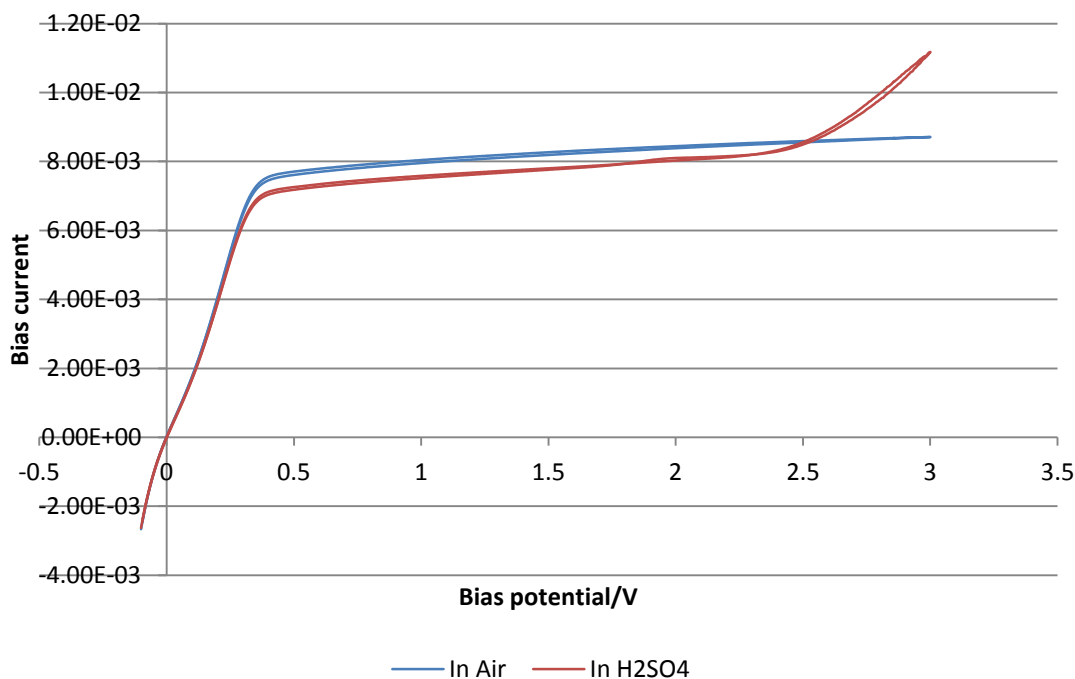


Figure 4.19. Comparison of DCCs of gold composite anode in air and in 0.5 M H_2SO_4 between -0.1 V and 3 V (pre bias).

Figure 4.20 shows a comparison of the CVs obtained between -0.25 and 1.65 V vs. SCE at $V_b = 0.0$ V, 0.2 V, 0.5 V and 1.0 V. The “lift off” of the CV becomes evident at $V_b = 1.0$ and the small cathodic peak can be seen appearing at more negative potentials with increasing V_b in accordance with expectation.

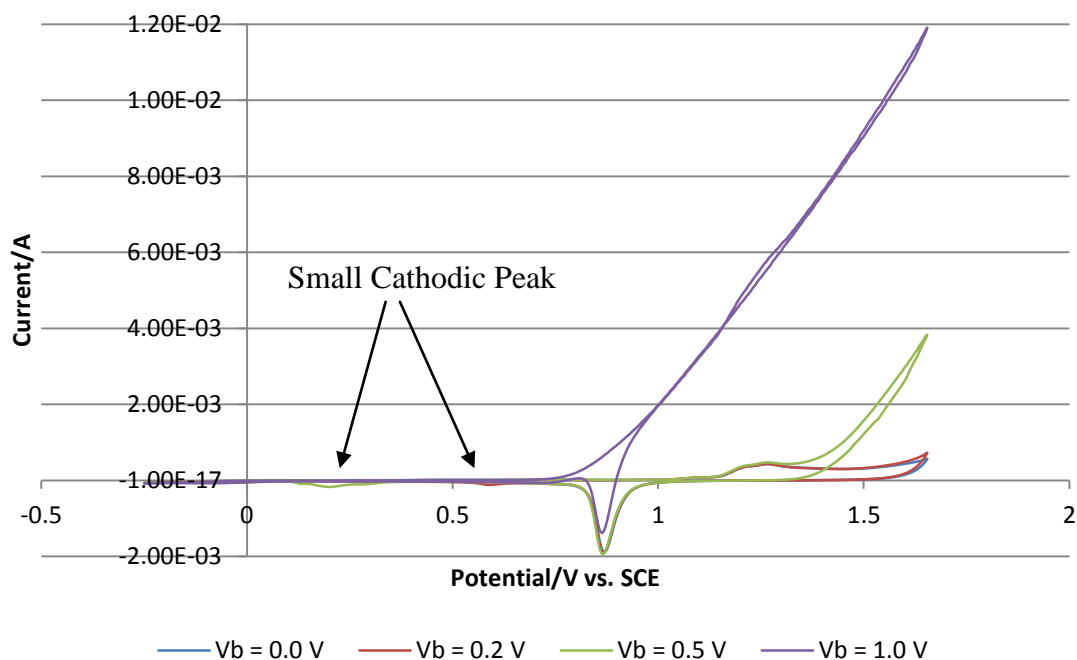


Figure 4.20. Comparison of CVs of gold composite anode in $0.5\text{ M H}_2\text{SO}_4$ between -0.25 V and 1.65 V vs. SCE, scan rate = 100 mV s^{-1} , $V_b = 0.0\text{ V}$, 0.2 V , 0.5 V and 1.0 V .

Figure 4.21 shows the reversibility of the system by comparison of CVs obtained at $V_b = 0\text{ V}$ both prior to and post bias potential application.

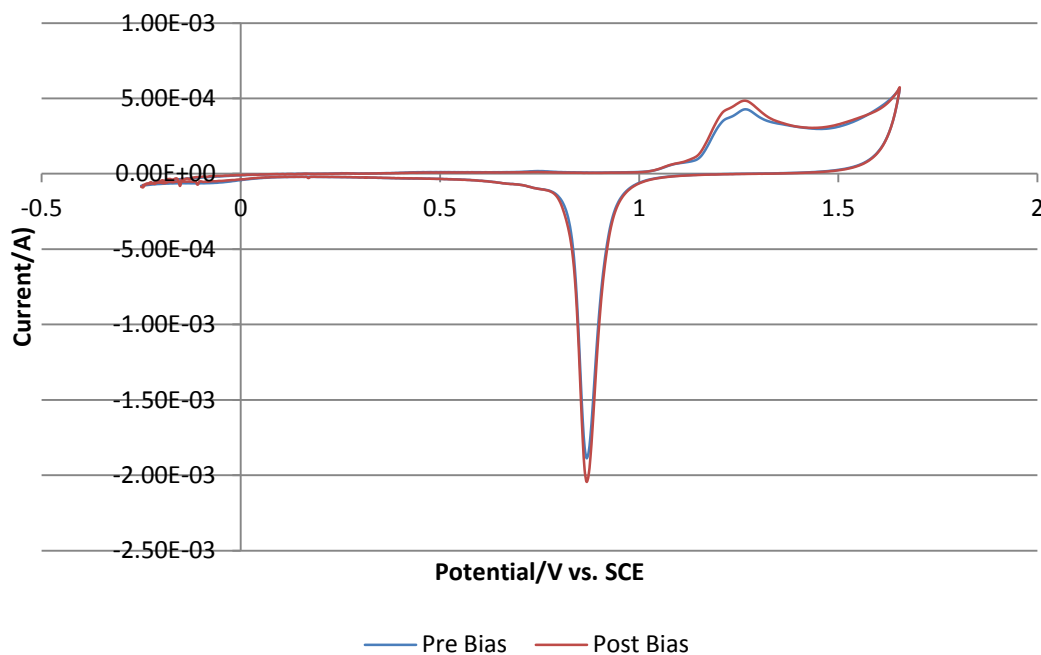


Figure 4.21. Comparison of CVs of a gold composite anode in $0.5\text{ M H}_2\text{SO}_4$ between -0.25 V and 1.65 V vs. SCE, scan rate = 100 mV s^{-1} , $V_b = 0.0\text{ V}$, pre and post the experiment shown in fig. 4.20.

In spite of the similarities observed in the CVs pre- and post- V_b application (fig. 4.21), comparison of the DCCs obtained prior to and post bias potential application display a considerable increase in current (10.7 mA) at 3 V after the bias potential was applied (fig. 4.22). This suggests that the application of bias ‘activates’ the anode. In accordance with the postulated model, this activation may be a result of residual surface states facilitating electron transfer into the conduction band of the TiO_2 , hence increasing the current achievable.

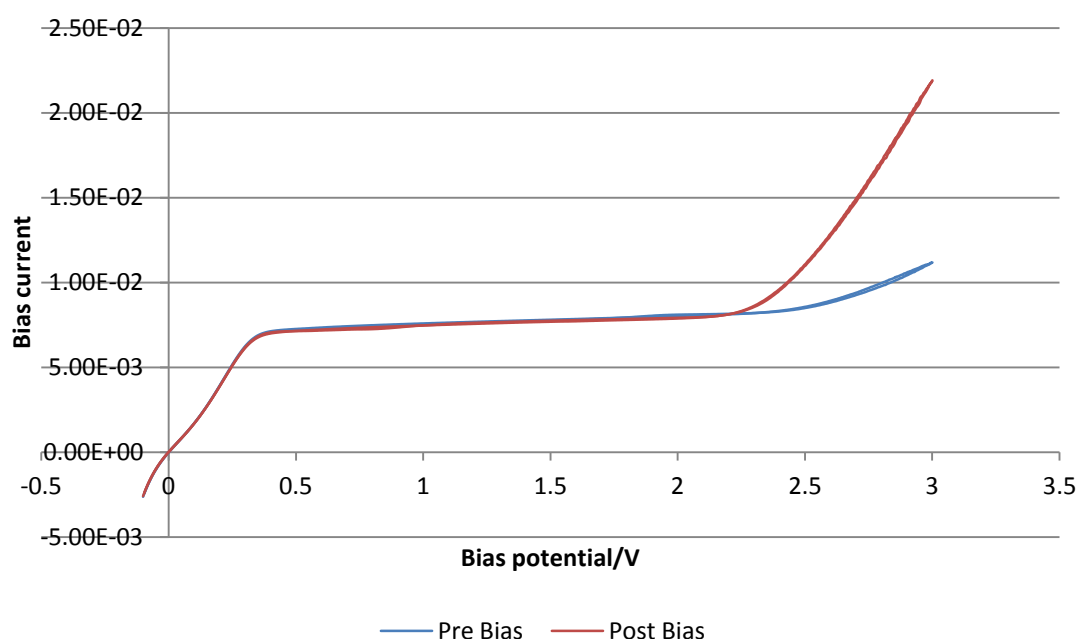


Figure 4.22. Comparison of DCCs of a gold composite anode in 0.5 M H_2SO_4 between -0.1 V and 3.0 V, pre and post bias.

Once characterised, the gold composite anode underwent electrodeposition with Pt as detailed in section 2.8.1 and the DCCs and CVs were repeated.

Figure 4.23 shows the comparison of the DCCs obtained in air and in 0.5 M H_2SO_4 prior to the application of bias potential. As expected, higher currents are generated when the anode is in solution compared with in air as more oxidisable species (i.e. OH) is present on the surface of the anode; as a result, more holes are ‘fired’ to the surface in accordance with quantum theory.

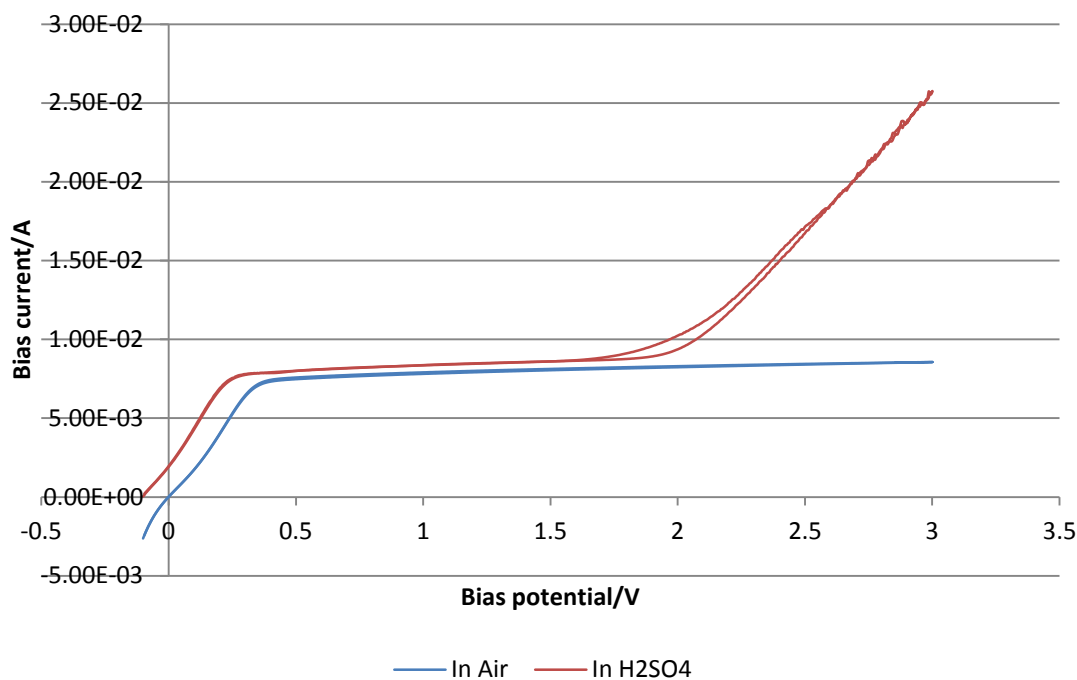


Figure 4.23. Comparison of DCCs of Pt coated gold composite anode in air and in 0.5 M H_2SO_4 between -0.1 V and 3 V (pre bias).

Figure 4.24 shows a comparison of the CVs obtained between -0.25 and 0.85 V vs. SCE at $V_b = 0.0$ V, 0.2 V, 0.5 V and 1.0 V. As with the gold anodes, the “lift off” of the CV becomes evident at $V_b = 1.0$, which is consistent with our theory that surface states are accessed at this bias potential. The hydride region is well defined, suggesting that the solution and the surface of the anode are free from contaminants.

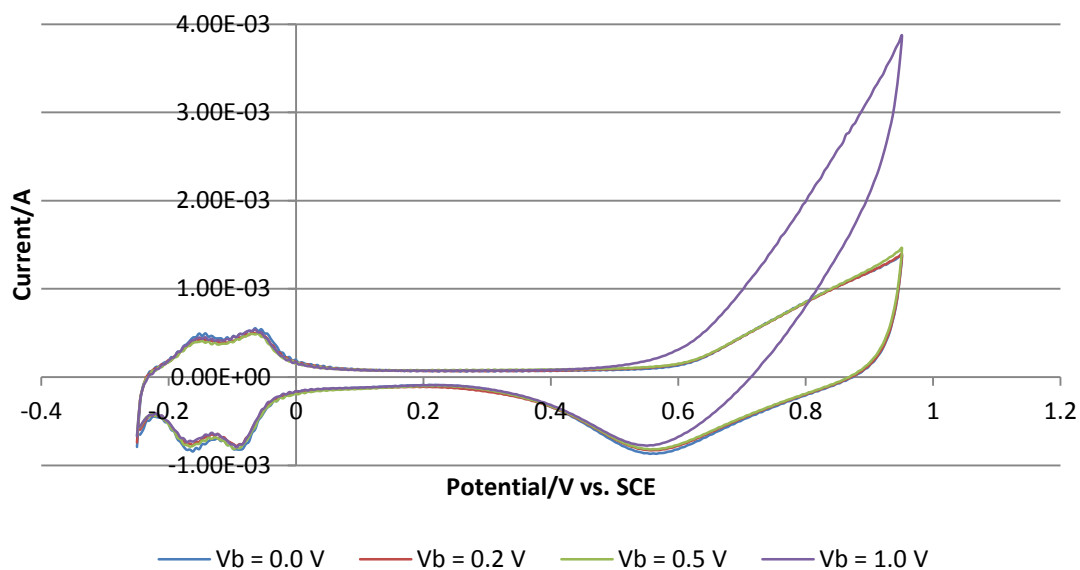


Figure 4.24. Comparison of CVs of a Pt coated gold composite anode in 0.5 M H₂SO₄ between -0.25 V and 0.85 V vs. SCE, scan rate = 100 mV s⁻¹, V_b = 0.0 V, 0.2 V, 0.5 V and 1.0 V.

Figure 4.25. shows a comparison of the CVs obtained at V_b = 0 before and after the application of bias potential. As with fig. 4.21, the CVs are virtually identical before and after the application of bias, confirming that the anode is stable.

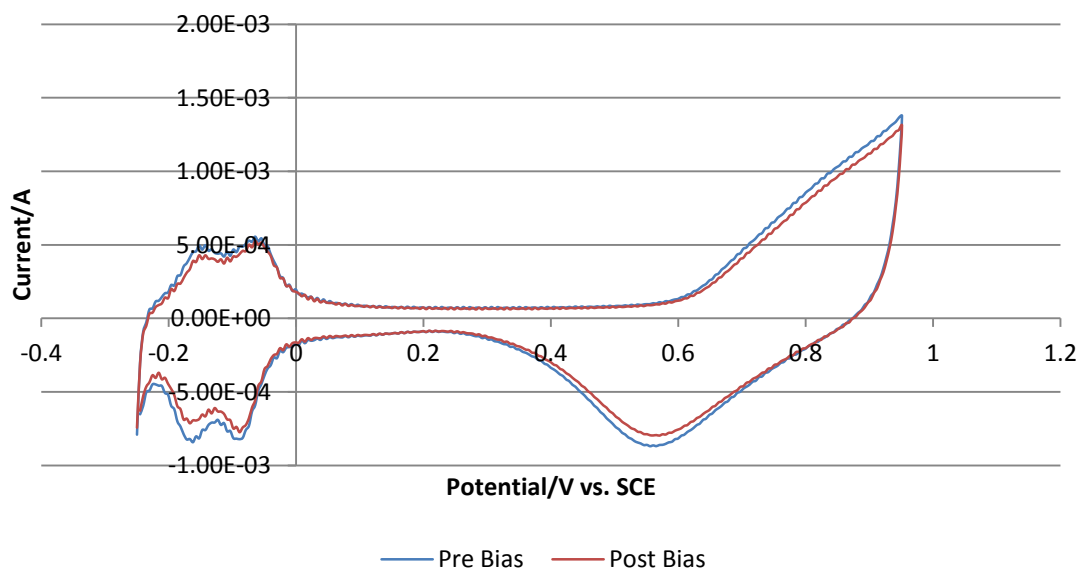


Figure 4.25. Comparison of CVs of a Pt coated gold composite anode in 0.5 M H₂SO₄ between -0.25 V and 0.85 V vs. SCE, scan rate = 100 mV s⁻¹, V_b = 0.0 V, pre and post bias.

Figure 4.26 shows a comparison of the DCCs obtained before and after the application of bias. As with the gold anode prior to electrodeposition, an increase in current is seen at 3 V in the DCC after the application of bias, suggesting that the anode has become ‘activated’ by the application of bias; however, the effect is less pronounced (8.9 mA), possibly due to the increased resistivity of the Pt.

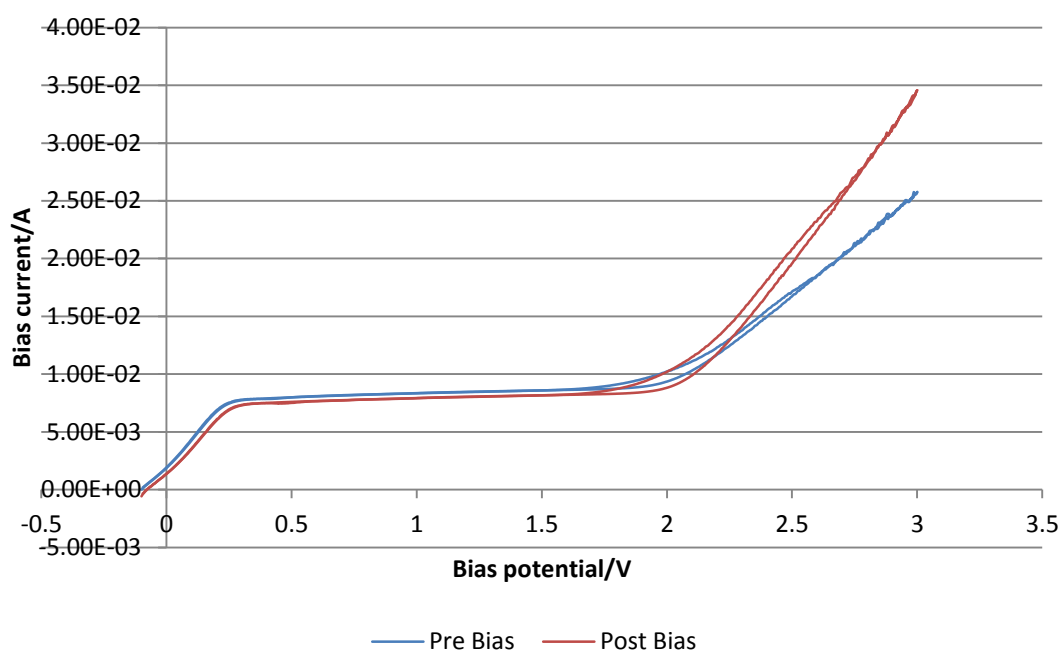


Figure 4.26. Comparison of DCCs of a Pt coated gold composite anode in 0.5 M H_2SO_4 between -0.1 V and 3 V, pre and post bias.

The Pt coated gold composite anode displayed good electrochemical behaviour and high currents when characterised *vs.* SCE. However, in order to use this anode to perform ECF, anhydrous conditions must be employed, necessitating the use for an alternative reference electrode (such as a Pt quasi reference electrode) in place of the SCE. In order to find the potential limits of the CV *vs.* Pt quasi RE, the experiment was first performed using a Pt wire in place of the composite anode.

Figure 2.47 shows the CV obtained from Pt wire in 0.5 M H_2SO_4 . This CV was obtained to establish the anodic and cathodic potential limits for Pt *vs.* Pt (quasi). Interestingly, the limit separation (1.2 V) is different to that observed *vs.* SCE (1.05 V).

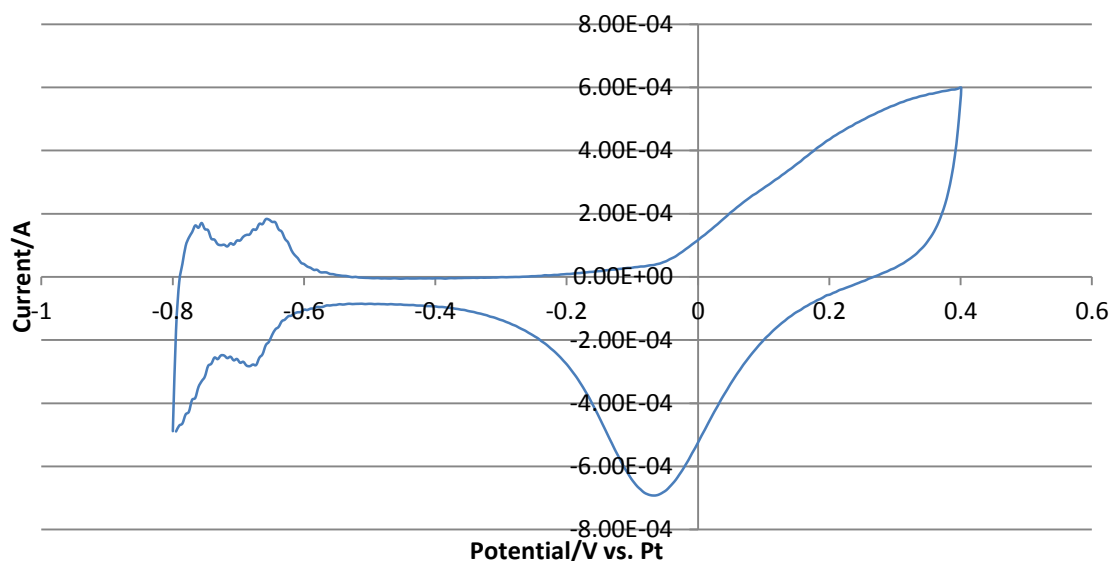


Figure 4.27. CV of Pt wire in 0.5 M H_2SO_4 between -0.80 V and 0.40 V vs. Pt (quasi reference electrode), scan rate = 100 mV s^{-1}

Once the limits were determined using the Pt wire, these were applied to the CV of the Pt coated gold anode vs. the Pt quasi RE. Figure 4.28 shows a comparison of the CVs obtained between -0.80 and 0.40 V vs. Pt (quasi) at $V_b = 0.0 \text{ V}$, 0.2 V, 0.5 V and 1.0 V. As before, the “lift off” of the CV becomes evident at $V_b = 1.0$.

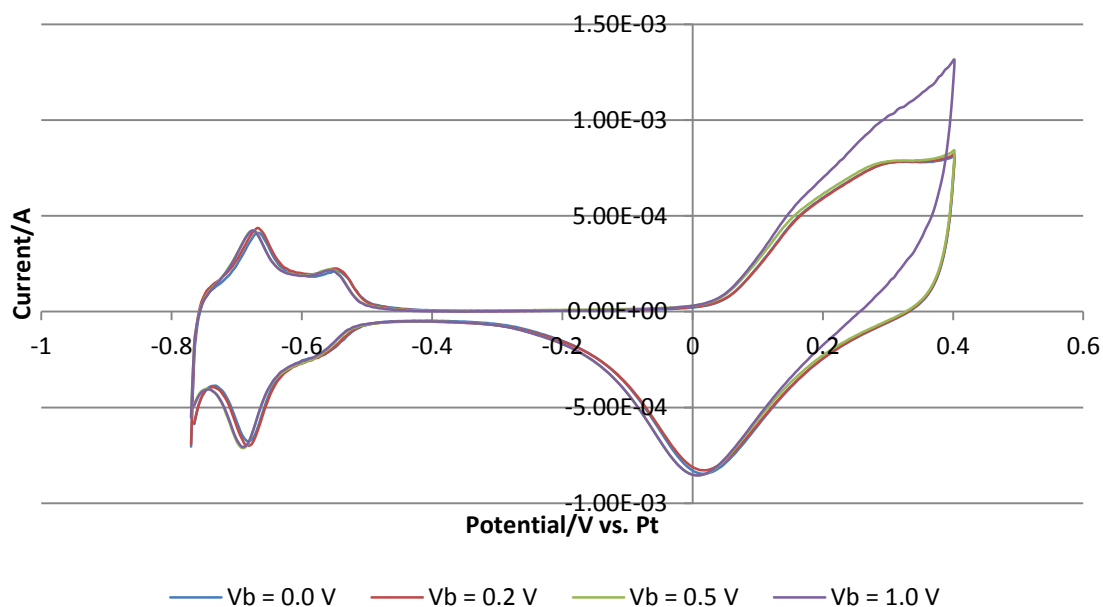


Figure 4.28. Comparison of CVs of a Pt coated gold composite anode in 0.5 M H_2SO_4 between -0.8 V and 0.4 V vs. Pt (quasi), scan rate = 100 mV s^{-1} , $V_b = 0.0 \text{ V}$, 0.2 V, 0.5 V and 1.0 V

Figure 4.29 shows a comparison of the CVs obtained at $V_b = 0$ before and after the application of bias potential. As expected the system displays complete reversibility.

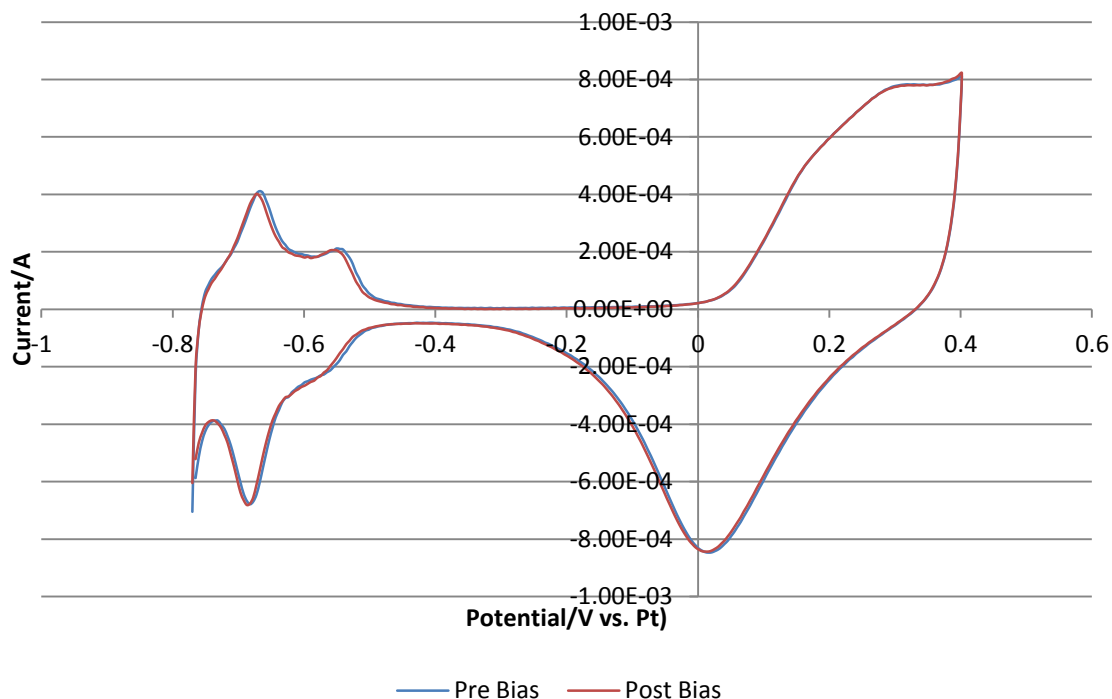


Figure 4.29. Comparison of CVs of a Pt coated gold composite anode in 0.5 M H_2SO_4 between -0.8 V and 0.4 V vs. Pt (quasi), scan rate = 100 mV s⁻¹, $V_b = 0.0$ V, pre and post bias

4.4.6. Effect of concentration and electrolyte.

Typically, the composite anodes have been characterised using 0.5 M H_2SO_4 as the electrolyte. In order to better understand the electrochemistry of the anodes, a study was performed to investigate the relationship between electrolyte type, electrolyte concentration and current. The starting point for this study was to determine the effects of different concentrations of H_2SO_4 on the DCC of the device.

Figure 4.30 shows the comparison of the DCCs obtained in air both before and after exposure to H_2SO_4 . Interestingly, higher currents are observed prior to exposure to the acid.

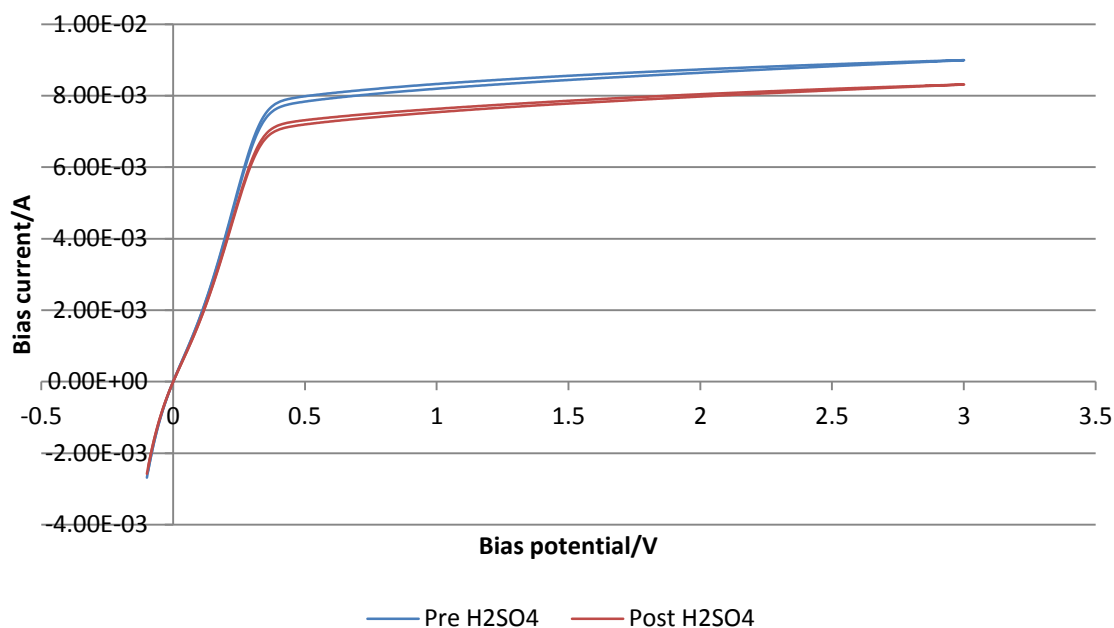


Figure 4.30. Comparison of DCCs of a Pt coated gold composite anode in air, pre and post H_2SO_4 , between -0.1 V and 3 V, scan rate = 100 $mV s^{-1}$

Figure 4.31 shows a comparison of the DCCs obtained in water and various concentrations of H_2SO_4 . In water, no “lift-off” occurs, suggesting that it is the ionic nature of the acidic solution which is causing this phenomenon. The degree of “lift-off” and the current achieved at 3 V increases clearly as a function of concentration, suggesting that the concentration of protons present at the surface of the anode is significant. In contrast to the current, the onset potential of the “lift-off” seems to be unaffected by the concentration. This would suggest that the number of catalytic sites is increasing, whilst the activity of the sites remains constant. At higher concentrations, the increase in current is less pronounced, perhaps suggesting that a saturation level is being achieved.

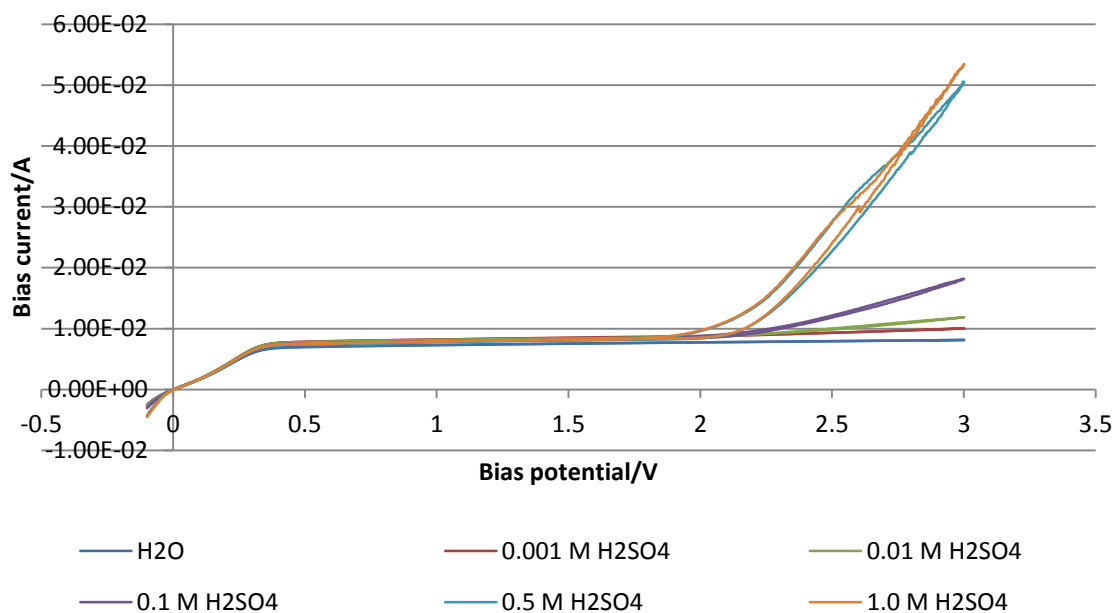


Figure 4.31. Comparison of DCCs of a Pt coated gold composite anode in: H_2O , 0.001 M H_2SO_4 , 0.01 M H_2SO_4 , 0.1 M H_2SO_4 , 0.5 M H_2SO_4 and 1.0 M H_2SO_4 between -0.1 V and 3 V, scan rate = 100 mV s^{-1}

There appears to be a clear relationship between electrolyte concentration and current. In order to determine how the behaviour differs with respect to the counter ions, the experiments were repeated using $HClO_4$.

Figure 4.32 shows the comparison of the DCCs obtained in air both before and after exposure to H_2SO_4 . As with the H_2SO_4 , higher currents are observed prior to exposure to the acid.

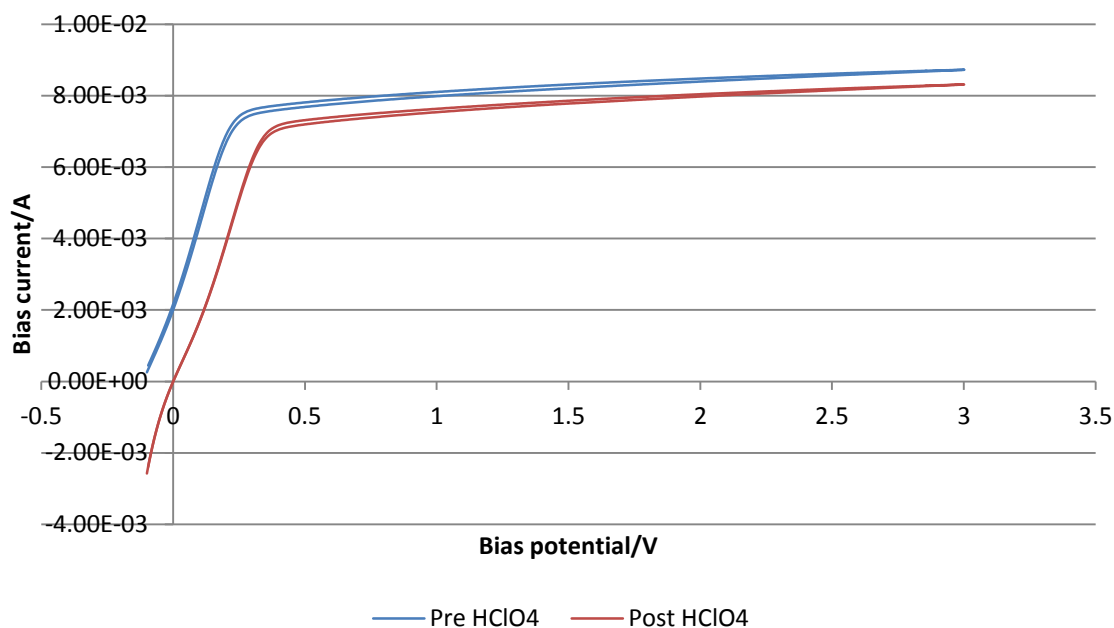


Figure 4.32. Comparison of DCCs of a Pt coated gold composite anode in air, pre and post HClO_4 , between -0.1 V and 3 V , scan rate = 100 mV s^{-1} .

Figure 4.33 shows a comparison of the DCCs obtained in water and various concentrations of HClO_4 . The trend observed is almost exactly the same as with H_2SO_4 , except the currents obtained are slightly lower, which may be an effect of the counter ion.

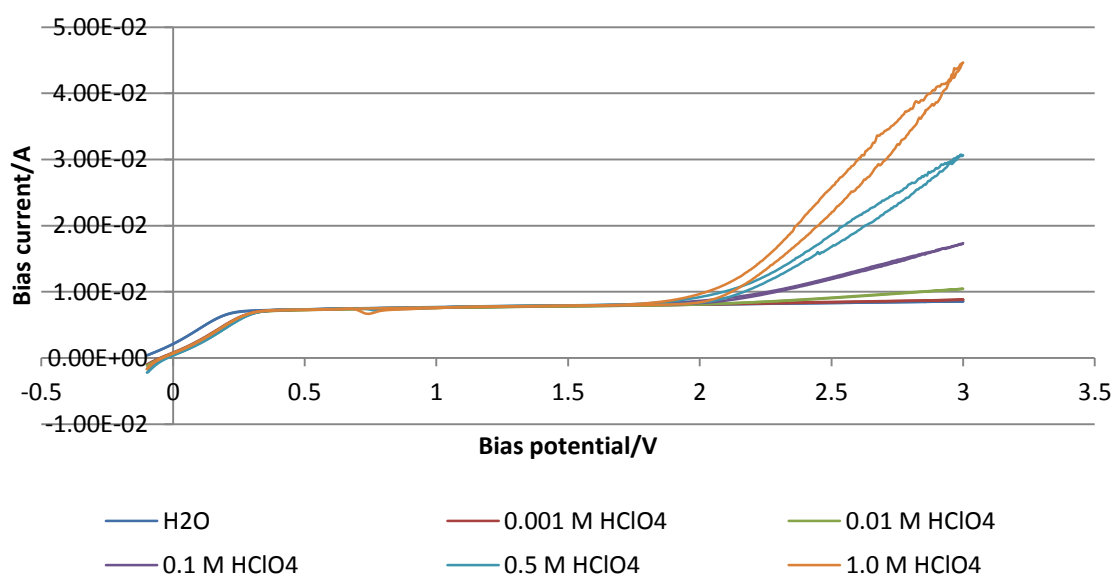


Figure 4.33. Comparison of DCCs of a Pt coated gold composite anode in: H_2O , 0.001 M HClO_4 , 0.01 M HClO_4 , 0.1 M HClO_4 , 0.5 M HClO_4 and 1.0 M HClO_4 between -0.1 V and 3 V , scan rate = 100 mV s^{-1}

Comparing the DCCs of the Pt coated gold composite anode in air prior to submersion in H_2SO_4 and HClO_4 respectively (fig. 4.34), it is clear that the currents obtained prior to submersion in HClO_4 are lower than the currents observed prior to H_2SO_4 . This may explain why the observed currents in HClO_4 are lower overall.

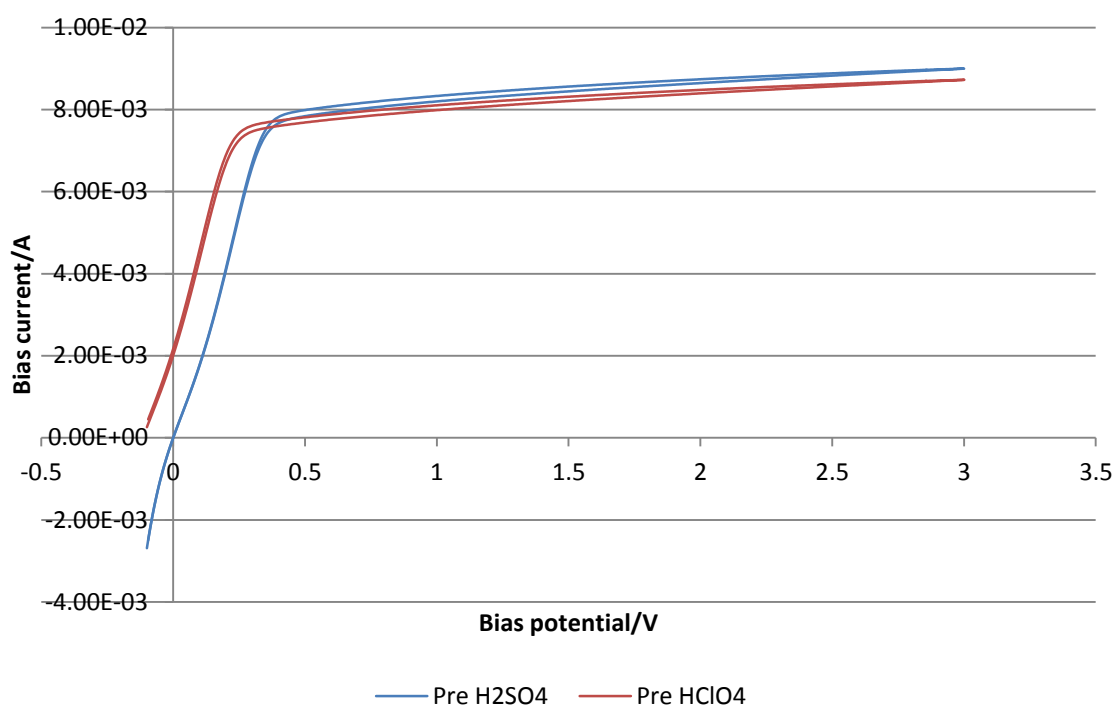


Figure 4.34. Comparison of DCCs of a Pt coated gold composite anode in air (pre H_2SO_4 and HClO_4), between -0.1 V and 3 V, scan rate = 100 mV s^{-1} .

The data reported above show that the extent of “lift-off” and the current achieved at 3 V varied as a function of proton concentration. To determine if this phenomenon was unique to acidic systems, it was decided to again repeat the experiments using hydroxide in place of acid.

Figure 4.35 shows the comparison of the DCCs obtained in air both before and after exposure to NaOH . Interestingly, higher currents are observed prior to exposure to base. This mimics the trend observed with acid, and suggests that, in each case, there are some irreversible effects with respect to the surface and/or activity of the anode.

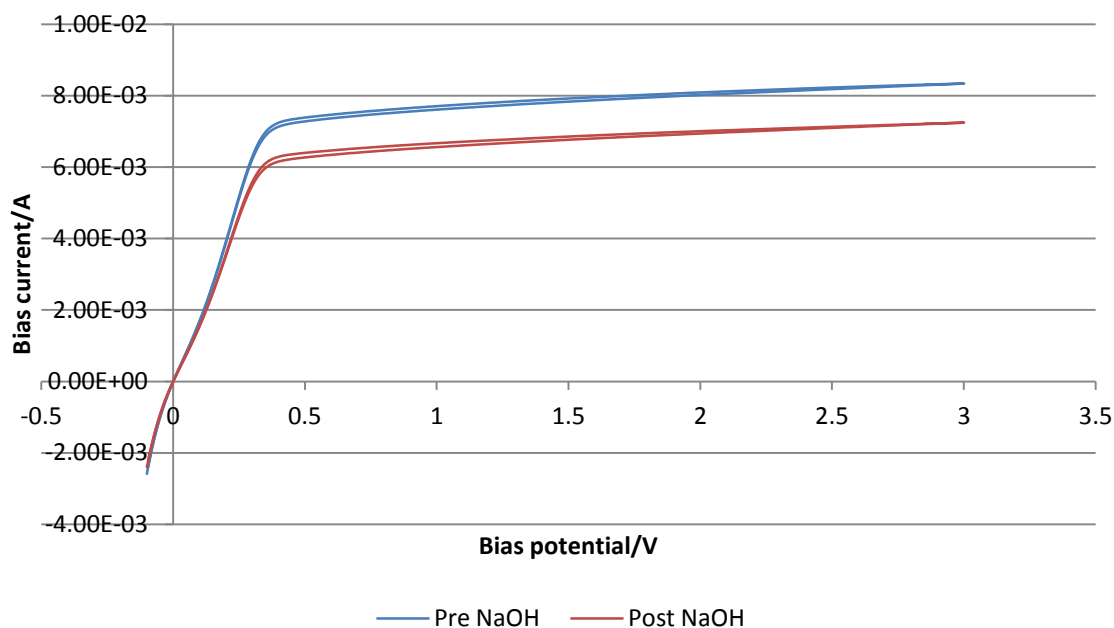


Figure 4.35. Comparison of DCCs of a Pt coated gold composite anode in air, pre and post NaOH, between -0.1 V and 3 V, scan rate = 100 mV s^{-1}

Figure 4.36 shows a comparison of the DCCs obtained in water and various concentrations of NaOH. The trend observed is identical to that observed in acidic media, suggesting that the currents achieved are dependent on the concentration of oxidisable species present at the surface of the anode, not protons.

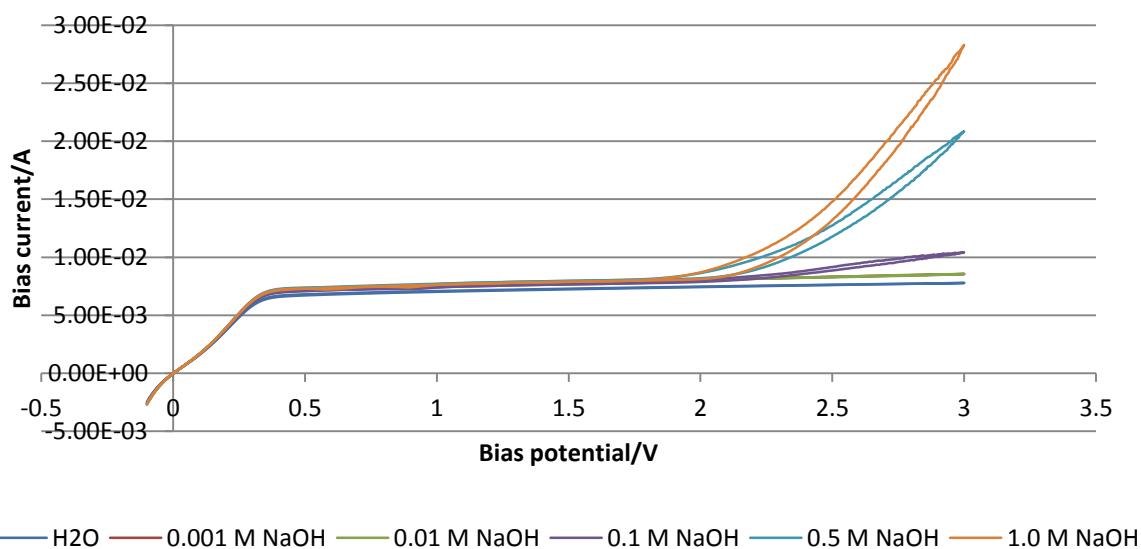


Figure 4.36. Comparison of DCCs of a Pt coated gold composite anode in: H_2O , 0.001 M NaOH, 0.01 M NaOH, 0.1 M NaOH, 0.5 M NaOH and 1.0 M NaOH between -0.1 V and 3 V, scan rate = 100 mV s^{-1}

From table 4.3, it is clear that the onset potential decreases with increasing concentration, until 0.1 M, when the potential appears to reach a steady state and hence becomes fairly constant. This trend was observed regardless of the electrolyte used. The difference in current appears to increase as a function of concentration, again, a trend that is seemingly independent of electrolyte.

Electrolyte Concentration/M	Electrolyte	Onset Potential/V	I at 3V/mA	Difference in I/mA*
0.001	H ₂ SO ₄	2.15	10.0	1.84
	HClO ₄	2.85	8.8	0.23
	NaOH	2.70	8.6	0.82
0.01	H ₂ SO ₄	1.95	11.9	3.74
	HClO ₄	1.90	10.5	1.93
	NaOH	2.70	8.5	0.72
0.1	H ₂ SO ₄	1.80	18.2	10.04
	HClO ₄	1.80	17.3	8.73
	NaOH	1.85	10.4	2.62
0.5	H ₂ SO ₄	1.85	50.5	42.34
	HClO ₄	1.78	30.6	22.03
	NaOH	1.85	20.9	13.12
1.0	H ₂ SO ₄	1.85	53.4	45.24
	HClO ₄	1.78	44.7	36.13
	NaOH	1.80	28.3	20.52

*Difference calculated by subtracting the current at 3 V at each concentration from the current at 3 V in water (I at 3V in H₂O = 8.16 mA (H₂SO₄ set), 8.57 mA (HClO₄), 7.78 mA (NaOH))

Table 4.3. Comparison of effect of concentration on DCCs in acidic and basic media

4.4.7. Irreversibility study

In order to determine if the smaller currents obtained when the DCCs were performed in HClO₄ and NaOH were due to irreversible effects, DCCs were repeated in 1.0 M H₂SO₄, 1.0 M HClO₄ and 1.0 M NaOH using the Pt coated gold composite anode and the maximum currents compared with the original currents achieved.

Figure 4.37 shows the DCCs obtained in air before and after the anode was exposed to the solutions. The currents achieved after exposure are lower than those obtained beforehand, suggesting that there are some irreversible effects caused by exposure to the solutions.

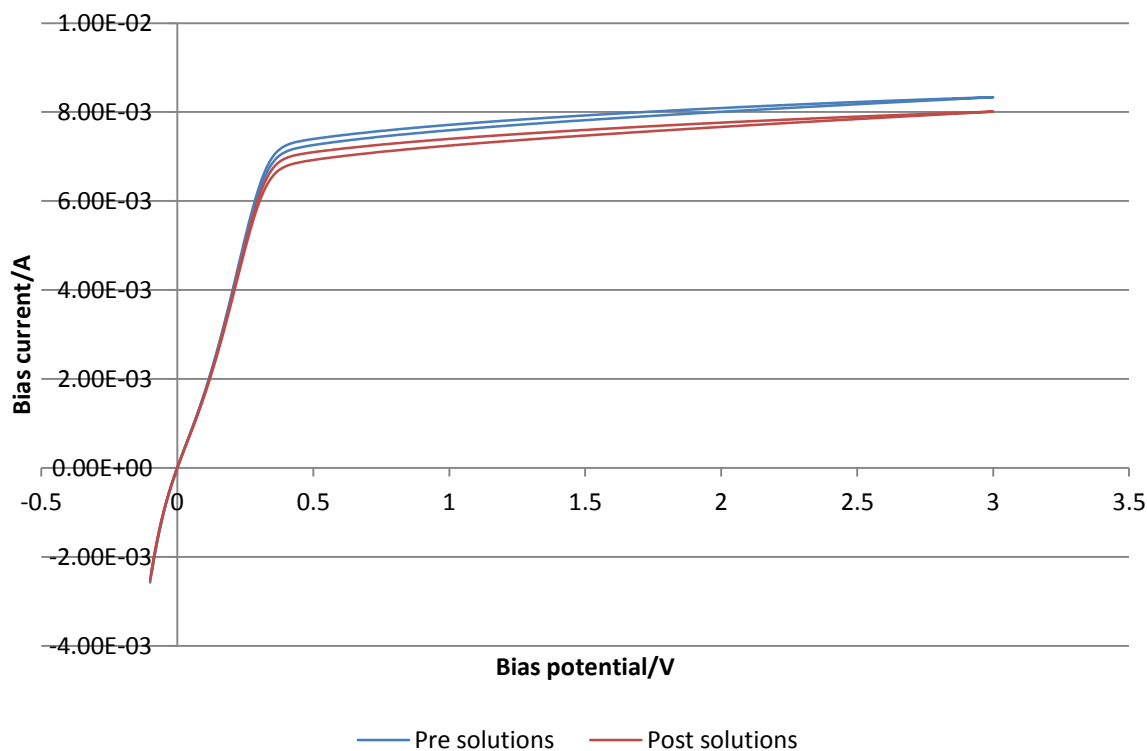


Figure 4.37. Comparison of DCCs of a Pt coated gold composite anode in air, pre and post solutions, between -0.1 V and 3 V, scan rate = 100 mV s^{-1}

Figure 4.38 shows the comparison of the water runs between each solution run. This shows how the current is changing over time in the same medium, directly after exposure to each solution. The currents obtained are reduced clearly after exposure to each solution, suggesting irreversible effects.

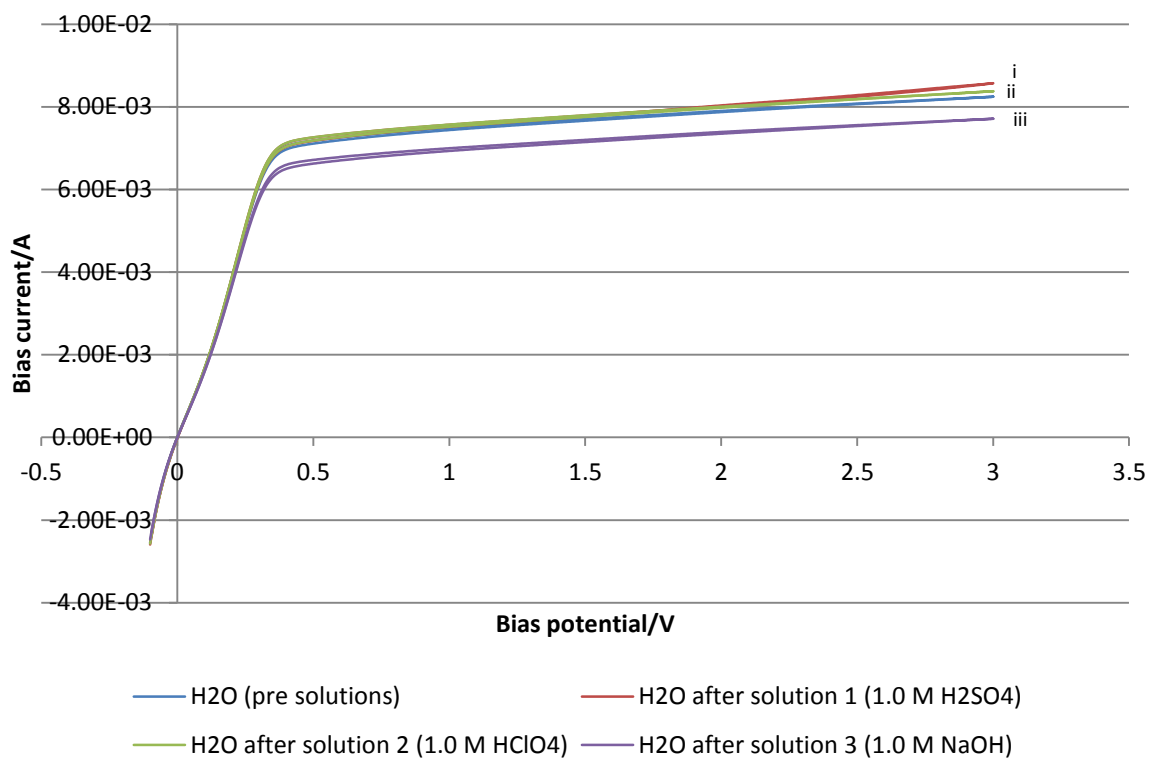


Figure 4.38. Comparison of DCCs of a Pt coated gold composite anode in H_2O , before and after each solution, between -0.1 V and 3 V, scan rate = 100 $mV s^{-1}$ in run order (i, ii and iii)

Figure 4.39 shows the comparison of the DCCs obtained in each solution. Again, there is a clear trend showing reduced currents with increased exposure to solution, suggesting irreversible effects.

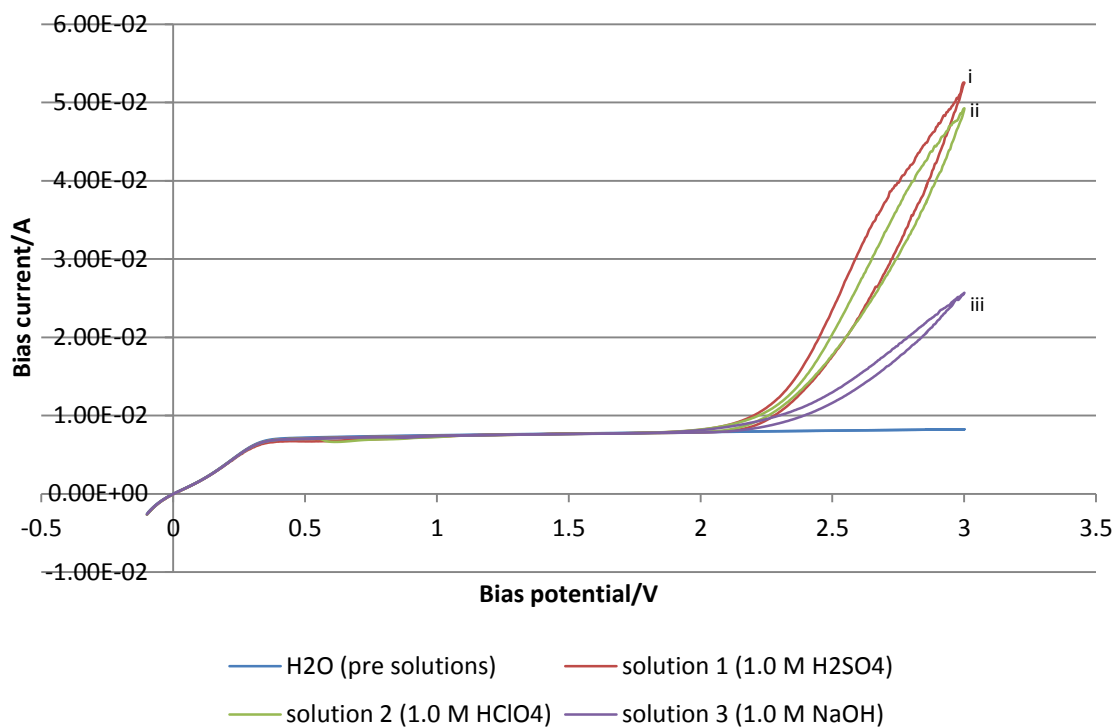


Figure 4.39. Comparison of DCCs of a Pt coated gold composite anode in: H_2O , 1.0 M H_2SO_4 , 1.0 M $HClO_4$ and 1.0 M $NaOH$, between -0.1 V and 3 V, scan rate = 100 mV s^{-1} in run order (i, ii and iii).

4.4.8. Anhydrous characterisation of composite anodes

Typically, the composite anodes are characterised using aqueous media; however, as discussed earlier, electrofluorination must be performed under anhydrous conditions. The Pt deposited has been fully characterised using aqueous electrochemistry and the limits for the Pt quasi reference electrode have been defined. The anode was therefore characterised under anhydrous conditions, using a glove box, in the fluorinating electrolyte, $Et_4NF \cdot 4HF$.

Figure 4.40 shows a comparison of the DCCs obtained in air both outside and inside the glove box. Interestingly, a higher current is obtained when the anode is inside the glove box.

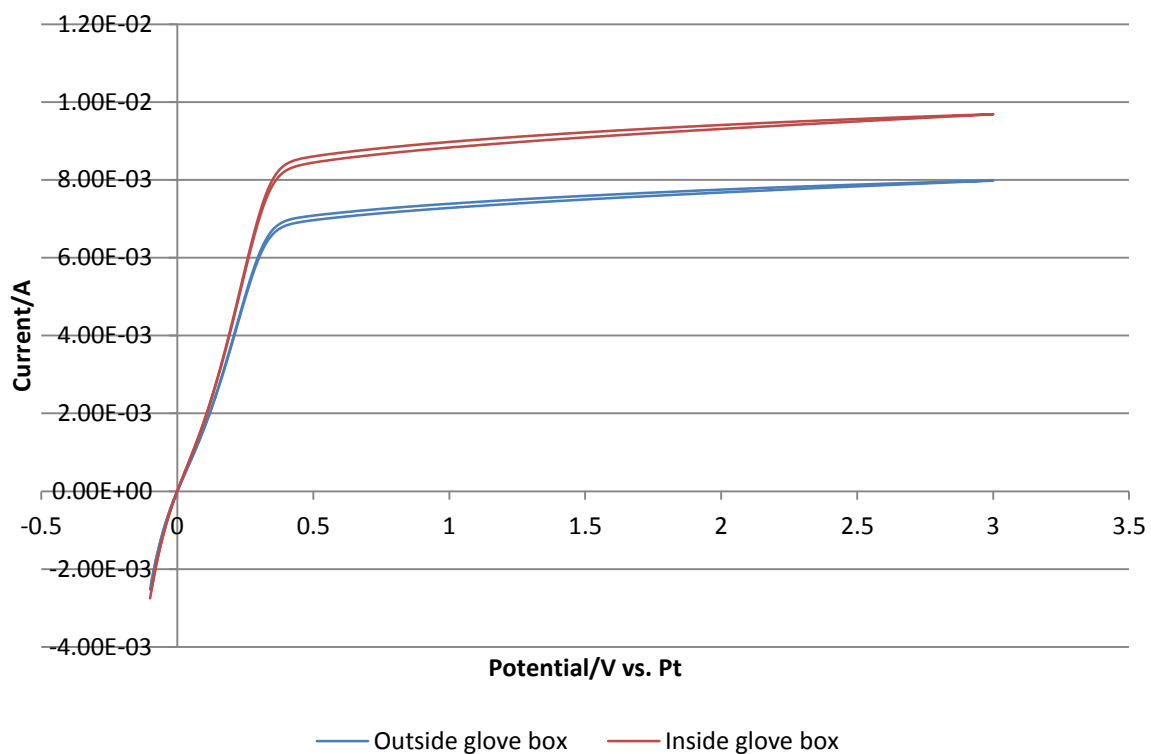


Figure 4.40. Comparison of DCCs of a Pt coated gold composite anode in air, outside and inside the glove box, between -0.1 V and 3 V, scan rate = 100 mV s^{-1}

Figure 4.41 shows comparison of the DCCs of the platinised gold composite anode in air and $\text{Et}_4\text{NF}\cdot 4\text{HF}$. Interestingly, the “lift off” of the DCC in solution occurs, suggesting that this phenomenon is independent of electrolyte.

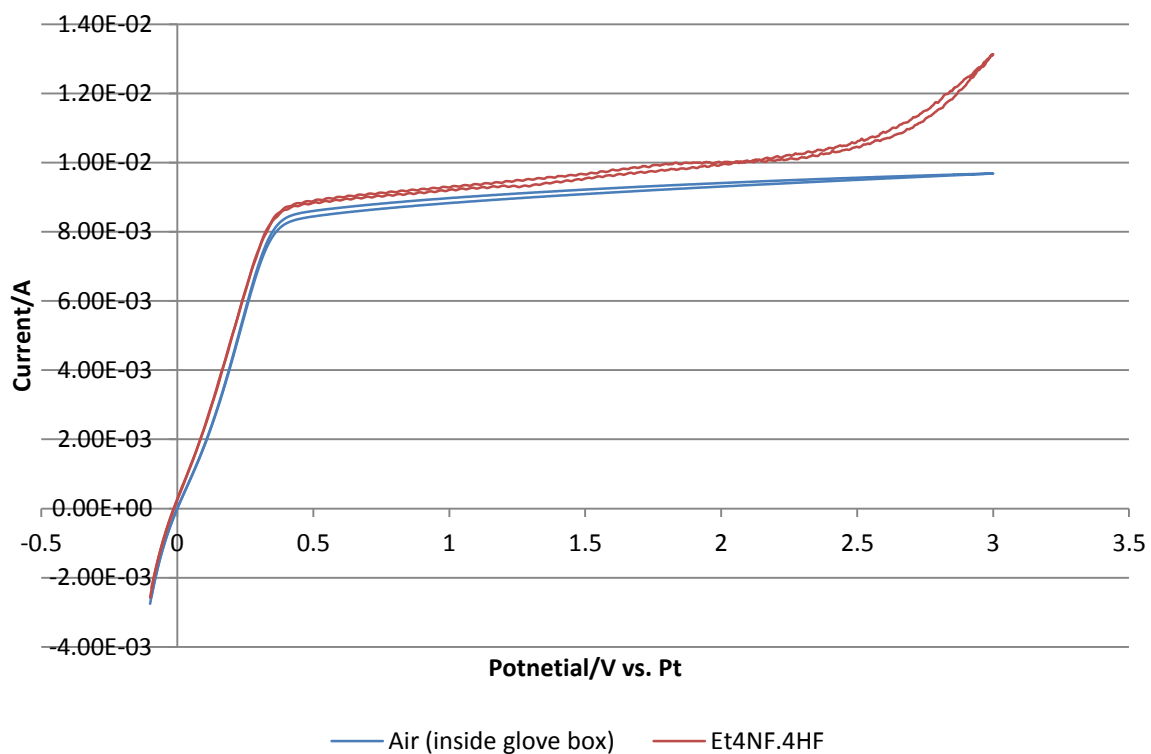


Figure 4.41. Comparison of DCCs of a Pt coated gold composite anode in air (inside glove box) and $\text{Et}_4\text{NF.4HF}$, between -0.1 V and 3 V, scan rate = 100 mV s^{-1}

Figure 4.42 shows the comparison of CV scans 2 and 3 in $\text{Et}_4\text{NF.4HF}$ between -0.2 V and 1.2 V vs. Pt. There is a clear oxidation peak just above 1 V vs. Pt which may be a feature of the Pt. This undefined CV would suggest that the grid is being dissolved.

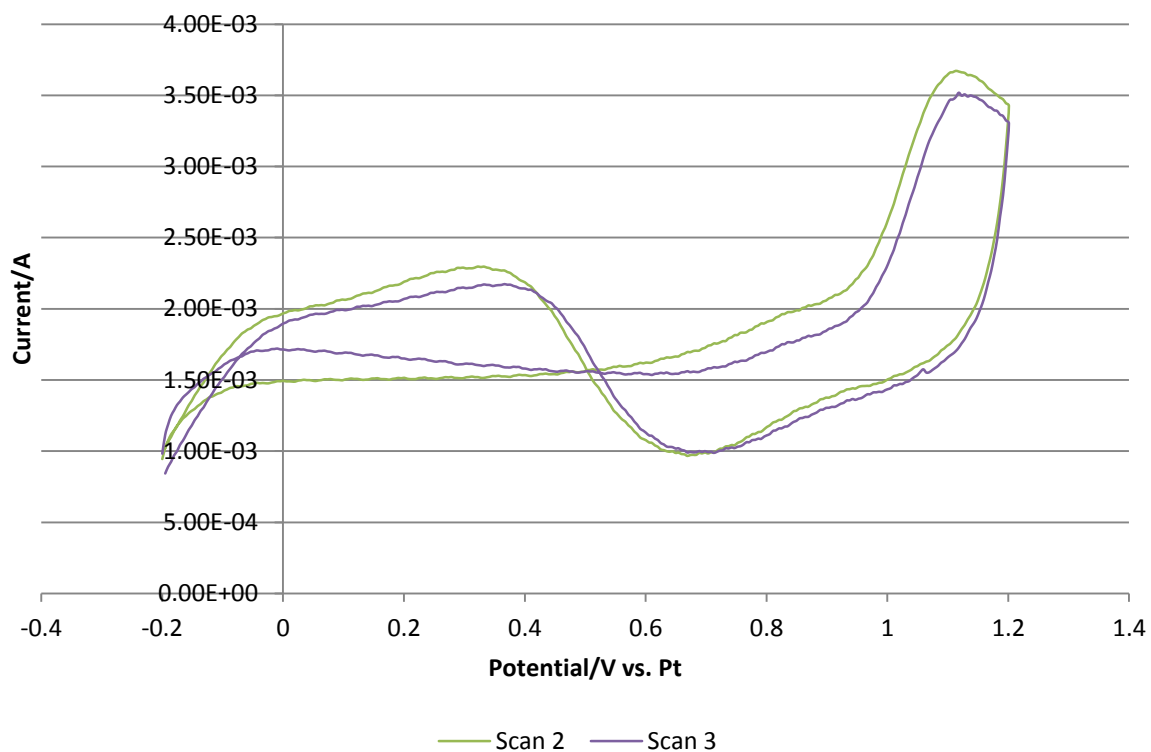


Figure 4.42. Comparison of CVs of a Pt coated gold composite anode in Et₄NF₄HF, between -0.2 V and 1.2 V, scans 2 and 3, scan rate = 100 mV s⁻¹

Figure 4.43 shows a comparison of CV scans 1 to 3 in Et₄NF₄HF between -0.2 and 1.4 V vs. Pt. More features seem to be present at this higher potential.

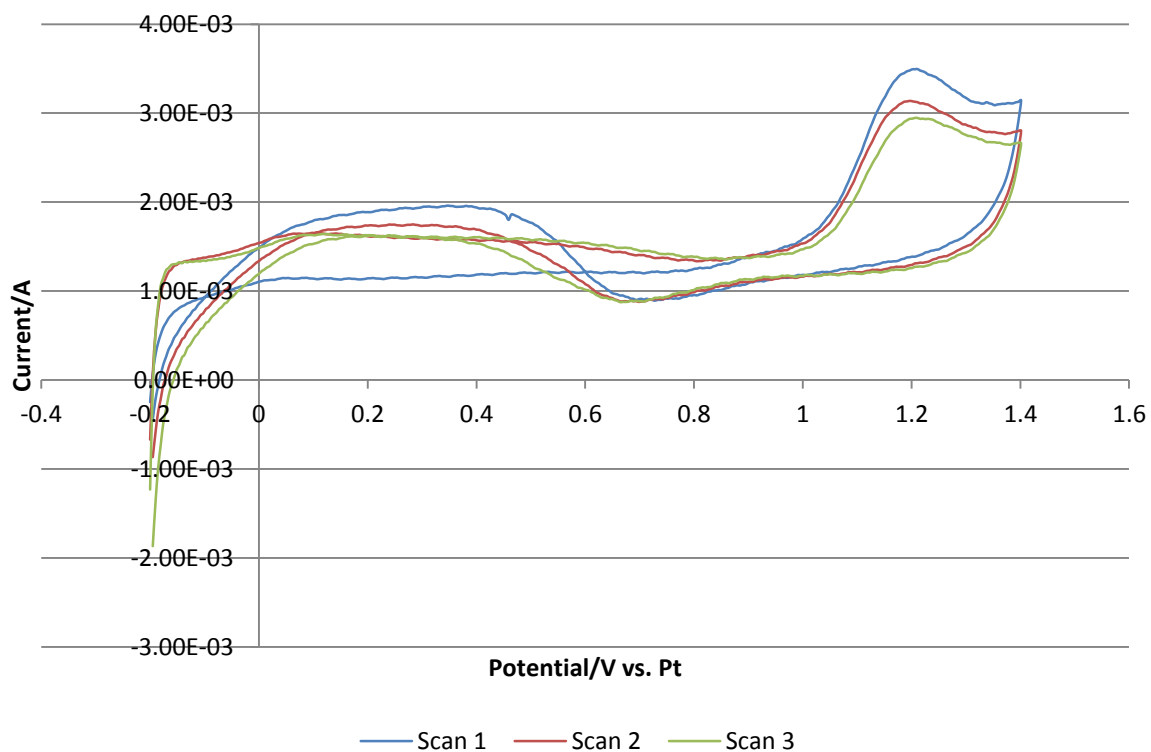


Figure 4.43. Comparison of CVs of a Pt coated gold composite anode in $\text{Et}_4\text{NF}\cdot 4\text{HF}$, between -0.2 V and 1.4 V , scans 1, 2 and 3, scan rate = 100 mV s^{-1}

Figure 4.44 shows a repeat of the comparison of CV scans 1 to 3 in $\text{Et}_4\text{NF}\cdot 4\text{HF}$ between -0.2 V and 1.2 V vs. Pt, after having been at 1.4 V vs. Pt. The CV has clearly changed, possible due to the stripping of the Pt.

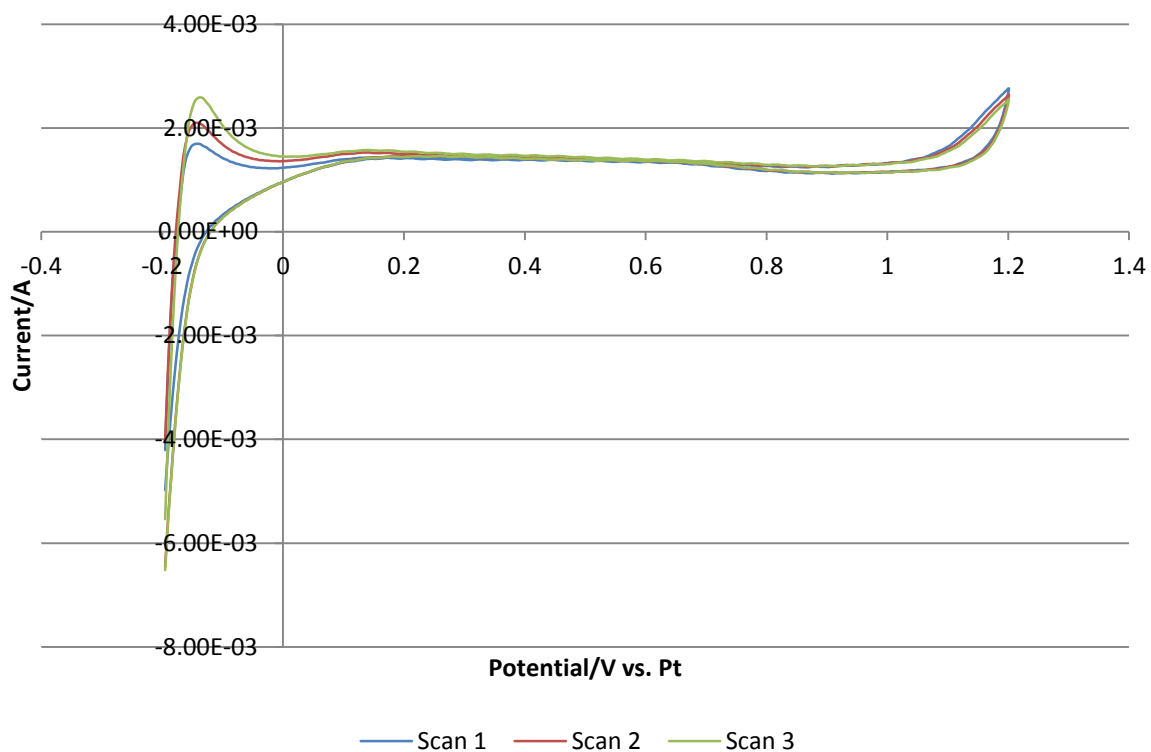


Figure 4.44. Comparison of CVs of a Pt coated gold composite anode in $\text{Et}_4\text{NF} \cdot 4\text{HF}$, between -0.2 V and 1.2 V vs. Pt (after 1.4 V vs. Pt), scans 1, 2 and 3, scan rate = 100 mV s^{-1}

After these CVs were obtained, the grid lifted completely away from the TiO_2 and the anode was destroyed. The destruction of the anode was thought to be due to chemical attack of fluoride at the edges of the metal grid. SEM data has shown there to be imperfections at the edges of the grid (fig. 4.45); the presence of these imperfections is thought to accelerate the stripping process.

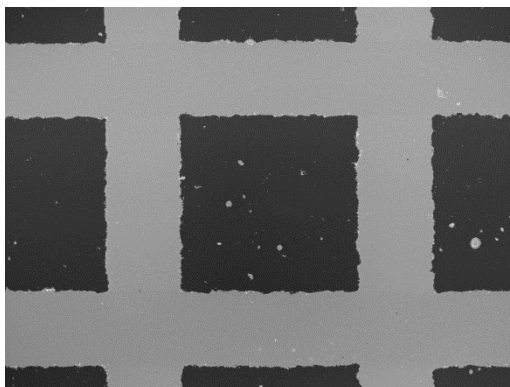
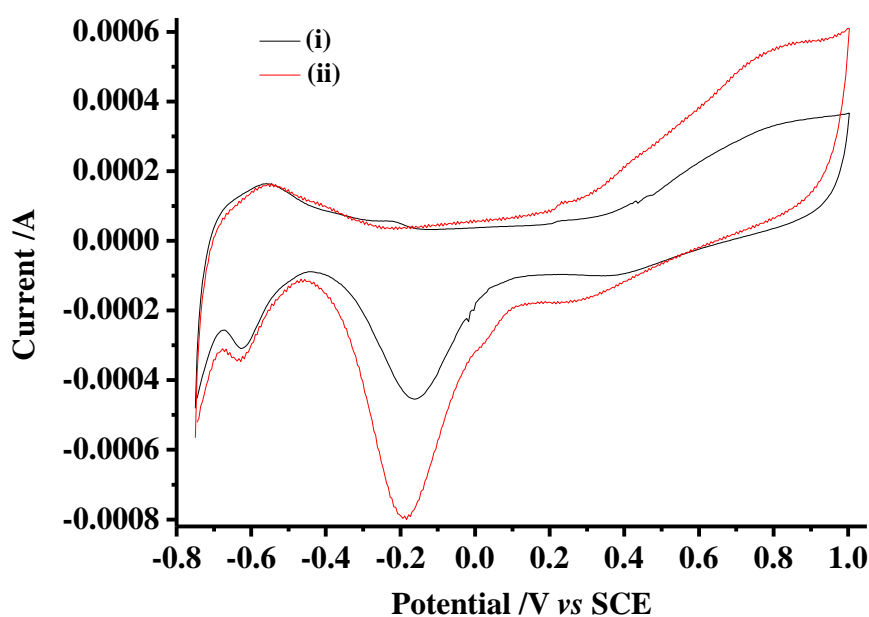


Figure 4.45. SEM showing imperfections at the edges of the Pt grid.

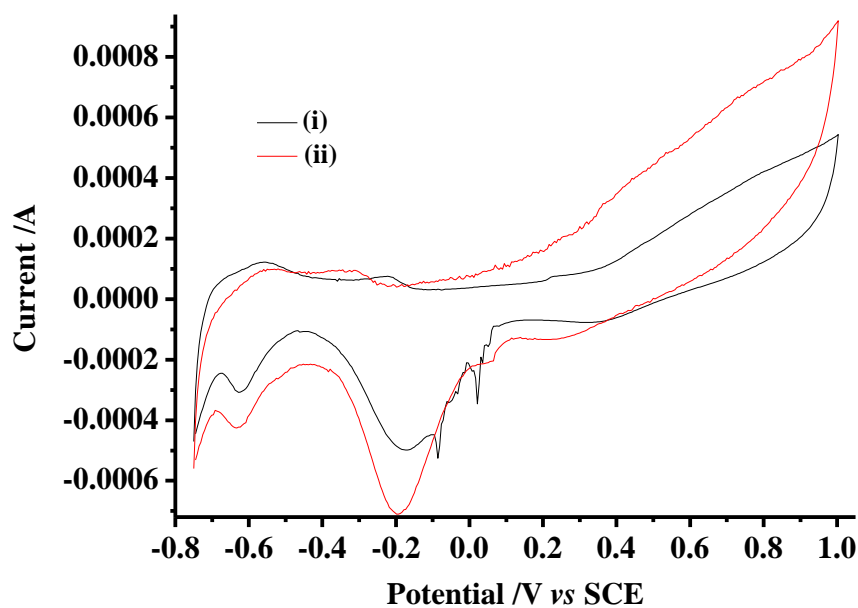
4.4.9. Initial studies on the oxidation of fluoride

As a first step in determining if the composite electrode could be employed in electrofluorination it was decided to investigate the electrochemical response of a Si/TiO₂/Pt electrode in alkaline solution (pH 9.7) in the presence of F⁻. Pt was chosen rather than gold due to the instability of the latter metal to dissolution at anodic potentials in halide-containing electrolytes.¹²¹⁻¹²² The alkaline pH was chosen to stabilize any OF⁻ (hypofluorite) that may be formed from the oxidation of F⁻, as OF⁻ is the reactive species which is essential in these types of electrophilic fluorination reactions.^{8, 123}

Figures 4.46(a) & (b) show cyclic voltammograms of the Si/TiO₂/Pt composite anode immersed in pH 9.7 0.1 M Na₂SO₄/NaOH in the absence and presence of 0.1 M KF (a) at V_b = 0V and (b) at V_b = 1.0V.



(a)

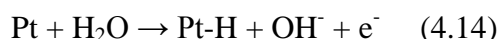


(b)

Figure 4.46 Cyclic voltammograms of the (Au)Si/TiO₂/Pt composite anode (Pt grid area ca. 2 cm²) immersed in pH 9.7 NaOH/0.1 M Na₂SO₄ in the (i) absence and (ii) presence of 0.1 M KF at, (a) $V_b = 0$ V and (b) $V_b = 1.0$ V. scan rate 100 mVs⁻¹.

The presence of KF appears to enhance the formation (and subsequent stripping) of the Pt oxide and, at $V_b > 0$, of the formation of oxygen (irreversible anodic current with onset near 0.95 V in figs. 4.46(a) & (b)) due to the holes at the TiO₂/Pt interface – the latter causing the enhanced cathodic currents at $E < 0.4$ V. This may be due to the displacement of strongly adsorbing sulphate and bisulfate ions from the Pt, and/or the TiO₂, the latter facilitating hole transfer to Pt.

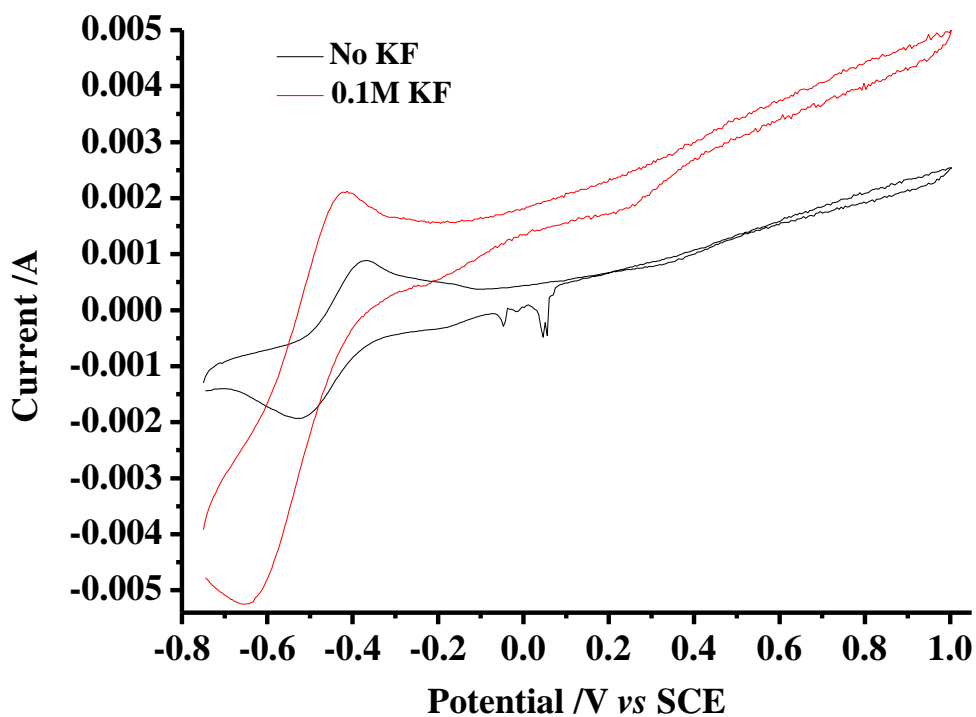
A single, well-defined reduction peak near -0.6 V corresponding (presumably) to:



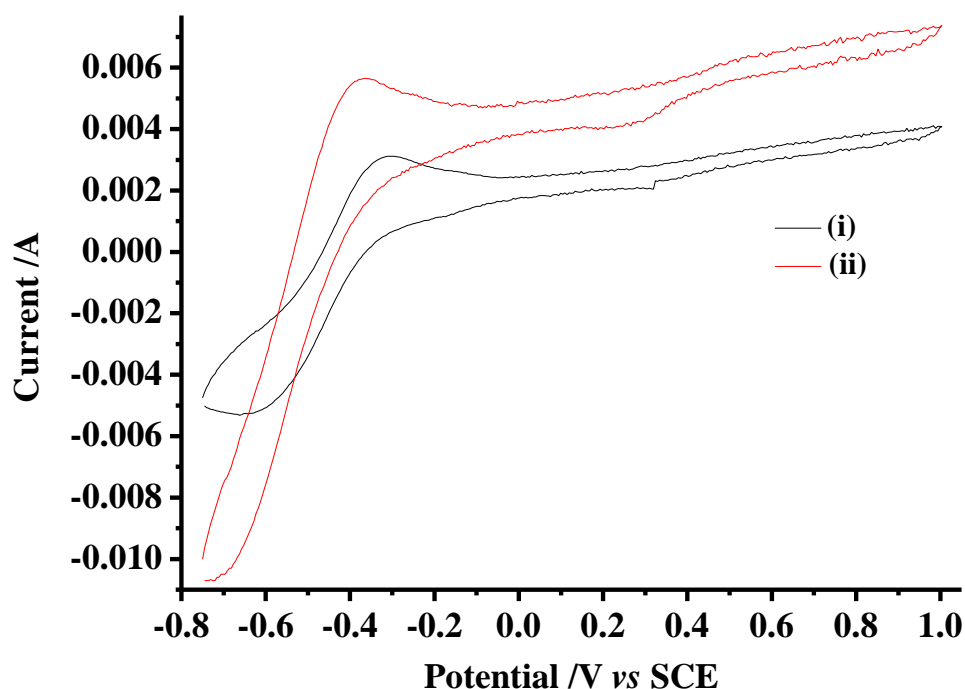
may also be observed in figs. 4.46(a) & (b). However, there is no corresponding wave due to the reverse reaction in the anodic sweep; this maybe due to the fact that the reverse process is slow, possibly due to ‘spill-over’ of the hydride into the TiO₂ lattice,¹²⁴⁻¹²⁵ and hence the feature is broadened over a range of potentials. Reduction of

water/ H^+ is known to occur at negative potentials at TiO_2 with the insertion of atomic hydrogen into the TiO_2 lattice.¹²⁶

There is a major change in the voltammetry between $V_b = 1$ V and $V_b = 2$ V, see figs. 4.46(a) and 4.47(a), with the appearance of a reversible or quasi-reversible wave centred near -0.45 V.



(a)



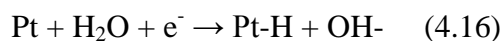
(b)

Figure 4.47. Cyclic voltammograms of the (Au)Si/TiO₂/Pt electrode in figs. 4.19(a) & (b) in the (i) absence and (ii) presence of 0.1 M KF at, (a) $V_b = 2$ V and (b) $V_b = 3$ V. scan rate 100mVs^{-1} .

The cathodic wave of this feature corresponds in potential to that of the hydride peak discussed above. The quasi-reversible wave may be attributed to the insertion and de-insertion of H into the TiO₂ lattice:¹²⁶



On increasing the bias voltage, see figs. 4.47(a) & (b), the peak currents associated with the insertion wave increase suggesting that the hole current through the TiO₂ is influencing the electrochemical insertion/de-insertion process: coupled with the coincidence in potential of Pt-H formation and atomic hydrogen formation/insertion into the TiO₂, this suggests that hydride formed on the Pt spills over into the TiO₂:



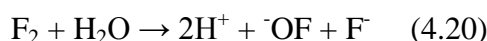
Increasing the bias voltage has no effect upon the TiO_2 until V_b attains values where new channels for the holes are opened up ($> 1 \text{ V}$).¹²⁷ These holes can oxidise H atoms:



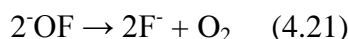
and/or recombine with electrons at/near the grid:



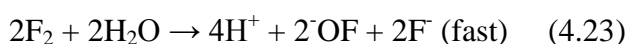
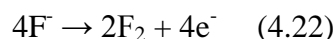
Interestingly, as may be seen from figs. 4.47(a) & (b), as well as the insertion/de-insertion peak currents increasing as V_b increases, the separation of the anodic and cathodic waves increases (which would not be expected for a surface process where diffusion in solution is not important). More importantly, the addition of KF has little effect upon the anodic peak potential of this feature, but causes the cathodic peak to move to more negative potentials, suggesting F^- is selectively slowing the insertion process down. It is also clear from figs. 4.47 (a) & (b) that F^- is significantly enhancing both insertion & de-insertion, but the latter *ca.* 2x the former, and the oxidation current in the anodic sweep. F_2 has the highest E^0 of 2.87 V,¹²⁸ significantly above that of water (1.23 V) and will react rapidly to produce HOF and HF:¹²⁹



HOF is itself unstable and decomposes rapidly to HF and O_2 (in alkaline solution, H_2O_2 in acid):¹²⁹



The enhanced electrochemical currents at $V_b > 1 \text{ V}$ in figs 4.47(a) & (b) may thus be due to enhanced water oxidation catalysed by a F-containing intermediate/surface species:



Overall:



At V_b where the new channels for h^+ transfer to the TiO_2 surface open up, the equilibrium (4.18) is dragged over to the left hand side as inserted H is oxidised, increasing the rates of (4.16) and (4.17), but slowing the insertion process.

At the end of the above experiments, the grid had been completely stripped from the TiO_2 surface, supporting the postulated generation of highly oxidising F-containing species. A blank experiment was performed in the absence of KF, proving that the destruction of the anode was due to the presence of the fluoride species, not the application of high currents.

In order to assess the exact nature and extent of the damage to the anode, scanning electron microscopy (SEM) and energy dispersive X-ray (EDX) analysis was performed.

Figure 4.48 shows an SEM image of the damaged composite anode. It is clear that areas of the Pt grid have flaked away, leaving large areas of damage to the electrode.

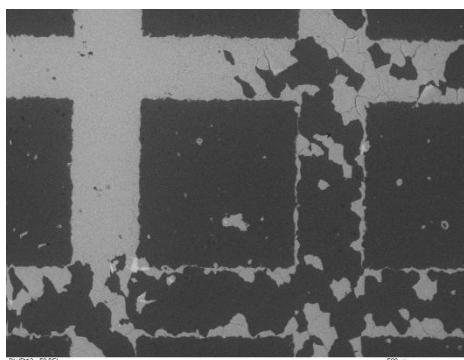
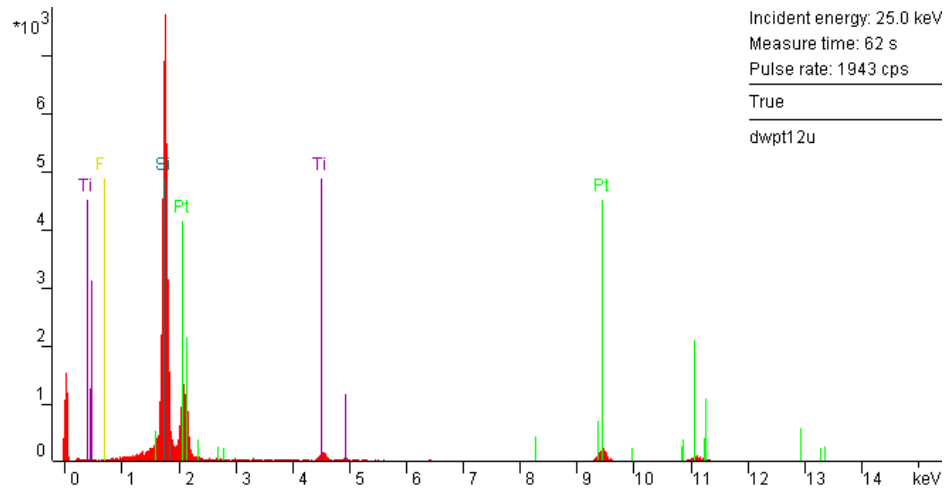


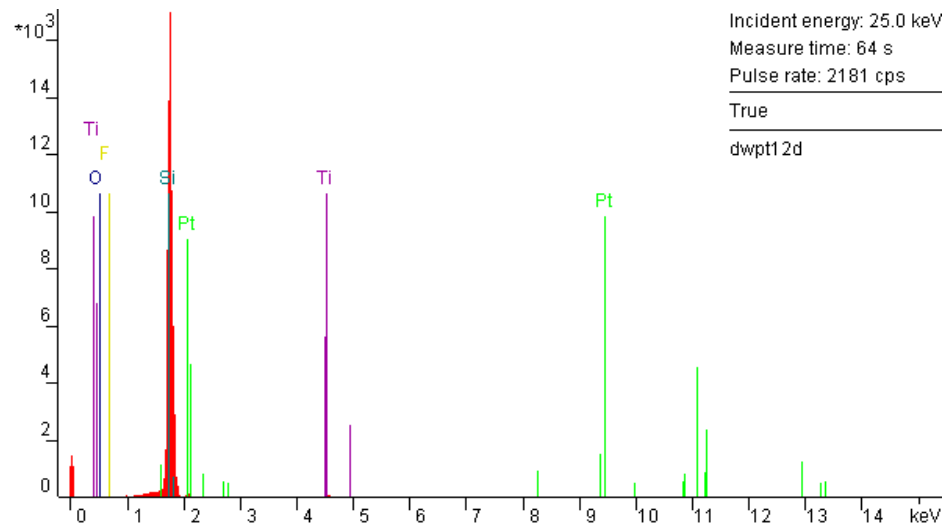
Figure 4.48. SEM image of the damaged composite anode taken at a resolution $\times 50$ using electron back scattering under low vacuum.

Figures 4.49(a) & (b) show EDX analysis of the undamaged and damaged areas of the grid respectively. By comparison of the spectra, it is clear that the undamaged area still contains Pt, Si and TiO_2 , whereas the damaged area shows no Pt. However, both Si and

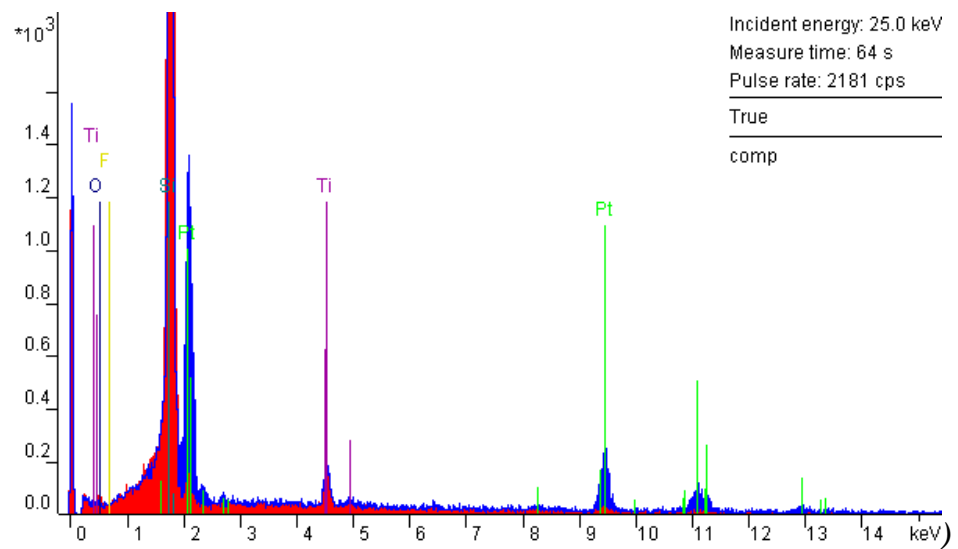
TiO₂ are still present, indicating that there has been no degradation of these components. It is also interesting to note that no fluorine is present in the damaged area, which may suggest that degradation occurred by the formation of stable Pt-F species such as PtF₄, causing “stripping” of the Pt.



(a)



(b)



(c)

Figure 4.49. EDX spectrum of an (a) undamaged and (b) damaged section of the destroyed composite anode. (c) An overlay of figs 4(a) and (b) for direct comparison.

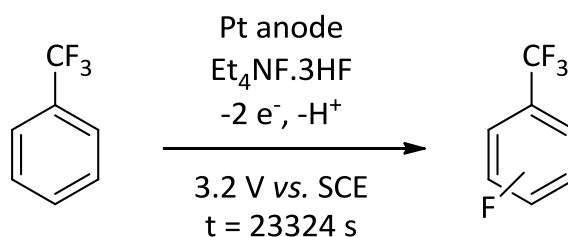
5. Composite ECF of Aromatics

As discussed in chapter 1, the ECF of aromatic substrates such as benzotrifluoride and anisole are well documented in the literature. For this reason, it was decided to use these substrates for initial trials into ECF using the composite anodes. As discussed chapter 4, the molten salt electrolytes used generally in ECF are destructive to the composite anodes; therefore it was decided to attempt the electrolyses using a milder source of fluoride, tetrabutylammonium fluoride (TBAF). This preliminary data presented in this chapter details the first attempts at composite ECF of these substrates.

5.1. Benzotrifluoride

5.1.1. Conventional electrolysis of benzotrifluoride

The ECF of the benzotrifluoride was originally reported by Knunyants *et al.* in 1971.⁴³ The authors reported that electrolysis of benzotrifluoride at a Pt anode with a constant potential of 3.2 V *vs.* SCE produced either mono-fluorinated product selectively or a mixture of both mono and di-fluorinated products, dependant on the amount of theoretical charged passed through the solution. They found that when 80% of the theoretical amount of electricity was passed, 3-fluorobenzotrifluoride was obtained selectively in 60% yield. However, when 170% of the theoretical amount of charge was passed, a mixture of 3-fluorobenzotrifluoride and 3,5-difluorobenzotrifluoride was obtained in yields of 30% and 12% respectively.



Scheme 5.1. Schematic representation of the conventional ECF of benzotrifluoride

The electrolysis was performed using an adaptation of the procedure described by Knunyants *et al.* as detailed in chapter 2 before the isomers were separated by column chromatography and analysed by ¹⁹F NMR. Prior to electrolysis, chronoamperometry was performed for 2 min at 0 V and 2 min at 3.2 V to establish a steady state current. Using the steady state current observed (45 mA), it was possible to calculate the length

of time for which the current should be passed as shown below. The transformation occurring is a 2 electron process (as shown below):



The number of moles of reagent (trifluorotoluene) = 6.8×10^{-3}

Therefore, $(6.8 \times 10^{-3}) \times 2$ (electrons involved in process) = 1.4×10^{-2} moles per e^-

Charge on 1 mole = F

Therefore, Charge per mole = $(1.4 \times 10^{-2}) \times 96480 = 1312 \text{ C}$

$t \text{ (s)} = \text{Charge per mole (C)} / I \text{ (A)}$

$= 1312 / 0.045$

$t = 29156 \text{ s}$ (for 100 % charge to pass)

Therefore the time for 80 % of the theoretical charge to pass = $29156 \times 0.8 = 23324 \text{ s}$

Figure 5.1 shows the chronoamperogram obtained during the electrolysis. After an initial decrease, the plot shows a steady increase of current with time until ca 3.5 hours, at which point a plateau is reached at a current of 70 mA. It is not clear exactly what process(es) is/are responsible for the current-time response in fig. 5.1; however, it is possible that the formation of charged intermediates (such as radical-cations) lowers the overall resistance of the solution.

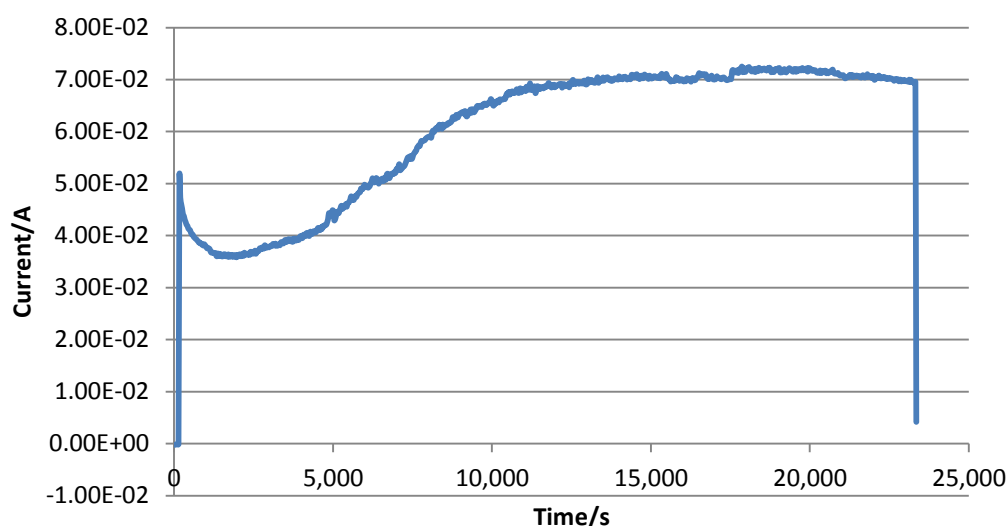


Figure 5.1. Chronoamperogram showing electrolysis of benzotrifluoride in 1.0 M TBAF/MeCN at 3.2 V vs Pt quasi reference electrode for 23324 s, recording data points every 28 s.

Upon comparison of the ^{19}F NMR spectra with those obtained from authentic samples, it was clear that the main isomers isolated were 2,5-difluorotrifluorotoluene (0.066 g, 5% yield) (fig. 5.2(a)), as evidenced by the peaks at $\delta/\text{ppm} = -61.1, -115.0$ and -119.6 ppm and 3,4-difluorotrifluorotoluene (0.021 g, 2% yield) (fig. 5.2(b)), as evidenced by the peaks at $\delta/\text{ppm} = -61.2, -129.8$ and -133.6 ppm.

The yields (which were determined by quantitative NMR using a fluorobenzene reference standard.) were extremely low, the major component of the mixture in each case being starting material. The differences in yield and product distribution are not uncommon in electroorganic systems, as evidenced by the conflicting results presented by Knunyants,⁴³ and Momota.¹³⁰ These differences could be due to any number of factors such as electrode size/separation, both of which contribute to the overall resistance of the system, or stirrer type/speed which will affect mass transport to and from the electrodes. Nevertheless, this provided a proof of principle that fluorinated products could be obtained using TBAF/MeCN in place of $\text{Et}_4\text{NF}\cdot 3\text{HF}$.

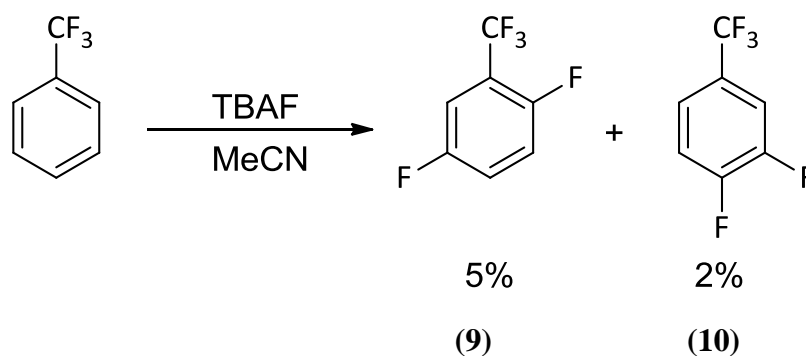


Figure 5.2. Structures of the main products observed from the ECF of benzotrifluoride: 2,5-difluorobenzotrifluoride (9) and 3,4-difluorobenzotrifluoride (10).

5.1.2. Composite electrolysis of benzotrifluoride on anode surface

The theoretical model detailed in chapter 4 postulates that highly energetic holes generated within the Si of the composite anodes migrate through the TiO_2 to the surface of the electrode; the holes are then able to oxidise species present at the TiO_2 /solution interface. It was reasoned, therefore, that application of bias voltage (i.e. generating current through the device as when a DCC is performed), along with irradiation of the anode surface with visible light, should facilitate the oxidation, and hence subsequent fluorination of, benzotrifluoride in TBAF.

The anode was clamped facing upwards and the benzotrifluoride/TBAF mixture was applied directly onto the anode surface. The surface was then irradiated using a light pipe as detailed in section 2.11 and the potential applied.

Figure 5.3 shows comparisons of the DCCs obtained with and without irradiation in both the absence and presence of the substrate. Upon addition of the substrate, the observed current at ambient light (250 lux) actually decreases; however, upon irradiation of the anode with the substrate, the observed current significantly increases in agreement with quantum theory which states that holes will not begin to travel to the surface unless there is something to receive them (e.g. an oxidisable species).¹¹⁶ The difference is more significant when the anode is irradiated as more holes are being generated by photochemical promotion of electrons from the valence band to the conduction band of the Si. When irradiated, the difference between the DCC without the substrate and the DCC with the substrate is 1.5 mA at a potential of 2.97 V.

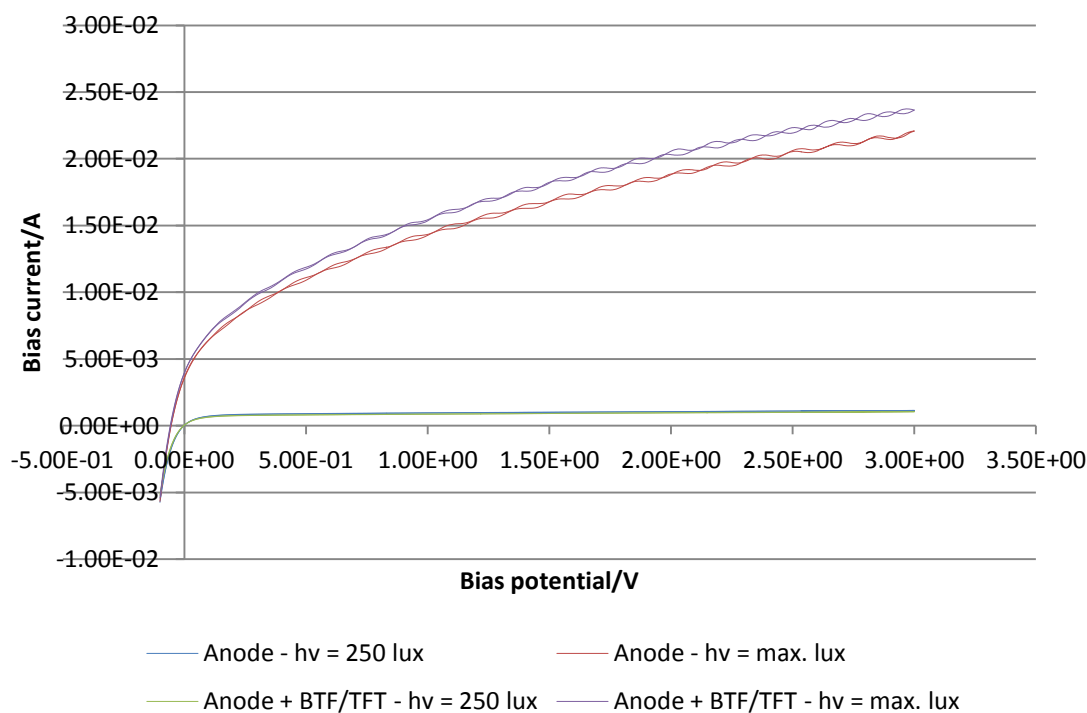


Figure 5.3. Comparison of DCCs of a gold composite anode, with and without benzotrifluoride/TBAF, in air between -0.1 V and 3.0 V, scan rate = 100 mV s^{-1} , $h\nu = 250$ lux (ambient light) and max. lux.

Figure 5.4 is typical of the chronoamperomograms observed for each electrolysis. There is a maximum increase in current of 4 mA. While this is not especially high, it does suggest that a species is being electrolysed.

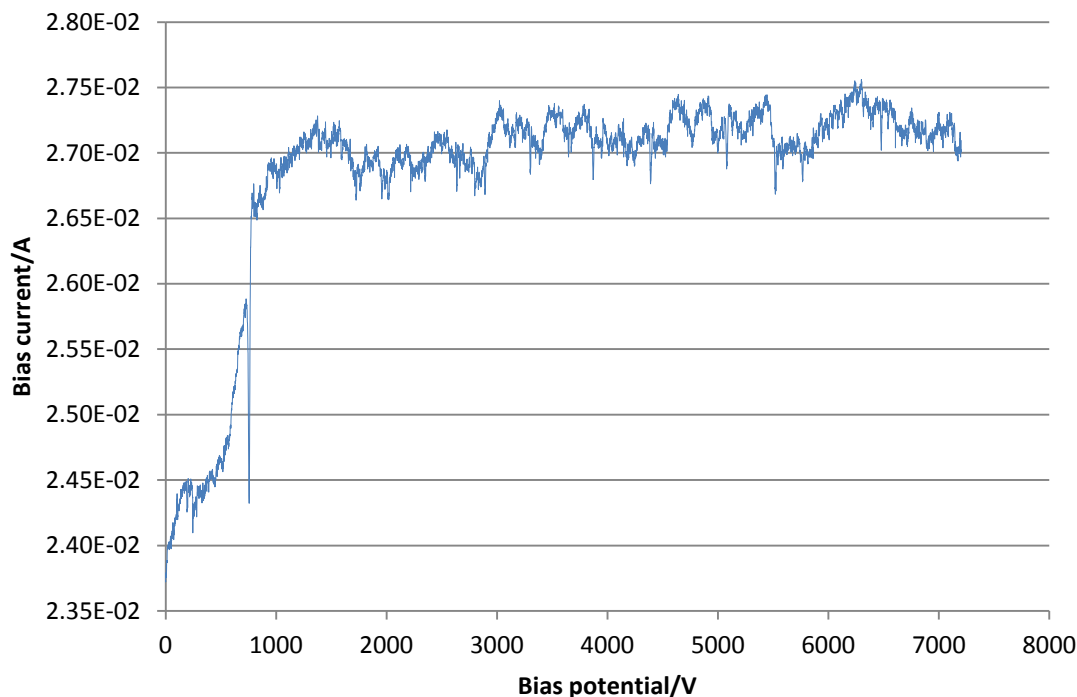


Figure 5.4. Chronoamperomogram of a gold composite anode with TFT/TBAF at potential of 3 V, $h\nu = \text{max. lux}$, $t = 7200 \text{ s}$.

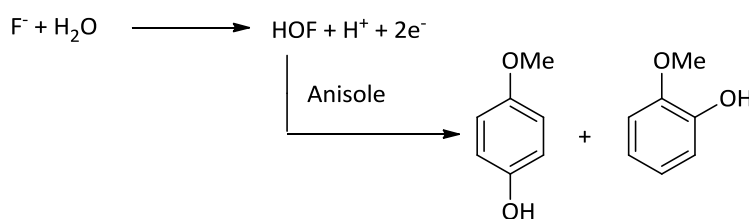
After electrolysis, the product was obtained as a gel on the surface of the anode. The gel was rinsed into 1.0 cm³ of diethyl ether/methanol (1:1) and analysed by ¹⁹F NMR. In each case, the product displayed a very small peak at -63 ppm and a large peak at -150 ppm in the ¹⁹F NMR. Both the TBAF and the mixture of TFT/TBAF were analysed before the electrolysis by ¹⁹F NMR. There was a clear peak in the NMR of TBAF at -150 ppm, and two peaks in the mixture before electrolysis at -63 ppm (TFT) and -150 ppm (TBAF). This suggests that only starting materials were recovered from the electrolysis in each case. It was considered that the TFT peak in the product was small due to evaporation of the substrate during electrolysis. Therefore, the experiment was repeated in a closed cell to allow any benzotrifluoride going into the gaseous phase to reach equilibrium with the substrate in the liquid phase, hence preventing any loss through evaporation. Unfortunately, the repeat experiment yielded the same result.

5.2. Anisole

5.2.1. Composite electrolysis of anisole on anode surface

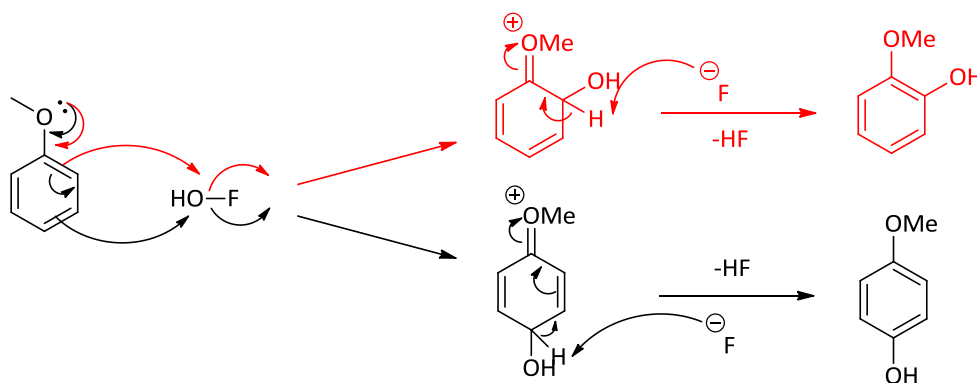
It was considered that the highly oxidising nature of the holes may in fact effect the oxidation of aqueous fluoride to hypofluorous acid (HOF), a good oxidising agent. Were this the case, the lack of fluorination observed upon the composite electrolysis of benzotrifluoride could be due to the electron withdrawing nature of the CF_3 group, deactivating, and thus reducing the nucleophilicity of, the aromatic ring, hence preventing the likelihood of electrophilic aromatic substitution.

In order to test the theory of hypofluorous acid generation, it was decided to use an arene with an electron-donating substituent that would be more active towards electrophilic aromatic substitution, such as anisole (scheme 5.2).



Scheme 5.2. Proposed route of electrochemical oxidation by generation of hypofluorous acid intermediate.

Scheme 5.3 shows the mechanisms by which electrophilic oxidation of anisole by hypofluorous acid would be expected to occur. The electronic properties of the electron donating methoxy substituent would most likely direct substitution to the *ortho* and *para* positions.



Scheme 5.3. Proposed mechanism of electrophilic oxidation of anisole by hypofluorous acid.

Figure 5.5 shows a comparison of the DCCs of a gold composite doped with 1 equivalent of anisole and 2 equivalents of TBAF in ethyl acetate, with and without irradiation. The maximum current achieved at ambient light (250 lux) is 1.7 mA, whereas the maximum current achieved at max. lux is 19 mA. That's a 17.3 mA increase in current at a cell voltage of 2.97 V. Due to the nature of the closed cell, DCCs without the substrate were not taken as the apparatus would have been moved in order to apply the substrate to the surface of the anode, rendering the results incomparable to those recorded with the substrate.

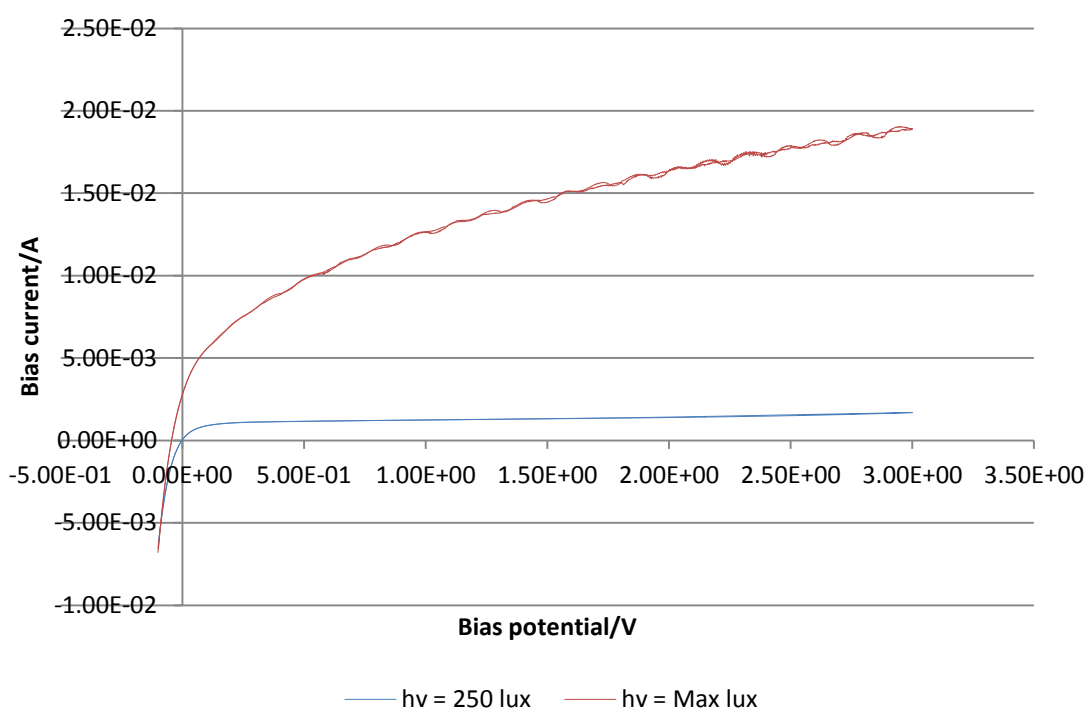


Figure 5.5. Comparison of DCCs of a gold composite anode doped with an anisole/TBAF/EtOAC substrate with and without irradiation, between -0.1 V and 3.0 V at a scan rate of 100 mV s^{-1} .

The chronoamperogram shown in fig. 5.6 shows a steady decline in current which is indicative of increasing resistance within the system. At 28620 s, 56664 s and 82485 s there appear to be spikes in the current; in each case the observed increase in current is *ca.* 1.6 mA, possibly indicating the depletion of a passivating film on the anode surface, hence, lowering the resistance until such a time as the film can regenerate by polymerisation of the substrate.

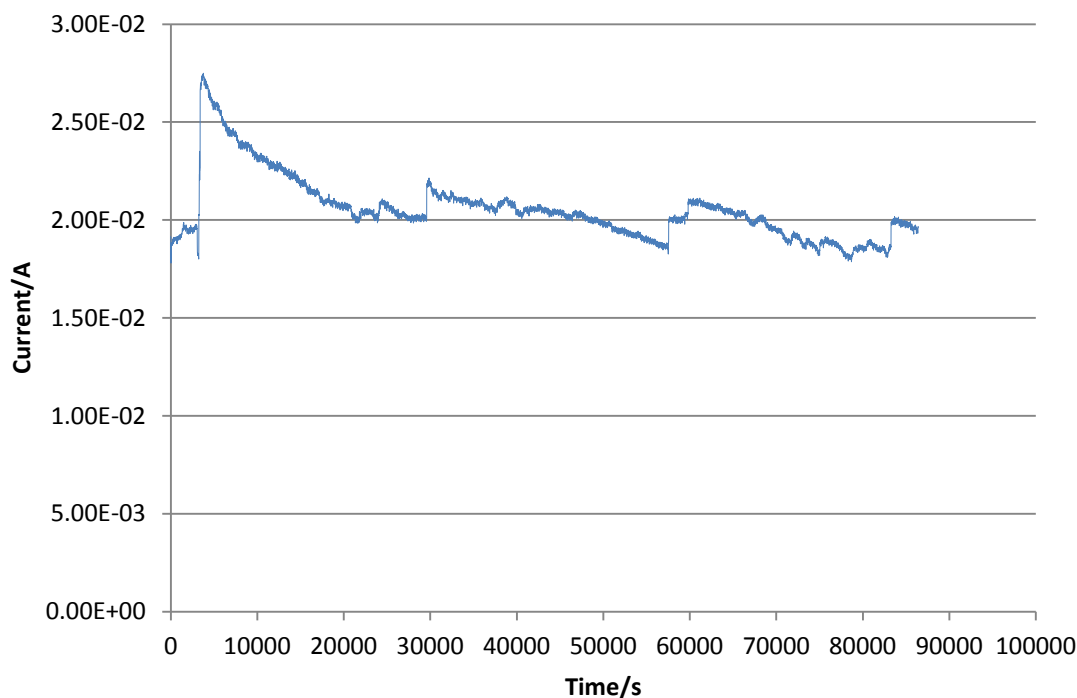


Figure 5.6. Chronoamperogram of a gold composite anode in anisole/TBAF/EtOAC, at an EC potential of 3.0 V and at maximum light intensity for 24 hours, recording a data point every 9 s.

Once the electrolysis was complete, the anode surface was rinsed with methanol (1 cm³) and analysed by ¹⁹F NMR, showing a single clear peak at -150 ppm, indicating that only TBAF was obtained.

5.2.2. Composite electrolysis of anisole in solution (no bias)

It became apparent that electrolysis on the surface of the composite anode presented too many problems to be feasible. It was therefore decided to attempt the composite electrolysis of anisole in a solution of TBAF/acetonitrile, a common electrolyte mixture for ECF. In this case, the composite anode was placed facing downwards with the anode surface just in contact with the surface of the solution as described in 2.12.4.

The DCCs obtained show, in each case, a marked increase in current upon irradiation of the anode (between 17 mA and 19 mA), irrespective of the medium in which the anode was placed as shown in fig. 5.7

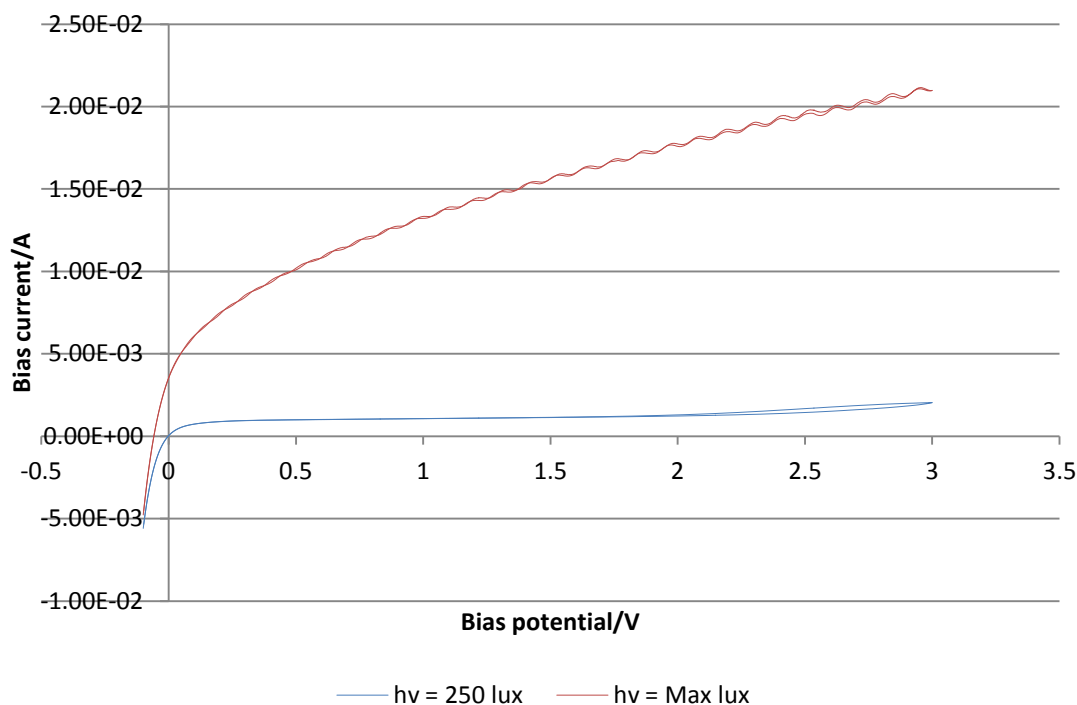
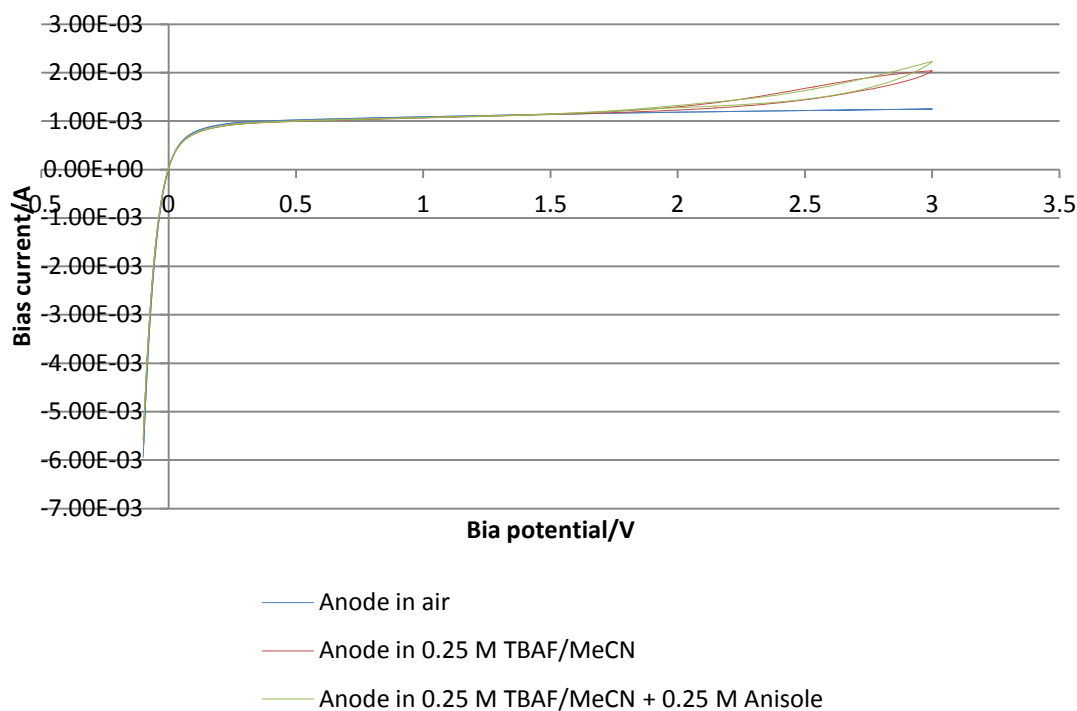
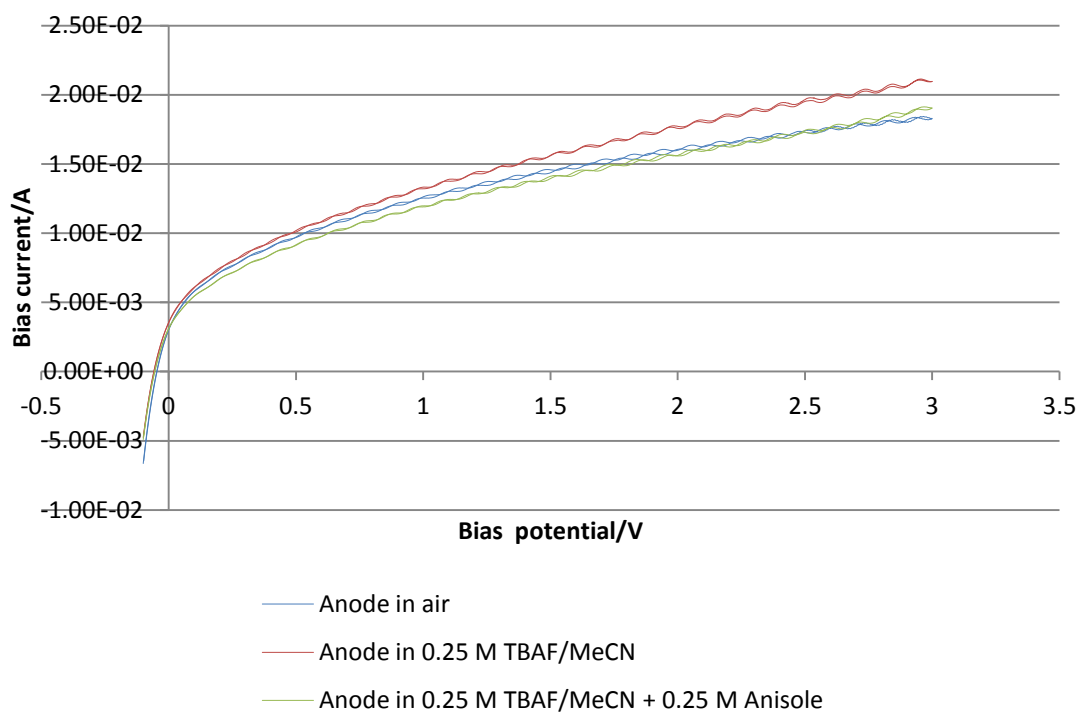


Figure 5.7. Comparison of DCCs of a gold composite anode in 0.25 M TBAF/MeCN between -0.1 V and 3 V, $h\nu = 250$ lux and max lux

When the anode is in contact with the solution, a slightly higher current is observed than in air, as well as a slight hysteresis. Interestingly, upon addition of the substrate, the current increases further; this may be an indication that the substrate is more readily oxidised than the electrolyte/solvent mixture (fig. 5.8).



(a)



(b)

Figure 5.8 Comparison of DCCs of a gold composite anode in: air, 0.25 M TBAF/MeCN and 0.25 M TBAF/MeCN + 0.25 M Anisole, between -0.1 V and 3 V at (a) 250 lux and (b) max lux.

Electrolysis was performed at a constant potential of 3 V vs. CE and the reaction mixture analysed by ^{19}F NMR. Unfortunately, analysis showed a single peak at -155 ppm, suggesting that only TBAF was recovered.

5.2.3. Biased composite electrolysis of anisole

None of the composite electrolyses reported so far were successful in generating fluorinated product. It was reasoned that this may be due to the relatively small currents being generated (ca 1 mA); our previous work detailed in chapter 4 would suggest that the application of bias potential along with irradiation of the anode surface would maximise the currents generated. It was therefore decided to repeat the electrolysis of anisole under these conditions.

Figure 5.9 clearly shows that the currents achieved after the addition of anisole were much lower than those achieved in just the electrolyte/solvent solution, suggesting that the electrode was damaged.

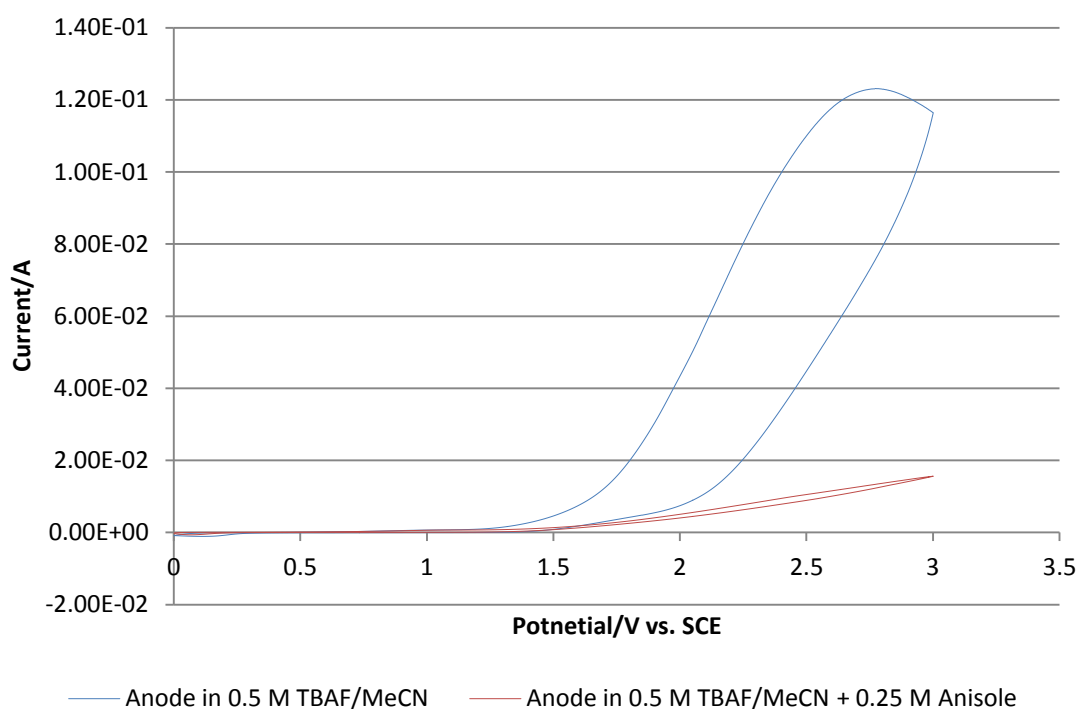


Figure 5.9. Comparison CVs of a gold composite anode in 0.5 M TBAF/MeCN with and without 0.25 M Anisole between 0 V and 3 V vs. SCE, scan rate = 100 mV s^{-1} .

It is clear from fig. 5.10 that at $V_b = 3 \text{ V}$ and $h\nu = \text{max}$, the anode is destroyed. After this run, it was noticed that the solution had turned yellow in colour, suggesting that the

gold had been dissolved from the surface of the anode. This was confirmed by visual assessment of the anode as seen in fig. 5.11.

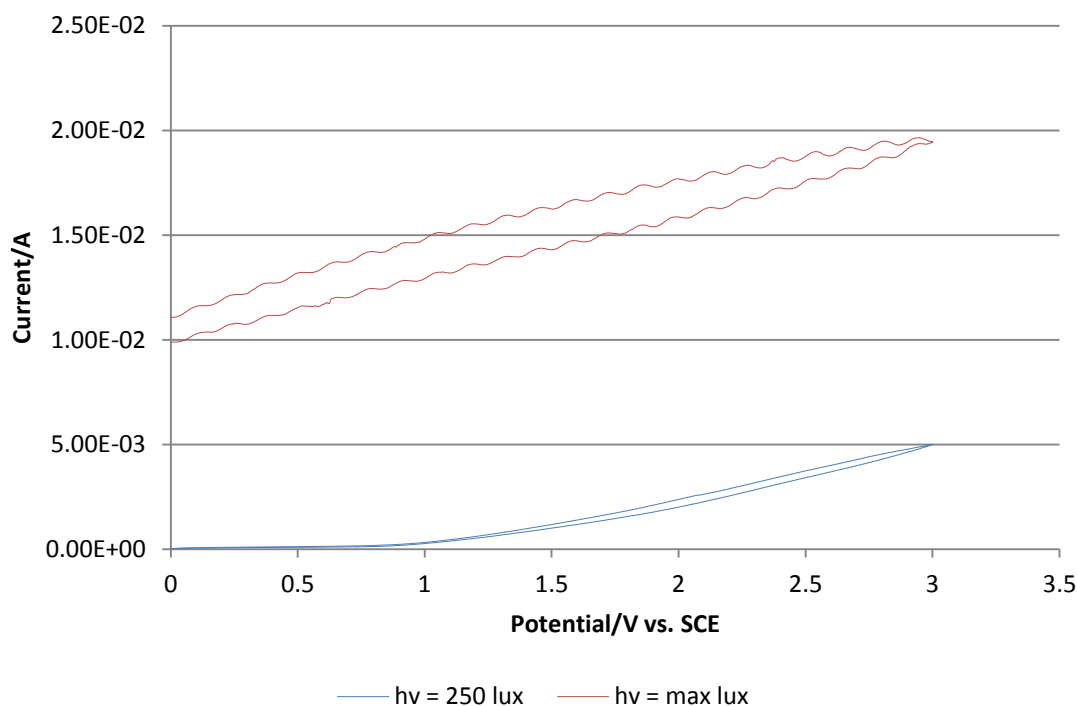


Figure 5.10. Comparison CVs of a gold composite anode in 0.5 M TBAF/MeCN + 0.25 M Anisole, between 0 V and 3 V vs. SCE, scan rate = 100 mV s^{-1} , $V_b = 3 \text{ V}$ at minimum and maximum light intensity.

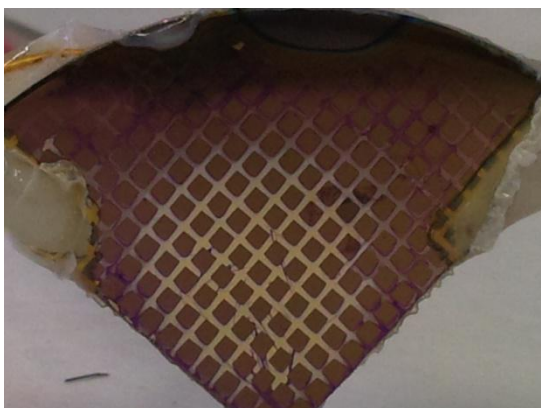


Figure 5.11. Photograph of the gold composite anode after DCCs and CVs with applied bias potential.

6. Electrochemical Fluoride Capture

One of the main challenges in fluorine chemistry is safe handling of the reagents. This is never more true than when using the radioactive isotope, fluorine-18. The potential risks associated with the handling of this material, necessitates the use for fully sealed, lead-lined fume cupboards, or hot cells. The constant demand to work more quickly, efficiently and safely with fluorine-18 provides an opportunity to develop new technologies to help facilitate these needs. One such technology which is used to great effect is flow technology or “continuous processing”. This has become a popular technology within the area of PET as it can operate as a sealed system which is operated remotely (or even automated), minimising operator exposure.

One area of the isotope isolation process which could be further improved upon, is the separation of the [^{18}F]fluoride from the ^{18}O enriched water. As discussed in chapter 1, section 1.1.3.3, this is currently achieved using an ion-exchange resin and phase-transfer agents, but work has shown that it is possible to selectively adsorb fluoride onto an anode by application of a cell voltage, and subsequently discharge the fluoride when required by reversal of the potential.

In order to explore this concept further, we developed an electrochemical cell (based upon a patent)¹³¹ designed to work in conjunction with a flow reactor (fig. 6.1).

The cell consists of a PTFE body with a glassy carbon (GC) anode, a Pt disc cathode and an electric heater (with thermocouple). The Ti wires connecting the electrodes to the potentiostat were fixed to the electrodes with silver araldite covered with araldite rapid. The electrodes were fixed into the cavity of the cell with a water-tight sealant.

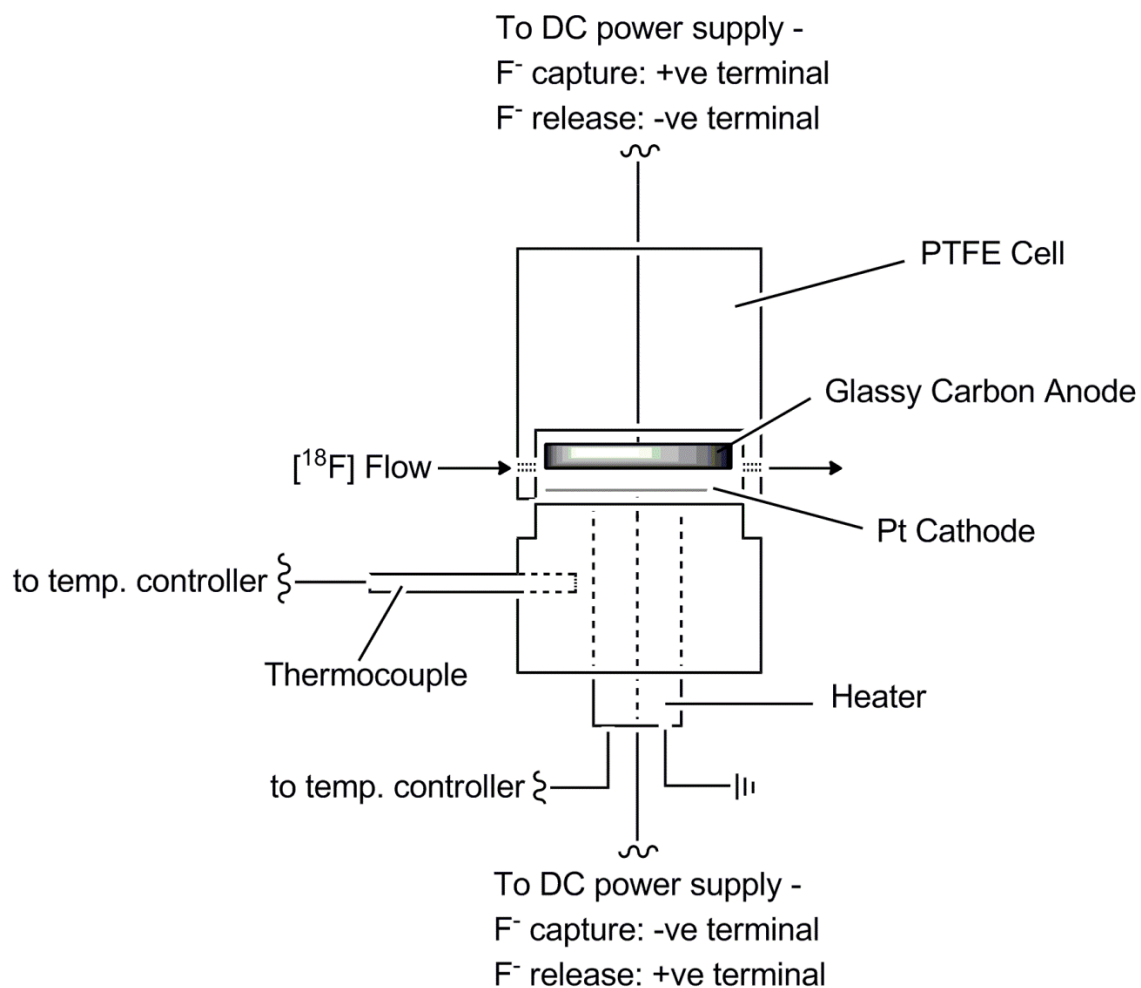


Figure 6.1. Schematic representation of the electrochemical fluoride capture flow cell.

The procedure was automated using a ModularLab flow system, which involved programming a series of valves in order to flow the reagents and solvents through the cell, remotely (fig. 6.2). The system was designed such that all transfers could be controlled using a single syringe pump, which was manipulated using Winpump software.

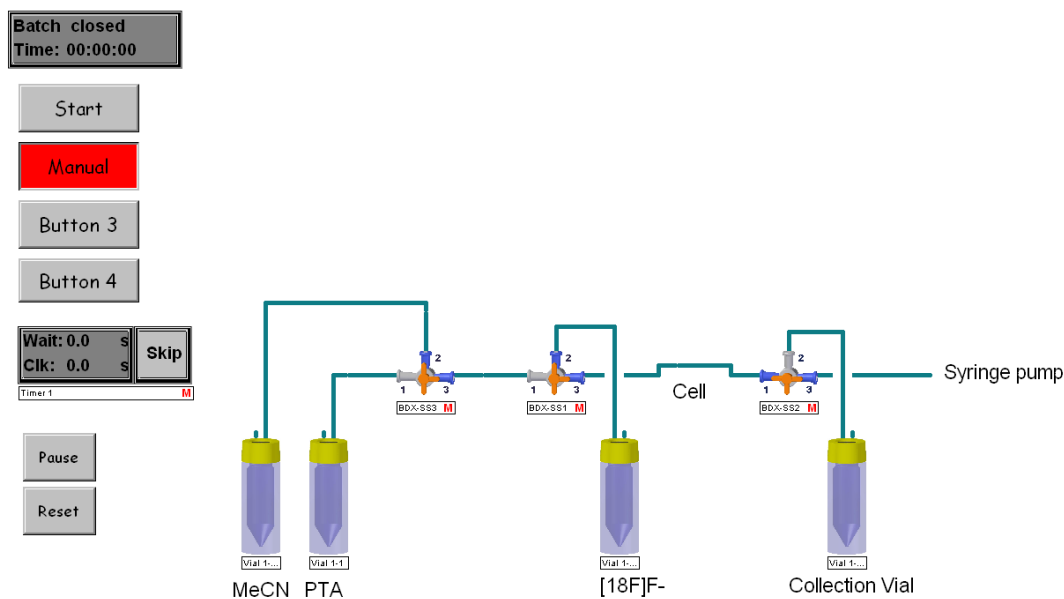


Figure 6.2. Schematic representation of the remote-controlled ModularLab flow system.

In practice, a charge of 10 V is placed across the cell using a DC power supply with the glassy carbon positive with respect to the Pt. The fluoride/water mixture is then passed through the cell and the fluoride adsorbed to the carbon surface, while the water flows out of the other end of the cell, to a collection vial. Acetonitrile is then passed through the cell to remove any residual water. Finally, the cell is heated to 80 °C and a phase transfer agent (PTA) is passed through the cell whilst the cell voltage is reversed, causing desorption of the fluoride which is dissolved in the PTA and collected in vial for use.

Due to time constraints, only one attempt at fluoride capture was performed, as detailed in section 2.13 and no meaningful results could be obtained. However, future work within in the group will focus on the development of this innovative technology, with a view to successful application to the isolation of fluorine-18.

7. Conclusions

In conclusion, studies on the effect of current density and electrolyte on the product distribution and overall yield resulting from the ECF of ethylene carbonate have shown that the highest yield of mono-fluorinated product was obtained using the electrolyte $\text{Et}_4\text{NF}\cdot 4\text{HF}$ with a current density of 100 mA cm^{-2} . All the major products of the electrolyses have been analyzed in detail by NMR for the first time, showing that both *syn*- and *anti*-(\pm)-4,5-difluoro-1,3-dioxolan-2-one display spectra typical of AA'XX' type spin systems. In addition, ECF of propylene carbonate has resulted in a more selective and efficient process with the mono-fluorinated analogue of propylene carbonate, (\pm)-4-fluoro-4-methyl-1,3-dioxolan-2-one being prepared for the first time in moderate yield (26%). The variation in regioselectivity/product distribution observed upon introduction of a tertiary centre has provided an insight into the mechanism of ECF of electron rich aliphatic compounds and hence generated a good basis for further investigation.

The EPR studies proved to be inconclusive as the same signal was observed upon electrolysis of the electrolyte without the substrate, suggesting that the signal is caused by decomposition. The signal is clearly asymmetric, suggesting that there is more than one radical species in solution. It is suggested that these signals arise as the MeCN is undergoing electrochemical deprotonation at the cathode and forming enamines *via* an electrochemical/radical version of the Thorpe reaction. At no time during voltammetry or electrolysis was an EPR signal observed. This could be due to the fact that:

- 1) No radical is formed during the process
- 2) A radical is formed, but in insufficient concentration for detection
- 3) A radical is formed, but reacts immediately with the electrolyte
- 4) The currents achieved were too small to drive the reaction

In spite of this, the mechanism for the ECF of cyclic carbonates is still considered most likely to go *via* a radical-cation intermediate, based on both the literature and the product distribution observed upon ECF of propylene carbonate, which would suggest the formation of an intermediate which is stabilised by a tertiary centre.

The composite anodes reported represent an entirely new concept which could potentially extend the scope of electrochemistry beyond that which is currently possible. The development of the composite anodes to date has mainly focussed on the characterisation of their electrochemical behaviour. The findings reported serve to further our understanding of these unique devices and have allowed the postulation of a mechanistic model to explain the observed electrochemical behaviour of the anodes. The model suggests that, instead of having a one dimensional control over the behaviour of an electrode (*via* its electrochemical potential) our composite anodes allow three dimensional control: V_b , electrochemical potential and visible light intensity. Thus it should be possible to ‘tune’ a composite anode to oxidize a target solution species by selecting a set of parameters corresponding to a suitable point on the 3-dimensional surface represented by V_b , electrochemical potential and light intensity.

Initial studies into composite electrochemical fluorination were unsuccessful, largely due to the corrosive nature of the fluoride species generated, and the necessarily high potentials required to generate these species. As we begin to further understand the composite anodes and their chemistry, we remain confident that composite ECF will be possible in the future.

8. Future Work

The next step in terms of the cyclic carbonate work would be to perform ECF of a number of analogues to investigate the effects of both steric and electronic parameters on the product distribution and selectivity of the ECF reaction, as well as structurally related compounds such as oxazolidinones. Potentially interesting substrates for investigation may be 4-phenyl-1,3-dioxolan-2-one (fig. 8.1(i)), 4-*t*Bu-1,3-dioxolan-2-one (fig. 8.1(ii)), 4-nitro-1,3-dioxolan-2-one (fig. 8.1(iii)) and 4-methoxy-1,3-dioxolan-2-one (fig. 8.1(iv)).

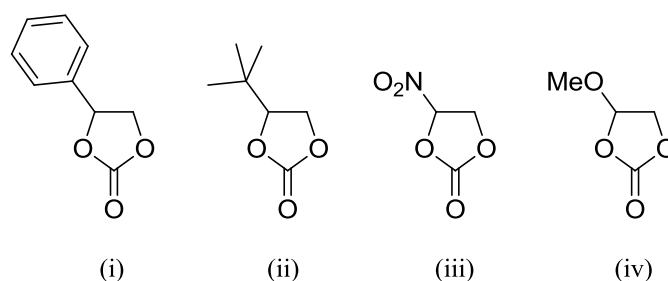
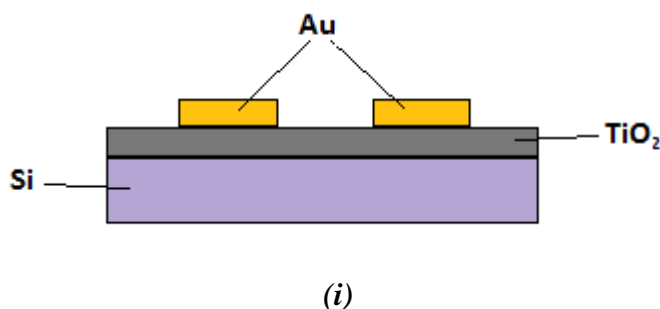
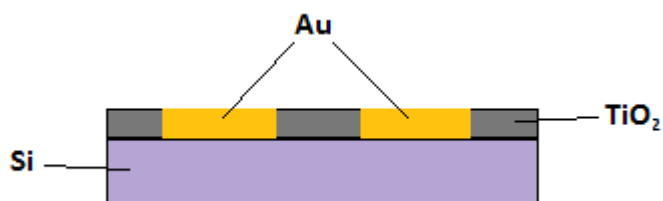


Figure 8.1. Suggested cyclic carbonates for further ECF.

The data obtained from such a study would further inform mechanistic understanding of the process. In addition to this, electrochemical radiofluorination of propylene carbonate could be performed using [^{18}F]Fluoride in $\text{Et}_4\text{NF}\cdot 4\text{HF}$.

In terms of the composite anodes, further development will be required to attain a device that will be useful for electrofluorination. The first problem to overcome is the fluoride stripping of the metal grid. One way in which this may be achieved is by recessing the grid into the TiO_2 , rather than depositing the grid on the surface of the TiO_2 (see fig. 8.2).





(ii)

Figure 8.2(i) Schematic showing current situation of gold grid with respect to TiO_2 on the composite anodes; **(ii)** schematic depicting suggested recession of gold grid into TiO_2 .

In order to investigate the ‘tunability’ of the composite anodes, it will be necessary to perform some basic electrochemical transformations using a well-studied reaction such as the Kolbe electrolysis to determine the effects of electrolysis using a combination of parameters. The best way to approach this may be to use a statistical design of experiments to determine the most significant factor contributing to the generation of the product.

Finally, more work is needed on the electrochemical fluoride capture cell to make it fully operational. One possible way to go about this would be to vary the cell voltage, flow rates and KF concentrations (within realistic limits for ^{18}F fluoride in ^{18}O water) to find the optimum conditions and/or saturation point of the anode.

References

1. Agricola, G., *De Re Metallica*. 1950 edition ed.; Dover Publications: New York, 1950.
2. Moissan, H., *Das Fluor und seine Verbindungen*. German Edition ed.; Berlin, 1900.
3. http://nobelprize.org/nobel_prizes/chemistry/laureates/1906/. (accessed 01/06/10).
4. Pauling, L., *The Nature of the Chemical Bond and the Structure of Molecules and Crystals: An Introduction to Modern Structural Chemistry*. Cornell University Press: Ithaca, New York, 1939.
5. O'Hagan, D., Understanding Organofluorine Chemistry. An Introduction to the C-F bond. *Chemical Society Reviews* **2008**, *37*, 308-319.
6. Chambers, R. D., *Fluorine in Organic Chemistry*. Blackwell Publishing Ltd.: Oxford, 2004; p 406.
7. Kirk, K. L., Fluorine in medicinal chemistry: Recent therapeutic applications of fluorinated small molecules. *Journal of Fluorine Chemistry* **2006**, *127* (8), 1013-1029.
8. Kirk, K. L., Fluorination in Medicinal Chemistry: Methods, Strategies, and Recent Developments. *Organic Process Research & Development* **2008**, *12* (2), 305-321.
9. Muller, K.; Faeh, C.; Diederich, F., Fluorine in Pharmaceuticals: Looking Beyond Intuition. *Science* **2007**, *317* (5846), 1881-1886.
10. Purser, S.; Moore, P.; Swallow, S.; Gouverner, V., Fluorine in Medicinal Chemistry. *Chemical Society Reviews* **2007**, *37* (2), 320-330.
11. Silverman, R. B., *The Organic Chemistry of Drug Design and Drug Action*. 2nd Edition ed.; Elsevier Academic Press: London, 2004; p 617.
12. Hagmann, W. K., The Many Roles for Fluorine in Medicinal Chemistry. *Journal of Medicinal Chemistry* **2008**, *51* (15), 4359-4369.
13. Miller, P. W.; Long, N. J.; Vilar, R.; Gee, A. D., Synthesis of ¹¹C, ¹⁸F, ¹⁵O, and ¹³N Radiolabels for Positron Emission Tomography. *Angewandte Chemie International Edition* **2008**, *47* (47), 8998-9033.
14. Haubner, R., PET radiopharmaceuticals in radiation treatment planning – Synthesis and biological characteristics. *Radiotherapy and Oncology* **2010**, *96* (3), 280-287.

15. Cai, L.; Lu, S.; Pike, V. W., Chemistry with [¹⁸F]Fluoride Ion. *European Journal of Organic Chemistry* **2008**, 2008 (17), 2853-2873.
16. Pillai, M. R. A.; Haji-Saeid, M. *Cyclotron Produced Radionuclides: Physical characteristics and Production Methods*; International Atomic Energy Agency: Vienna, 2009; p 266.
17. Schubiger, P. A.; Lehmann, L.; Friebe, M., *PET Chemistry: The Driving Force in Molecular Imaging*. Springer: 2007; Vol. 62.
18. Wong, R.; Iwata, R.; Saiki, H.; Furumoto, S.; Ishikawa, Y.; Ozeki, E., Reactivity of electrochemically concentrated anhydrous [¹⁸F]fluoride for microfluidic radiosynthesis of ¹⁸F-labeled compounds. *Applied Radiation and Isotopes* **2012**, 70 (1), 193-199.
19. Reischl, G.; Kienzle, G.; Machulla, H. J., Electrochemical radiofluorination: Labeling of benzene with [¹⁸F]fluoride by nucleophilic substitution. *Journal of Radioanalytical and Nuclear Chemistry* **2002**, 254 (2), 409-411.
20. Reischl, G.; Kienzle, G. J.; Machulla, H. J., Electrochemical radiofluorination. Part 2. Anodic monofluorination of substituted benzenes using [¹⁸F]fluoride. *Applied Radiation and Isotopes* **2003**, 58 (6), 679-683.
21. Kienzle, G. J.; Reischl, G.; Machulla, H. J., Electrochemical radiofluorination. 3. Direct labeling of phenylalanine derivatives with [¹⁸F]fluoride after anodic oxidation. *Journal of Labelled Compounds and Radiopharmaceuticals* **2005**, 48 (4), 259-273.
22. <http://www.laboratory-journal.com/applications/chromatography/radio-ion-chromatography-hot-insights> (accessed 01.06.2013).
23. Sandford, G., Elemental fluorine in organic chemistry (1997-2006). *Journal of Fluorine Chemistry* **2007**, 128 (2), 90-104.
24. Lal, G. S.; Pez, G. P.; Syvret, R. G., Electrophilic NF Fluorinating Agents. *Chemical Reviews* **1996**, 96 (5), 1737-1756.
25. <http://www.alfa.com/en/docs/FluorinatingAgents.pdf>. (accessed 02/06/10).
26. Vlasov, V. M., Fluoride ion as a nucleophile and a leaving group in aromatic nucleophilic substitution reactions. *Journal of Fluorine Chemistry* **1993**, 61 (3), 193-216.
27. Suschitzky, H., The Balz-Schiemann Reaction. *Advances in Fluorine Chemistry* **1965**, 4, 1.
28. Peters, D.; Miethchen, R., Symptoms and treatment of hydrogen fluoride injuries. *Journal of Fluorine Chemistry* **1996**, 79 (2), 161-165.

29. Noel, M.; Suryanarayanan, V.; Chellammal, S., A review of recent developments in the selective electrochemical fluorination of organic compounds. *Journal of Fluorine Chemistry* **1997**, *83* (1), 31-40.
30. Rozhkov, I. N., Radical-cation Mechanism of the Anodic Fluorination of Organic Compounds. *Russian Chemical Reviews* **1976**, *45* (7), 615.
31. Masaki, S.; Tamejira, H., Modern Synthetic Methods for Fluorine-Substituted Target Molecules. *Angewandte Chemie International Edition* **2005**, *44* (2), 214-231.
32. Ilayaraja, N.; Noel, M., Galvanostatic and potentiostatic fluorination of 2-indanone, 1-indanone and 1,3-indandione in Et₃N · 4HF medium. Adsorption effects on yield and product selectivity. *Journal of Electroanalytical Chemistry* **2010**, *638* (1), 39-45.
33. Fuchigami, T.; Tajima, T., Selective Anodic Fluorination of Heterocyclic Compounds. In *Fluorine-Containing Synthons*, American Chemical Society: Washington, DC, 2009; pp 276-287.
34. Fuchigami, T.; Shimojo, M.; Konno, A.; Nakagawa, K., Electrolytic partial fluorination of organic compounds. 1. Regioselective anodic monofluorination of organosulfur compounds. *The Journal of Organic Chemistry* **1990**, *55* (25), 6074-6075.
35. Simons, J. H.; Harland, W. J., The Electrochemical Process for the Production of Fluorocarbons. *Journal of The Electrochemical Society* **1949**, *95*, 47-66.
36. Lund, H.; Baizer, M. M., *Organic Electrochemistry: An Introduction and Guide*. 3rd ed.; Marcel Dekker Inc.: New York, 1991; p 1550.
37. Greenwood, N. N.; Earnshaw, A., *Chemistry of the Elements*. 1st Edition ed.; Pergamon Press: Oxford, 1984.
38. Sawyer, D. T.; Roberts, J. L., *Experimental Electrochemistry for Chemists*. 1st ed.; John Wiley & Sons, Inc.: 1974; p 435.
39. Childs, W. V.; Ruehlen, F. N. Electrochemical Fluorination of Organic Compounds. 3-511-761, May 12 1970, 1970.
40. Fox, H. M.; Ruehlen, F. N.; Childs, W. V., Electrochemical Fluorination. *Journal of The Electrochemical Society* **1971**, *118* (7), 1246-1249.
41. Hamann, C. H.; Hamnet, A.; Vielstich, W., *Electrochemistry*. 2nd ed.; Wiley-VCH Verlag GmbH & Co.: Weinheim, 2007; p 531.
42. Fuchigami, T., Unique solvent effects on selective electrochemical fluorination of organic compounds. *Journal of Fluorine Chemistry* **2007**, *128* (4), 311-316.

43. Knunyants, I. L.; Rozhkov, I. N.; Bukhtiarov, A. V., Electrochemical Fluorination at High Anodic Potentials. *Russian Academy of Sciences, Chemical Series* **1971**, (6).
44. Momota, K.; Kato, K.; Morita, M.; Matsuda, Y., Electrochemical fluorination of aromatic compounds in liquid R₄NF·mHF--Part III. Fluorination of trifluoromethylbenzenes. *Electrochimica Acta* **1994**, *39* (5), 681-690.
45. Shainyan, B. A.; Danilevich, Y. S.; Bel'skii, V. K.; Stash, A. I.; Grigor'eva, A. A.; Chuvashov, Y. A., Selective Aromatic Electrochemical Fluorination of Methyl Phenyl Sulfone. *Russian Journal of Organic Chemistry* **2002**, *38* (10), 1462-1464.
46. Shainyan, B. A.; Danilevich, Y. S.; Grigor'eva, A. A.; Chuvashov, Y. A., Selective Electrochemical Aromatic Fluorination of Acetophenone and Benzophenone. *Russian Journal of Organic Chemistry* **2003**, *39* (11), 1581-1586.
47. Shainyan, B.; Danilevich, Y., Electrochemical fluorination of aromatic compounds in anhydrous HF. *Russian Journal of Organic Chemistry* **2006**, *42* (2), 214-219.
48. Fuchigami, T.; Tajima, T., Selective Anodic Fluorination of Heterocyclic Compounds. In *Fluorine-Containing Synthons*, American Chemical Society: Washington, DC, 2005; pp 276-287.
49. Sunaga, T.; Atobe, M.; Inagi, S.; Fuchigami, T., Highly Efficient and Selective Electrochemical Fluorination of Organosulfur Compounds in Et₃N·3HF Ionic Liquid Under Ultrasonication. *Chemical Communications* **2009**, 956-958.
50. Hasegawa, M.; Ishii, H.; Cao, Y.; Fuchigami, T., Regioselective Anodic Monofluorination of Ethers, Lactones, Carbonates, and Esters Using Ionic Liquid Fluoride Salts. *Journal of The Electrochemical Society* **2006**, *153* (10), D162-D166.
51. Schwarz, M.; Speiser, B., Combinatorial micro-electrochemistry. Part 5. Electrosynthesis screening of the electroreductive coupling of α -unsaturated esters and allyl bromides in a room temperature ionic liquid. *Electrochimica Acta* **2009**, *54* (14), 3735-3744.
52. Fuchigami, T.; Tajima, T., Highly selective electrochemical fluorination of organic compounds in ionic liquids. *Journal of Fluorine Chemistry* **2005**, *126* (2), 181-187.
53. Narizuka, S.; Koshiyama, H.; Konno, A.; Fuchigami, T., Electrolytic partial fluorination of organic compounds. Part 15. Stereochemical study of the anodic

monofluorination of [alpha]-phenylsulfenyl acetates. *Journal of Fluorine Chemistry* **1995**, *73* (1), 121-127.

54. Higashiya, S.; Sato, T.; Fuchigami, T., Electrolytic partial fluorination of organic compounds Part 25. Regioselective anodic fluorination of naphthalene- and pyridine-acetate and -acetonitrile derivatives. *Journal of Fluorine Chemistry* **1998**, *87* (2), 203-208.

55. Hou, Y.; Fuchigami, T., Electrolytic partial fluorination of organic compounds: 38. Solvent effects on electrolytic fluorination of ethyl [alpha]-(2-pyrimidylthio)acetate. *Electrochemistry Communications* **1999**, *1* (10), 445-448.

56. Ishii, H.; Hou, Y.; Fuchigami, T., Electrolytic Partial Fluorination of Organic Compounds. Part 41:[] Highly Selective Electrolytic Fluorination of Dimethoxyethane, its Homologues, and Crown Ethers. *Tetrahedron* **2000**, *56* (45), 8877-8881.

57. Ishii, H.; Yamada, N.; Fuchigami, T., Electrolytic partial fluorination of organic compound. Part: 53 Highly regioselective anodic mono- and difluorination of 4-arylthio-1,3-dioxolan-2-ones. A marked solvent effect on fluorinated product selectivity. *Tetrahedron* **2001**, *57* (44), 9067-9072.

58. Suzuki, K.; Fuchigami, T., Highly efficient anodic fluorination of 4-(p-chlorophenylthio)methyl-1,3-dioxolan-2-one: marked solvent effects on electrochemical fluorination. *Electrochemistry Communications* **2004**, *6* (2), 183-187.

59. Cao, Y.; Fuchigami, T., Electrochemical partial fluorination of organic compounds: 82: Anodic [alpha]-fluorination of five-membered cyclic thiocarbonates. *Electrochimica Acta* **2006**, *51* (12), 2477-2482.

60. Zagipa, B.; Nagura, H.; Fuchigami, T., Electrolytic partial fluorination of organic compounds: 89: Regioselective anodic fluorination of tetrazolyl sulfides. *Journal of Fluorine Chemistry* **2007**, *128* (10), 1168-1173.

61. Suzuki, K.; Inagi, S.; Fuchigami, T., Electrochemical fluorination of organic compounds: 92. Anodic fluorination of sulfides having oxazolidinone and its application to the synthesis of fluoroallylamine. *Electrochimica Acta* **2009**, *54* (3), 961-965.

62. Sartori, P.; Ignat'ev, N., The actual state of our knowledge about mechanism of electrochemical fluorination in anhydrous hydrogen fluoride (Simons process). *Journal of Fluorine Chemistry* **1998**, *87* (2), 157-162.

63. Christensen, P. A.; Egerton, T. A.; Lin, W. F.; Meynet, P.; Shao, Z. G.; Wright, N. G., A novel electrochemical device for the disinfection of fluids by OH radicals. *Chemical Communications* **2006**, (38), 4022-4023.
64. Fuyura, T.; Kamlet, A. S.; Ritter, T., Catalysis for Fluorination and Trifluoromethylation. *Nature* **2011**, *473*, 470-477.
65. Ma, J.-A.; Cahard, D., Update 1 of: Asymmetric Fluorination, Trifluoromethylation, and Perfluoroalkylation Reactions. *Chemical Reviews* **2008**, *108* (9), PR1-PR43.
66. Shimizu, M.; Hiyama, T., Modern Synthetic Methods for Fluorine-Substituted Target Molecules. *Angewandte Chemie International Edition* **2005**, *44* (2), 214-231.
67. Smith, M. B.; March, J., *March's Advanced Organic Chemistry*. 6th ed.; John Wiley & Sons: New Jersey, 2007.
68. Sawamura, T.; Takahashi, K.; Inagi, S.; Fuchigami, T., Electrochemical Fluorination Using Alkali-Metal Fluorides. *Angewandte Chemie International Edition* **2012**, *51* (18), 4413-4416.
69. Dimitrov, A.; Pfeifer, D.; Jonethal, U.; Rudiger, S.; Seppelt, K., Mechanistic studies on the electrochemical fluorination of trialkylamines and tetraalkylammonium salts. *Journal of Fluorine Chemistry* **1997**, *82* (2), 143-150.
70. McMillan, R.; Slegel, H.; Shu, Z. X.; Wang, W., Fluoroethylene carbonate electrolyte and its use in lithium ion batteries with graphite anodes. *Journal of Power Sources* **1999**, *81-82*, 20-26.
71. Mogi, R.; Inaba, M.; Jeong, S.-K.; Iriyama, Y.; Abe, T.; Ogumi, Z., Effects of Some Organic Additives on Lithium Deposition in Propylene Carbonate. *Journal of the Electrochemical Society* **2002**, *149* (12), A1578-A1583.
72. Choi, N.-S.; Yew, K. H.; Lee, K. Y.; Sung, M.; Kim, H.; Kim, S.-S., Effect of fluoroethylene carbonate additive on interfacial properties of silicon thin-film electrode. *Journal of Power Sources* **2006**, *161* (2), 1254-1259.
73. Kong, L.; Su, Z.; Gao, J.; Sun, J., The Influence of Fluoroethylene Carbonate on the LiCoO₂/Electrolyte Interface. *ECS Meeting Abstracts* **2010**, *1003* (1), 197-197.
74. North, M.; Pasquale, R.; Young, C., Synthesis of cyclic carbonates from epoxides and CO₂. *Green Chemistry* **2010**, *12* (9), 1514-1539.

75. Kember, M. R.; Buchard, A.; Williams, C. K., Catalysts for CO₂/epoxide copolymerisation. *Chemical Communications (Cambridge, United Kingdom)* **2011**, 47 (1), 141-163.
76. Clegg, W.; Harrington, R. W.; North, M.; Pizzato, F.; Villuendas, P., Cyclic carbonates as sustainable solvents for proline-catalysed aldol reactions. *Tetrahedron: Asymmetry* **2010**, 21 (9–10), 1262-1271.
77. Kobayashi, M.; Inoguchi, T.; Iida, T.; Tanioka, T.; Kumase, H.; Fukai, Y., Development of direct fluorination technology for application to materials for lithium battery. *Journal of Fluorine Chemistry* **2003**, 120 (2), 105-110.
78. Lancaster, M., *Green Chemistry: An Introductory Text*. 2nd ed.; RSC Publishing: Cambridge, UK, 2010.
79. Hasegawa, M.; Ishii, H.; Fuchigami, T., Electroorganic synthesis under solvent-free conditions. Highly regioselective anodic monofluorination of cyclic ethers, lactones, and a cyclic carbonate. *Tetrahedron Letters* **2002**, 43 (8), 1503-1505.
80. Rozhkov, I. N.; Alyev, I. Y., Anodic oxidation of p-disubstituted benzenes in the presence of fluoride ion. *Tetrahedron* **1975**, 31 (8), 977-981.
81. Kirsch, P., *Modern Fluoroorganic Chemistry*. 1 ed.; Wiley-VCH: Darmstadt, 2004; p 308.
82. Lund, H.; Baizer, M. M., *Organic Electrochemistry: An Introduction and a Guide*. 3rd ed.; Marcel Dekker Inc.: New York, 1991; p 1576.
83. Akitt, J. W.; Mann, B. E., *NMR and Chemistry: An Introduction to Modern NMR Spectroscopy*. 4th ed.; Nelson Thornes: Cheltenham, UK, 2000.
84. Karplus, M., Contact Electron-Spin Coupling of Nuclear Magnetic Moments. *The Journal of Chemical Physics* **1959**, 30 (1), 11-15.
85. Weil, J. A.; Bolton, J. R., *Electron Paramagnetic Resonance: Elementary Theory and Practical Applications*. 2nd ed.; John Wiley & Sons: Hoboken, New Jersey, 2007.
86. Lund, A.; Shiotani, M.; Shimada, S., *Principles and Applications of ESR Spectroscopy*. Springer: 2011.
87. Baron, H.; Remfry, F. G. P.; Thorpe, J. F., CLXXV.-The formation and reactions of imino-compounds. Part I. Condensation of ethyl cyanoacetate with its sodium derivative. *Journal of the Chemical Society, Transactions* **1904**, 85, 1726-1761.
88. Clayden, J.; Greeves, N.; Warren, S.; Wothers, P., *Organic Chemistry*. 1st ed.; Oxford University Press: Oxford, 2001.

89. Egerton, T. A.; Christensen, P. A.; Kosa, S. A. M.; Onoka, B.; Harper, J. C.; Tinlin, J. R., Photoelectrocatalysis by titanium dioxide for water treatment. *International Journal of Environment and Pollution* **2006**, *27*, 2-19.
90. Mills, A.; Le Hunte, S., An overview of semiconductor photocatalysis. *Journal of Photochemistry and Photobiology A: Chemistry* **1997**, *108* (1), 1-35.
91. Christensen, P. A.; Egerton, T. A.; Wright, N. G. Methanol Fuel Cells. WO/2007/010207, 25 January 2007, 2007.
92. Roppischer, H.; Bumai, Y. A.; Feldmann, B., Flatband Potential Studies at the n-Si/Electrolyte Interface by Electroreflectance and C-V Measurements. *Journal of The Electrochemical Society* **1995**, *142* (2), 650-655.
93. Trasatti, S., The Electrode Potential. In *Comprehensive Treatise of Electrochemistry*, Bockris, J. O. M.; Conway, B. E.; Yeager, E., Eds. Plenum: New York, 1980; Vol. 1, pp 45-78.
94. Trasatti, S., THE ABSOLUTE ELECTRODE POTENTIAL - AN EXPLANATORY NOTE (RECOMMENDATIONS 1986). *Pure and Applied Chemistry* **1986**, *58* (7), 955-966.
95. Hess, K., *Advanced Theory of Semiconductor Devices*. Wiley: 2000.
96. Mott, N. F.; Davies, E. A., *Electronic Processes in Non-crystalline Materials*. 2nd ed.; Clarendon: Oxford, 1979.
97. Poznyak, S. K.; Pergushov, V. I.; Kokorin, A. I.; Kulak, A. I.; Schlapfer, C. W., Structure and Electrochemical Properties of Species Formed as a Result of Cu(II) Ion Adsorption onto TiO₂ Nanoparticles. *Journal of Physical Chemistry B* **1999**, *103* (8), 1308-1315.
98. Kulak, A. I.; Kokorin, A. I.; Sviridov, D. V., Electrolyte electroreflectance study of TiO₂ films modified with metal nanoparticles. *Journal of Materials Research* **2001**, *16* (08), 2357-2361.
99. Mizubayashi, W.; Yasuda, N.; Ota, H.; Hisamatsu, H.; Tominaga, K.; Iwamoto, K.; Yamamoto, K.; Horikawa, T.; Nabatame, T.; Toriumi, A. In *Carrier separation analysis for clarifying leakage mechanism in unstressed and stressed HfAlO_x/SiO₂ stack dielectric layers*, Reliability Physics Symposium Proceedings, 2004. 42nd Annual. 2004 IEEE International, 25-29 April 2004; 2004; pp 188-193.
100. Deskins, N. A.; Dupuis, M., Intrinsic Hole Migration Rates in TiO₂ from Density Functional Theory. *Journal of Physical Chemistry C* **2008**, *113* (1), 346-358.

101. Christensen, P. A.; Egerton, T. A.; Wright, N. G. Electrochemical Device. WO/2006/024869, 09 March 2006, 2006.
102. Anderson, P. W., Absence of Diffusion in Certain Random Lattices. *Physical Reviews* **1958**, *109* (5), 1492-1505.
103. Miller, A.; Abrahams, E., Impurity Conduction at Low Concentrations. *Physical Reviews* **1960**, *120* (3), 745-755.
104. Fox, M. A.; Chen, C. C., Mechanistic features of the semiconductor photocatalyzed olefin-to-carbonyl oxidative cleavage. *Journal of the American Chemical Society* **1981**, *103* (22), 6757-6759.
105. Haick, H.; Paz, Y., Remote Photocatalytic Activity as Probed by Measuring the Degradation of Self-Assembled Monolayers Anchored near Microdomains of Titanium Dioxide. *Journal of Physical Chemistry B* **2001**, *105* (15), 3045-3051.
106. Haick, H.; Paz, Y., "Dark" Photocatalysis: The Degradation of Organic Molecules Anchored to Dark Microdomains of Titanium Dioxide. *ChemPhysChem* **2003**, *4* (6), 617-620.
107. Kawahara, K.; Ohko, Y.; Tatsuma, T.; Fujishima, A., Surface diffusion behavior of photo-generated active species or holes on TiO₂ photocatalysts. *Physical Chemistry Chemical Physics* **2003**, *5* (21), 4764-4766.
108. Salvador, P.; Gutierrez, C., The nature of surface states involved in the photo- and electroluminescence spectra of n-titanium dioxide electrodes. *Journal of Physical Chemistry* **1984**, *88* (16), 3696-3698.
109. Salvador, P., Subbandgap photoresponse of n-TiO₂ electrodes: Transient photocurrent-time behaviour. *Surface Science* **1987**, *192* (1), 36-46.
110. Salvador, P., Kinetic approach to the photocurrent transients in water photoelectrolysis at n-titanium dioxide electrodes. 1. Analysis of the ratio of the instantaneous to steady-state photocurrent. *Journal of Physical Chemistry* **1985**, *89* (18), 3863-3869.
111. Chongyang, L.; Yixuan, C.; Wenzhao, L., Direct observation of elementary steps in charge transfer mediated by surface states on TiO₂ electrode under illumination. *Surface Science* **1985**, *163* (2-3), 383-390.
112. Laser, D.; Gottesfeld, S., Photocurrents Induced by Subbandgap Illumination in a Ti-Oxide Film Electrode. *Journal of The Electrochemical Society* **1979**, *126* (3), 475-478.

113. Paulik, M. G.; Brooksby, P. A.; Abell, A. D.; Downard, A. J., Grafting Aryl Diazonium Cations to Polycrystalline Gold: Insights into Film Structure Using Gold Oxide Reduction, Redox Probe Electrochemistry, and Contact Angle Behavior. *Journal of Physical Chemistry C* **2007**, *111* (21), 7808-7815.
114. Chowdhury, A.-N.; Alam, M. T.; Okajima, T.; Ohsaka, T., Fabrication of Au(1 1 1) facet enriched electrode on glassy carbon. *Journal of Electroanalytical Chemistry* **2009**, *634* (1), 35-41.
115. Trasatti, S.; Petrii, O. A., REAL SURFACE-AREA MEASUREMENTS IN ELECTROCHEMISTRY. *Pure and Applied Chemistry* **1991**, *63* (5), 711-734.
116. Bockris, J. O. M.; Reddy, A. K. N.; Gamboa-Aldeco, M., *Modern Electrochemistry 2A*. Kluwer Academic/Plenum Press: 2000.
117. Burke, L. D.; Nugent, P. F., The electrochemistry of gold: I the redox behaviour of the metal in aqueous media. *Gold Bull* **1997**, *30* (2), 43-53.
118. Bard, A. J.; Parsons, R.; Jordan, J., *Standard Potentials in Aqueous Solution*. 5th ed.; Marcel Dekker: New York, 1985.
119. Rogers, E. I.; Silvester, D. S.; Aldous, L.; Hardacre, C.; Compton, R. G., Electrooxidation of the Iodides [C4mim]I, LiI, NaI, KI, RbI, and CsI in the Room Temperature Ionic Liquid [C4mim][NTf2]. *The Journal of Physical Chemistry C* **2008**, *112* (16), 6551-6557.
120. Hamnett, A., Semiconductor Electrochemistry. In *Electrode Kinetics: Reactions*, Compton, R. G., Ed. Elsevier: Amsterdam, 1987; Vol. 27, pp 62 - 242.
121. Qi, P. H.; Hiskey, J. B., Electrochemical behavior of gold in iodide solutions. *Hydrometallurgy* **1993**, *32* (2), 161-179.
122. Marsden, J. O.; House, C. I., *The Chemistry of Gold Extraction*. 2nd ed.; Society for Mining, Metallurgy and Exploration: Littleton Co, USA, 2006.
123. Purrington, S. T.; Kagen, B. S.; Patrick, T. B., Application of elemental fluorine in organic synthesis. *Chemical Reviews* **1986**, *86* (6), 997-1018.
124. Roland, U.; Salzer, R.; Summchen, L.; Can, L.; Qin, X., Electronic Effects of Hydrogen Spillover on Titania. In *Studies in Surface Science and Catalysis*, Elsevier: 1997; pp 339-348.
125. Herrmann, J.-M.; Guerrero-Ruiz, A.; Rodriguez-Ramos, I., Electronic Processes in Hydrogen Spillover. In *Studies in Surface Science and Catalysis*, Elsevier: 2001; pp 189-196.

126. Roland, U.; Roessner, F.; Can, L.; Qin, X., A New Model on the Nature of Spillover Hydrogen. In *Studies in Surface Science and Catalysis*, Elsevier: 1997; pp 191-200.
127. Christensen, P. A.; Carroll, M. A.; Linares-Moya, D.; Molyneux, D.; Rosamond, M. C.; Wood, D., A Novel Composite Anode: The Electrooxidation of Organic Molecules via Formation of Highly Energetic Holes. *The Journal of Physical Chemistry C* **2011**, *115* (21), 10777-10783.
128. Fujishima, A.; Rao, T. N.; Tryk, D. A., Titanium dioxide photocatalysis. *Journal of Photochemistry and Photobiology C: Photochemistry Reviews* **2000**, *1* (1), 1-21.
129. Poll, W.; Pawelke, G.; Mootz, D.; Appelman, E. H., The Crystal Structure of Hypofluorous Acid: Chain Formation by O-H...O Hydrogen Bonds. *Angewandte Chemie International Edition in English* **1988**, *27* (3), 392-393.
130. Momota, K.; Yonezawa, T.; Mukai, K.; Morita, M., Competitive fluorination on methyl-group and benzene-ring during the anodic fluorination of fluorotoluenes in Et₄NF center dot mHF. *Journal of Fluorine Chemistry* **1998**, *87* (2), 173-178.
131. Yazami, R. Fluoride Ion Electrochemical Cell. US8377586 B2, 2013.